Effects of the dipole-dipole interaction on the physics of ultracold quantum gases

Marta Abad Garcia

PhD Thesis

EFFECTS OF THE DIPOLE-DIPOLE INTERACTION ON THE PHYSICS OF ULTRACOLD QUANTUM GASES

Marta Abad Garcia

Universitat de Barcelona

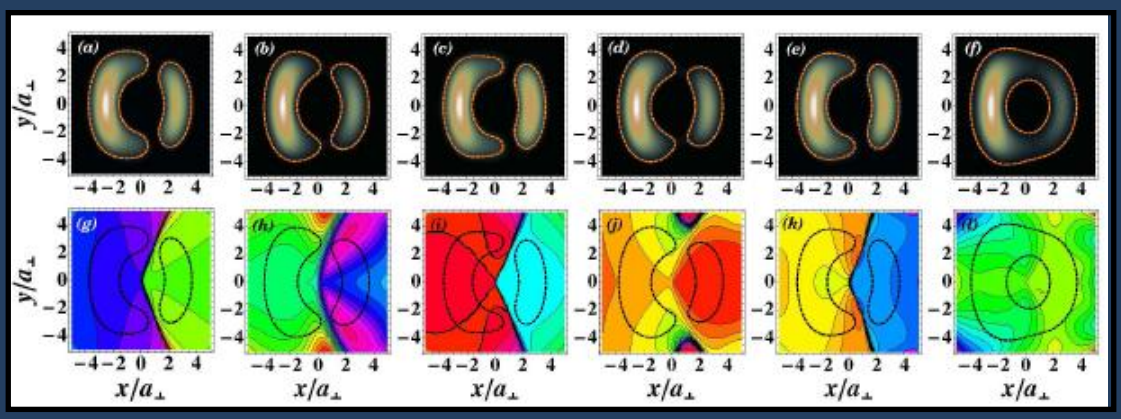

Tesi doctoral - PhD Thesis

Universitat de Barcelona

EFFECTS OF THE DIPOLE-DIPOLE INTERACTION ON THE PHYSICS OF ULTRACOLD QUANTUM GASES

Marta Abad Garcia

Directors:

Dra. Montserrat Guilleumas Morell

Dr. Martí Pi Pericay

Tesi doctoral presentada a la Universitat de Barcelona, dins del programa de doctorat de Física. Curs 2011/12.

Doctoral thesis presented in the University of Barcelona, within the PhD program of Physics. Academic year 2011/12.

Al meu avi,
Àngel Garcia Gual

Contents

List of Figures

List of Tables

Agraïments

Hi ha molta gent que m'ha ajudat de maneres diferents al llarg de la realització d'aquesta tesi, així que m'agradaria donar-los les gràcies.

En primer lloc, vull agrair als meus directors, la Muntsa Guilleumas i el Martí Pi, el seu treball i suport durant aquests anys, i també la lectura crítica de tota la tesi. M'agradaria agrair-li a la Muntsa tot el que m'ha ensenyat, el seu temps i paciència, la seva amistat, i totes les oportunitats que m'ha donat i m'ha animat a aprofitar. M'agradaria agrair al Martí el seu temps, les discussions, les explicacions (i en molts casos calia més d'una vegada) i sobretot per insistir i mantenir el seu punt de vista. També vull agrair-li al Ricardo Mayol totes les discussions al llarg d'aquests anys, sobre física i fora d'ella, i per llegir diverses parts de la tesi. I també m'agradaria agrair al Manel Barranco el seu suport, sobretot durant el primer any, abans d'obtenir la beca.

Quiero agradecer muy especialmente a Dora Jezek la colaboración durante estos años (¡y espero que no termine!), las discusiones siempre útiles y a veces algo animadas, las carcajadas que junto con Muntsa se oían en todo el pasillo del departamento, su hospitalidad en Buenos Aires; también quiero darle las gracias por leer varias partes de esta tesis, y en general por su amistad y lindas conversaciones.

Vull donar les gràcies al Departament d'Estructura i Constituents de la Matèria i especialment a l'àrea de Física Atòmica i Nuclear. I a tots aquells que han contribuït a fer que funcionés el Journal Club (com a mínim durant un temps), el David Mateo, el José María Escartín, el Bruno Juliá, i a tota la gent que ha fet xerrades i ha participat al JC. Espero que sobrevisqui els anys que vénen (ànim, Arianna!). I també m'agradaria donar les gràcies a la gent que ha donat el seu suport i ha participat en les II Jornadas de Jóvenes Investigadores en Física Atómica y Molecular (JIIFAM) i a la que participarà al First Flash Talks Meeting, perquè sempre dóna força i motiva trobar-se a altres estudiants de doctorat, i s'aprèn molt en la organització d'aquestes trobades.

M'agradaria també agrair a les persones amb qui he compartit despatx durant aquests anys, el David Mateo, l'Alberto Hernando, el Francesc Malet i el Xavi Roca. I també al José María Escartín, amb qui no hem compartit despatx, però que és una font d'informació inigualable.

I'm very much indebted to all the group at the BEC Center in Trento for their hospitality and for a very good time during spring 2011, and very especially to Alessio Recati, Sandro Stringari, Augusto Smerzi, and also Franco Dalfovo. I'd also like to thank Alessio for reading selected parts of this thesis. And indeed, I'd like to thank the PhD's and post-docs there, Yun Li, Natalia Matveeva and Konstantin, Robin Scott, Francesco Piazza, Philipp Hyllus, Michael Klawuun und Maria, Yan-Hua Huo, Onur Umucalilar, etc., and also Beatrice Ricci, for the great fun during many discussions, pizzas, excursions and

some zombie movies.

Els estic molt agraïda a tots els meus amics de Barcelona (i voltants) pel seu suport durant tots aquests anys. Vull agrair especialment al grup de cerveses dels divendres a la tarda, l'Anna Alemany, el David Mateo, el Víctor López i la Lara, el Saül Vélez, el Miguel-Ángel Escobedo, l'Ausiàs-March, el Gianluca Arauz, i a la resta de gent que ha anat venint de tant en tant. Vull agrair al Fran Villagrasa la seva amistat durant aquests anys, els dinars a la gespa i els tès al Gòtic. I també a l'atre grup de cerveses, especialment a l'Albert Benseny, el Josep Mas i l'Osamu Takayama, que ja ens hem perdut en el recompte de cervesetes! I a l'Alberto Hernando, el Diego Villuendas, el Dani Puigdomènech, el Roger Mor, el Francesco Aprile i el Ferran Barroso, per tots els fantàstics dinars durant més d'un any, i també els prove its!

Finalment, i potser tant importants com els primers, vull agrair a la tota la meva família (o famílies) pel seu suport i per animar-me en molts moments, a la meva mare, el meu pare, el Jose, la Loli, la Vini, el meu avi Àngel, el meu avi Manel, i tota la resta. Molt especialment, vull agrair a la meva mare el seu recolzament en diversos moments difícils i per cuidar tan bé de mi aquests últims mesos.

Aquesta tesi ha estat possible gràcies a la beca FI (beca predoctoral per a la formació de personal investigador), amb el suport del Comissionat per a Universitats i Recerca (CUR) del Departament d'Innovació, Universitats i Empresa (DIUE) la Generalitat de Catalunya i del Fons Social Europeu. I també a la beca BE (beca per estades de recerca a l'estranger), amb el suport del Departament d'Universitats, Recerca i Societat de la Informació de la Generalitat de Catalunya.

Badalona,
12 de desembre de 2011

Resum / Abstract

En aquesta tesi s'estudien els efectes de la interacció dipol-dipol en la física dels gasos quàntics ultrafreds, tant de caràcter bosònic com fermiònic, i dins del marc teòric del règim de camp mig. Aquest tipus d'interacció es dóna en gasos atòmics ultrafreds (per exemple de ^{52}Cr o ^{164}Dy) a través del moment dipolar magnètic atòmic, i en gasos moleculars ultrafreds a través del moment dipolar elèctric o magnètic. La interacció dipol-dipol entre dues partícules, ja siguin àtoms o molècules, és anisòtropa i de llarg abast. La primera propietat fa que el comportament del sistema depengui molt fortament de la geometria que es considera, mentre que la propietat de llarg abast fa que una partícula pugui influir en la dinàmica d'una altra partícula que s'en troba allunyada.

En el cas de gasos quàntics d'àtoms bosònics, o condensats de Bose-Einstein, la interacció dipol-dipol es pot estudiar en aproximació de camp mig a través de l'equació de Gross-Pitaevskii, que ara conté un nou terme no-lineal degut a la interacció dipolar (a més a més del terme d'interacció de contacte o d'ona-s). Aquest terme addicional converteix l'equació en no-local. Per tal de resoldre-la, calculem el potencial dipolar de camp mig en l'espai de Fourier i fem evolucionar l'equació en temps imaginari (per tal de trobar l'estat fonamental o l'estat de vòrtex) o bé en temps real utilitzant el mètode de Hamming inicialitzat amb un mètode de Runge-Kutta de quart ordre (per tal d'obtenir l'evolució dinàmica del sistema).

Utilitzant aquests mètodes numèrics, en aquesta tesi investiguem, d'una banda, condensats dipolars confinats en trampes harmòniques, i de l'altra condensats dipolars confinats en trampes toroidals. En el primer cas ens focalitzem en l'estudi de l'estat fonamental i de l'estat de vòrtex quantitzat. L'anàlisi de l'estat fonamental ens serveix per entendre l'efecte de l'anisotropia i el llarg abast de la interacció. Les simulacions prediuen una deformació anisòtropa de la densitat atòmica, així com l'existència de densitats amb el màxim fora del centre (anomenades densitats bicòncaves o tipus glòbul vermell, en anglès dites *biconcave* o bé *red-blood-cell*, degut a la seva similitud amb les cèl·lules sanguínies). Minimitzant l'energia del condensat dipolar respecte transformacions d'escala deduïm el teorema del virial per a aquest sistema, que ens serveix per a comprovar la precisió dels resultats numèrics. Estudiant la dinàmica de les excitacions col·lectives (en concret, del mode quadrupolar radial o de superfície) veiem que la interacció dipolar en modifica la freqüència. Hem comparat els resultats numèrics obtinguts de la simulació de l'equació de Gross-Pitaevskii depenent del temps als resultats que provenen de l'aproximació de Thomas-Fermi per a condensats dipolars, trobant molt bon acord quan la correcció a la freqüència deguda a l'energia cinètica es té en compte en l'aproximació de Thomas-Fermi. Per altra banda, l'estudi dels estats de vòrtex ens permet estudiar la geometria del nucli

del vòrtex (*vortex core*) i fer una predicció de la freqüència crítica necessària per formar-ne un, així com de la barrera energètica que cal superar perquè el vòrtex es desplaci des de la superfície fins al centre del gas. Acabem l'estudi dels condensats dipolars en trampes harmòniques simulant dinàmicament la precessió d'un vòrtex descentrat en un condensat no rotant. En aquest cas veiem que l'efecte de la interacció dipolar és disminuir la freqüència de precessió, comparant amb el cas on només hi són presents les interaccions de contacte.

El segon gran tema que tractem dins dels condensats dipolars és el cas en què aquests estan confinats en trampes toroidals. En aquesta geometria els efectes dipolars es veuen fortament magnificats quan l'eix de polarització dels dipols és perpendicular a l'eix de simetria de la trampa. En el marc de la tesi hem vist que l'estat fonamental presenta una distribució anisòtropa de densitat al llarg de l'angle azimutal (és a dir, al llarg de l'anell definit per un potencial efectiu generat per la trampa toroidal i el potencial dipolar de camp mig), que es tradueix en un camp de velocitats també anisòtrop quan es consideren corrents persistents (vòrtexs metaestables). En reduir la magnitud de la interacció de contacte es produeix un trencament espontani de simetria en el sistema, on tots els àtoms es situen només en un els pics de densitat. L'estructura anisòtropa de la densitat es pot entendre com l'adaptació del sistema al potencial efectiu en forma de doble pou al llarg de l'anell. Hem estudiat la dinàmica d'aquest sistema quan el nombre inicial d'àtoms als pous de potencial de la dreta i de l'esquerra està desequilibrat, predient oscil·lacions de Josephson i d'autoatrapament (*self-trapping*) depenent de la condició inicial. Això ens ha portat a anomenar aquest nou sistema Junció de Josephson Autoinduïda (*Self-induced Josephson Junction*). Hem comprovat que aquesta dinàmica es pot estudiar dins del marc d'un model de dos modes, ja que les prediccions del model donen resultats qualitativament correctes (per exemple, l'amplitud de les oscil·lacions està en bon acord amb els resultats de la simulació numèrica de l'equació de Gross-Pitaevskii, tot i que la freqüència doni un valor més alt en el model). En una tercera fase del projecte de condensats dipolars en trampes toroidals hem estudiat en detall el règim d'autoatrapament i hem vist que la inversió del flux de partícules està fortament lligada al creuament de vòrtexs quantitzats a través de les unions de Josephson. Aquest resultat obre les portes a establir una relació més directa entre el règim dinàmic de salts de fase (*phase-slips*), àmpliament estudiat en heli superfluid, i el règim d'autoatrapament propi dels condensats.

En el cas de gasos quàntics de partícules dipolars fermiòniques, hem estudiat com les excitacions col·lectives, en concret el mode quadrupolar radial, permeten distingir entre els règims hidrodinàmic (que pot ser tant degut a la rapidesa de les interaccions com a la superfluidesa) i no-col·lisional (que té lloc quan les interaccions són a tan baixa freqüència que efectivament es poden negligir). Hem calculat la freqüència d'aquest mode analíticament en aproximació de camp mig i generalitzant els resultats de l'aproximació de Thomas-Fermi per a gasos de Fermi ideals confinats. D'una banda, observem que la freqüència en règim hidrodinàmic és menor que en gasos de fermions no-dipolars (on les col·lisions vénen donades per la interacció de contacte), mentre que en el règim no-col·lisional la freqüència és major o menor que la corresponent al sistema no interactuant depenent de la geometria de la trampa harmònica. Per altra banda, prediem que reduint la deformació de la trampa (*aspect ratio*) tindria lloc un salt observable en les mesures experimentals de la freqüència del mode quadrupolar radial, que marcaria la transició

entre el règim no-col·lisional i l'hidrodinàmic, per exemple quan tingués lloc la transició a l'estat superfluid.

§ § §

In this thesis we study the effects of the dipole-dipole interaction on the physics of ultracold quantum gases, both bosonic and fermionic, within the theoretical framework provided by the mean-field regime. This kind of interaction takes place in ultracold atomic gases (for instance ^{52}Cr or ^{164}Dy) due to their atomic magnetic dipole moment, and in ultracold molecular gases due to the magnetic or electric dipole moment. The dipole-dipole interaction between two particles, either atoms or molecules, is anisotropic and long-range. The first property causes the behavior of the system to depend rather strongly on its geometry, while the property of long-range causes a particle to influence the dynamics of a distant particle.

In the case of quantum gases of bosonic atoms, or Bose-Einstein condensates, the dipole-dipole interaction can be studied within mean-field approximation using the Gross-Pitaevskii equation, which now contains a new non-linear term due to the dipole-dipole interaction (in addition to the the *s*-wave contact term). This additional term turns the equation into a non-local equation. In order to solve it, we compute the mean-field dipolar potential in Fourier space and evolve the equation in imaginary time (to find the ground state or a vortex state) or in real time using the Hamming's method initialized with a fourth-order Runge-Kutta method (to obtain the dynamical evolution of the system).

Using these numerical methods, in this thesis we investigate, on the one hand dipolar condensates confined in harmonic traps, and on the other dipolar condensates confined in toroidal traps. In the first case, our focus is on the study of the ground state and the quantized vortex state. The analysis of the ground state helps us understand the effect of the anisotropic and long-range character of the interaction. The simulations predict an anisotropic deformation of the atomic density, as well as the existence of densities with the maximum away from the center (known as biconcave or red-blood-cell density structures, due to their similarity to the shape of red-blood cells). Minimizing the energy of the dipolar condensate with respect to scaling transformations we derive the virial theorem for this system, which we use to check the accuracy of the numerical results. By studying the dynamics of collective excitations (in particular, the radial quadrupole mode) we see that the dipolar interaction modifies the oscillation frequency. We have compared the numerical results obtained from the simulation of the time-dependent Gross-Pitaevskii equation with the results coming from the Thomas-Fermi approximation for dipolar condensates, finding a very good agreement when the correction to the frequency due to the kinetic energy is taken into account in the Thomas-Fermi approximation. On the other hand, the study of vortex states allows us to study the geometry of the vortex core and give a prediction of the critical frequency necessary to nucleate a vortex, as well as the energy barrier that has to be overcome to bring the vortex from the surface to the center of the gas. We finish the study of dipolar condensates in harmonic traps by dynamically simulating the precession frequency of an off-center vortex in a non-rotating condensate. In this case, we see that the effect of the dipolar interaction is to reduce the precession frequency, compared to the case where the only interactions present are contact interactions.

The second subject we address within dipolar condensates is the case where these are confined in toroidal traps. In this geometry the dipolar effects are strongly magnified when the polarization axis of the dipoles is perpendicular to the trap symmetry axis. Within this thesis we have seen that the ground state shows an anisotropic density distribution along the azimuthal angle (that is, along the ring defined by an effective potential generated by the toroidal trap plus the mean-field dipolar potential), which is translated into an anisotropic velocity field when persistent currents are considered (metastable vortices). When the strength of the contact interaction is reduced, the system overcomes a spontaneous symmetry breaking, characterized by all the atoms located in only one of the density peaks. The anisotropic structure of the density can be understood as the adaptation of the system to the double-well effective potential along the ring. We have studied the dynamics of this system when the initial number of atoms in the left and right wells is imbalanced, predicting Josephson and self-trapping oscillations depending on the initial condition. This has led us to name this new system as Self-induced Josephson Junction. We have checked that this dynamics can be studied within a two-mode model, since the predictions of the model give qualitatively correct results (for instance, the amplitude of the oscillations is in good agreement with the results of the numerical simulation of the Gross-Pitaevskii equation, although the frequency gives a higher value in the model). In a third step of the project on dipolar condensates in toroidal traps, we have studied in detail the self-trapping regime and we have seen that the particle flux inversion is closely related to the crossing of vortices across the Josephson junctions. This result opens the door to establishing a more direct connection between the phase-slip regime, widely addressed in superfluid helium, and the self-trapping regime of condensates.

In the case of quantum gases of fermionic dipolar particles, we have studied how the collective oscillations, in particular the radial quadrupole mode, allow one to distinguish between hydrodynamics (due either to fast interactions or to superfluidity) and the collisionless regime (where interactions take place at such a low frequency that they can be effectively neglected). We have analytically calculated the frequency of this mode in the mean-field approximation, generalizing the results from the Thomas-Fermi approximation for trapped ideal Fermi gases. On the one hand, we observe that the frequency in the hydrodynamic regime is smaller than in non-dipolar Fermi gases (where collisions come from contact interactions), while in the collisionless regime the frequency is larger or smaller than that corresponding to the non-interacting system depending on the geometry of the harmonic trap. On the other hand, we predict that reducing the trap deformation (aspect ratio) an observable jump in the frequency of the radial quadrupole mode would take place, which would correspond to the transition between the collisionless and hydrodynamic regimes, for instance when the gas undergoes the transition to the superfluid state.

Chapter 1

Introduction

But if you were worried about the price,
then why were you in the shop?

Terry Pratchett, *Equal Rites*

Bose-Einstein condensation is a many-body quantum phenomenon that takes place in dilute gases of bosonic particles when their temperature is reduced below a critical temperature, which is typically of the order of tens to hundreds of nanoKelvin. Below this temperature the de Broglie wavelengths of individual atoms become comparable to the size of the cloud and their wave functions start to overlap, giving rise to quantum coherence phenomena in the gas. The resulting many-particle state, the Bose-Einstein condensate (BEC), is characterized by the macroscopic occupation of a single-particle state.

Bose-Einstein condensation was first predicted by S. Bose [Bose24] and A. Einstein [Ein24, Ein25] between 1924 and 1925 by developing a statistical theory for an ideal gas of indistinguishable integer-spin particles (bosons). They predicted that for temperatures tending to zero the occupation number of the ground state would diverge. This strange behavior was then thought to be just a theoretical limit, until some connexion to superfluidity in He-4 was suspected in the late 30s [Lon38]. Superfluid helium, however, is not a pure Bose-Einstein condensate, since the strong interactions, large density and correlations in the liquid prevent the atoms from being all in a single-particle state. The fraction of condensed atoms in helium amounts only to about the 10 %. In contrast, atomic gases well below the critical temperature constitute pure condensed systems (for large numbers of atoms, when thermal and quantum depletion effects can be neglected).

Real systems are interacting and even at temperatures of nanoKelvins above the absolute zero, interactions between atoms are not negligible, and in fact they are very important for the physics of BECs. These interactions are usually well approximated by s-wave contact collisions, which are characterized by a single parameter: the s-wave scattering length, a. The condensate state of a gas is not the stable configuration at $T = 0$, which would be a solid, but is instead metastable. It can only be reached if the gas is weakly interacting and the density is sufficiently low (a typical order of magnitude is $n \sim 10^{14}$ atoms/cm^3), which means that the gas is dilute. The diluteness condition is satisfied if

$na^3 \ll 1$, that is when the mean interparticle distance is much larger than the scattering length. From the theoretical point of view, even if weak, interactions make the problem more difficult to solve. In 1961, Gross [Gro61] and Pitaevskii [Pit61] independently derived an equation for the condensate wave function at the mean-field level. It has the shape of a non-linear Schrödinger equation, and is known as Gross-Pitaevskii equation. This equation is widely used to address the physics of condensates (see, for instance, [Dal99]), and in particular the results in this thesis are based on the Gross-Pitaevskii framework (except for those in Chapter 8, where we deal with fermions instead of bosons).

Bose-Einstein condensation was first achieved in 1995 using ^{87}Rb [And95] and ^{23}Na [Dav95] atoms in the University of Colorado and in the Massachusetts Institute of Technology, respectively[1]. The first BECs were obtained with alkali atoms, since their atomic structure makes them the perfect candidates for optical cooling. The whole cooling procedure (laser cooling, trapping and evaporative cooling) was achieved in a time of the order of seconds and temperatures were reduced from about 300 K to about 100 nK (9 orders of magnitude). Figure 1.1 shows the momentum distribution at three different temperatures (higher than, of the order of and lower than the critical temperature, respectively from left to right), measured in the experiment reported in Ref. [Cor96]. The left picture shows a broad thermal distribution, while the narrow peak in the picture on the right is due to the condensate. Since the early experiments, Bose-Einstein condensation has been achieved in a number of atomic species: ^{87}Rb [And95], ^{23}Na [Dav95], ^{7}Li [Bra95], H [Fri98], ^{39}K [Mod01], He* [Rob01], Cs [Web03], ^{174}Yb [Tak03], ^{52}Cr [Gri05], ^{40}Ca [Kra09], ^{84}Sr [Ste09, Mar09], ^{164}Dy [Lu11]. The case of ^{7}Li is special because s-wave interactions are attractive, so that the condensate is in general unstable. Metastable helium, He*, is also a special case: since the ground state of helium at low temperatures leads to a liquid phase, it has to be condensed not on the atomic ground state but in an excited state. Chromium (and also dysprosium) is also particular, since it has a large dipole moment that affects some aspects of the physics of condensates. Apart from the atomic condensates listed above, homonuclear molecules (such as Li_2 [Joc03, Zwi03] and K_2 [Reg04]) have been cooled down to condensation. Spinor condensates (where different hyperfine components are condensed) and mixtures (condensates involving more than one species) are also accessible in experiments. Condensation of bosonic particles has also motivated the achievement of an atomic degenerate Fermi gas (for instance, with ^{6}Li, ^{40}K, etc.), focusing especially on reaching the superfluid phase. Nowadays strong experimental effort is devoted to cool down to degeneracy a gas of heteronuclear molecules [Ni08, Mir11]. Such a system possesses an electric dipole moment (instead of magnetic) which can be tuned by changing the applied electric field. In this way, strong dipolar effects can be achieved.

The experimental realization of a Bose-Einstein condensate of chromium atoms [Gri05, Bea08] has encouraged research on the new field of dipolar gases at very low temperature. While the contact interaction is isotropic, the dipolar potential is anisotropic and long range. The atom-atom interaction is then determined by the balance of both

[1] This led to the Nobel Prize in Physics 2001 to Eric A. Cornell, Wolfgang Ketterle and Carl E. Wieman "for the achievement of Bose-Einstein condensation in dilute gases of alkali atoms, and for early fundamental studies of the properties of the condensates".

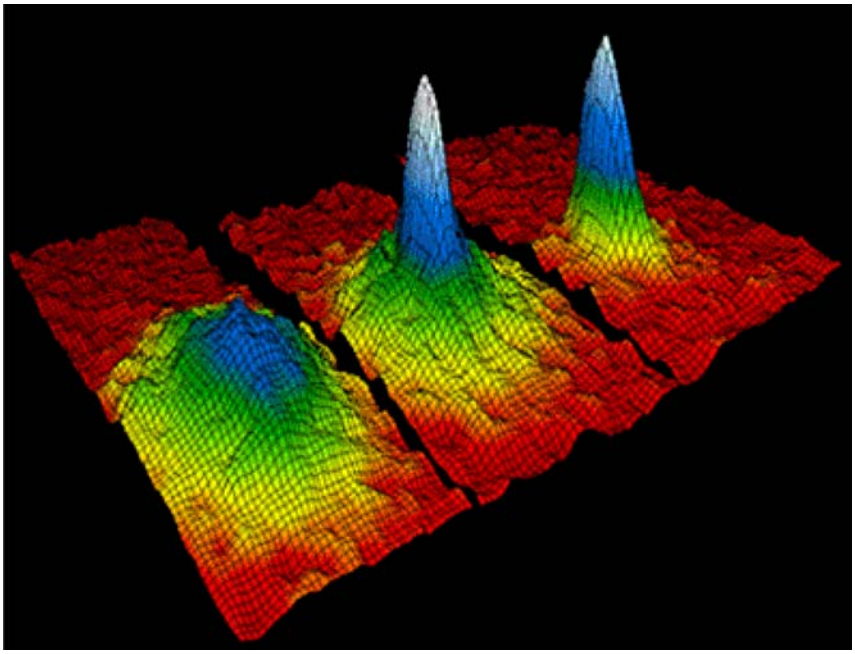

Figure 1.1: Experimental realization of a Bose-Einstein condensate. From left to right, the momentum distribution in the gas is shown for three different decreasing temperatures. In the left, above the critical temperature, the gas shows a broad momentum distribution, indicating a thermal cloud. In the right, below the critical temperature, the gas forms a condensate and the momentum distribution becomes very narrow. For intermediate temperatures, the thermal and condensed atoms coexist, showing a bimodal distribution. From Ref. [Cor96].

potentials, giving rise to interesting phenomena in a dipolar Bose-Einstein condensate (dBEC) (see [Lah09] for a review). One of the most astounding and clear effects of the presence of dipolar interactions in a condensate is their anisotropic character, which shows up in the density distribution and becomes even clearer in expansion experiments, where it can lead to inhibition of the condensate inversion [Lah07]. The anisotropy of the dipole-dipole interaction affects the stability of the condensate, which in contrast to s-wave condensates crucially depends on the trap geometry, the scattering length, the magnetic (or electric) moment of the atoms and the number of trapped dipoles [Gor00, San00, Dell04, Ebe05, Ron07, Dut07, Koch08]. For certain values of the strength of the dipolar interaction and the trap anisotropy, the appearance of new structured biconcave ground states has been predicted [Ron07, Dut07] close to the instability threshold. The problem of collapse has been a main subject of intensive experimental [Lah08, Metz09] and theoretical investigations [Tic08, Par09, Wil09b]. In contrast to s-wave condensates, collapse in dipolar condensates can be either global or local. The first is due to the attractive interactions, as in s-wave condensates (see, for instance, [Lah09]), but in dipolar condensates the anisotropic and long range nature of the interactions leads to d-wave collapse, as shown in Fig. 1.2. The second, however, is closely related to the roton-maxon spectrum that dipolar condensates present [San03, Maz09], in contrast to s-wave condensates. When the roton mode touches zero the dipolar condensate becomes unstable [Ron07]. In dipolar Fermi gases this leads to density-wave structures [Sun10], while the

absence of a stabilizing Fermi energy in dBECs leads to structured collapse [Lah08, Par09].

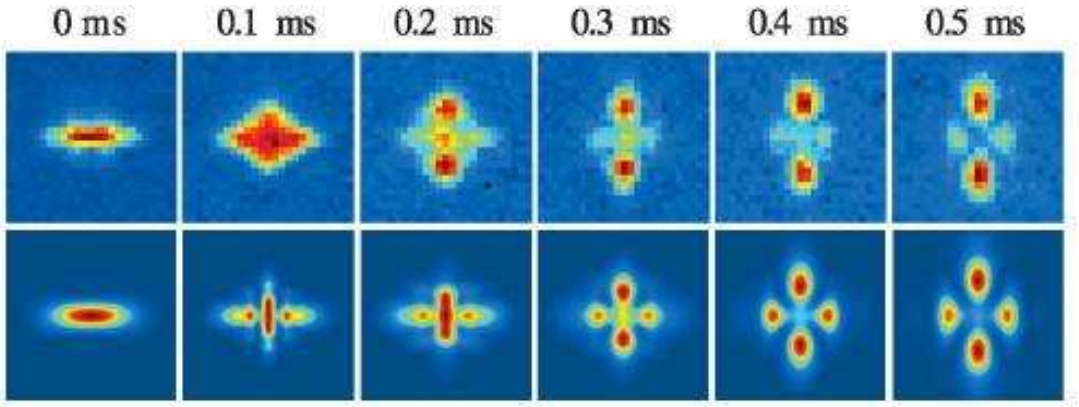

Figure 1.2: Experimental (top row) and numerical (bottom row) collapse structures in dipolar condensates. From Ref. [Lah08].

Analogously to *s*-wave condensates, the behavior of collective excitations in a dipolar gas constitutes a subject of strong interest. The reason lies in the fact that collective modes give information about the equation of state of the system or its collisional regime. This is of special importance in dipolar Fermi gases, as we will see later. In dBECs collective excitations have received much attention [Gor02, Yi02, Dell04, Ron06a, Bis10, Bij10]. Dipolar interactions affect the frequency of different modes, compared to *s*-wave interactions. In this thesis we will mainly focus on the radial quadrupole mode.

Quantized vortex states are a clear signature of the superfluid state of matter. In superfluid He they have received much attention [Don91], but their observation is very difficult since the vortex core is very small. In contrast, the tunability of BECs and the experimentalists' ability to control their properties in a very precise way offer a new mechanism to observe and study vortices. The first vortex experiments in BECs were reported in Refs. [Mat99, Mad00, Abo01], where by expanding the condensate cloud a single vortex was seen as a high depletion region in the density. In analogy to helium, vortex states in BECs can be generated by rotating the confining potential. As shown in Fig. 1.3, for small rotation frequencies the condensate shows no vorticity, while above a critical rotation frequency the superfluid responds to rotation by nucleating a quantized vortex line. If the trap is rotated faster, several vortices can be nucleated and they organize themselves in a triangular Abrikosov lattice [Abo01].

Dipolar interactions introduce a new degree of freedom in the physics of vortices in BECs, and dipolar condensates constitute a unique testing ground of the interplay between different interatomic interactions in the superfluid properties. Although vortices have not been experimentally observed in dBECs yet, much insight has been gained from the theoretical side. The anisotropy of the interaction has been seen to affect both the structure of the core [Yi06], which becomes anisotropic, as well as the patterns that vortex lattices form, which can part from the Abrikosov structure and display other lattice kinds [Coo05, Zha05, Yi06, Kom07]. Again, the density deformation introduced by the vortex

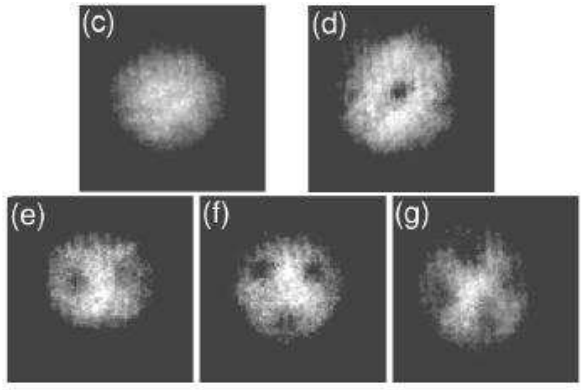

Figure 1.3: Experimental pictures showing the vortex nucleation process in a Bose-Einstein condensate. In (c) the initial vortex-free state is shown. In (d)–(g) states with one, two, three and four vortices are shown, respectively. From Ref. [Mad00].

has been related to the existence of a roton mode [Wil08]. The critical frequency for vortex nucleation has been calculated and has been shown to depend on the trap anisotropy and the scattering length [Dell07, Abad09, Yuce10]. On the other hand, the presence of vortices affects the stability of a dipolar condensate [Wil08, Yi06]. In Ref. [Wil09a], the authors have studied the stability and excitations of singly and doubly quantized vortices in dipolar BECs, while in Ref. [Kla09] a phase transition has been predicted between straight and twisted vortex lines. Also, the transverse instability of vortex lines has been studied in Ref. [Kla08]. The onset of instability to vortex formation in rotating dBECs has been addressed [Bij07, Bij09], as well as the critical frequencies for the appearance of one and several vortices in a quasi-2D geometry [Tic10, Mal11a].

Since the s-wave scattering length can be experimentally controlled, it is appealing to study vortex states in different regimes, going from a purely dipolar (i.e. $a = 0$) to a purely contact interaction condensate, passing through BECs with both s-wave and dipolar interactions. As a tends to zero, the dipolar interaction becomes comparatively stronger and its effect on the physics of vortices is enhanced. In the framework of this thesis we consider vortex states in three-dimensional rotating dipolar condensates. Concerning this subject, our aim is to investigate the effect of the dipolar interaction on the vortex properties when the contact interaction is low enough to consider that the dipole-dipole interaction is dominant.

The availability of dBECs in harmonic traps [Gri05, Bea08] opens the possibility of studying their properties in more complex confining potentials. Optical lattices have been addressed in the literature (see the review [Tre11] and references therein), as well as double-well potentials [Xio09, Asad09]. More recently, toroidal traps [Abad10a, Zol11, Mal11b] have also been considered, and ring-shaped optical lattices [Maik11]. Experimentally, toroidal traps can be realized, for instance, by shining the condensate with a blue-detuned laser beam [Ryu07]. Due to the anisotropic character of the dipole-dipole interaction, the properties of a dipolar condensate are critically determined by the toroidal geometry of the confining potential, especially in those situations where the trap symmetry axis and the magnetization direction are not parallel. In the context of this thesis we concentrate in the particular situation in which the magnetization direction is perpendicular to the trap symmetry axis. Under this circumstance, the density does not conserve the azimuthal symmetry of the confining potential, but presents two well defined peaks in the direction

perpendicular to the magnetization. When the scattering length is reduced the height of these peaks increases. This effect has also been predicted in dipolar Fermi gases confined in very narrow rings [Dut06, Zol11], and in ring-shaped optical lattices [Maik11]. For a small enough value of the scattering length, just above collapse, one of the density peaks disappears, giving rise to a symmetry breaking phenomenon. Spontaneous symmetry breaking in quantum gases has recently attracted a lot of interest, especially in double-well confining potentials. Within the framework of dipolar condensates, symmetry breaking phenomena have been predicted to appear in external double wells [Xio09, Asad09]. In Ref. [Xio09], the authors have observed that depending on the magnetization direction the system undergoes a symmetry breaking, while in Ref. [Asad09] it is the strength of the dipolar interaction that drives the same kind of phenomenon.

Regarding vortex states, it has been recently shown that purely *s*-wave condensates in toroidal traps are capable of sustaining (metastable) vortex states, which produce observable persistent flows [Ryu07]. This fact has attracted renewed interest in the physics arising in multiply connected geometries. In particular, in the past years, the formation [Wei08], stability [Cap09], dynamics [Mas09, Cat09], and dissipation [Pia09] of vortices in toroidal traps have been investigated. The particular characteristics of dipolar interactions in BECs raise numerous questions regarding the physics of vortices in such systems. In this work we study stationary vortex states whose vorticity is along the symmetry axis of the toroidal trap. Since the dipolar interaction introduces an angular density structure, the velocity field of the vortices is accordingly modified. To gain insight into this effect, we study the velocity fields created by phase-imprinted vortex states as a function of the scattering length, i.e. of the angular anisotropy of the condensate density. Similar results have been obtained in Ref. [Mal11b], where an exhaustive study of the persistent currents in a 2D dipolar condensate confined in a toroidal trap is reported. In this case the tunability of the dipolar interaction comes from the polarization angle with respect to the trap axis, instead of the tuning of the *s*-wave scattering length.

The density distribution that dBECs show in toroidal traps can be understood in terms of an effective ring-shaped potential with two Josephson junctions. The potential landscape of this system shows two wells where the density is maximum and two barriers separating them. There exists therefore a clear analogy between this configuration and a two-well system, but now, due to the annular geometry, with two weak links instead of one. This opens the possibility of studying self-induced Josephson junctions [Abad11a].

Josephson effects are a signature of quantum coherence in macroscopic many-body systems. Firstly predicted and observed when two superconductors were connected through a weak link (see [Tin96]), Josephson effects have also been experimentally observed in a variety of systems: in superfluid helium flowing through a sub-micrometer aperture [Ave95] and through an array of nano-apertures [Per97, Hos05]; in contact-interacting BECs confined in a double-well trap [Alb05, Levy07] and in an optical lattice [Cat01]; and recently in exciton-polariton systems in semiconductors [Lag10]. All these systems are realizations of a Josephson junction. Internal Josephson dynamics has been also experimentally observed between different hyperfine states of a spinor Bose-Einstein condensate [Zib10]. In Bose-Einstein condensates, due to the nonlinearity introduced by the s-wave contact

interaction, there appears a new phenomenon called macroscopic quantum self-trapping [Sme97, Rag99, Alb05], characterized by the locking of most of the atoms in one of the two wells. Figure 1.4 shows the experimental measurement of the oscillations in a double-well potential [Alb05].

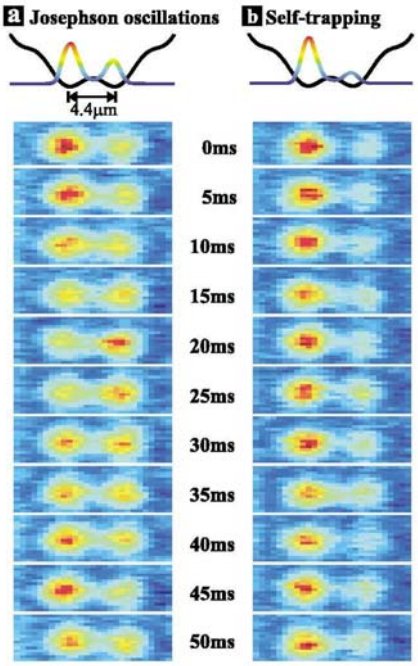

Figure 1.4: Absorption images during Josephson (left) and self-trapping (right) oscillations of a condensate confined in a double-well potential. In the Josephson regime the atoms tunnel back and forth between the two wells, while in the self-trapping regime the atoms remain mostly in the left well. From [Alb05].

Josephson dynamics in dipolar condensates [Xio09, Asad09] and in spinor dipolar condensates [Yas10] has been addressed in the literature for external double well potentials, but in this thesis we investigate the behavior of a junction created by the dipolar interaction itself. We show that this self-induced Josephson junction (SIJJ) is capable of sustaining Josephson oscillations, as well as macroscopic quantum self-trapping, in complete analogy with previous works with purely s-wave [Sme97, Alb05] or purely dipolar [Xio09, Asad09] condensates in external double-well potentials.

Looking in detail into the self-trapping regime of the SIJJ we show that it is closely related to phase-slip dynamics [Abad11b]. Phase-slippage is a dynamical process generally related to AC Josephson junctions (see, for instance, Refs. [Tin96] and [Don91]). In this regime the phase difference increases linearly in time and proportionally to the external voltage applied or chemical potential difference between two superfluid baths. This linear growth can be interpreted as a periodic change of the phase difference by an amount of 2π, or as the system periodically undergoing a phase-slip. The current understanding is that phase slips are related to the dynamical creation of vortices, which cross the flow path and leave a 2π phase behind [And66]. This process has been widely addressed in superfluid helium (see, for instance, [Don91]) and is receiving increasing attention in BECs [Pia09, Pia11, Ram11].

Chromium atoms are not the only system where dipolar effects are present. Very recently, dysprosium, ^{164}Dy, has been condensed [Lu11], with a magnetic dipole moment larger

than ^{52}Cr atoms. On the other hand, the availability of heteronuclear molecules close to degeneracy [Ni08], for which the electric dipole moment would be externally controllable, offers a new and unique framework. Up until now the molecules in the experiments have been of fermionic character, which has encouraged strong research in dipolar Fermi gases. Fermi gases, in contrast to Bose gases, do not condense at low temperatures, since the Pauli exclusion principle does not allow two fermions to occupy the same state; instead, fermions become degenerate at ultracold temperatures. This means that all the states are occupied up to the Fermi energy. In the presence of interactions, there exists a phase transition between the normal (degenerate) gas and the superfluid state [Gio08], which can either appear due to Cooper-pairing of fermions, condensation of molecular dimers, or in the unitarity regime. In a polarized Fermi gas, where s-wave interactions are suppressed, dipolar interactions can lead to superfluidity via p-wave pairing [Bar04].

As well as in condensates, collective excitations in dipolar Fermi gases can provide indirect information about the equation of state [Sogo09, Lima10a, Lima10b], long-range effects [Hua10, Mat11], collisional regimes, etc. In particular, a good candidate to experimentally determine in which phase the gas is is the frequency of the radial quadrupole mode, which has a different value for hydrodynamic systems and a collisionless gas. Notice however that hydrodynamics in a Fermi gas can be reached either when the gas is in the collisional regime (where hydrodynamics is guaranteed by collisions that are much faster than a characteristic oscillation period of the process under study) or in the superfluid regime (where hydrodynamics comes from quantum coherence).

In this thesis we calculate the frequency of the radial quadrupole mode for a dipolar Fermi gas [Abad11c], both in the collisionless as well as in the hydrodynamic regimes. This mode is much independent on the equation of state, but only depends on the collisional regime of the gas. In this way, the frequency in the hydrodynamic regime differs from that in the collisionless regime, but it is the same for collisional fermions or superfluid systems. In the hydrodynamic regime, the frequency of the radial (or surface) quadrupole mode does not part greatly from the s-wave value [Lima10b], $\sqrt{2}\omega_\perp$ [Vic99]. This situation changes in the collisionless regime, where dipolar interactions can introduce large deviations from the non-interacting value, $2\omega_\perp$. We show that this difference in frequency can be used to determine whether the system lies in the hydrodynamic or collisionless regimes.

Outline of this thesis

This thesis is structured in five differentiated parts. The first part (Chapters 2 and 3) gives a theoretical introduction to dBECs and vortex states in a condensate. The second part (Chapters 4–7) is devoted to the results obtained concerning dipolar Bose-Einstein condensates and quantized vortices in such systems. The third part (Chapter 8) introduces ultracold dipolar Fermi gases, and establishes a possible method to distinguish between the normal and superfluid phases of the gas, or between the collisionless and collisional hydrodynamic regimes, through the frequency of the quadrupole mode. The fourth part (Chapter 9) draws the conclusions of the work, and gives some possible issues for the future. Finally a few appendices are presented to complement the information given in the main text. The information is organized as follows.

In Chapter 2 the main aspects of the mean-field theory of dipolar condensates relevant

for the results presented are derived. In Sec. 2.1 we describe the two kinds of interactions that are present in dBECs: s-wave interactions and dipolar interactions. Using the expression of these two-body interactions, we derive in Sec. 2.2 the Gross-Pitaevskii equation for a dipolar condensate. This is the equation that we solve numerically throughout the work. The chapter ends with the Thomas-Fermi approximation of both a purely s-wave condensate and a dipolar condensate, Sec. 2.3.

Chapter 3 is devoted to the physics of vortices in condensates. We first write the hydrodynamic equations for a dBEC and describe the velocity field of a vortex in Sec. 3.1, giving its main properties. In Sec. 3.2 we address the topic of the vortex core, deriving the density profile for a vortex state in a trapped non-interacting condensate, and discussing structure of a vortex in the interacting gas in terms of the healing length, both in the uniform case and the trapped gas in the Thomas-Fermi regime. The phenomenology regarding vortex states in BECs is briefly reviewed in Sec. 3.3, commenting the experiments most related to this thesis. In Sec. 3.4 the Gross-Pitaevskii equation is written in the rotating frame, which allows to find a way of calculating the critical rotation frequency for vortex nucleation. In Sec. 3.5 some considerations to the numerical generation of vortex states are discussed.

Harmonically confined dipolar condensates are discussed in Chapter 4. We start in Sec. 4.1 by describing the ground state of a dipolar condensate, focusing especially on the effect of the anisotropic character of the interaction on the condensate density. We see that for a certain combination of dipolar strength and trap geometry, biconcave density structures can exist. In Sec. 4.2 we derive the virial theorem for a dBEC by minimizing the energy with respect to a scaling transformation of the density. Section 4.3 is devoted to the frequency of the radial quadrupole mode, which is analyzed both numerically by solving the Gross-Pitaevskii equation and analytically within the Thomas-Fermi approximation.

Chapter 5 addresses quantized vortices in harmonically confined dipolar condensates. In Sec. 5.1 we study the structure and formation of centered vortex lines. We describe the structure of the vortex core and how it changes due to the presence of dipolar interactions. The critical frequency for vortex formation is calculated as a function of the scattering length, and the energy barrier the system needs to overcome to nucleate a vortex in the center is presented, together with an estimation obtained from Thomas-Fermi results. Finally, in Sec. 5.2 the effect of dipolar interactions on the precession frequency of an off-centered vortex is studied.

In Chapter 6 we consider a dipolar condensate confined in a toroidal trap, with the dipoles aligned perpendicularly to the trap axis. We first describe the ground state configuration in Sec. 6.1, which shows an anisotropic density structure along the ring. This affects the vortex velocity field, which is analyzed in Sec. 6.2 for one and two vortex states.

In Chapter 7 the anisotropic density structures predicted in Chapter 6 are shown to work as a Josephson junction when an initial population imbalance is introduced between the two wells. In Sec. 7.1 we characterize such a junction, showing that it sustains both Josephson oscillations and a self-trapping regime. In Sec. 7.2 we develop a two-mode model to describe the junction and compare the results with those obtained numerically. The self-trapping regime of the self-induced Josephson junction is studied in detail in Sec. 7.3 and it is shown to be related to a phase-slip dynamics characterized by the crossing of vortices through the junctions.

In Chapter 8 we move to dipolar Fermi gases, and in particular we concentrate on how dipolar interactions affect the frequency of the quadrupole mode, which is insensitive to the equation of state of the system and allows us thus to distinguish between different collisional regimes.

Finally, some appendices are given at the end to complement the information of the main block of the thesis. In Appendix A we describe the imaginary-time step method, which has been used to numerically find stationary solutions of the Gross-Pitaevskii equation. Appendix B addresses the Hamming's method (predictor–corrector–modifier) used to solve the time dependent Gross-Pitaevskii equation. Appendix C introduces the 4th-order Runge-Kutta method, used both to initialize the Hamming's algorithm and to solve the equations of the two-mode model for a Josephson junction. We also derive, in Appendix D, the Gross-Pitaevskii equation by applying a variational procedure to the action integral and the energy functional. In Appendix E we develop in detail the quantum harmonic oscillator, from which the ground state of a trapped non-interacting quantum gas can be built. In Appendix F we derive the two-mode equations for a self-induced Josephson junction. Lastly, we devote Appendix G to derive the 3D and radial virial expressions for dipolar gases using the method of commutators, instead of the variations of the energy functional addressed in Chapters 4 and 8.

Chapter 2

Dipolar Bose-Einstein condensates

Bose-Einstein condensation is a quantum many-body effect that appears in a gas of bosons at very low temperature. Such a system is described by the Hamiltonian

$$H = \sum_{i=1}^{N} -\frac{\hbar^2}{2m}\nabla_i^2 + \sum_{i=1}^{N} V_{\text{ext}}(\mathbf{r}_i) + \sum_{i<j} v_{\text{int}}(\mathbf{r}_i, \mathbf{r}_j) \ , \tag{2.1}$$

where N is the number of particles (atoms or molecules), $\hbar$ is the reduced Planck constant ($\hbar = h/2\pi$, with h the Planck constant), m is the mass of a particle, V_{ext} is a one-body external potential and v_{int} is a two-body interaction potential. In many experimental situations V_{ext} can be approximated by a harmonic potential, which in absence of interactions leads to the quantum harmonic oscillator Hamiltonian (see Appendix E). In general, however, interactions are not negligible and they introduce important effects in the physics of the condensate. They also make the exact problem very difficult to solve, and approximations have to be made. One of the most adopted approximations is to consider interactions within a mean-field framework, analogously to the Hartree-Fock theory for fermions. This is equivalent to developing a semiclassical theory for condensates, which captures the main features of the system, but fails to describe for instance correlations between particles. In the situations we will explore within this thesis, the mean-field framework is the most suitable.

The main aim of this chapter is to review the mean-field formalism leading to the Gross-Pitaevskii equation. First, in Sec. 2.1 we describe the two-body interactions that are present in a dipolar Bose-Einstein condensate, namely s-wave contact interactions (Sec. 2.1.1) and dipole-dipole interactions (Sec. 2.1.2). At this point, in Sec. 2.2, we introduce the mean-field formalism, in which the large number of atoms in the lowest energy state allows one to treat the field operators as complex numbers, yielding the time-dependent (Sec. 2.2.1) and stationary (Sec. 2.2.2) Gross-Pitaevskii equations for a dipolar condensate. When the confining potential is harmonic, it provides characteristic length and energy scales that can be used to find a dimensionless form of the Gross-Pitaevskii equation, from which it is easy to identify the relevant parameters that will play a role in the physics of dipolar condensates (Sec. 2.2.3). The applicability conditions of the mean-field theory for condensates and its limitations are discussed (Sec. 2.2.4). Finally, in Sec. 2.3, we address an important limit of the Gross-Pitaevskii equation, known as the

Thomas-Fermi regime, where the quantum pressure term can be neglected. For a purely s-wave condensate (Sec. 2.3.1), the Thomas-Fermi approximation provides with analytical solutions to most problems, and some of them have become "pocket" formulae to find the order of magnitude of some important quantities. For dipolar condensates (Sec. 2.3.2), the Thomas-Fermi approximation becomes more complicated, but still provides a set of equations that are easier to solve than the Gross-Pitaevskii equation.

2.1 Two-body interactions

2.1.1 Two-body contact interaction: the s-wave scattering length

When temperature is very low in a gas, the number of open scattering channels is drastically reduced. If, moreover, the gas is dilute (meaning that the interparticle distance is much larger than a characteristic scattering length) the only open channel for identical bosonic particles is the s-wave channel. This means that the only relevant two-body collisions taking place are those where the relative angular momentum between the atoms is zero. Also, many-body collisions are suppressed for both the diluteness and the low temperature conditions. In a Bose-Einstein condensate, therefore, atoms collide mainly via two-body s-wave interactions. For fermionic atoms notice that the situation is quite different, since the Pauli exclusion principle precludes two identical fermions from being in the same state, that is from colliding via the s-wave channel. Therefore, in a polarized fermionic gas interactions are suppressed and the system acts as an ideal gas (there are residual p-wave and higher order interactions but their strength is so small that in most cases they can be effectively neglected). In contrast, in unpolarized or several-species Fermi gases, s-wave interactions remain as the most important contribution to the scattering process.

If one looks at the two-body interaction potential, two main regions can be distinguished. In terms of the relative coordinate $\mathbf{r} = \mathbf{r}_1 - \mathbf{r}_2$ one can define the range of the potential r_0. For $r > r_0$ the potential is dominated by a r^{-6} tail (van der Waals interactions), which is very small in atomic collisions and can in general be neglected[1]. For $r < r_0$ the potential has some structure: for instance, it might show a minimum and then a repulsive barrier for $r \to 0$. There might or might not be a (weakly) bound state in this minimum.

From the point of view of scattering theory, it is important to know the behavior of the scattered wave function at large r. Since we are dealing with ultracold systems, the relevant scattering process occurs at an energy $E \to 0$, that is, at a wave vector $k \to 0$. The behavior of the scattered wave function can be learned by expanding it in partial waves (that is, in the basis characterized by the quantum number of total angular momentum ℓ); in the low energy limit, the term that contributes most to the process is the $\ell = 0$ term (s-wave term). It introduces a phase-shift $\delta_0 = -ka$, giving rise to a total

[1]This is not so when helium superfluids or molecular condensates are considered, since there van der Waals interactions can be large. Also, one has to be cautious in dipolar condensates, especially when the dipole moment is very large. In these situations the atoms might notice each other even at long separations.

cross section $\sigma = 8\pi a$ for identical bosons. This scattering theory is discussed in detail in Refs. [Pet02, Pit03].

It turns out that for condensates the microscopic details of the scattering potential are in general unimportant and can be included in one parameter: the s-wave scattering length a. The two-body potential is then usually assumed to take the simplest form: a contact potential characterized by a Delta function,

$$v_{\rm sw}(\mathbf{r} - \mathbf{r}') = g\delta(\mathbf{r} - \mathbf{r}') \ , \tag{2.2}$$

where the coupling constant g is related to the s-wave scattering length through

$$g = \frac{4\pi\hbar^2 a}{m} \ . \tag{2.3}$$

The interaction potential (2.2) is often called *pseudo-potential*. The scattering length can either have positive or negative values. In the first case, which is the case of the majority of condensed atomic species, two-body interactions are repulsive and the ground state is always stable. When the scattering length is negative, contact interactions are attractive and the condensate becomes unstable if a critical number of particles, N_{cr}, is exceeded[2] (see Ref. [Dal99]). This is the case, for instance, of ^{7}Li [Bra95]. Attractive interactions, therefore, bring about instability and collapse to the system.

Although the scattering properties come fixed by the atomic species taking part in the collision, they can be manipulated externally, making use of Feshbach resonances (see, for instance, reviews [Koh06] and [Chin10]). In particular, by changing the external magnetic field present in the condensate region, the scattering length can be tuned to arbitrarily large or small, positive or negative values. In fact, at certain values of magnetic field B the scattering length diverges, and this is what is properly called a Feshbach resonance. At each side of the resonance the divergent branches of the scattering length go to $+\infty$ and $-\infty$, respectively. This fact has been of the utmost importance in superfluid Fermi gases, since the Feshbach resonance technique has allowed experimentalists to go from the $a > 0$ side of the resonance (where fermions with opposite spin feel repulsion and couple to form molecules, giving rise to a molecular BEC) to the $a < 0$ side (where the attraction leads the atoms to Cooper pairing and to a BCS superfluid). In the crossover between these two superfluids the scattering length crosses the resonance and reaches infinity, entering the regime of unitarity (sometimes also called universal regime). The unitarity regime of a Fermi gas is receiving a lot of attention in the field, since there is only one length scale in the system and therefore the gas presents universal properties (see, for instance, review [Gio08]).

In this thesis we are mainly interested in dipolar condensates, and ^{52}Cr condensates constitute their paradigmatic example. Figure 2.1 shows the Feshbach resonances of a ^{52}Cr gas, obtained experimentally by the group at Stuttgart [Wer05]. We can see that not all resonances look the same, but that there are broader and narrower ones. Since there is a limit to the precision at which the magnetic field can be experimentally controlled,

[2]For $N < N_{cr}$ the condensate is in a metastable state, provided by a local minimum of energy. For $N = N_{cr}$ this local minimum disappears and the system is brought to the global minimum, where it collapses.

in practice it might be difficult to reach all desired values of a. In this respect, wider resonances allow a better control of the zero crossing of the scattering length. This is very important in dipolar condensates, were contact interactions are always accompanied by dipolar interactions. If the scattering length can be tuned to zero, then dipolar interactions become much relevant and their effects can be addressed and measured. In chromium condensates, using the resonance at 58.9 mT, the scattering length can be controlled to a precision of ± 1 a_B [Lah07], where a_B is the Bohr radius. Even in alkali gases, which have a dipole moment much smaller than chromium atoms, the usage of wide Feshbach resonances with a soft zero crossing has led to the observation of dipolar effects in ^{39}K [Fat08] and ^{7}Li [Pol09]. There is however a limit to the tunability of the scattering length via Feshbach resonances: losses. When the scattering properties change, the probability of inelastic collisions (usually three-body recombination) is higher, and this means that atoms are lost from the condensate because they form molecules.

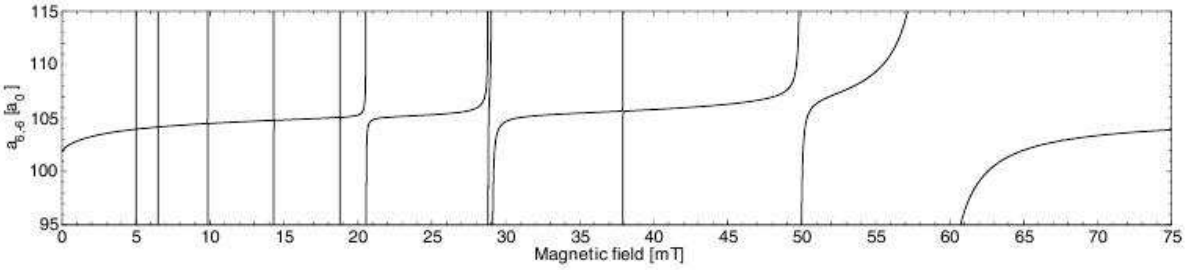

Figure 2.1: Feshbach resonance spectrum for ^{52}Cr. Taken from Ref. [Wer05].

2.1.2 Long-range interaction: the dipole-dipole interaction

Apart from the contact collisions in the paragraph above, atoms and molecules might interact through other mechanisms. For instance, charged particles feel a Coulomb potential, particles with dipole moment interact via a dipole-dipole potential, or there could also be spin-orbit coupling between different parts of the system. In this thesis we want to explore some aspects of the physics that the dipole-dipole interaction introduces in condensates (and ultracold Fermi gases in Chapter 8). This interaction occurs when particles are dipoles, that is when they possess a dipole moment, and in general in systems without a net electric charge.

There are two kinds of dipole moments that particles can exhibit: electric dipole moment (μ_e) and magnetic dipole moment (μ_m). The electric dipole moment comes from charge separation in space, for instance when an electric field is applied to a polar molecule. The electrons separate from the positively charged part of the molecule according to this field and the whole molecule becomes a dipole. The electric dipole moment is therefore tunable, since it is controlled by an external electric field. There have recently been important advances towards the achievement of ultracold quantum gases of molecules with large electric dipole moments, especially in fermionic systems [Ni08]. In these systems, extremely large dipolar effects can be achieved, since the electric dipole moment can be thousands of times larger than the magnetic dipole moment.

The second kind of dipole moment is the magnetic dipole moment. It is present in both atomic and molecular systems and it comes from the total angular momentum of atoms (that is, the combination of electronic spin, nuclear spin and orbital angular momentum). It is therefore fixed by the species we are considering. All atoms possess a magnetic dipole moment, but it is in general very small for the majority of systems that have been condensed (for example, $\mu_m \sim 1\,\mu_B$ in alkali gases, where μ_B is the Bohr magneton). However, in 2005 the group at Stuttgart achieved the first Bose-Einstein condensate of ^{52}Cr atoms [Gri05], and some years later it was also achieved by the group at Paris (Villetaneuse) [Bea08]. The particularity of chromium atoms is that their magnetic moment ($\mu_m = 6\,\mu_B$) is six times larger than in alkali atoms so that dipolar effects can be seen and tested in the real system. Recently, dysprosium (^{164}Dy) atoms have been condensed [Lu11], which possess a magnetic dipole moment larger than chromium ($\mu_m = 10\,\mu_B$). Dipolar effects can also be seen in alkali gases, despite their small magnetic dipole moment, provided the scattering length is tuned to vanishingly small values, as was proven in Refs. [Fat08] and [Pol09] for ^{39}K and ^{7}Li, respectively. The ^{52}Cr condensate is the system that we have in mind throughout most part of the thesis, although the physics exposed can be applied to other dipolar species (see Sec. 2.2.3).

The interaction between two (classical) magnetic dipoles $\boldsymbol{\mu}_1$ and $\boldsymbol{\mu}_2$ located at positions $\mathbf{r}_1$ and $\mathbf{r}_2$ (see Fig. 2.2) is given by

$$v_{\text{dip}} = -\frac{\mu_0}{4\pi}\frac{(\boldsymbol{\mu}_1\cdot\boldsymbol{\mu}_2)r_{12}^2 - 3(\boldsymbol{\mu}_1\cdot\mathbf{r}_{12})(\boldsymbol{\mu}_2\cdot\mathbf{r}_{12})}{r_{12}^5}\ , \tag{2.4}$$

with μ_0 the magnetic permeability of vacuum and $\mathbf{r}_{12} = \mathbf{r}_1 - \mathbf{r}_2$. Considering that the dipoles are identical and aligned along, say, the z direction, we have $\boldsymbol{\mu}_1 = \boldsymbol{\mu}_2 = \mu\hat{e}_z$, and the dipole-dipole potential becomes

$$v_{\text{dip}}(\mathbf{r}_1 - \mathbf{r}_2) = d^2\frac{1-3\cos^2\theta}{|\mathbf{r}_1-\mathbf{r}_2|^3} = d^2\frac{1}{|\mathbf{r}_1-\mathbf{r}_2|^3}\left(1 - 3\frac{(z_1-z_2)^2}{|\mathbf{r}_1-\mathbf{r}_2|^2}\right)\ . \tag{2.5}$$

The angle θ is the angle that the vector $\mathbf{r}_1 - \mathbf{r}_2$ forms with the magnetization axis, z, see Fig. 2.2. This expression turns out to be the same for electric and magnetic dipoles, with the only difference entering in the definition of the coupling constant d^2. It is given by $d^2 = \mu_0\mu_m^2/4\pi$ for magnetic dipoles and by $d^2 = \mu_e^2/4\pi\epsilon_0$ for electric dipoles (with ϵ_0 the electric permittivity of vacuum). We want to note here that we call the prefactor of v_{dip} as d^2. This notation is not generalized in the literature, but it is convenient in this thesis since it is easy to use both in magnetic and electric dipoles. Moreover, it is independent of the unit system in which electromagnetic quantities are expressed, and this avoids some confusion.

From Eq. (2.5) we can readily see that dipolar interactions, in contrast to contact interactions, are characterized by two main properties. The first one is that dipole-dipole interactions are long-range, due to the $1/r^3$ dependence. This means that particles that are far away will feel each other. We should be cautious with that, especially if d^2 is very large (as in the case of dipolar molecules), since it might turn out that in the long-range limit dipole-dipole interactions are of the same order as van der Waals interactions. One should then reconsider the whole scattering approximations (see, for instance, the

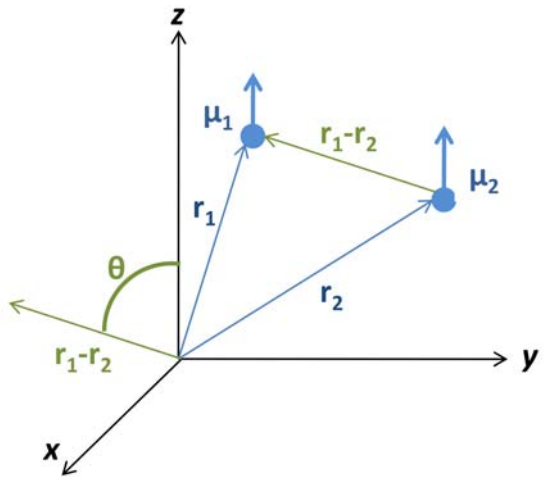

Figure 2.2: Scheme of the quantities entering the dipole-dipole interaction, see Eqs. (2.4) and (2.5).

discussion in the review [Lah09]). The second property, and the one we will exploit most, is that dipole-dipole interactions are anisotropic, which is related to the term $\cos^2\theta$ in Eq. (2.5). In the two limiting cases of $\theta = 0$ and $\theta = \pi/2$ the dipole-dipole interaction is negative or positive, respectively. This means that when two dipoles are head to tail, they attract each other, while if they are sitting side by side they feel repulsion. There is a special value of θ, called the magic angle, where $v_{\rm dip}(\mathbf{r}_1 - \mathbf{r}_2) = 0$ [Gio02]. In a three-dimensional dipolar condensate, repulsion and attraction will always coexist. While the former tends to stabilize the gas, the latter brings about collapse.

Finally, let us comment on the relation between contact and dipole-dipole interactions (see review [Lah09]). The first point is that the separation of the scattering process into contact and long-range parts is not straightforward, and has led to some discussion. The conclusion seems to be that considering the two interactions separately is correct away from shape resonances[3], and at the level of mean-field theory. The second point is that the dipole moment and the scattering length are not independent, since they form part of the same scattering process. This subject has been addressed in Ref. [Ron06b], showing that the scattering length depends rather strongly on the dipole moment. This is not much relevant in this thesis, however, since we consider that the magnetic dipole moment is fixed, or that the scattering length is zero for fermions due to the Pauli exclusion principle (Chapter 8).

2.2 Mean-field regime: the Gross-Pitaevskii equation

To derive the mean-field equations for a Bose-Einstein condensate, or Gross-Pitaevskii equations, a possible approach is to address the many-body problem in second quantization formalism (an alternative approach, concerning variations of the action integral and the energy functional, is given in Appendix D). In terms the field operators $\hat{\Psi}(\mathbf{r})$ and $\hat{\Psi}^\dagger(\mathbf{r})$,

[3]Shape resonances appear when two scattering channels are very close. The energy of the system and the scattering cross section become very large. In contrast, Feshbach resonances appear when a bound state is very close in energy to the collision threshold.

which have the meaning of destroying and creating a particle at position $\mathbf{r}$, respectively, the Hamiltonian takes the form

$$\hat{H} = \int \mathrm{d}\mathbf{r}\, \hat{\Psi}^\dagger(\mathbf{r}) \left[-\frac{\hbar^2}{2m}\nabla^2 + V_{\mathrm{ext}}(\mathbf{r}) \right] \hat{\Psi}(\mathbf{r}) + \frac{1}{2}\int \mathrm{d}\mathbf{r}\, \mathrm{d}\mathbf{r}'\, \hat{\Psi}^\dagger(\mathbf{r})\hat{\Psi}^\dagger(\mathbf{r}')v_{\mathrm{int}}(\mathbf{r}-\mathbf{r}')\hat{\Psi}(\mathbf{r}')\hat{\Psi}(\mathbf{r}) \ . \tag{2.6}$$

Since the field operator is indeed an operator, its time evolution is given by the Heisenberg equation,

$$i\hbar\frac{\partial}{\partial t}\hat{\Psi}(\mathbf{r},t) = \left[\hat{\Psi}(\mathbf{r},t), \hat{H}\right] \ , \tag{2.7}$$

which leads to the time evolution equation for the field operator

$$i\hbar\frac{\partial}{\partial t}\hat{\Psi}(\mathbf{r},t) = \left[-\frac{\hbar^2}{2m}\nabla^2 + V_{\mathrm{ext}}(\mathbf{r}) + \int \mathrm{d}\mathbf{r}'\, \hat{\Psi}^\dagger(\mathbf{r}',t)v_{\mathrm{int}}(\mathbf{r}-\mathbf{r}')\hat{\Psi}(\mathbf{r}',t) \right] \hat{\Psi}(\mathbf{r},t) \ . \tag{2.8}$$

Bose-Einstein condensation occurs when the number of particles occupying the same single-particle state becomes very large, of the order of the total number of particles, $N_0 \sim N$. Under this condition, operators can be treated as complex numbers. In particular, it is useful to decompose the field operator as

$$\hat{\Psi}(\mathbf{r},t) = \Psi(\mathbf{r},t) + \hat{\Psi}'(\mathbf{r},t) \ , \tag{2.9}$$

where $\Psi(\mathbf{r},t) = \langle\hat{\Psi}(\mathbf{r},t)\rangle$ is its mean value, or condensate wave function, and $\hat{\Psi}'$ takes care of the non-condensed fraction. Expression (2.9) is usually referred to as Bogoliubov prescription. At zeroth order (that is, substituting the operator $\hat{\Psi}(\mathbf{r},t)$ for the scalar wave function $\Psi(\mathbf{r},t)$ in Eq. (2.8)) one obtains the time evolution equation

$$i\hbar\frac{\partial}{\partial t}\Psi(\mathbf{r},t) = \left[-\frac{\hbar^2}{2m}\nabla^2 + V_{\mathrm{ext}}(\mathbf{r}) + \int \mathrm{d}\mathbf{r}'\, \Psi^*(\mathbf{r}',t)v_{\mathrm{int}}(\mathbf{r}-\mathbf{r}')\Psi(\mathbf{r}',t) \right] \Psi(\mathbf{r},t) \ . \tag{2.10}$$

This approximation constitutes a mean-field approximation. Notice that interactions render the problem non-linear, and that in general $\Psi(\mathbf{r},t)$ will have to be found self-consistently, often using numerical methods. The condensate wave function, Ψ, can be identified with the order parameter of the transition between normal and condensed phases of the Bose gas. It is zero for $T > T_c$ and starts increasing below T_c until it reaches the value of N for $T = 0$ (it reaches 1 if the wave function is normalized to unity). For further information and more details, see for instance the books by E. Lipparini [Lip03], L. Pitaevskii and S. Stringari [Pit03] and C. J. Pethick an H. Smith [Pet02], or also the review by the Trento group on condensates [Dal99].

2.2.1 Time-dependent Gross-Pitaevskii equation (TDGP)

At the mean-field level and away from shape resonances, the two-body interaction potential can be written as

$$v_{\mathrm{int}}(\mathbf{r}-\mathbf{r}') = v_{\mathrm{sw}}(\mathbf{r}-\mathbf{r}') + v_{\mathrm{dip}}(\mathbf{r}-\mathbf{r}') = g\delta(\mathbf{r}-\mathbf{r}') + d^2\frac{1-3\cos^2\theta}{|\mathbf{r}-\mathbf{r}'|^3} \ . \tag{2.11}$$

The equation governing the time evolution of the condensate wave function, Eq. (2.10), becomes

$$i\hbar\frac{\partial}{\partial t}\Psi(\mathbf{r},t)=\left[-\frac{\hbar^2}{2m}\nabla^2+V_{\rm ext}(\mathbf{r})+g\left|\Psi(\mathbf{r},t)\right|^2+d^2\int \mathrm{d}\mathbf{r}'\left|\Psi(\mathbf{r}',t)\right|^2\frac{1-3\cos^2\theta}{|\mathbf{r}-\mathbf{r}'|^3}\right]\Psi(\mathbf{r},t)\ . \tag{2.12}$$

This equation is called the time-dependent Gross-Pitaevskii equation (TDGP) and gives the evolution in time of the condensate wave function, Ψ, for a dipolar condensate. It was independently derived by Gross (1961) and Pitaevskii (1961) for purely s-wave condensates (that is, with $d=0$). Equation (2.12) allows us to address dynamical phenomena in the condensate: collective oscillations, vortex precession, interference, etc. Note that Eq. (2.12) gives an energy- and parity-conserving dynamics, and cannot be used to study vortex formation or deexcitation processes, among other phenomena. The numerical method we have used throughout the thesis to solve Eq. (2.12) is based on a Hamming's algorithm initialized by a fourth-order Runge-Kutta method (see Appendices B and C, respectively, for a detailed description of the methods). An alternative procedure to derive the TDGP Eq. (2.12) based on a variational procedure applied to the quantum action will be detailed in Appendix D.

2.2.2 Stationary Gross-Pitaevskii equation (GP)

In order to find stationary solutions of the TDGP Eq. (2.12), or the equation that leads to them, we recall the definition of Ψ in terms of the field operator $\hat{\Psi}$, $\Psi(\mathbf{r},t)=\langle\hat{\Psi}(\mathbf{r},t)\rangle$ (see [Pit03]). The average has to be taken over stationary states, that is, with a phase that evolves in time as $e^{-iEt/\hbar}$. Now for the average to be different from zero according to the laws of quantum mechanics, the states in the left and in the right must differ of one particle. Using occupation number representation for the stationary states, this means

$$\Psi(\mathbf{r},t)=\langle N|e^{iE_Nt/\hbar}\,\hat{\Psi}\,e^{-iE_{N+1}t/\hbar}|N+1\rangle=e^{-i(E_{N+1}-E_N)t/\hbar}\,\langle N|\hat{\Psi}|N+1\rangle\ . \tag{2.13}$$

The phase factor can be recognized (at first order) as the chemical potential, since

$$\mu=\frac{\partial E}{\partial N}\approx E_{N+1}-E_N\ . \tag{2.14}$$

We find therefore that if the condensate is in a stationary state, the order parameter evolves in time with a phase proportional to the chemical potential,

$$\Psi(\mathbf{r},t)=\psi(\mathbf{r})e^{-i\mu t/\hbar}\ . \tag{2.15}$$

Notice that $\Psi(\mathbf{r},t)$ and $\psi(\mathbf{r})$ are normalized to the number of particles. The fact that there appears the chemical potential instead of the energy can be traced back to the fact that the phenomenon of condensation is naturally defined in the grand-canonical ensemble. It means that the condensate acts as a reservoir of particles, which is related to the assumption that the creation and annihilation operators are treated as complex numbers. Also, it can be regarded as a requirement to the theory that the number of particles is conserved (or that the mean number of particles is kept constant, that is, that

the system is in equilibrium), which imposes the appearance of μ as a Lagrange multiplier when the equations are derived from the energy functional (see Appendix D).

Introducing Eq. (2.15) into Eq. (2.12), one finds the time-independent (or stationary) Gross-Pitaevskii equation (GP),

$$\left[-\frac{\hbar^2}{2m}\nabla^2 + V_{\rm ext}(\mathbf{r}) + g\,|\psi(\mathbf{r})|^2 + d^2\int \mathrm{d}\mathbf{r}'\,|\psi(\mathbf{r}')|^2\,\frac{1-3\cos^2\theta}{|\mathbf{r}-\mathbf{r}'|^3}\right]\psi(\mathbf{r}) = \mu\psi(\mathbf{r})\ . \quad (2.16)$$

It is a non-linear Schrödinger equation and has to be solved numerically. It is also a non-local equation, due to dipolar interactions. There are two important limits to this equation: if interactions are neglected ($g = 0$ and $d = 0$) one recovers the results for the non-interacting condensate (Appendix E); if interactions are so large that the kinetic energy (quantum pressure) term can be neglected, the Thomas-Fermi regime is reached and analytical (for $d = 0$) or pseudo-analytical (for $d \neq 0$) solutions can be found (Sec. 2.3). Away from these two limits, there are mainly two numerical methods that have been used to find its solution: imaginary-time propagation and conjugate gradient. The method used throughout this thesis has been imaginary-time propagation, and an explanation of it is given in Appendix A.

It is sometimes convinient to define the mean-field dipolar potential,

$$V_{\rm dip}(\mathbf{r}) = \int \mathrm{d}\mathbf{r}'|\psi(\mathbf{r}')|^2 v_{\rm dip}(\mathbf{r}-\mathbf{r}') = \int \mathrm{d}\mathbf{r}'|\psi(\mathbf{r}')|^2\frac{1-3\cos^2\theta}{|\mathbf{r}-\mathbf{r}'|^3}\ , \quad (2.17)$$

which is the term that appears in the GP equation. We will see in the following chapters that the shape of this potential determines to a great extent the density distribution of atoms. In this way, the mean-field dipolar potential $V_{\rm dip}$ can be sometimes thought of as an extra trapping potential, but self-induced by the dipolar atoms themselves.

The energy of a dipolar condensate is given by the energy functional

$$E = E_{\rm kin} + E_{\rm ext} + E_{\rm sw} + E_{\rm dip}\ , \quad (2.18)$$

where the different terms are, respectively, the kinetic energy

$$E_{\rm kin} = \frac{\hbar^2}{2m}\int \mathrm{d}\mathbf{r}\,|\nabla\psi(\mathbf{r})|^2\ , \quad (2.19)$$

the confining potential energy,

$$E_{\rm ext} = \int \mathrm{d}\mathbf{r}\,V_{\rm ext}(\mathbf{r})|\psi(\mathbf{r})|^2\ , \quad (2.20)$$

the contact interaction energy,

$$E_{\rm sw} = \frac{g}{2}\int \mathrm{d}\mathbf{r}\ |\psi(\mathbf{r})|^4\ , \quad (2.21)$$

and the mean-field dipolar energy,

$$E_{\rm dip} = \frac{1}{2}\int \mathrm{d}\mathbf{r}\ |\psi(\mathbf{r})|^2\int \mathrm{d}\mathbf{r}'\,v_{\rm dip}(\mathbf{r}-\mathbf{r}')\,|\psi(\mathbf{r}')|^2\ . \quad (2.22)$$

Using the factorization $\psi = \sqrt{n}e^{iS}$ (called Madelung transformation, see Sec. 3.1.1), with S the phase of the wave function and $n = |\psi|^2$ the density, the kinetic energy can be written as

$$E_{\rm kin} = \frac{\hbar^2}{2m}\int \mathrm{d}\mathbf{r}\left[\left(\nabla\sqrt{n}\right)^2 + n\left(\nabla S\right)^2\right] \ . \tag{2.23}$$

The first term on the right-hand side is called quantum pressure (or zero-point kinetic energy) and becomes especially important at the surface of the condensate, or when the density presents an oscillating behavior. Notice that it can also be written in terms of $\sqrt{n}\nabla^2\sqrt{n}$. When it is negligible one enters the Thomas-Fermi regime (see Sec. 2.3). The second term on the right-hand side of Eq. (2.23) is related to the superfluid velocity that can be present in the superfluid (for instance, when vortices are considered).

If we take Eq. (2.16), multiply it by ψ^* and integrate the whole equation over $\mathbf{r}$, we see that the chemical potential is related to the different energy terms by

$$E + E_{\rm sw} + E_{\rm dip} = \mu N \ , \tag{2.24}$$

where E is the total energy given by Eq. (2.18). This equation can be thought of as a test of the code we are using to solve the GP equation. Another good check comes from the virial theorem, which will be derived in Sec. 4.2 for a dipolar condensate in a harmonic trap (see Chapter 6 for its extension to the case of a toroidal trap, and Appendix G for a derivation of the virial theorem using commutators).

Equations (2.12) and (2.16) are integro-differential equations, with the integral part brought about by dipolar interactions. In general, such kind of equations are complicated to solve. Let us comment briefly on how the dipolar term has been treated to solve these equations numerically [Gor02]. Basically we have made use of the convolution theorem and have written

$$\int \mathrm{d}\mathbf{r}'\left|\psi(\mathbf{r}')\right|^2 v_{\rm dip}(\mathbf{r}-\mathbf{r}') = \mathcal{F}^{-1}\left[\tilde{n}\,\tilde{v}_{\rm dip}\right] \ , \tag{2.25}$$

where $\mathcal{F}^{-1}$ stands for the inverse Fourier transform, and $\tilde{n}$ and $\tilde{v}_{\rm dip}$ are, respectively, the Fourier transforms of the density and of the dipole-dipole potential. The first one has been calculated numerically, using the FFTW library [Fri05]. The Fourier transform of $v_{\rm dip}$ is analytical and can be easily calculated by using the identity [Dell04]

$$v_{\rm dip}(\mathbf{r}) = -d^2\frac{\partial^2}{\partial z^2}\frac{1}{r} - d^2\frac{4\pi}{3}\delta(\mathbf{r}) \ , \tag{2.26}$$

where for simplicity we are using r to denote $|\mathbf{r}-\mathbf{r}'|$, and analogously for all coordinates, and we are assuming the magnetization axis to be the z axis. The delta term appears in order to regularize the divergence for $r \to 0$. We can recognize $1/r$ as the Coulomb potential. The Fourier transforms of both the Coulomb potential (see, for instance, Jackson's book, Ref. [Jac99]) and the Dirac delta are very well known, and using the properties of the Fourier transform (see footnote 2 of Appendix G) we get

$$\tilde{v}_{\rm dip}(\mathbf{k}) = -d^2\frac{4\pi}{3}(1-3\cos^2\theta_p) = -d^2\frac{4\pi}{3}\left(1-3\frac{k_z^2}{k^2}\right) \ . \tag{2.27}$$

Note that although the dipole-dipole potential is not well defined at $r = 0$, its Fourier transform is well defined everywhere. Equation (2.27) can also be obtained by expanding

the imaginary exponential entering the definition of Fourier transform in terms of the spherical Bessel function, and then performing the angular integrals using the properties of the integration of three spherical harmonics (an example of this method is given in Appendix G, Sec. G.2.2).

2.2.3 Dimensionless GP equation and dimensionless parameters

Until now we have considered a general external potential, $V_{\rm ext}$, to derive the Gross-Pitaevskii equation, but in most experimental situations the confinement of the gas can be approximated by a harmonic potential with cylindrical (or axial) symmetry. Taking the axis of symmetry to be the z axis, it is written as

$$V_{\rm ho} = \frac{1}{2} m\omega_\perp^2 \left(r_\perp^2 + \lambda^2 z^2\right) \ , \tag{2.28}$$

where $r_\perp^2 = x^2 + y^2$ is the radial coordinate, $\omega_\perp$ is the frequency in the radial direction, and $\lambda = \omega_z/\omega_\perp$ is the trap anisotropy or trap aspect ratio, with ω_z the frequency along z. The harmonic potential provides a natural length scale: the radial oscillator length, $a_\perp = \sqrt{\hbar/(m\omega_\perp)}$. It is also useful, especially for anisotropic harmonic potentials, to introduce the oscillator length $a_{\rm ho} = \sqrt{\hbar/(m\omega_{\rm ho})}$, with $\omega_{\rm ho} = (\omega_x\omega_y\omega_z)^{1/3}$ the geometric mean of the frequencies. Both $a_{\rm ho}$ and $a_\perp$ are typically of the order of $1\,\mu$m and provide an order of magnitude of the width of the condensate.

The geometry of the potential (2.28) determines to a great extent the geometry of the condensate. If two-body interactions are isotropic, the geometry of the condensate is the same as that of the trap. For $\lambda = 1$, the condensate is spherical. For $\lambda > 1$ it shows an oblate geometry, being the width in z smaller than the width along $r_\perp$. The condensate is then usually referred to as pancake- or disk-shaped. For $\lambda < 1$ the geometry is prolate, meaning that the extent of the condensate is larger in the z direction than in the radial direction. Such kind of condensates are usually called cigar-shaped. If two-body interactions are anisotropic due to the dipole-dipole potential, the aspect ratio of the condensate does not follow exactly λ, since magnetostriction effects tend to enlarge the condensate in the direction where the dipoles are attractive. This topic will be discussed in Chapter 4.

Taking advantage of the length and energy scales provided by the harmonic trapping potential (respectively, $a_\perp$ and $\hbar\omega_\perp$), the GP Eq. (2.16) can be expressed in dimensionless units. This gives rise to the dimensionless GP equation,

$$-\frac{1}{2}\tilde{\nabla}^2\tilde{\psi} + \frac{1}{2}\left(\tilde{r}_\perp^2 + \lambda^2\tilde{z}^2\right)\tilde{\psi} + 4\pi\frac{Na}{a_\perp}|\tilde{\psi}|^2\tilde{\psi} + \frac{Nd^2m}{\hbar^2 a_\perp}\int \mathrm{d}\tilde{\mathbf{r}}' \left|\tilde{\psi}(\tilde{\mathbf{r}}')\right|^2 \frac{1-3\cos^2\theta}{|\tilde{\mathbf{r}}-\tilde{\mathbf{r}}'|^3}\tilde{\psi} = \tilde{\mu}\tilde{\psi} \ , \tag{2.29}$$

where the tilde indicates dimensionless quantities, that is $\tilde{r} = r/a_\perp$, $\tilde{\mu} = \mu/(\hbar\omega_\perp)$, etc. We have also imposed that the dimensionless wave function is normalized to unity instead of N, which gives the relation $\psi(\mathbf{r}) = \sqrt{N/a_\perp^3}\,\tilde{\psi}(\tilde{\mathbf{r}})$. We see from Eq. (2.29) that there are three parameters that control the physics of dipolar condensates: λ, $Na/a_\perp$ and $Nd^2m/(\hbar^2 a_\perp)$. The first parameter, the trap anisotropy, controls the geometry of the condensate. The second parameter, $Na/a_\perp$, gives the ratio between the strength of s-wave

interactions with respect to the harmonic trapping. If this parameter is very large one enters the Thomas-Fermi regime (see Sec. 2.3). The third parameter, usually denoted by D, gives the strength of dipolar interactions with respect to the strength of the confinement,

$$D = \frac{N d^2 m}{\hbar^2 a_\perp} \ . \tag{2.30}$$

It is especially relevant when the condensate is purely dipolar, that is when $a = 0$. The quantity $d^2 m/\hbar^2$ has units of length, which allows us define a characteristic length scale for dipolar interactions. This definition is not unique in the literature, but it turns out that a good definition is provided by

$$a_{dd} = \frac{d^2 m}{3\hbar^2} \ . \tag{2.31}$$

The factor 1/3 appears such that a homogeneous condensate is unstable for $a < a_{dd}$ [San03]. This is also valid for a dipolar condensate in the Thomas-Fermi regime. For ^{52}Cr, $a_{dd} \sim 15\, a_B$. Since at zero magnetic field $a \sim 100\, a_B$, we can understand that dipolar effects in chromium will be only significant if the scattering length is reduced by using the technique of Feshbach resonances.

It is easy to see from Eq. (2.29) that once the trap geometry is fixed, the physics of the dipolar condensate will be determined by the balance between contact and dipolar interactions. The dimensionless parameter that contains this information is usually denoted by ε_{dd} and is given by

$$\varepsilon_{dd} = \frac{4\pi d^2}{3g} = \frac{d^2 m}{3\hbar^2 a} = \frac{a_{dd}}{a} \ . \tag{2.32}$$

A homogeneous dipolar condensate or a dipolar condensate in the Thomas-Fermi regime become unstable when $\varepsilon_{dd} > 1$ [San03, Dell04]. Note that the factor 1/3 is the same as introduced in the definition of a_{dd}, while the factor 4π is introduced to cancel the 4π that appears in the definition of d^2 for both magnetic and electric dipoles (see Sec. 2.1.2). To avoid this factor, sometimes a parameter $C_{dd} = 4\pi d^2$ is introduced, being $C_{dd} = \mu_0 \mu_m^2$ for magnetic dipoles and $C_{dd} = \mu_e^2/\epsilon_0$ for electric dipoles. Then $\varepsilon_{dd} = C_{dd}/3g$.

As said before, the system we have in mind throughout most part of this thesis is a condensate of ^{52}Cr atoms. Using Eq. (2.29) the physics that we address can be extended to any other atomic species with non-vanishing dipole moment, such as ^{164}Dy, ^{39}K, ^{7}Li, etc., or even to bosonic molecular systems for which Eq. (2.11) for the total two-body potential remains valid.

2.2.4 Validity and limitations of the Gross-Pitaevskii theory

For Eqs. (2.12) and (2.16) to be applicable there are some conditions that have to be fulfilled. We have already encountered them, but they are summarized here.

1. They describe a condensate at $T = 0$. To address finite temperatures, a normal (thermal) cloud has to be added to the description of the system. A possibility is to describe the cloud with a Boltzmann equation (see for instance Ref. [Zar09]), coupled to the GP equation by collision integrals.

2. The Gross-Pitaevskii theory is valid to describe dilute condensates. This means that the interparticle separation must be much larger than the characteristic length of collisions (for contact interactions, it is the scattering length that plays this role). A good characterization of the diluteness condition is imposing that $x = na^3 \ll 1$, with x the diluteness parameter and n the averaged density of the condensate. Notice that diluteness is also an experimental requirement: since a Bose-Einstein condensate is a metastable state of matter, condensation can only be achieved for densities much smaller than those that would lead to clustering and solidification.

3. The Gross-Pitaevskii theory is a mean-field theory, in the sense that the interaction potential appearing in the equations is a "mean" potential, that is, it is integrated among all the particles. To solve exactly the many-body Hamiltonian, Eq. (2.1), one should use for instance Monte-Carlo integration techniques. This technique provides the exact result, but the calculations are usually time- and memory-consuming, and good computers can only reach numbers of particles of the order of thousands (in typical experiments $N \sim 10^4 - 10^6$).

4. It is implicit in the GP equations that the order parameter, or condensate wave function, describes a superfluid. In this respect, GP theory will be valid as long as the system is in the superfluid state. If there are inhomogeneities in the confining potential that make the system be composed of several localized wave functions (for instance, in deep optical lattices), the theory is no longer applicable. One should then move, for instance, to Bose-Hubbard formalism.

5. We have derived GP equations in 3D. They are not strictly true in lower dimensionality systems, since in such systems two-body interactions cannot be written as in Eqs. (2.2) and (2.5). However, GP can be used to study the limit of quasi-2D and quasi-1D systems, where the confinement in one or two directions, respectively, is so strong that the condensate wave function can be factorized. The wave function along the strong confinement directions is then usually taken to be the ground state of the harmonic oscillator and the dependence on these directions is integrated out from the GP equation.

6. Even if $T = 0$, in a real system interactions prevent all the particles to be in the same single-particle state. There is always a fraction of particles occupying excited states known as quantum depletion. To derive the GP equation quantum depletion is neglected, which is a good approximation only for large N. To treat properly the condensate plus the higher energy occupied states one should work with the density matrix. A possible method is to use exact diagonalization techniques, but then only systems with low particle numbers can be addressed.

7. We have seen that GP equations come from a zeroth order expansion of the field operator, which is treated as a complex number. This means, for instance, that we are missing two-body (and higher order) correlations.

Despite all these restrictions, the Gross-Pitaevskii theory works perfectly well to describe a Bose-Einstein condensate in the majority of experimental situations. In addition,

and surprisingly, it can predict the onset of some phenomena that are not properly taken into account in the theory. One example is the collapse of the condensate. The equations derived above describe an equilibrium state and collapse is clearly a phenomenon out of equilibrium. However, the GP equation predicts correctly the conditions under which collapse will occur (for instance, collapse due to attractive interactions). Another example is that despite correlations are smoothed out by taking a complex number instead of the annihilation operator, there are some remnants that the condensate wave function retains. This in fact is general for Hartree-Fock-like approximations.

2.3 Thomas-Fermi approximation (TF)

When the number of atoms in the condensate is very large, the effects of quantum pressure become negligible compared to interactions and the term $(\nabla\sqrt{n})^2$ in Eq. (2.23) can be effectively set to zero. This is usually referred to as the Thomas-Fermi approximation of a condensate[4]. If there are no velocity fields in the gas, the whole kinetic energy is neglected; otherwise we should maintain the velocity term ∇S.

2.3.1 Thomas-Fermi approximation for an s-wave condensate

Without the kinetic energy term, the Gross-Pitaevskii Eq. (2.16) for an s-wave condensate ($d = 0$) becomes

$$V_{\text{ext}}(\mathbf{r})\psi + g|\psi|^2\psi = \mu\psi \ . \tag{2.33}$$

From this equation the density of the condensate is given in the Thomas-Fermi approximation by

$$n(\mathbf{r}) = \begin{cases} \dfrac{\mu - V_{\text{ext}}(\mathbf{r})}{g} & \text{for } \mu > V_{\text{ext}} \\ 0 & \text{elsewhere} \end{cases} \ ,$$

which can be recognized as a form of a local-density approximation (see, for instance, Ref. [Lip03]). The geometry of the condensate density follows that of the trapping potential. Let us consider an axially symmetric harmonic trap, given by the potential Eq. (2.28). In the region where it is nonzero, the density can be written as

$$n(\mathbf{r}) = n_0 \left(1 - \frac{r_\perp^2}{R_\perp^2} - \frac{z^2}{R_z^2}\right) \ , \tag{2.34}$$

where $n_0 = \mu/g$ is the density at the center of the trap. We have introduced the Thomas-Fermi radii in the radial and z directions, respectively $R_\perp$ and R_z, given by $R_i = \sqrt{2\mu/(m\omega_i^2)}$. The density of a condensate in the Thomas-Fermi approximation is thus an inverted parabola. Notice that the Thomas-Fermi radii correspond to the classical turning points.

[4]Note that, even if the underlying idea is the same (i.e. neglecting the quantum pressure of the ground state) the Thomas-Fermi approximation has a different manifestation whether the system is bosonic or fermionic. The case of fermions will be briefly described in Chapter 8.

The chemical potential is found from the normalization of the density, Eq. (2.34), to N:

$$\mu = \frac{1}{2}\hbar\omega_\perp \left(15\lambda \frac{Na}{a_\perp}\right)^{2/5} . \tag{2.35}$$

Using this expression, the TF radii and the central density can be found,

$$R_\perp = \sqrt{\frac{2\mu}{m\omega_\perp^2}} = a_\perp \left(15\lambda \frac{Na}{a_\perp}\right)^{1/5} \tag{2.36}$$

$$R_z = \sqrt{\frac{2\mu}{m\omega_z^2}} = \frac{a_\perp}{\lambda} \left(15\lambda \frac{Na}{a_\perp}\right)^{1/5} \tag{2.37}$$

$$n_0 = \frac{15}{8\pi}\frac{N}{R_\perp^2 R_z} . \tag{2.38}$$

From these values and the density (2.34), most magnitudes can be calculated analytically. Note that the relevant parameter in the TF regime is $Na/a_\perp$, which we have already encountered in the dimensionless GP Eq. (2.29). It gives the ratio between the strength of the contact interactions and the confining potential. When $Na/a_\perp \gg 1$ the Thomas-Fermi approximation agrees well with the results obtained solving the full Gross-Pitaevskii equation (2.16).

2.3.2 Thomas-Fermi approximation for a dipolar condensate

The theory of the Thomas-Fermi approximation for dipolar condensates has been developed in Refs. [Dell04, Ebe05] and has been applied to study the rotation [Dell07], expansion and collective excitations [Gio06] of dBECs. It is based on the fact that the inverted parabola (2.34) is an exact solution of the equation

$$\mu = V_{\rm ho}(\mathbf{r}) + gn(\mathbf{r}) + V_{\rm dip}(\mathbf{r}) , \tag{2.39}$$

where $V_{\rm dip}(\mathbf{r})$ is the mean-field dipolar potential Eq. (2.17). The Thomas-Fermi radii are used here as variational parameters to find the equilibrium configuration. Since the dipolar potential is rather more involved and difficult to treat than the contact interaction potential, the dipolar Thomas-Fermi approximation becomes more complicated. In particular, the dipolar TF approximation relies on a transcendental equation that has no analytical solution. For an axially symmetric harmonic potential, Eq. (2.28), this equation reads

$$\frac{\kappa^2}{\lambda^2}\left[3\varepsilon_{dd}\frac{f(\kappa)}{1-\kappa^2}\left(\frac{\lambda}{2}+1\right) - 2\varepsilon_{dd} - 1\right] = \varepsilon_{dd} - 1 , \tag{2.40}$$

where $\kappa = R_\perp/R_z$ is the condensate anisotropy parameter and ε_{dd} is given by Eq. (2.32). For $\varepsilon_{dd} > 1$ the TF dipolar condensate is unstable, although metastable solutions can exist, as discussed in Refs. [Dell04, Ebe05]. The function $f(\kappa)$ comes from the angular integration of the dipolar potential and is given by

$$f(\kappa) = \frac{1+2\kappa^2}{1-\kappa^2} - \frac{3\kappa^2}{(1-\kappa^2)^{3/2}} \tanh^{-1}\sqrt{1-\kappa^2} . \tag{2.41}$$

It decreases monotonically from $f(\kappa \to 0) = 1$ to $f(\kappa \to \infty) = -2$, crossing zero at $\kappa = 1$ (a plot of this function will be shown in Chapter 8, Fig. 8.2). The ground state density profile is thus characterized by the equilibrium Thomas-Fermi radii, given by

$$R_\perp = \left[\frac{15gN}{4\pi m\omega_\perp^2}\kappa\left\{1 - \varepsilon_{dd}\left(1 - \frac{3}{2}\frac{\kappa^2}{1-\kappa^2}f(\kappa)\right)\right\}\right]^{1/5} \tag{2.42}$$

$$R_z = \left[\frac{15gN}{4\pi m\omega_\perp^2}\frac{\kappa^2}{\lambda^2}\left\{1 + 2\varepsilon_{dd}\left(1 - \frac{3}{2}\frac{1}{1-\kappa^2}f(\kappa)\right)\right\}\right]^{1/5} \tag{2.43}$$

and by the density

$$n = \frac{15}{8\pi}\frac{N}{R_\perp^2 R_z}\left(1 - \frac{r_\perp^2}{R_\perp^2} - \frac{z^2}{R_z^2}\right) \ . \tag{2.44}$$

The different contributions to the energy functional, Eq. (2.18), are [Dell04, Gio06]

$$E_{\rm ho} = \frac{1}{7}N\frac{m\omega_\perp^2}{2}\left(2R_\perp^2 + \lambda^2 R_z^2\right) \tag{2.45}$$

$$E_{\rm sw} = \frac{15}{7}\frac{N^2\hbar^2 a}{m}\frac{1}{R_\perp^2 R_z} \tag{2.46}$$

$$E_{\rm dip} = -\frac{15}{7}\frac{N^2\hbar^2 a}{m}\frac{\varepsilon_{dd}}{R_\perp^2 R_z}f(\kappa) \ . \tag{2.47}$$

If the system has no cylindrical symmetry, the anisotropy function, $f(\kappa)$, depends on the aspect ratios $\kappa_x = R_x/R_z$ and $\kappa_y = R_y/R_z$ and has the form [Gio06]

$$f(\kappa_x, \kappa_y) = 1 + 3\kappa_x\kappa_y\frac{E(\varphi\backslash\alpha) - F(\varphi\backslash\alpha)}{(1-\kappa_y^2)\sqrt{1-\kappa_x^2}} \ , \tag{2.48}$$

where $F(\varphi\backslash\alpha)$ and $E(\varphi\backslash\alpha)$ are the incomplete elliptic integrals of first and second kind [Abr72] and their arguments are given by:

$$\sin^2\alpha = \frac{1-\kappa_y^2}{1-\kappa_x^2} \tag{2.49}$$

$$\sin\varphi = \sqrt{1-\kappa_x^2} \ . \tag{2.50}$$

Much information about $f(\kappa_x, \kappa_y)$ can be found in Ref. [Gio06]. It can be seen that when the two arguments are equal, $\kappa_x = \kappa_y$, one recovers expression (2.41).

Chapter 3

Physics of vortices in Bose-Einstein condensates

A condensate in three dimensions is a superfluid[1], i.e. a quantum fluid characterized by zero viscosity that flows without dissipation. One of the clearest evidences of superfluidity in a system is the appearance of quantized vortices. If the trap is rotated at low frequency the superfluid cannot follow the movement and remains at rest. As the rotation frequency is increased and reaches a critical value Ω_c, the system responds to rotation by creating a centered vortex state. This process is usually called vortex nucleation. A hole in the density appears in the center and the superfluid flows around it with quantized circulation. This flow is irrotational and has an angular momentum of $N\hbar$, where N is the number of atoms in the condensate. This kind of experiment is known as the rotating bucket experiment, since it was the method used in He to obtain vortices [Don91], and the vortex that appears is called a vortex line.

In this chapter we summarize some aspects of the physics of vortices in condensates. It is organized as follows. In Sec. 3.1 we derive the hydrodynamic equations for a condensate and introduce the vortex velocity field (Sec. 3.1.1). We discuss the main properties of the vortex line: quantized circulation, vorticity and angular momentum (Sec. 3.1.2). In Sec. 3.2 we address the structure of vortex lines, that is the vortex core, for s-wave condensates in the non-interacting limit (Sec. 3.2.1) and for the interacting gas (Sec. 3.2.2), both the homogeneous case and the Thomas-Fermi regime. In Chapter 5 we will see how dipolar interactions modify the structure of the core. Section 3.3 is devoted to the experimental methods used to create (Sec. 3.3.1) and detect (Sec. 3.3.2) vortex states of different kinds. Also some of the measurements that can be done with vortices, and that have some relevance for this thesis, are discussed (Sec. 3.3.3). In Sec. 3.4 we comment on how vortices in rotating condensates are treated within the mean-field framework, that is with the GP equation in the rotating frame. From the mean-field energy of the vortex state in the laboratory frame and in the rotating frame (Sec. 3.4.1), a thermodynamical argument can be used to calculate the critical frequency for vortex nucleation (Sec. 3.4.2).

[1] In 3D Bose gases, condensation is always accompanied by superfluidity. However, this is not the case in lower dimensional systems, where one might have a non-superfluid condensate. This topic is discussed in the appendix of Ref. [Blo08]. Throughout this thesis we consider the two terms as equivalent, since we deal only with situations where condensates are also superfluids.

Finally, in Sec. 3.5 we comment on the method used to numerically find vortex solutions. Notice that the results in Sec. 3.1, Sec. 3.4 and Sec. 3.5 are valid both for dipolar and purely contact interacting condensates, while Sec. 3.2 and Sec. 3.3 refer basically to s-wave condensates. The effect of dipolar interactions will be treated in Chapters 5 and 6.

3.1 The vortex velocity field

3.1.1 Hydrodynamic equations for a dipolar condensate

The condensate order parameter $\psi(\mathbf{r})$ is in general a complex function, so it can be written in terms of a modulus and a phase, using the Madelung transformation [Don91], as

$$\psi(\mathbf{r}) = \sqrt{n(\mathbf{r})}\, \mathrm{e}^{iS(\mathbf{r})} \ , \tag{3.1}$$

where $n(\mathbf{r})$ is the atom density and $S(\mathbf{r})$ the phase of the wave function. The ground state of a condensate has an arbitrary phase, so it is usually taken to be zero and the wave function becomes real. As we will see in what follows, a nonzero (inhomogeneous) phase gives rise to a velocity field in the condensate. Equation (3.1) is completely general for a superfluid system, therefore for a condensate in 3D. It expresses the fact that condensates are hydrodynamic systems. Using expression (3.1) one can calculate the current density, $\mathbf{j}(\mathbf{r})$, as

$$\mathbf{j} = -i\frac{\hbar}{2m}\left(\psi^*\boldsymbol{\nabla}\psi - \psi\boldsymbol{\nabla}\psi^*\right) = \frac{\hbar}{m}\mathrm{Im}\left[\psi^*\boldsymbol{\nabla}\psi\right] = n\frac{\hbar}{m}\boldsymbol{\nabla}S \ . \tag{3.2}$$

Using the hydrodynamic relation $\mathbf{j} = n\mathbf{v}$, one sees immediately that the superfluid velocity is related to the phase by

$$\mathbf{v}(\mathbf{r}) = \frac{\hbar}{m}\boldsymbol{\nabla}S(\mathbf{r}) \ . \tag{3.3}$$

Now if Eq. (3.1) is treated as an ansatz for the condensate wave function (which in general depends also on time) and is substituted into the Gross-Pitaevskii Eq. (2.12), a set of two coupled equations is found for $n(\mathbf{r},t)$ and $\mathbf{v}(\mathbf{r},t)$ (or equivalently, in terms of $n(\mathbf{r},t)$ and $S(\mathbf{r},t)$),

$$\frac{\partial n}{\partial t} + \nabla\cdot(n\mathbf{v}) = 0 \tag{3.4}$$

$$m\frac{\partial \mathbf{v}}{\partial t} + \boldsymbol{\nabla}\left(-\frac{\hbar^2}{2m}\frac{1}{\sqrt{n}}\nabla^2\sqrt{n} + V_{\mathrm{ext}} + gn + V_{\mathrm{dip}} + \frac{1}{2}mv^2\right) = 0 \ . \tag{3.5}$$

These equations are known as hydrodynamic equations and have been successfully used in a number of calculations, both for s-wave and dipolar condensates (see, for instance, Refs. [Dal99, Pet02, Pit03, Lah09]). They are general, in the sense that they are exactly equivalent to the Gross-Pitaevskii equation. The first equation, Eq. (3.4), is the continuity equation, which expresses the conservation of mass. The second equation, Eq. (3.5), tells us that the superfluid is irrotational. If the quantum pressure term is neglected, we recover the Thomas-Fermi approximation (see Sec. 2.3.1).

3.1.2 Velocity field of a vortex line

From Eq. (3.3), we see that inhomogeneities in the phase bring about velocity fields, and therefore currents, in the condensate. One of the most interesting is the vortex line, which is basically a straight line with zero density, around which the condensate flows with quantized velocity (properly speaking, it is the circulation of the velocity that is quantized, as we will see below). In a medium with cylindrical symmetry a vortex line corresponds to a phase of the wave function $S(\mathbf{r}) = \kappa\varphi$, with κ the winding number and φ the azimuthal coordinate. This gives rise to the Feynman-Onsager ansatz for a vortex line in a superfluid,

$$\psi(\mathbf{r}) = \sqrt{n(r_\perp, z)}\, \mathrm{e}^{i\kappa\varphi} \ . \tag{3.6}$$

The associated velocity field is given by

$$\mathbf{v}(\mathbf{r}) = \frac{\kappa\hbar}{m r_\perp}\hat{\varphi} \ . \tag{3.7}$$

Figure 3.1 shows $\mathbf{v}(\mathbf{r})$ and $S(\mathbf{r})$ for a singly quantized vortex line ($\kappa = 1$). The velocity of the fluid is larger as we approach the center of the condensate, and it diverges exactly on the vortex line, $r_\perp = 0$. The direction of the flow of atoms follows effectively that of the growth of the phase gradient, which is anticlockwise. Looking only at the phase (right panel), a vortex can be thought of as lines of constant phase that emerge from a (singular) point in space. This representation of vortices in terms of phase lines will be used in Chapter 7 to relate self-trapping dynamics in the self-induced Josephson junction to vortex dynamics. Since the velocity diverges, in order to maintain a finite value of the wave function everywhere, the density must be zero at $r_\perp = 0$. To allow this, there is a region close to the line where the density goes from zero to some maximum value in a smooth way. This region is known as the vortex core, and is related to the healing length in interacting condensates (see Sec. 3.2).

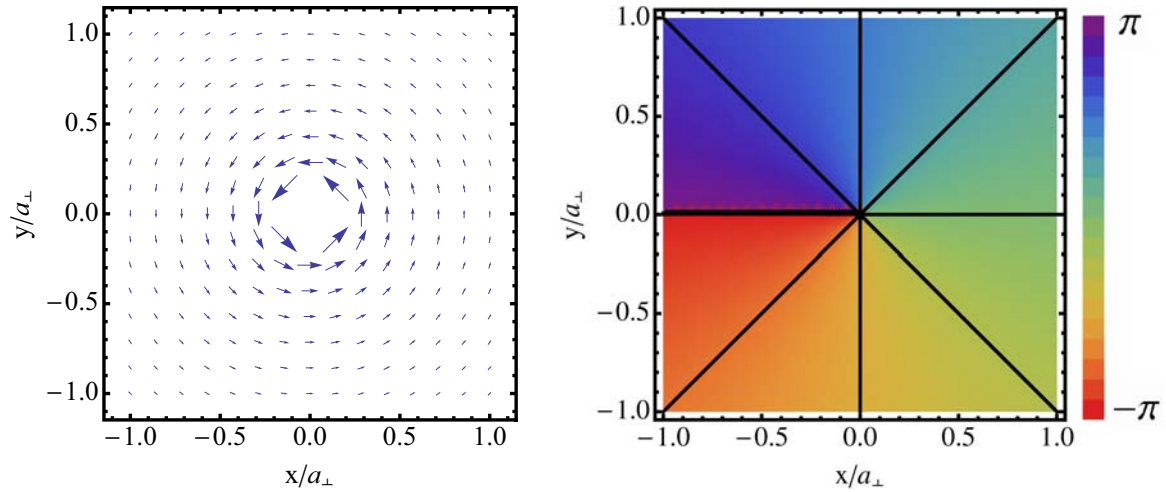

Figure 3.1: Velocity field (left) and phase distribution (right) of a centered quantized vortex line on the plane $z = 0$. Notice that the central region in the left panel is not drawn because of the divergence of the velocity for $r \to 0$.

To see that the velocity field of a vortex line, Eq. (3.7), is indeed quantized, we need to look at the circulation of the velocity along a closed circuit around the line, given by

$$\Gamma = \oint \mathbf{v} \cdot \mathrm{d}\boldsymbol{\ell} = \frac{\hbar\kappa}{m} \oint \frac{1}{r_\perp} \hat{\varphi} \cdot \mathrm{d}\boldsymbol{\ell} = \frac{\hbar\kappa}{m} \oint \frac{1}{r_\perp} r_\perp \mathrm{d}\varphi = \frac{\hbar\kappa}{m} \Delta\varphi = \frac{h}{m}\kappa \ . \tag{3.8}$$

In the last step we have used that the condensate wave function must be single-valued and its phase can only change by multiples of 2π along a closed circuit (note that the multiplicity is contained in the integer value κ). The circulation therefore is a quantized quantity, with h/m the quantum of circulation and κ the quantization number. For a singly quantized vortex (either line or ring, straight or bended), $\kappa = 1$. For multiply quantized vortices, $\kappa > 1$. The latter however are very difficult to obtain, since it is energetically favorable for a multiply quantized system to organize itself in multiple singly quantized vortices rather than a big multiply quantized vortex [Don91]. Exceptions to this statement arise in highly rotating traps, where giant vortices have been experimentally observed [Eng03], or in toroidal traps, where the vortex core is provided by the hole in the trapping potential [Ryu07].

The vorticity associated to the vortex velocity field, Eq. (3.7), is given by

$$\boldsymbol{\omega} = \boldsymbol{\nabla} \times \mathbf{v} = \frac{h\kappa}{m} \delta(\mathbf{r}_\perp) \hat{z} \ . \tag{3.9}$$

The fluid is therefore irrotational everywhere except along the line $r_\perp = 0$. The two-dimensional Delta function, $\delta(\mathbf{r}_\perp)$, arises from the divergence of the velocity at $r_\perp = 0$. Its presence can be understood as follows. If we take the curl of Eq. (3.7) naively, we see that the vorticity is zero. But rewriting the circulation integral by means of Stokes theorem,

$$\Gamma = \oint \mathbf{v} \cdot \mathrm{d}\boldsymbol{\ell} = \int (\nabla \times \mathbf{v}) \cdot \mathrm{d}\boldsymbol{\mathcal{S}} = \int \boldsymbol{\omega} \cdot \mathrm{d}\boldsymbol{\mathcal{S}} = \frac{h\kappa}{m} \ , \tag{3.10}$$

we see that the surface integral of the vorticity is finite, so that the vorticity cannot be zero. This is mathematically translated in the presence of a two dimensional Delta function centered on the vortex line that provides a circulation (surface integral) $h\kappa/m$ [2].

The z component of the angular momentum of a vortex state can also be easily calculated using ansatz (3.6),

$$L_z = \left\langle \psi(\mathbf{r}) \left| -i\hbar \frac{\partial}{\partial\varphi} \right| \psi(\mathbf{r}) \right\rangle = -i\hbar \int \mathrm{d}\mathbf{r}\, n(\mathbf{r}) e^{-i\kappa\varphi} \frac{\partial e^{i\kappa\varphi}}{\partial\varphi} = -i^2\hbar\kappa \int \mathrm{d}\mathbf{r}\, n(\mathbf{r}) = \hbar\kappa N \ , \tag{3.11}$$

where N is the number of particles in the condensate. For typical experiments, $N \sim 10^6$. This means that a vortex state has macroscopic angular momentum, being the angular momentum per particle $\kappa\hbar$. In this respect, a vortex is a highly excited state of the system. Note that the angular momentum L_z is only a good quantum number if the system shows cylindrical symmetry. In the case of off-center vortices (Chapter 5) or azimuthal density distributions (Chapter 6), $L_z \neq \hbar\kappa N$ but is rather a smaller quantity.

[2] This same kind of reasoning is used to introduce the Delta function in Coulomb problems, where the quantity $\nabla^2 \dfrac{1}{|\mathbf{r} - \mathbf{r}'|}$ appears (see, for instance, Ref. [Jac99]).

Until now we have implicitly assumed that $\kappa > 0$, which gives rise to an anticlockwise flow (see Fig. 3.1). If it was clockwise, the vortex would be called an antivortex, and would correspond to $\kappa < 0$ and angular momentum $L_z = -|\kappa|N\hbar$. For a non-rotating system, the vortex and the antivortex states are degenerate.

3.2 Structure of the vortex core

We have said above that close to the vortex line there is a region where the density goes from zero to some finite value. This region is the vortex core, and is determined by the interactions and the centrifugal term, $mv^2/2$ in Eq. (3.5), introduced by the vortex velocity field, which pushes the atoms away from the vortex line and defines a low density region around it. In general, to find the structure of the core one has to solve the Gross-Pitaevskii equation. However, there are some limits where it is possible to find an analytical solution for the vortex core, or at least find a characteristic length for its width. In this section we will assume a purely s-wave condensate and will address the problem of the vortex core when the gas is harmonically confined and non-interacting (Sec. 3.2.1), and when it is interacting (Sec. 3.2.2). Dipolar effects on the vortex core will be explored in Chapters 5 and 6, respectively for a harmonically confined dipolar condensate and one where the trapping potential has toroidal geometry.

3.2.1 Vortex core in non-interacting condensates

We are interested in the structure of the vortex core of a singly quantized vortex in a non-interacting harmonically trapped condensate. Substituting ansatz (3.6) with $\kappa = 1$ and $\psi_v(r_\perp, z) \equiv \sqrt{n(r_\perp, z)}$ into the Gross-Pitaevskii Eq. (2.16) gives

$$-\frac{\hbar^2}{2m}\nabla^2\psi_v + \frac{\hbar^2}{2mr_\perp^2}\psi_v + V_{\rm ho}\psi_v = \mu\psi_v \ , \tag{3.12}$$

where we have written the laplacian in cylindrical coordinates and have simplified the exponential factor. Notice that in the non-interacting case the chemical potential corresponds to the energy per particle, $\mu = E/N$. The centrifugal term $\sim 1/r_\perp^2$ is related to the kinetic energy due to the flow of atoms. We assume that $V_{\rm ho}$ is a harmonic potential with cylindrical symmetry, see Eq. (2.28), which is usually the experimentally relevant situation. The wave function can be decomposed as $\psi_v = CR(r_\perp)Z(z)$, where C is a constant that will be determined by normalization. The equation for Z is just the quantum harmonic oscillator (see Appendix E), and its solution is given by $Z(z) \propto \exp\left[-z^2/2a_z^2\right]$, with a_z the oscillator length in the z direction. The equation for R is

$$-\frac{1}{r_\perp}\frac{\mathrm{d}}{\mathrm{d}r_\perp}\left[r_\perp\frac{\mathrm{d}R}{\mathrm{d}r_\perp}\right] + \frac{1}{r_\perp^2}R + \frac{1}{a_\perp^4}r_\perp^2 R = \frac{2m\mu_\perp}{\hbar^2}R \ . \tag{3.13}$$

The radial harmonic oscillator length, $a_\perp = \sqrt{\hbar/(m\omega_\perp)}$, defines the length scale of the system. It is easy to check that the solution to the radial Eq. (3.13) has the form

$$R(r_\perp) \propto r_\perp \exp\left[-r_\perp^2/2a_\perp^2\right] \ . \tag{3.14}$$

In the limit $r_\perp \to 0$, the solution shows the asymptotic behavior $R(r_\perp \to 0) \propto r_\perp$. Taking the wave function, ψ_v, to be normalized to the number of particles, N, we find that the density of a vortex line in a harmonically trapped, non-interacting condensate is given by

$$n(r_\perp, z) = \frac{1}{\pi^{3/2}} \frac{N}{a_\perp^2 a_z} \left(\frac{r_\perp}{a_\perp}\right)^2 \exp\left[-\frac{1}{a_\perp^2}\left(r_\perp^2 + \lambda^2 z^2\right)\right] . \tag{3.15}$$

The density profile in the $z = 0$ plane is shown in Fig. 3.2(a) (solid line), together with the corresponding ground state profile (dashed line). The size of the vortex core is given by the radial oscillator length, $a_\perp$.

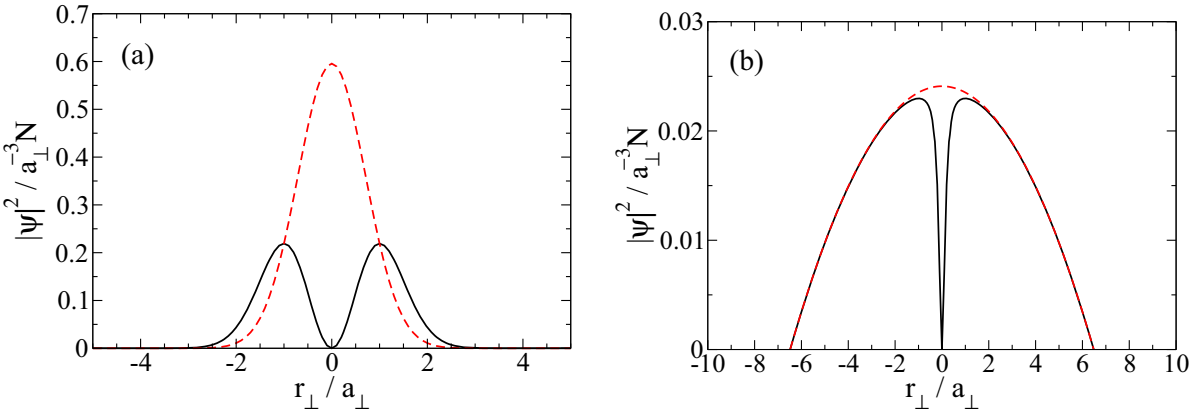

Figure 3.2: Structure of the vortex core of a trapped condensate (with $N = 10^4$, $\omega_\perp = 200 \times 2\pi$ s^{-1}, $\lambda = 11$ and $a = 100\, a_B$) in the non-interacting regime (a) and in the Thomas-Fermi regime (b). The corresponding ground state is shown in dashed.

3.2.2 Vortex core in interacting condensates

If we consider a vortex line in a uniform condensate, the GP equation can be written for the modulus of the wave function, $\psi_v(r_\perp)$, as

$$-\frac{\hbar^2}{2m}\frac{1}{r_\perp}\frac{\mathrm{d}}{\mathrm{d}r_\perp}\left[r_\perp \frac{\mathrm{d}\psi_v}{\mathrm{d}r_\perp}\right] + \frac{\hbar^2}{2m r_\perp^2}\psi_v + \frac{4\pi\hbar^2 a}{m}\psi_v^3 = \mu\psi_v \ , \tag{3.16}$$

where we have used the definition of g, Eq. (2.3). The chemical potential is that of the uniform Bose gas, $\mu = gn$, with n the (uniform) density. Following Ref. [Pit03], we write $\psi_v(r_\perp) = \sqrt{n}\, f(r_\perp/\xi)$, which takes into account that for large distances from the vortex line ψ_v must tend to its bulk value $\sqrt{n}$. The quantity ξ is called the healing length and is given by $\xi = 1/\sqrt{8\pi n a}$. Using this ansatz, the equation becomes

$$\frac{\mathrm{d}^2 f}{\mathrm{d}x^2} + \frac{1}{x}\frac{\mathrm{d}f}{\mathrm{d}x} + \left(1 - \frac{1}{x^2}\right) f - f^3 = 0 \ , \tag{3.17}$$

where we have introduced the dimensionless variable $x = r_\perp/\xi$. For a typical atom density $n \sim 10^{14}\,\mathrm{cm}^{-3}$ and a scattering length $a = 100\, a_B$, we find $\xi = 0.27\,\mu$m. The healing length

gives the length scale at which a perturbation in the density recovers the bulk value. It is sometimes also known as coherence length.

For the trapped gas in the Thomas-Fermi regime the definition of healing length above is still valid if we consider the density n as the density at the center of the trap, n_0. The expression for the healing length then becomes

$$\xi = \frac{1}{\sqrt{8\pi n_0 a}} \,, \tag{3.18}$$

and as above it introduces a new length scale in the problem. Figure 3.2(b) shows the vortex profile in the plane $z = 0$ for a condensate in the Thomas-Fermi limit, following the ansatz

$$n(r_\perp, z) = n_0 \left(1 - \frac{r_\perp^2}{R_\perp^2} - \frac{z^2}{R_z^2}\right) \left(1 - \frac{\xi^2}{r_\perp^2 + \xi^2}\right) \tag{3.19}$$

for the density (see Sec. 2.3.1 for the definition n_0, $R_\perp$ and R_z). The product of the first two factors in Eq. (3.19) describes the ground state density, while the third factor models the vortex core shape. Notice that this ansatz is not an exact solution of the corresponding Gross-Pitaevskii equation (even neglecting the quantum pressure term), but it can be used as a variational ansatz with parameters $R_\perp$, R_z and ξ. Taking their definitions directly (without applying any variational procedure), the error introduced in the normalization of the density is less than 1% in the case of Fig. 3.2. Comparing the profiles for the non-interacting condensate, Fig. 3.2(a), and for the condensate in the TF limit, Fig. 3.2(b), we see that the reduction of the peak density by a factor ~ 10 is accounted for by a larger extension of the condensate in the TF regime. We clearly see in this figure that the effect of interactions is to reduce the density at the center of the trap while increasing the extent of the cloud, both in the ground state and in the presence of a vortex.

3.3 Experiments with vortices

One of milestone experiments in the field of Bose-Einstein condensation is the creation and detection of quantized vortex states. The presence of vortices in a condensate is a clear prove that condensates are also superfluids. The first vortex experiments in BECs were reported in Refs. [Mat99, Mad00, Abo01], where by expanding the condensate cloud single vortices and vortex lattices were detected as empty holes in the density. Since then vortices have attracted a lot of attention and much investigation has been carried out. In this section we summarize some of the main results that have been obtained experimentally, focusing on how vortices can be generated and detected. The information contained in this section is not exhaustive, and does not pretend to be, but we will address those topics that are more relevant for this thesis.

3.3.1 Creation of vortices

There are several methods for creating vorticity in a condensate, based on mainly two processes: stirring and phase imprinting. Both stirring and phase imprinting are general methods that can be implemented in many different ways. Also, they can be combined

depending on the experimental setup and the system at hand. For instance, the first vortex experiments in condensates [Mat99] used coherent transitions between the two species of a BEC mixture, whose ac Stark effect was controlled by a rotating laser beam. In a way, they used both phase-imprinting and rotation (sometimes this method is referred to as phase engineering).

The first method, stirring, is the cold atom counterpart of the rotating bucket experiment in superfluid helium. In this method (see for instance Refs. [Mad00, Hod02]), the vortex state is obtained by rotating a slightly deformed trap[3] at an angular frequency $\Omega > \Omega_c$, where Ω_c is the critical rotation frequency. At this frequency the trap responds to rotation in a quantized way, nucleating a vortex at the center (see Fig. 1.3). The nucleation process is mediated by the instability of a collective mode [Dal00], giving a critical frequency as predicted by $\Omega_c = \min[\omega_m/m]$, with m the third component of angular momentum corresponding to the excitation of frequency ω_m (notice that this is analogous to the Landau criterion for the superfluid velocity [Don91]). For wide stirring beams, the mode that becomes unstable is the surface quadrupole mode (see [Str96]), for which $m = 2$ and $\omega_2 = \sqrt{2}\omega_\perp$. This gives rise to a critical frequency $\Omega_c = \omega_\perp/\sqrt{2}$ which agrees very well with experiments [Mad01]. If the trap is rotated faster (but always with $\Omega < \omega_\perp$), many vortices are nucleated and they organize themselves in a triangular lattice [Abo01], called Abrikosov lattice in analogy to vortices in superconductors (see, for instance, Ref. [Tin96]). For frequencies $\Omega \to \omega_\perp$, the number of vortices becomes so large that the distance between them is smaller than the vortex cores, entering the strongly interacting regime (see reviews [Blo08, Fet09]), where highly correlated states are predicted to form. For $\Omega = \omega_\perp$ the condensate is unstable. Notice that vortices can also be obtained by rotating the normal gas (above the critical temperature) and then cooling it down until condensation is reached [Hal01].

The second method for creating vortex states in a condensate is phase imprinting. It uses optical fields (lasers and microwaves) to create an inhomogeneous phase in the condensate, with the symmetry required by the vortex state. The difficulty of implementing this method in the experiment lies in the need to go from a ground state with maximum density at the center to a vortex state with zero density at the center. This can be overcome, for instance, by working with two different species. In this case the second species can produce a hole in the density of the first species [Mat99]. Another possibility for phase-imprinting is to transfer angular momentum directly from light to the atoms, for instance using a Laguerre-Gaussian beam [And06]. This family of laser beams carry angular momentum along the direction of propagation, and can be used to transfer the desired angular momentum to the atoms. This method has been used, for instance, to obtain vortex states and persistent currents in a toroidal geometry [Ryu07], where the hole in the density is provided by the trapping potential. Apart from vortex states, phase imprinting is a natural way to generate solitons in the condensate.

In addition to vortex lines and lattices, other vortex configurations can exist, but

[3]The deformation of the trap is crucial in experiments where the trapping potential has cylindrical symmetry. If the deformation is not introduced, the system is an eigenstate of $\hat{L}_z$ and it is thus not possible to go from zero angular momentum (ground state) to a macroscopic angular momentum ($N\hbar$ for a centered vortex). The deformed trap is usually taken to be elliptical and the ellipse rotates in time, conferring angular momentum to the condensate.

are in general non-equilibrium situations, such as vortex dipoles or vortex rings. They are dynamically generated as decay products of some excited state, such as a soliton [And01, Dut01], or by collision of condensates with a different phase [Sch07]. A vortex dipole is a coupled pair of vortex and antivortex with a particular dynamics [Mar01b], reminiscent of electrical charges: if two vortices with the same charge (either two vortices or two antivortices) repel each other, two vortices with opposite charge attract each other. Vortex dipoles are generally defined in 2D systems, where there is no bending of the cores. In 3D systems, depending on the geometry, the vortices can be so bended that the vortex dipole closes on itself and forms a vortex ring. Vortex dipoles have been experimentally observed in the literature [Nee10], as well as vortex rings [And01, Sho09].

Another method to dynamically generate vorticity is by drag of an object, which can be for instance a focused laser beam. Again this method comes directly from helium, where vortices (in general, vortex rings) can be created by moving an ion through the superfluid (see [Don91]). This method for creation of vortices is associated to a critical velocity for the object, v_c: below v_c the superfluid remains at rest, while above v_c quantized vortices appear. In superfluid helium, the critical velocity is related to the Landau critical velocity. In condensates, however, there seems to be some controversy and the mechanism leading to the critical velocity is under discussion. Related to this method of vortex creation, there has recently been an extreme implementation of it by shaking the whole condensate [Henn09a]. For large oscillations of the cloud, the system becomes turbulent and a tangled mess of vortices and antivortices in all directions appear [Henn09b] and collisions, mergings and annihilations can be studied.

3.3.2 Detection of vortices

In order to detect vortex states in a condensate, two main methods have been used. On the one hand, expansion of the condensate leads to a measurable density with a hole in the middle (see Figs. 1.1 and 3.4). If the zero density at the center did not correspond to a vortex, during expansion it would fill up with atoms. On the other hand, vortex states can also be detected by interferometry. If two condensates, one with a vortex and the other without, are left to expand and interfere, the resulting interference fringes show a dislocation at the vortex location. This is shown in Fig. 3.3, where the results from a numerical simulation are compared to the experiment reported in [Che01]. In the real experiment dislocations are harder to see, but can anyway be used to detect vorticity.

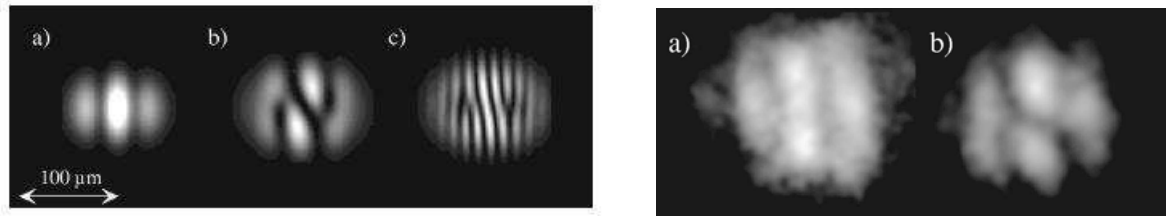

Figure 3.3: Left panel: Numerical prediction of the interference pattern when two condensates collide with (a) zero vortices, (b) one vortex and (c) two vortices. Right panel: Experimental measurement of interference fringes for two condensates with (a) zero vortices and (b) one vortex. From [Che01].

3.3.3 Vortex dynamics

Centered vortex lines are stationary states of the Gross-Pitaevskii equation. However, in the experiments, vortices can present some dynamics. One of the most clear examples is the motion of an off-center vortex, which follows nearly circular trajectories, showing thus precession around the trap symmetry axis. This precession mode is shown in a series of pictures from [And00] in Fig. 3.4. The period of the orbit can be related to the excitation of the anomalous mode (see for instance [Fet09]), and also to the frequency (Ω_m) at which the energy of a centered vortex becomes a local minimum in the rotating frame [Svi00] (see Sec. 3.4).

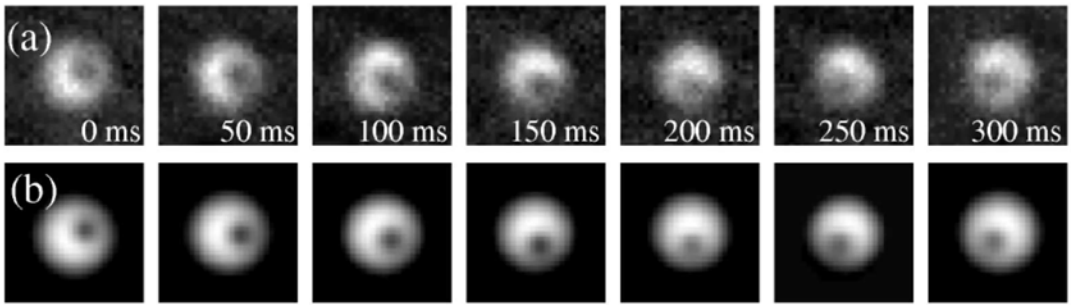

Figure 3.4: Precession of an off-axis vortex in a BEC. Top row: experimental measurements. Bottom row: corresponding numerical simulations. From [And00].

Another interesting dynamical aspect of quantized vortices is their effect on the frequency of collective excitations. The presence of a vortex, and thus of an axis of quantization, breaks the degeneracy between the $\pm m$ components of the excitation. For the quadrupole mode, for instance, the frequency splitting of the modes $m = +2$ and $m = -2$ allows for a precise measurement of the angular momentum [Zam98, Che00]. Excitation of this particular mode can lead to the generation of Kelvin modes [Bre03], which are helicoidal excitations of the vortex line.

3.4 Gross-Pitaevskii equation in the rotating frame

As we have seen, vortex states are the way a superfluid responds to rotation. To study them from a theoretical point of view and in the mean-field framework, it is sometimes useful to write the GP equation in the rotating frame (see, for instance, Ref. [Fet09]),

$$-\frac{\hbar^2}{2m}\nabla^2\psi + V_{\text{ext}}\psi + g|\psi|^2\psi + \int \mathrm{d}\mathbf{r}' v_{\text{dip}}(\mathbf{r}-\mathbf{r}')|\psi(\mathbf{r}')|^2\psi - \Omega\hat{L}_z\psi = \mu\psi \ , \qquad (3.20)$$

where the rotation has been assumed to be around the z axis, that is $\mathbf{\Omega} = \Omega\,\hat{\mathbf{z}}$, with Ω the rotation frequency. The angular momentum operator is defined as $\mathbf{L} = \mathbf{r} \times \mathbf{p}$. The z-component of this operator is $\hat{L}_z = -i\hbar\partial_\varphi$ and its expectation value is denoted by L_z. The term $-\Omega\hat{L}_z$ favors solutions with $L_z > 0$, that is, solutions that present anticlockwise rotation. Since for axially symmetric configurations $[H, \hat{L}_z] = 0$, the solutions (eigenstates) of Eq. (3.20) are the same as those of Eq. (2.16). Energetically, however, these solutions differ due to the rotation energy.

3.4.1 Energy functional in the rotating frame

The energy functional in the rotating frame is given by

$$E^{(\mathrm{rot})} = E_{\mathrm{kin}} + E_{\mathrm{ext}} + E_{\mathrm{sw}} + E_{\mathrm{dip}} - E_{\mathrm{rot}} \ , \tag{3.21}$$

where the first four terms are given by Eqs. (2.19)–(2.22) and

$$E_{\mathrm{rot}} = \int \mathrm{d}\mathbf{r}\psi^*(\mathbf{r})\hat{L}_z\psi(\mathbf{r}) = \Omega L_z \tag{3.22}$$

is the energy given to the system by the "classical" rotation of its container (which is indeed a classical rotator, since it is either a magnetic or an optical trap). Notice that the last identity only holds for axially symmetric systems, since only there is L_z well defined. When the rotation of the container Ω is small, the superfluid cannot follow and $L_z = 0$, and therefore $E_{\mathrm{rot}} = 0$. There is no energy transfer from the rotating container to the superfluid. However when the rotation frequency reaches the critical rotation frequency, $\Omega = \Omega_c$, the superfluid responds to rotation by nucleating a vortex at the center. Its angular momentum jumps to the finite value $L_z = N\hbar$ and the rotation energy transfered to the superfluid becomes $E_{\mathrm{rot}} = N\hbar\Omega_c$.

From Eq. (3.21) we can write

$$E^{(\mathrm{lab})} = E^{(\mathrm{rot})} + \Omega L_z \ , \tag{3.23}$$

where $E^{(\mathrm{lab})}$ is the energy measured in the laboratory frame. Let us briefly comment here on the solutions of Eq. (3.20). For $\Omega = 0$, obviously $\psi = \psi_{\mathrm{gs}}$ and $E^{(\mathrm{rot})} = E^{(\mathrm{lab})} = E_{\mathrm{gs}}$, where ψ_{gs} and E_{gs} denote respectively the wave function and the energy of the ground state. For $\Omega < \Omega_c$, the solution is the ground state and still $E^{(\mathrm{rot})} = E^{(\mathrm{lab})} = E_{\mathrm{gs}}$, since $L_z = 0$. There exists a metastable frequency [Fet09], $\Omega_m < \Omega_c$, for which the vortex state becomes metastable, i.e. a centered and a slightly displaced vortex have the same energy in the rotating frame. It is related to the precession frequency of a slightly off-center vortex state (see also Sec. 5.2). For $\Omega > \Omega_m$ a centered vortex state is a metastable solution of Eq. (3.20), since the energy is a local minimum. In this condition, and still above the critical frequency, $E_v^{(\mathrm{rot})} > E_{\mathrm{gs}}$. Below Ω_c, the vortex state becomes the solution of Eq. (3.20), that is it minimizes the functional (3.21). Note that $E_v^{(\mathrm{lab})} > E_{\mathrm{gs}}$ always, since the vortex state is an excited eigenstate of the mean-field Hamiltonian.

3.4.2 Critical frequency for vortex nucleation

From Eq. (3.23) it is possible to define the critical frequency, Ω_c, as the frequency at which the energy of the vortex in the rotating frame equals the energy of the ground state, $E_v^{(\mathrm{rot})} = E_{\mathrm{gs}}$ (notice that the ground state energy is independent of the reference frame, since for this state $L_z = 0$). From this thermodynamical argument the critical frequency is written as

$$\Omega_c = \frac{1}{N\hbar}\left(E_v^{(\mathrm{lab})} - E_{\mathrm{gs}}\right) \ . \tag{3.24}$$

In the s-wave Thomas-Fermi limit (see Sec. 2.3.1) it is possible to find an analytical expression for Ω_c using Eq. (3.24) [Lun97],

$$\Omega_c = \frac{5}{2}\frac{\hbar}{mR_\perp^2}\ln\frac{0.671R_\perp}{\xi} \ . \tag{3.25}$$

Equation (3.24) (or its Thomas-Fermi version, Eq. (3.25)) provides an approximation to the experimental critical frequency, although they don't agree perfectly. Equation (3.24) gives a critical frequency smaller than the experimental frequency (see for instance [Mad00]). This discrepancy can be interpreted as the existence of a nucleation energy barrier (see Sec. 5.1.3) that the system needs to overcome in order to bring the vortex from the surface to the center of the condensate.

3.5 Numerical generation of vortex states

Numerically, centered vortex states can be generated by imaginary time evolution (see Appendix A) of the Gross-Pitaevskii equation (2.16), imposing an initial phase $e^{i\varphi}$ to the ground state wave function and letting the system evolve without any constraint. In this way, the minimization procedure is constrained to a local energy minimum and the vortex solution is found. In cartesian coordinates, the initial wave function reads

$$\psi_{\rm ini}(x,y,z) = \psi_{\rm gs}(x,y,z)\frac{x+iy}{\sqrt{x^2+y^2}} \ . \tag{3.26}$$

Note that the phase term is not well defined for $x = y = 0$. Since at this point (vortex core) the density must be zero, without loss of generality we set $\psi_{\rm ini}(0,0,z) = 0$. This method only holds if the vortex is initially imposed at the center of the trap. If it is slightly displaced from $x = y = 0$, the imaginary time converges to the real energy minimum, that is the ground state solution, with $L_z = 0$. Notice that the method is equivalent to the minimization of the energy functional in the laboratory frame, that is, with $\Omega = 0$. It works due to the possibility that the imaginary time falls into a metastable state (if the simulation is not run for enough time). In general this is considered a drawback of the imaginary-time propagation, but in this case it turns out to be useful for the calculation.

A more physical mechanism to numerically generate vortex states is to solve the Gross-Pitaevskii equation in the rotating frame, Eq. (3.20). For small rotation frequencies the algorithm converges to the ground state ($L_z = 0$), since the rotational energy $E_{\rm rot}$ is not enough to bring a vortex to the center of the condensate. For frequencies larger than a certain critical frequency, $\Omega_c^{\rm num}$, the vortex solution is found. In analogy to the experiments, for even larger frequencies, vortex lattice states can be generated. In general $\Omega_c^{\rm num} \neq \Omega_c$. Again this discrepancy can be understood with the concept of energy barriers: in the imaginary-time evolution the vortices are created at the external surface of the condensate (where the density is close to zero and the phase fluctuations are large) and then they enter the condensate. In this process they need to overcome a nucleation energy barrier, since off-axis vortices have a higher energy than centered vortices (this topic will be addressed in detail in Sec. 5.1.3, in Chapter 5).

Finally, we want to say some words about the dynamical nucleation of vortex states. If one wants to study the nucleation process numerically, using a mean-field theory[4], via a time dependent simulation, one needs to break the symmetry of the equations in both time and space. The latter is accounted for by introducing a trapping potential that is slightly elliptical, as is done in the experiments [Mad00]. In a way, it is equivalent to exciting the surface quadrupole mode and bring it close to instability. The time symmetry is broken by using a time-dependent potential, as for instance a time-dependent rotation frequency [Lobo04], or including dissipation [Tsu02, Kas03]. If the simulation is energy conserving (that is, in the absence of time-dependent potentials or dissipation terms), even if the trap is slightly deformed, no dynamical nucleation of vortices can be numerically studied. The dynamical nucleation process was beautifully addressed in Ref. [Kas03] including dissipation in the TDGP, as is shown in Fig. 3.5.

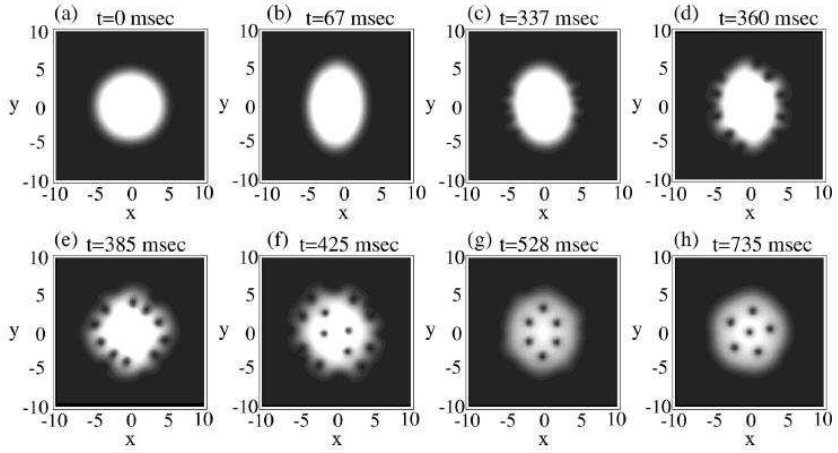

Figure 3.5: Numerical simulation of the vortex nucleation process: the axially symmetric ground state (a) is elliptically deformed (b) and this deformation is rotated in time above a critical frequency (c). After some time instability takes place at the surface (d) and vortices enter the condensate (e–g), organizing themselves in a lattice geometry (h). From [Kas03].

[4]Notice that during vortex nucleation there is a symmetry breaking where the order parameter changes from even parity (ground state) to odd parity (vortex state). It has been shown that at Ω_c the system enters a strongly correlated regime which cannot be addressed within mean-field [Dag09b]. Gross-Pitaevskii equation predicts instability, whereas direct diagonalization methods predict entanglement between a zero and a two-vortex state.

Chapter 4

Ground state of harmonically confined dipolar condensates

Since the experimental achievement of an atomic condensate with strong dipolar interactions in 2005 [Gri05] (see also [Bea08]), the physics of dipolar Bose-Einstein condensates (dBECs) has received much attention (for a review see [Lah09]). The most explored system has been the harmonically confined condensate, since up to date is the only geometry available in experiments. In this chapter we address the ground state of this system and study its static and dynamical properties. In some cases, the reproducibility of the results in the literature has provided us with a good check of the numerical code.

This chapter is organized as follows. In Sec. 4.1 we analyze the anisotropic deformation of the density profiles (Sec. 4.1.1), and we find that for certain parameters the maximum density appears away from the center of the trap, giving rise to a biconcave-shaped dipolar condensate (Sec. 4.1.2). In Sec. 4.2 we develop the 3D virial theorem for a dipolar condensate confined in a harmonic potential, which we have routinely used as a check of the accuracy of the simulations, especially of the spatial grid where the equations are solved. In Sec. 4.3 we address collective excitations of the condensate, focusing on the surface quadrupole mode. We solve the TDGP equation to find the frequency of oscillation (Sec. 4.3.1), and compare it with the result provided by the Thomas-Fermi approximation (Sec. 4.3.2), which has been obtained by minimization of the action (see also Chapter 8).

Before starting the discussion, let us comment some numerical considerations that will be applied during most part of this thesis. We have seen in Chapter 2 that the mean-field dipolar interactions can bring about anisotropy (due to the $\cos^2\theta$ term) and long-range effects (due to their $1/r^3$ dependence) to the physics of condensates. Also they render the GP equation a non-local equation, and this makes its numerical solution complicated. Throughout this thesis we routinely use the imaginary-time step method (see Appendix A) to solve the GP Eq. (2.16). This method can become quite time-consuming, but it leads to the ground state without the need to start from a configuration close to the solution (as happens in conjugate gradient method, which in contrast is much faster). To solve the TDGP Eq. (2.12) we use a Hamming's algorithm (see Appendix B) initialized by a fourth-order Runge-Kutta (see Appendix C). Both equations are in all cases solved in three dimensions. We use Fourier transform techniques to calculate the mean-field dipolar potential, as described in Sec. 2.2. The spatial grid used in the simulations has

been chosen such that the density goes to zero (i.e., is at least 12 orders of magnitude smaller than the peak density) at the borders, and such that it is large enough to avoid the effect of the replicas of the interaction potential. These replicas appear naturally when we go to Fourier space to perform the Fourier transform, since the real space system has finite dimensions. To check that our results are not affected by this, we take a grid where the energy does not change significantly when the grid extent is increased.

4.1 Ground state of a dipolar Bose-Einstein condensate

Before studying vortex states it is interesting to characterize the ground state wave function of the system, $\psi_{\rm gs}(\mathbf{r})$. We are interested in finding a set of parameters that allow us to explore different stable regimes of the condensate. As has been extensively discussed in the literature (see Chapter 1, or Ref. [Lah09] for a review), instability is related to the attractive part of the dipolar interaction, which arises in the direction where the dipoles are located head-to-tail. The stability diagram has been calculated in Ref. [Ron07] for a purely dipolar condensate. It is shown in the left panel of Fig. 4.1, in terms of the dipolar parameter D, see Eq. (2.30), and λ. We can distinguish three main regions: the unstable region (in white), the region where the ground state shows a maximum density at the center (in blue), and the region where the ground state shows a biconcave structure (in darker blue). The latter does not appear for all trap aspect ratios, but only in isolated islands. As a starting point, we have checked that the results of our full 3D calculation are in agreement with this stability diagram. Since pancake configurations are more stable than those spherical or cigar-shaped, we work with a pancake geometry with an aspect ratio of $\lambda = 11$, which we will keep for most of the thesis. We see from Fig. 4.1 that for this trap aspect ratio the dBEC shows both a "normal" ground state for $D \lesssim 70$ and a biconcave ground state for $70 \lesssim D \lesssim 85$, while for $D \gtrsim 85$ it becomes unstable.

Apart from dipolar interactions, a dBEC also shows contact interactions, characterized by the s-wave scattering length. Since they are repulsive for chromium, contact interactions help to stabilize the system. Depending on the trap aspect ratio, there exists a critical scattering length below which the condensate is unstable. This is shown in the right panel of Fig. 4.1, as reported in [Koch08]. For $\lambda = 11$, the critical scattering length is predicted to be $a_c \simeq -10\, a_B$.

We have seen in Sec. 2.2.3 that it is possible to define a length scale for dipolar interactions in a condensate of chromium, $a_{dd} \sim 15\, a_B$. This parameter cannot be identified with a scattering length due to dipole-dipole interactions, but is telling us that in order to observe dipolar effects, the s-wave scattering length should be comparable to a_{dd}. This is equivalent to saying that the dipolar parameter $\varepsilon_{dd} = a_{dd}/a$ should be as large as possible. Since the magnetic dipole moment is fixed for chromium[1], magnifying dipolar effects

[1]The magnetic dipole moment of chromium atoms cannot be changed since it comes from their electronic and nuclear structure. However, there are some techniques that allow for an effective tuning of the dipolar moment. One of them is relevant if the physics that we want to address is in a quasi-2D configuration. In this case, changing the angle between trap and polarization axes leads to a tuning on the effective dipolar interaction on the plane (see for instance [Mal11a]). Another mechanism relies on

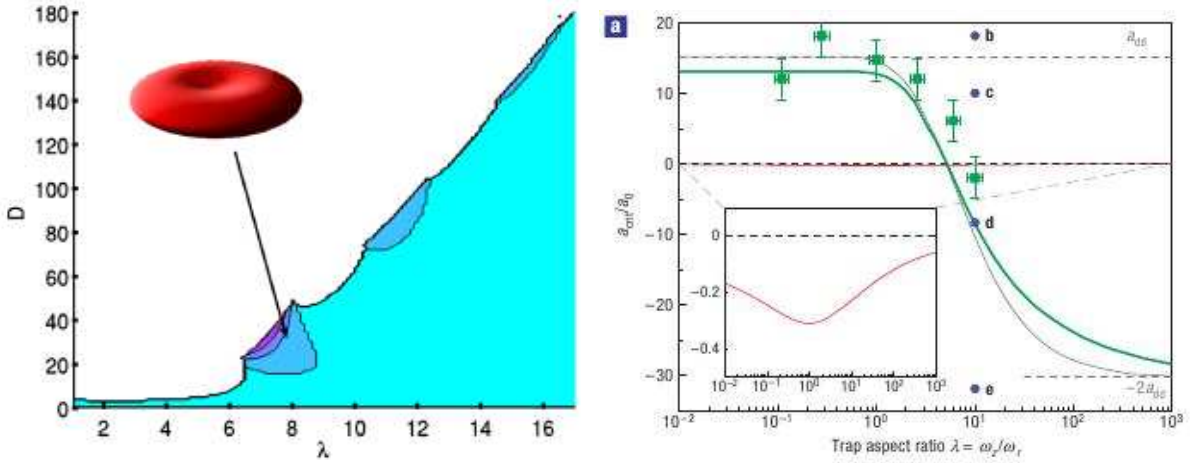

Figure 4.1: Left: Stability diagram in parameter space $D - \lambda$, taken from Ref. [Ron07]. The white region marks the region where the condensate is unstable; the blue region marks the stable region; the darker blue "islands" mark the biconcave configurations. Right: Critical values of the s-wave scattering length below which a dBEC with $N = 2 \times 10^4$ and $\omega_{\rm ho} = 700 \times 2\pi$ s^{-1} is unstable, from Ref. [Koch08]. The square symbols mark the experimental measurements; the thick solid line (green) is the prediction of the GP Eq. (2.16); the thin solid line is the solution provided by the dipolar TF approximation (see Sec. 2.3.2). Inset: Corresponding stability curve for a purely s-wave condensate.

means reducing the scattering length via Feshbach resonances. Then the anisotropic nature of the interaction becomes important and its effects can be experimentally measured. This is the picture we have in mind throughout the thesis whenever dipolar effects are enhanced.

4.1.1 Anisotropic deformation of the ground state

The anisotropy of the ground state is one of the most visible and studied properties of a dipolar condensate. It has received strong attention, both theoretically and experimentally. When the interactions are isotropic, the shape of the condensate follows that of the confining potential[2]. This is no longer the case for dipolar interactions. The main effect of their anisotropic nature on the ground state of the system is to deform the condensate with respect to the trap geometry. This effect, which is called magnetostriction (electrostriction for electric dipoles), is a direct consequence of the anisotropy of the dipolar potential and depends on the specific trap that is considered. For a spherical trap, the effect of the

the coupling of the dipole moment to a rotating magnetic field. If it is rotated fast enough, one can also achieve an effective tuning of the dipole-dipole interaction [Gio02]. Notice that the situation will be different for condensates of heteronuclear molecules, where the dipole moment should be externally controllable with an electric field.

[2]Note that isotropic interactions do not imply that the condensate aspect ratio, κ, coincides with the trap anisotropy, λ. It is only under the Thomas-Fermi approximation for s-wave condensates that $\kappa = \lambda$. In the non-interacting limit, $\kappa = \sqrt{\lambda}$ and in intermediate situations one has to solve the GP equation. However, what is true for isotropic interactions is that if $\lambda = 1$ then $\kappa = 1$, as well as if $\lambda > 1$ then $\kappa > 1$ and if $\lambda < 1$ then $\kappa < 1$.

dipolar interaction is to squeeze the cloud along the repulsive direction while stretching it in the attractive direction. Although this might be somewhat counter-intuitive, it is easily explained by taking into consideration the particular shape of the dipolar potential [Stu05]: since the dipolar potential shows a saddle configuration with two minima along the magnetization axis (attractive direction) it is less expensive for the system to accommodate more dipoles along this direction than along the repulsive one, thus the cloud size becomes larger in the former and smaller in the latter.

The magnetostriction effect is also present in pancake-shaped traps, but in this geometry the stretching and squeezing might be different. Also, the fact that the dipoles are aligned along the trap symmetry axis or forming an angle with it introduces a quantitative difference. We analyze the two limiting cases of magnetization parallel and perpendicular to the symmetry axis.

First, we address the case of the magnetization axis parallel to the trap symmetry axis (z). We consider a condensate of chromium containing $N = 10^5$ atoms in a trap with frequencies $\omega_\perp = 8.4 \times 2\pi$ s^{-1} and $\omega_z = 92.5 \times 2\pi$ s^{-1}, interacting via s-wave ($a = 5\,a_B$) and dipolar ($\mu_m = 6\,\mu_B$) interactions. The asymmetry parameter of such a configuration is $\lambda = 11$ and the dipolar parameters take the values $D = 50$ and $\epsilon_{dd} \simeq 3$ [3]. To analyze the magnetostriction effect in this geometry, we compare the root-mean-square (rms) radii along $r_\perp$ and z, denoted respectively by $R_{\rm rms}$ and $Z_{\rm rms}$, in three different situations: a purely s-wave condensate, a condensate with s-wave plus dipolar interactions, and a purely dipolar condensate (the corresponding density profiles can be seen in Fig. 5.1 together with those of a vortex). The results are given in Table 4.1. Comparing the purely s-wave condensate with the dipolar plus s-wave, we see that the condensate stretches in both directions when dipolar interactions are added, in contrast to what is found in a spherical trap. The same situation takes place when contact interactions are added to a purely dipolar condensate. Notice that even if both radii increase, the cloud aspect ratio $\kappa = R_{\rm rms}/Z_{\rm rms}$ also increases, which is in agreement with the experimental results reported in Ref. [Stu05]. The difference of behavior with respect to the spherical case can be understood as follows. In the pancake-shaped trap the condensate is tightly confined in the z direction so that the energy decrease achieved by putting more and more dipoles along the magnetization direction has to overcome a stronger trapping potential. The result of this energetic balance is that the system cannot accommodate so many atoms along the z axis, and hence the cloud has to stretch also radially.

Table 4.1: Root-mean-squared (rms) radii and aspect ratio of a dBEC with $\lambda = 11$ and magnetization along the trap axis.

Interaction	$R_{\rm rms}$ (μm)	$Z_{\rm rms}$ (μm)	κ
s-wave	9.157	1.106	8.279
dipolar + s-wave	12.435	1.288	9.654
Dipolar	11.618	1.282	9.062

When the dipoles are aligned perpendicularly to the trap axis (say, they are aligned

[3] Notice that a condensate in the Thomas-Fermi regime is unstable for $\varepsilon_{dd} > 1$ [Dell04], but the configuration we are dealing with is clearly away from the TF range of validity (in particular, the density profiles, see Fig. 5.1, are far from an inverted parabola).

along y), the cylindrical symmetry of the system is broken and anisotropic effects become even more evident. In a pancake-shape trap, collapse occurs at larger scattering lengths (compared to the parallel configuration), so that the dipolar condensate is in general less stable. Figure 4.2 shows density profiles along the three directions of space for different scattering lengths. Analogously to the parallel case, for a large scattering length ($a = 100\,a_B$) the dipolar effects are almost negligible, since contact interactions control mostly the physics of the system. The condensate is still pancake shaped, with the x and y sizes almost equal and the z size much smaller due to the trap anisotropy. When the scattering length is reduced (to, for instance, $a = 20\,a_B$) the dipolar effects become enhanced and the magnetization direction is privileged, yielding therefore a larger size than in the perpendicular direction (x). For a further reduction of the scattering length down to $a = 12\,a_B$ the condensate resembles a cigar with a similar size in the x and z directions but a much larger one along y. For $a < 12\,a_B$ the system becomes unstable due to the attractive component of the interaction. We will see in Chapter 6 that if the trap is toroidal instead of harmonic, collapse curiously occurs at the same scattering length. In a dBEC confined in a pancake trap potential with the dipoles aligned perpendicularly to the trap axis, a change in the scattering length is directly translated to a significant change in the condensate geometry. In this particular case, just by reducing the scattering length from $100\,a_B$ to $12\,a_B$, it is possible to tune the geometry from a nearly pancake-shaped to a nearly cigar-shaped condensate.

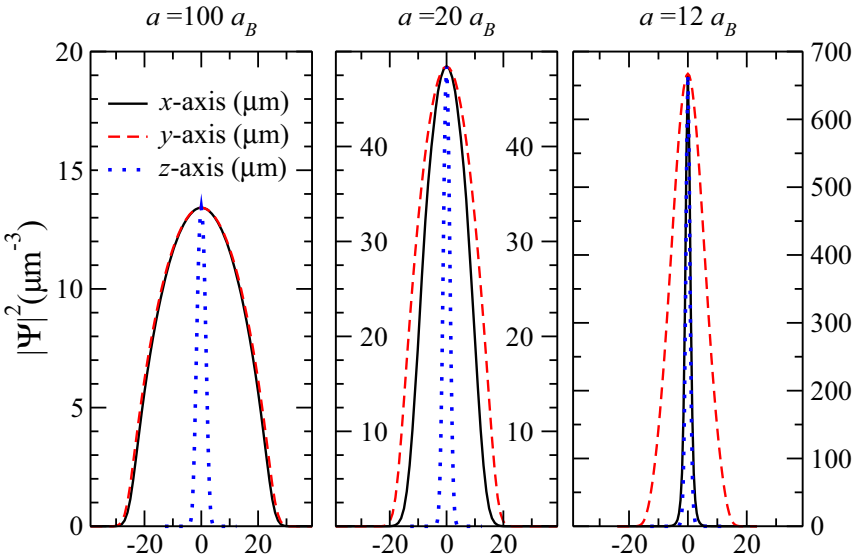

Figure 4.2: Ground state densities along the x-axis (solid line), y-axis (dashed line) and z-axis (dotted line) for a harmonically trapped condensate with $\lambda = 11$ for three different scattering lengths: $a = 100, 20, 12\,a_B$ (from left to right). The magnetization axis (y) is perpendicular to the trap symmetry axis (z).

4.1.2 Red-blood cell (biconcave) density structure

From Fig. 4.1 (left panel) we see that for large D, before collapse occurs, a dBEC with $\lambda = 11$ shows a biconcave structure. We have discussed in Sec. 4.1.1 that the dipolar potential

shows two minima along the magnetization direction. In general, they do not affect dramatically the structure of the ground state density, but in the biconcave regions the two minima of the dipolar potential become deep enough to exceed the trapping potential. When this happens the corresponding density shows its maximum value away from the center. These structures are known as biconcave or red-blood-cell density structures (see Ref. [Ron07]). As shown in Fig. 4.1, biconcave densities appear in isolated regions of the parameter space defined by D and λ (for $a = 0$), especially close to the instability threshold. These structures are both energetically and dynamically stable. However, if the value of D is slightly increased the condensate enters the unstable regime and undergoes collapse, which is thought to be of angular type [Ron07]. Biconcave density structures have been predicted to occur also at finite scattering lengths [Lu10]. They can become more pronounced in the presence of vortices, where more than one maximum can be seen in the density profile [Wil08]. In analogy with helium, this hints at a relation between biconcave structure and the roton mode in a dipolar gas [Ron07, Wil08].

Figure 4.3 shows the density profiles of two different stable ground state configurations of a purely dipolar ($a = 0$) condensate, one of them having a normal shape, while the other shows a biconcave structure. They both correspond to a condensate confined in a harmonic potential with asymmetry $\lambda = 11$ ($\omega_\perp = 8.4 \times 2\pi$ s^{-1} and $\omega_z = 92.5 \times 2\pi$ s^{-1}), but two different numbers of trapped atoms: $N = 10^5$ (solid line) and $N = 1.6 \times 10^5$ (dashed line), which correspond to dipolar interaction parameters $D = 50$ and $D = 80$, respectively. These density structures agree well with the stability diagram of Ref. [Ron07].

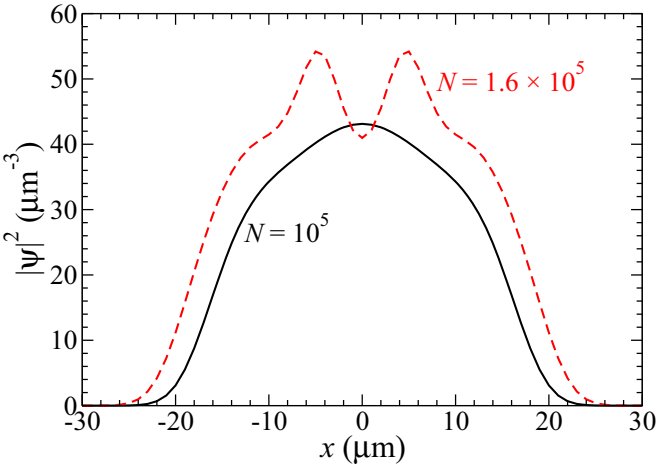

Figure 4.3: Density profiles of two different stable ground state configurations of a purely dipolar condensate, one of them having a normal shape, while the other shows a biconcave structure. The two curves correspond to dipolar parameters $D = 50$ and $D = 80$, corresponding to $N = 10^5$ and $N = 1.6 \times 10^5$, for a trap with $\lambda = 11$.

4.2 Virial theorem for a dipolar condensate

Virial expressions are relations between the different energy contributions that have to be fulfilled if the system is in equilibrium. In the case of a non-interacting system in a harmonic potential we find the well-known result $E_{\rm kin} = E_{\rm ho}$. To derive the virial theorem for a dipolar condensate we consider that the external potential is the 3D harmonic potential, $V_{\rm ho} = m/2\,(\omega_x^2 x^2 + \omega_y^2 y^2 + \omega_z^2 z^2)$. The virial theorem can be found by imposing that the energy must be a minimum and independent of a scaling $\mathbf{r} \to \nu\mathbf{r}$ of the coordinates, where ν is here an arbitrary scaling parameter. The condensate wave function scales as

$\Psi(\mathbf{r}) \to \Psi_\nu(\mathbf{r}) = C\Psi(\nu\mathbf{r})$, where C is a normalization constant. The principle of scale invariance ensures that the norm of the wave function is preserved, that is

$$\int \mathrm{d}\mathbf{r}\, |\psi(\mathbf{r})|^2 = \int \mathrm{d}\mathbf{r}\, |\psi_\nu(\mathbf{r})|^2 = |C|^2 \int \mathrm{d}\mathbf{r}\, |\psi(\nu\mathbf{r})|^2 = N \ , \tag{4.1}$$

which gives $C = \nu^{3/2}$. Using this result, we can find the scaling laws for the different terms of the energy. For the kinetic energy, it gives

$$\begin{aligned} E_{\mathrm{kin},\nu} &= \frac{\hbar^2}{2m} \int \mathrm{d}\mathbf{r}\, |\nabla\psi_\nu(\mathbf{r})|^2 = \nu^3 \frac{\hbar^2}{2m} \int \nu^{-3} \mathrm{d}(\nu\mathbf{r}) \nu^2 \, |\nabla_{\nu\mathbf{r}} \psi(\nu\mathbf{r})|^2 = \\ &= \nu^2 \frac{\hbar^2}{2m} \int \mathrm{d}\mathbf{r}' \, |\nabla'\psi(\mathbf{r}')|^2 = \nu^2 E_{\mathrm{kin}} \ , \end{aligned} \tag{4.2}$$

where we have introduced the variable $\mathbf{r}' = \nu\mathbf{r}$ for clarity. The harmonic oscillator energy scales as

$$\begin{aligned} E_{\mathrm{ho},\nu} &= \int \mathrm{d}\mathbf{r}\, V_{\mathrm{ho}}(\mathbf{r}) |\psi_\nu(\mathbf{r})|^2 = \frac{m}{2} \int \mathrm{d}\mathbf{r}\, \left(\omega_x^2 x^2 + \omega_y^2 y^2 + \omega_z^2 z^2\right) |\psi_\nu(\mathbf{r})|^2 = \\ &= \frac{m}{2} \int \nu^{-3} \mathrm{d}\mathbf{r}' \, \nu^{-2} \left(\omega_x^2 (x')^2 + \omega_y^2 (y')^2 + \omega_z^2 (z')^2\right) \nu^3 |\psi(\mathbf{r}')|^2 = \\ &= \nu^{-2} \int \mathrm{d}\mathbf{r}' \, V_{\mathrm{ho}}(\mathbf{r}') |\psi(\mathbf{r}')|^2 = \nu^{-2} E_{\mathrm{ho}} \ . \end{aligned} \tag{4.3}$$

For the contact interaction we find

$$E_{\mathrm{sw},\nu} = \frac{g}{2} \int \mathrm{d}\mathbf{r}\ |\psi_\nu(\mathbf{r})|^4 \ = \frac{g}{2} \int \nu^{-3} \mathrm{d}\mathbf{r}' \, \nu^6 \, |\psi(\mathbf{r}')|^4 = \nu^3 \frac{g}{2} \int \mathrm{d}\mathbf{r}' \ |\psi(\mathbf{r}')|^4 = \nu^3 E_{\mathrm{sw}} \ . \tag{4.4}$$

Finally, the scaling law for the dipolar interaction gives

$$\begin{aligned} E_{\mathrm{dip},\nu} &= \frac{1}{2} \frac{\mu_0 \mu_m^2}{4\pi} \int \mathrm{d}\mathbf{r}_1 \int \mathrm{d}\mathbf{r}_2 |\psi_\nu(\mathbf{r}_1)|^2 |\psi_\nu(\mathbf{r}_2)|^2 \frac{1 - 3\cos^2\theta}{|\mathbf{r}_1 - \mathbf{r}_2|^3} = \\ &= \frac{1}{2} \frac{\mu_0 \mu_m^2}{4\pi} \int \nu^{-3} \mathrm{d}\mathbf{r}_1' \int \nu^{-3} \mathrm{d}\mathbf{r}_2' \nu^6 |\psi(\mathbf{r}_1')|^2 |\psi(\mathbf{r}_2')|^2 \nu^3 \frac{1 - 3\cos^2\theta}{|\mathbf{r}_1' - \mathbf{r}_2'|^3} \\ &= \nu^3 \frac{1}{2} \frac{\mu_0 \mu_m^2}{4\pi} \int \mathrm{d}\mathbf{r}_1' \int \mathrm{d}\mathbf{r}_2' |\psi(\mathbf{r}_1')|^2 |\psi(\mathbf{r}_2')|^2 \frac{1 - 3\cos^2\theta}{|\mathbf{r}_1' - \mathbf{r}_2'|^3} = \nu^3 E_{\mathrm{dip}} \ . \end{aligned} \tag{4.5}$$

Grouping all the terms, we find that the total energy scales as

$$E_\nu = \nu^2 E_{\mathrm{kin}} + \nu^{-2} E_{\mathrm{ho}} + \nu^3 E_{\mathrm{sw}} + \nu^3 E_{\mathrm{dip}} \ . \tag{4.6}$$

Imposing the equilibrium condition,

$$\left. \frac{dE_\nu}{d\nu} \right|_{\nu=1} = 0 \ , \tag{4.7}$$

one finds the virial theorem for a dipolar condensate,

$$2E_{\mathrm{kin}} - 2E_{\mathrm{ho}} + 3E_{\mathrm{sw}} + 3E_{\mathrm{dip}} = 0 \ . \tag{4.8}$$

It is the same expression as for a degenerate gas of dipolar fermions [Sogo09]. The virial theorem can be used as a test of the accuracy of the numerical algorithm. Notice that the virial theorem, Eq. (4.8), is not affected by the rotation energy $E_{\rm rot}$, since this energy term is not sensitive to a scaling of the density, that is $E_{{\rm rot},\nu} = E_{\rm rot}$ (see Sec. 3.4.1 for its definition).

The virial theorem derived in this section is an isotropic 3D virial theorem, in the sense that the three directions of space are scaled in the same way. However, other kinds of scaling can be used. For instance, one can think of scaling only in one direction, in the radial coordinates (x and y), etc. In Sec. 4.3.2 and in Chapter 8 we will use the radial virial theorem, which is not straightforward to find for dipolar gases. The scaling argument used in this section is not the only method to derive virial relations. In Appendix G we derive the 3D virial expression above using a complementary method based on commutators of the Hamiltonian with a given excitation operator.

4.3 Collective excitations of the ground state: surface quadrupole mode

Collective excitations are an important subject in the physics of condensates, since they give information about physical properties that cannot be directly measured in the experiments. One of the most important collective modes is the dipole mode, which corresponds to the center of mass motion of a condensate in a harmonic trap. The dipole-mode oscillation frequency in direction i is thus ω_i, with $i = x, y, z$. The dipole mode is unaffected by two-body interactions, fulfilling Kohn's theorem. It allows experimentalists to determine the trap frequencies with high precision, while from the computational point of view it can be used as a check of a numerical code. We have indeed numerically checked that the trap frequencies are recovered from the dipole mode frequencies when a proper boost is applied to the initial wave function. For instance, if the operator $e^{i\tilde{\lambda}k_x x}$, with $\tilde{\lambda}$ a small parameter, is applied to the initial wave function (similarly to the quadrupole excitation below) the expectation value $\langle x\rangle(t)$ oscillates in time at a frequency ω_x. This perturbation of the initial wave function is equivalent to a displacement of the center of mass of the condensate.

Another collective mode that has been widely addressed in the literature is the radial quadrupole mode. It gives rise to oscillations of the density on the plane xy that alternatively stretch and squeeze the condensate along x and y, while they do not affect the density along z. This mode is a surface mode, and is quite independent of the equation of state of the system. Regarding the physics of vortices this mode has been excited to rotate the trap in optical stirring experiments [Mad00], as well as to create helical waves in vortices, or Kelvin modes [Bre03]. The radial quadrupole mode is of special importance in the physics of fermions, as we will see in Chapter 8.

In this section we study the shift that dipolar interactions produce in the frequency of the radial quadrupole mode, for a polarization parallel to the trap axis. We solve the TDGP equation for a small amplitude perturbation of the wave function with quadrupolar symmetry and compare the result with that corresponding to a purely contact interacting condensate (Sec. 4.3.1). In a second stage we use the Thomas- Fermi approximation

for dipolar condensates to find an expression for the frequency of the radial quadrupole (Sec. 4.3.2). We check that both methods agree well and that, in contrast to s-wave interactions, the frequency of the quadrupole mode for dipolar condensates in the Thomas-Fermi regime depends on the trap aspect ratio, as well as on the strength of the interactions.

4.3.1 Numerical calculation of the quadrupole mode

To find the frequency of the quadrupole mode numerically, we calculate the response to a small-amplitude perturbation of the wave function with quadrupolar symmetry. The method consists on mainly three steps. In the first one, the ground state of the system is found by evolving the GP Eq. (2.16) in imaginary-time until convergence is reached. In a second step, we perturb this wave function with the proper operator and let it evolve by simulating the TDGP Eq. (2.12) in real-time dynamics. We have considered the $t = 0$ perturbed wave function to be of the type

$$\Psi(\mathbf{r}, t = 0) = e^{i\tilde{\lambda}(x^2-y^2)}\psi(\mathbf{r}) \ , \tag{4.9}$$

where $\tilde{\lambda}$ is the parameter that controls the strength of the perturbation. It must be small in order to stay in the regime where linear response theory works, that is, the regime where ansatz (4.9) is a solution of the linearized GP equation and where the response is characterized by a single frequency. The perturbation (4.9) imposes a velocity field $\mathbf{v} \propto \boldsymbol{\nabla}(x^2 - y^2)$. During the time evolution we have recorded the expectation value of $x^2 - y^2$. As a third step, the Fourier transform of $\langle x^2 - y^2\rangle(t)$ is computed and the quadrupole spectrum is obtained. Since the signal that we want to transform is finite, the frequency peaks in the spectrum present some replica. In order to get rid of them we apply a Hann window before the Fourier transform, namely:

$$\tilde{f} = \begin{cases} \frac{1}{2} f \left[1 - \cos\left(\dfrac{2\pi t}{T}\right)\right] & \text{if } t < T \\ 0 & \text{if } t > T \end{cases} \tag{4.10}$$

with f the signal obtained during the numerical evolution and $\tilde{f}$ the actual signal we Fourier-transform. In this expression T represents the time reached by the simulation.

We consider a system of $N = 150000$ atoms of ^{52}Cr with the dipole moments oriented along the z axis in an axisymmetric trap with frequencies $\omega_\perp = 200 \times 2\pi$ s^{-1} and $\omega_z = 40 \times 2\pi$ s^{-1} (which makes $\lambda = 0.2$). Since purely dipolar condensates are unstable in cigar-shaped traps (see Fig. 4.1), we assume a scattering length of $a = 20\, a_B$, which can be reached experimentally via Feshbach resonances. For this configuration, $\varepsilon_{dd} = 0.76$ and $Na/a_\perp = 161$. Figure 4.4 shows the quadrupole mode frequency for a purely s-wave condensate and one with s-wave plus dipolar interactions. Indeed, we can see that there is a general shift of the spectrum induced exclusively by the dipole-dipole interaction.

Notice that in the s-wave case, the frequency of the quadrupole mode calculated numerically is larger than the $\sqrt{2}\omega_\perp$ value predicted within Thomas-Fermi approximation [Str96]. The difference is accounted for by the kinetic energy, which is nonzero in the numerical simulation and has been taken to be negligible in the Thomas-Fermi limit. The

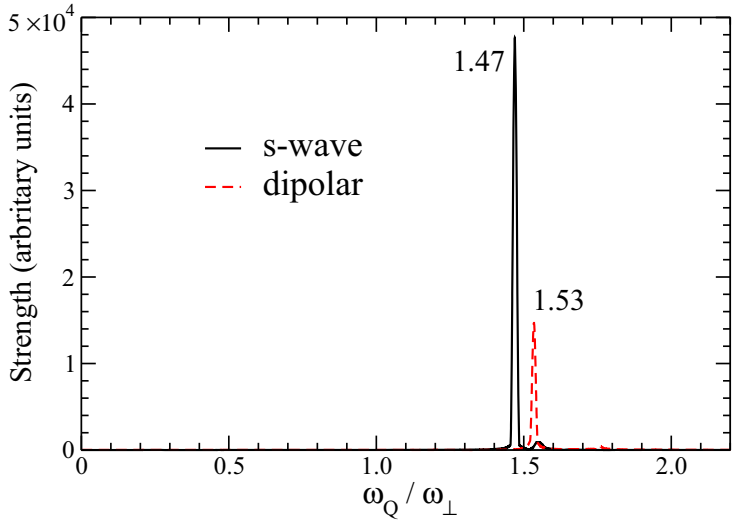

Figure 4.4: Frequency splitting of the quadrupolar mode induced by dipolar interactions as predicted by the numerical simulation of the TDGP Eq. (2.12). The solid black curve corresponds to a purely s-wave condensate and the dashed red line to a dipolar plus s-wave condensate.

first correction to the $\sqrt{2}\omega_\perp$ result is given by (see for instance [Zam98])

$$\omega_Q = \sqrt{2}\omega_\perp \left[1 + \frac{E_{\mathrm{kin}_\perp}}{E_{\mathrm{ho}_\perp}}\right]^{1/2} , \tag{4.11}$$

yielding a frequency $\omega_Q = 1.48\omega_\perp$[4], which is very close to the $1.47\omega_\perp$ of the numerical simulation.

4.3.2 Quadrupole mode in the Thomas-Fermi regime

There are several methods to calculate analytically the frequency of collective oscillations in the Thomas-Fermi regime: linearization of the hydrodynamic Eqs. (3.4) and (3.5), using a sum rule approach, or minimization of the action. All these methods have been successfully used for contact interacting condensates. For systems that in addition interact via a dipolar potential, we find that a variational procedure applied to the action is the easiest method. This will be the case both for dipolar condensates in the Thomas-Fermi regime, as well as for a dipolar gas of fermions (which will be addressed in Chapter 8 using the method detailed here).

The basic idea of the method is to apply a variational principle to the action,

$$S = \int dt \left\langle \Psi \left| H - i\hbar\frac{\partial}{\partial t} \right| \Psi \right\rangle , \tag{4.12}$$

where the variations are taken with respect to the parameters that characterize the excitation of the wave function Ψ. For the quadrupole mode, the excited wave function has the form

$$\Psi = e^{i\alpha(t)(x^2-y^2)}\psi_b(e^{-b(t)}x, e^{b(t)}y, z) , \tag{4.13}$$

[4]The values for the kinetic and the harmonic oscillator energies have been calculated numerically from the converged ground state, $E_{\mathrm{kin}_\perp} = 2.6199 \times 10^4\,\hbar\omega_\perp$ and $E_{\mathrm{ho}_\perp} = 2.7113 \times 10^5\,\hbar\omega_\perp$.

with α and b the variational parameters taking care of the velocity field and the deformation of the density brought about by the excitation, respectively. Notice that the phase factor in Eq. (4.13) has the same form as in Eq. (4.9). In contrast, the density modulation is fixed in (4.13) by parameter b, while it is obtained from the time evolution of the wave function in the computational method.

The first term under the action integral is the energy functional corresponding to the state Ψ. By introducing Eq. (4.13) into the energy functional Eq. (2.18) and taking the quantum pressure term to be negligible (TF approximation), we find that the different terms of the energy functional (see Eqs. (2.19)–(2.22)) are given by

$$E_{\rm kin}(\alpha) = \int {\rm d}\mathbf{r}\, n(\mathbf{r}) \frac{1}{2} m v^2 = \frac{2\hbar^2}{m} \alpha^2 N \langle r_\perp^2 \rangle \tag{4.14}$$

$$E_{\rm ho}(b) = \int {\rm d}\mathbf{r}\, n(\mathbf{r}) \frac{1}{2} m \omega_\perp^2 (r_\perp^2 + \lambda^2 z^2) = E_{\rm ho} + m\omega_\perp^2 b^2 N \langle r_\perp^2 \rangle \tag{4.15}$$

$$E_{\rm sw}(b) = \int {\rm d}\mathbf{r} [n(\mathbf{r})]^2 \frac{1}{2} g = E_{\rm sw} \tag{4.16}$$

$$E_{\rm dip}(b) = E_{\rm dip}(e^b R_\perp, e^{-b} R_\perp, R_z) = E_{\rm dip} - \frac{15}{14} \frac{N^2 \hbar^2 a}{m} \frac{\varepsilon_{dd}}{R_\perp^2 R_z} b^2 N g(\kappa) \ , \tag{4.17}$$

where the kinetic energy contribution corresponds to the term coming from the phase factor, according to Eq. (3.3). The dependence on $R_x = e^b R_\perp$ and $R_y = e^{-b} R_\perp$ in the dipolar energy is contained in the anisotropy function $f(x, y)$ given by Eq. (2.48). Finally, $E_{\rm ho}$, $E_{\rm sw}$ and $E_{\rm dip}$ are the ground state energy terms, given by Eqs. (2.45)–(2.47). Notice that these terms correspond to a second-order expansion in α and b. The function $g(\kappa)$ corresponds to a second derivative of $f(e^b\kappa, e^{-b}\kappa)$ with respect to b, see Eq. (8.24). This function goes to zero for $\kappa \to 0$ and $\kappa \to \infty$ and reaches a maximum around $\kappa = 2.37$. It will be discussed in greater detail in Chapter 8 (see Fig. 8.2). The second term in the action integral gives

$$\left\langle \Psi \left| -i\hbar \frac{\partial}{\partial t} \right| \Psi \right\rangle = 2\hbar \dot{\alpha} b N \langle r_\perp^2 \rangle \ , \tag{4.18}$$

where $\dot{\alpha}$ refers to the time derivative of α. Taking all the terms together, the action can be written as

$$S = S_0 + \int dt \left[\frac{2\hbar^2}{m} \alpha^2 N \langle r_\perp^2 \rangle + m\omega_\perp^2 b^2 N \langle r_\perp^2 \rangle - \frac{15}{14} \frac{N^2 \hbar^2 a}{m} \frac{\varepsilon_{dd}}{R_\perp^2 R_z} b^2 g(\kappa) + 2\hbar \dot{\alpha} b N \langle r_\perp^2 \rangle \right] \ , \tag{4.19}$$

where S_0 is the action of the ground state. Taking now variations with respect to α and b and setting them to zero, one finds the two coupled equations

$$2\frac{\hbar}{m}\alpha - \dot{b} = 0 \tag{4.20}$$

$$2m\omega_\perp^2 b \langle r_\perp^2 \rangle - \frac{15}{7} \frac{N\hbar^2 a}{m} \frac{\varepsilon_{dd}}{R_\perp^2 R_z} b g(\kappa) + 2\hbar \dot{\alpha} \langle r_\perp^2 \rangle = 0 \ , \tag{4.21}$$

which can be rewritten in the shape of a harmonic oscillator, $\ddot{b} + \omega^2 b = 0$ and analogously

for α. The frequency ω corresponds to the quadrupole mode, which is given by

$$\omega_Q = \sqrt{2}\omega_\perp \left[1 - \frac{1}{4}\frac{\varepsilon_{dd}}{1+\varepsilon_{dd}\left(\frac{3}{2}\frac{\kappa^2 f(\kappa)}{1-\kappa^2} - 1\right)} g(\kappa)\right]^{1/2}, \tag{4.22}$$

where we have used that $\langle r_\perp^2 \rangle = 2/7\, R_\perp^2$. For zero dipolar interactions ($\varepsilon_{dd} = 0$), we recover the quadrupole mode frequency for an s-wave condensate in the TF limit, $\omega_Q = \sqrt{2}\omega_\perp$ [Str96]. Figure 4.5(a) shows the behavior of the quadrupole frequency as a function of the scattering length, which is related to ε_{dd} by Eq. (2.32), for a condensate of ^{52}Cr. The vertical dotted line indicates the value of a_{dd}, below which a dBEC in the TF regime is dynamically unstable[5]. For completeness, Fig. 4.5(b) shows the dependence of κ/λ on a for different trap aspect ratios. We clearly see from both figures that the dipolar effect on the frequency and on the condensate deformation becomes larger as the scattering length is reduced. For $\lambda = 0.2$, the condensate shows unstable behavior for scattering lengths around $a_{dd} \sim 15\, a_B$, which can be clearly recognized as a sharp reduction of ω_Q (notice that this is in agreement with the stability diagram shown in the right panel of Fig. 4.1). For $a < a_{dd}$, the value of ω_Q becomes imaginary and the condensate is predicted to collapse. For larger trap aspect ratios, the TF approximation gives metastable solutions [Dell04], and collapse due to the quadrupole mode is predicted to occur at $a < a_{dd}$. We see that the most stable configuration is that with the largest λ.

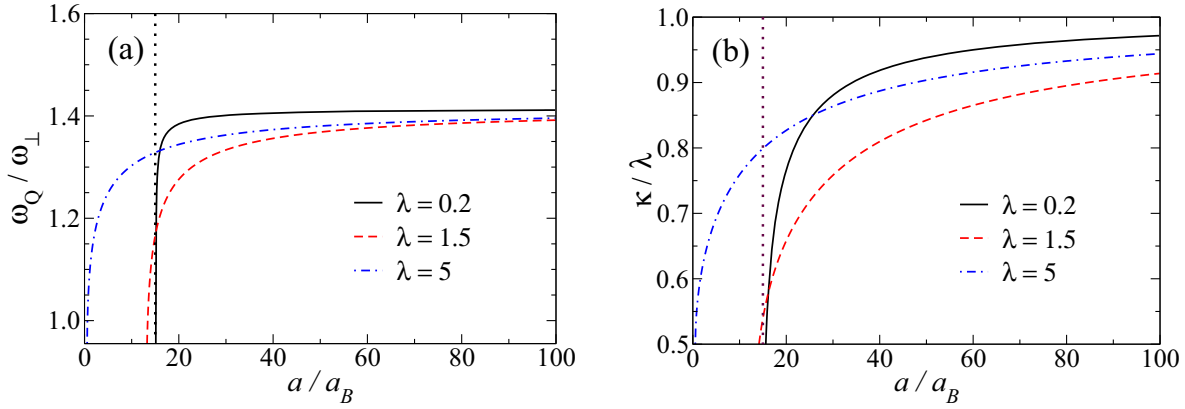

Figure 4.5: (a) Quadrupole mode frequency as a function of the scattering length for different trap aspect ratios. (b) Ratio κ/λ between the condensate and the trap aspect ratios as a function of the scattering length.

From Eq. (4.22) we see that $\omega_Q < \sqrt{2}\omega_\perp$ for a dBEC, independently of the trap aspect ratio considered. For the case in Fig. 4.4, Eq. (4.22) predicts $\omega_Q = 1.38\omega_\perp$. The discrepancy between this and the numerical result can be understood in terms of the kinetic energy. To derive Eq. (4.22) we are setting the quantum pressure term to zero, but it might not be totally negligible. The correction to the frequency would be analogous

[5]Notice that even if it is predicted to be unstable for $a < a_{dd}$, for large λ the TF solution is (energetically) stable [Dell04]. This is the reason why the curves ω_Q in Fig. 4.5(a) are drawn below a_{dd}.

to Eq. (4.11), yielding $\omega_Q = 1.54\omega_\perp$[6], which is very close to the numerical result, $1.53\omega_\perp$. Notice that this correction causes the quadrupole mode frequency to be larger than the hydrodynamic result $\sqrt{2}\omega_\perp$, which is indeed what we find with the numerical simulations. Very recently the radial quadrupole frequency has been calculated adding corrections beyond the mean-field TF approximation [Lima11], finding a positive correction that could raise the value of ω_Q above $\sqrt{2}\omega_\perp$.

[6]The values for the kinetic and the harmonic oscillator energies have been calculated numerically from the converged ground state, $E_{\mathrm{kin}_\perp} = 0.3884 \times 10^5\, \hbar\omega_\perp$ and $E_{\mathrm{ho}_\perp} = 1.6064 \times 10^5\, \hbar\omega_\perp$.

Chapter 5

Vortex states in harmonically confined dipolar condensates

Quantized vortex states are a clear signature of superfluidity in a system. In Chapter 3 we have described the main features of vortices in contact interacting condensates. In this chapter we extend the study of quantized vortices to harmonically confined dipolar condensates, with the aim of analyzing how the new long-range and anisotropic interaction modifies them.

The chapter is organized as follows. In Sec. 5.1 we address the static properties of the vortex state. We look at the structure of the vortex core (Sec. 5.1.1) and characterize the nucleation process by studying the rotation frequency (Sec. 5.1.2) and the energy barrier the system needs to overcome (Sec. 5.1.3). In Sec. 5.2 the TDGP equation is applied to study the precession of the vortex in presence of dipolar interactions.

5.1 Vortex states in a dipolar condensate

We have numerically computed a vortex state by imprinting a phase to the initial wave function and solving the GP equation (2.16) in the rotating frame without fixing the vorticity during the minimization process. We have used ansatz (3.26) for the initial wave function and have solved the GP equation (2.16) in imaginary time. As expected, for small values of Ω the system converges to a vortex-free configuration that corresponds to the ground state, while for values of the angular frequency equal or slightly larger than the critical one, a centered vortex state configuration minimizes the energy in the rotating frame. We have checked that the circulation is quantized around the vorticity line.

In this section, the system in which we are interested is characterized by $N = 10^5$, $\omega_\perp = 8.4 \times 2\pi$ s^{-1} and $\omega_z = 92.5 \times 2\pi$ s^{-1} ($\lambda = 11$), with the dipoles aligned along the trap symmetry axis (z). For chromium, this corresponds to $D = 50$. The ground state of this configuration has been discussed in Sec. 4.1 and the corresponding density profile along x is shown in Fig. 5.1 (middle panel, solid line).

5.1.1 Structure of the vortex core

The vortex states we have obtained are straight vortex lines. For a condensate with only contact interaction the local healing length, Eq. (3.18), provides a characteristic length for describing the core size of a vortex. In the presence of dipole-dipole interactions the parameter thus defined does no longer provide a good estimate of the vortex core size. Figure 5.1 shows the density profiles for the ground state and the vortex state of a condensate interacting via: s-wave interactions only (left panel), s-wave plus dipolar interactions (middle panel), and dipolar interactions only (right panel). The contact interaction is characterized by $a = 5\,a_B$. For this set of parameters, $a_\perp = 4.81\,\mu$m and $\xi = 0.294\,\mu$m.

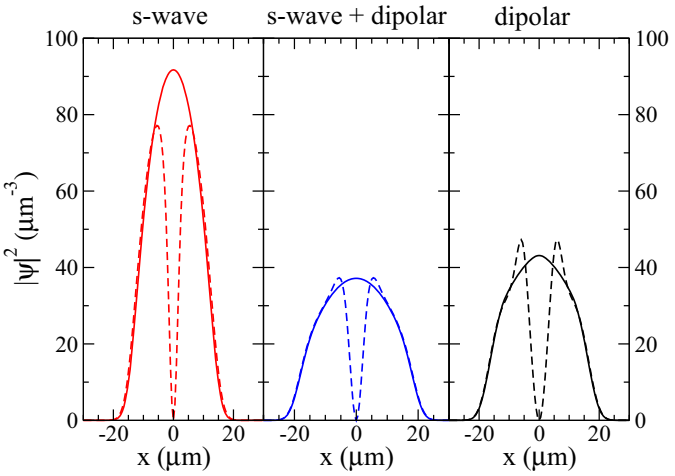

Figure 5.1: Density profiles for vortex (dashed) and ground (solid) states of condensates whose atoms interact via s-wave (left panel), s-wave plus dipolar (middle panel) and dipolar (right panel) interactions, for $a = 5\,a_B$.

A possible characterization of the core is given by Eq. (3.19), which has been applied to dipolar condensates in Ref. [Dell07] assuming the variational ansatz for the vortex density profile

$$n_v(r_\perp, z) = n_0 \left(1 - \frac{r_\perp^2}{R_\perp^2} - \frac{z^2}{Z^2}\right)\left(1 - \frac{\beta^2}{r_\perp^2 + \beta^2}\right), \tag{5.1}$$

with β, $R_\perp$ and Z variational parameters. Clearly, the quotient between the vortex and ground state densities in the TF limit is zero at the vortex position and unity outside the vortex core (see Sec. 3.2, Fig. 3.2). In particular, it is easy to verify that β corresponds to the radius at which this quotient is equal to $1/2$ at the $z = 0$ plane. Using the numerically calculated vortex and ground state densities $n_v(\mathbf{r})$ and $n_{\rm gs}(\mathbf{r})$, we propose as a definition of the core radius β the $r_\perp$ value in the $z = 0$ plane that satisfies:

$$f(r_\perp = \beta, z = 0) = \frac{n_v(r_\perp = \beta, z = 0)}{n_{\rm gs}(r_\perp = \beta, z = 0)} = \frac{1}{2}\,. \tag{5.2}$$

This generalizes ansatz (5.1) to numerically generated densities. The density profile along the x axis, $n_v(x, y = 0, z = 0)$, is shown in Fig. 5.2(a) for a vortex in a condensate with dipolar plus contact interactions (solid line) and with only contact interaction (dashed line), with $a = 5\,a_B$. In the inset, the ratio f is depicted as a function of the distance to the vortex core for both cases. We can see that f does not take the value $f = 1$ outside the core. This is due to the fact that the system does not lie in the TF regime and the structure

of the condensate surface becomes important. When no dipolar effects are considered, the deviation from the value $f = 1$ is larger, since the density is more Gaussian-like than an inverted parabola, meaning that for this configuration the condensate is close to the non-interacting limit. Nevertheless, Eq. (5.2) still provides a good definition of the vortex core.

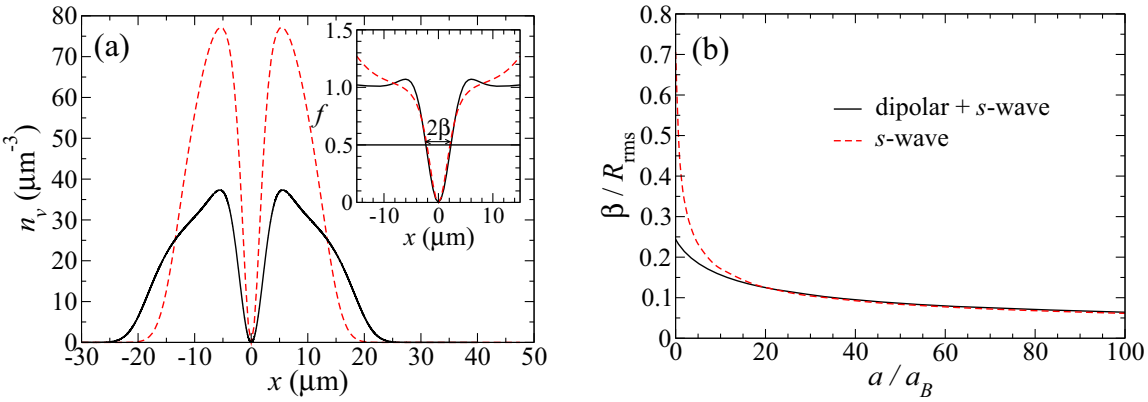

Figure 5.2: (a) Vortex density profile as a function of x at $y = z = 0$ for BECs with contact ($a = 5\,a_B$) plus dipolar interaction (solid line) and only contact interaction (dashed line). Inset: f as a function of the distance to the vortex core for both cases; the value of the core radius β is also indicated. (b) Ratio of the vortex core size (β) and the radial size of the condensate with respect to the scattering length. Solid curve: s-wave plus dipolar interactions. Dashed curve: only s-wave interactions.

Figure 5.2(b) shows the ratio $\beta/R_{\rm rms}$ of the vortex core size to the radial size ($R_{\rm rms} = \sqrt{\langle r_\perp^2 \rangle}$) of the disk-shaped condensates of Fig. 5.2(a) for different values of the s-wave scattering length. The effect of dipolar interactions for large scattering lengths is to slightly increase the relative value of the core size with respect to the radial size of the condensate above the value of the purely s-wave case, as already discussed [Dell07]. However, when $a < 20a_B$, the ratio $\beta/R_{\rm rms}$ is smaller for a condensate with dipolar interactions than in a purely contact interaction BEC. This is due to the small repulsive interaction brought by the dipole-dipole potential, which becomes noticeable only for small scattering lengths. This interaction has the effect of decreasing the central density of the condensate as compared to the purely s-wave case and this causes a smaller core radius and a broader ground state.

5.1.2 Critical rotation frequency and vortex generation

As we have discussed in Chapter 3, the inclusion of vorticity in a condensate is accompanied by an energy cost due to the appearance of angular momentum. In a frame rotating at an angular frequency Ω about the z axis (see Sec. 3.4), the energy of a condensate carrying angular momentum L_z is $E^{(\rm lab)} - \Omega L_z$. At low rotation frequencies this energy is minimal without the vortex (ground state configuration). But if Ω is large enough the creation of a vortex can become favorable due to the $-\Omega\hat{L}_z$ term in Eq. (3.20). This happens at the critical frequency Ω_c given by Eq. (3.24).

The critical rotation frequency depends on the interaction parameters (scattering length, dipole moment), as well as on the number of atoms and the trap geometry. We plot Ω_c in Fig. 5.3(a) as a function of the scattering length, for the same condensate as in Sec. 5.1.1 (see also Sec. 4.1.1). As a reference we have also calculated the critical angular velocity necessary to nucleate a vortex in the corresponding non-dipolar condensate (dashed curve). For large scattering lengths, the dipolar condensate is controlled by contact interactions and the critical frequency becomes equal to that of the non-dipolar condensate. For smaller scattering lengths the inclusion of the dipole-dipole interaction decreases the value of Ω_c. It is hence energetically easier to nucleate a vortex when dipolar interactions are present. This can be understood as follows: in the pancake geometry the mean-field interaction between dipoles is repulsive on average, giving rise to a maximum of density smaller than in the purely s-wave condensate (see Fig. 5.1) which makes it easier to take the atoms away from the z axis and nucleate a centered vortex. Note that in the non-interacting limit, the critical frequency tends to $\omega_\perp$, as is expected from the theory. In the dipolar condensate, for $a = 0$ the value of Ω_c is about one fourth of $\omega_\perp$.

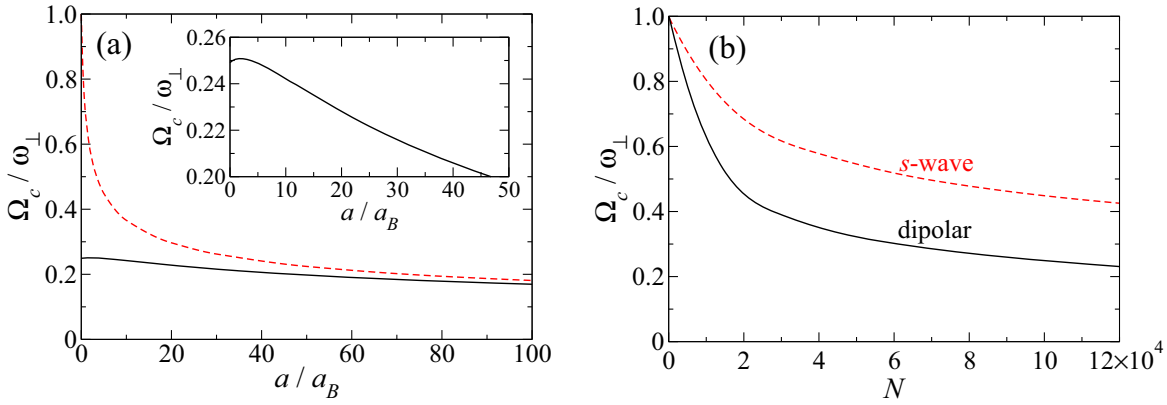

Figure 5.3: (a) Critical angular velocity for a singly quantized vortex in a pancake trap with aspect ratio $\lambda = 11$, as a function of the s-wave scattering length. The solid line corresponds to s-wave plus dipolar interactions. The dashed line corresponds to only s-wave contact interaction. Inset: behavior of $\Omega_c(a)$ around $a \sim 0$ for a condensate with s-wave plus dipolar interactions. (b) Critical angular velocity as a function of the number of atoms. The solid line corresponds to a dipolar condensate, and the dashed line to a condensate with only contact interaction ($a = 5\,a_B$).

The inset of Fig. 5.3(a) shows a detail of the behavior of $\Omega_c(a)$ for small values of the s-wave scattering length, corresponding to the case of contact plus dipolar interactions. Ω_c presents a maximum around a scattering length $a \simeq 2a_B$, which corresponds to a dimensionless parameter $\epsilon_{dd} = 7.57$. The presence of this maximum is a consequence of the balance between contact and dipolar interactions and appears just before collapse.

The critical angular velocity for producing a vortex is plotted in Fig. 5.3(b) as a function of the number of atoms, for a purely dipolar condensate (solid line) and for a condensate with only contact interaction with $a = 5\,a_B$ (dashed line). For a given number of atoms the effective repulsion of the dipolar interaction in a pancake shaped condensate is larger than the repulsive contact interaction; therefore, Ω_c is smaller in a purely dipolar condensate. However, both curves have a similar behavior: Ω_c decreases with increasing N, as the repulsion also increases.

5.1.3 Energy barrier

The critical frequency calculated in Sec. 5.1.2 is based on a thermodynamical consideration that takes into account the energy of the vortex at the center of the trap and thus provides a lower bound to the experimental critical frequency. This difference can be understood in terms of an energy barrier the system needs to overcome to bring the vortex from the surface to the center of the condensate [Svi00, Kra02]. That is, the nucleation of a vortex is associated with the existence of an energy barrier in the configuration space between the initial vortex-free state and the final centered vortex state. The formation energy of a vortex can be estimated by calculating the energy of a single off-center vortex as a function of the vortex core position.

We calculate the energy barrier, $\Delta E(d_v, \Omega)$, as the vortex energy in the rotating frame as a function of the vortex distance from the symmetry axis, $d_v = \sqrt{x_v^2 + y_v^2}$. It is defined with respect to the ground state energy as $\Delta E(d_v, \Omega) = E^{(\mathrm{rot})}(d_v, \Omega) - E_{\mathrm{gs}}$, and it is related to the energy in the laboratory frame by Eq. (3.23). Note that the energy barrier depends on the actual value of Ω but the energy in the laboratory frame does not. For $\Omega = \Omega_c$ and $d_v = 0$ we have $\Delta E(0, \Omega_c) = 0$ since under these conditions the energy of a centered vortex is exactly the rotation energy, which comes directly from the definition of critical frequency, Eq. (3.24). For a vortex near the boundary of the condensate $L_z \to 0$ [Gui01], whence $\Delta E(d_v, \Omega) \to 0$. Between these two limits, the energy barrier reaches a maximum value $\Delta E_{\max}$ at the position $d_{v_{\max}}$, corresponding to the extra energy the system needs in order to carry the vortex from the surface to the center of the condensate.

We generate an off-axis vortex at position $\mathbf{r}_v = (x_v, y_v, z)$ using the ansatz [Jez08a]

$$\psi_{\mathrm{ini}}(\mathbf{r}) = \psi_{\mathrm{gs}}(\mathbf{r}) \, \frac{(x - x_v) + i\,(y - y_v)}{\sqrt{(x - x_v)^2 + (y - y_v)^2}} \,, \tag{5.3}$$

which generalizes ansatz Eq. (3.26) for a centered vortex line. The energy $\Delta E(d_v, \Omega)$ is calculated by solving the GP equation in the rotating frame, taking Eq. (5.3) as initial wave function. In order to obtain the solution for the displaced vortex, which is not a minimum of Eq. (3.20), we have imposed that during the minimization process the initial nodal planes are kept constant, that is:

$$\mathrm{Re}\,[\Psi(x_v, y, z)] = 0 \quad \forall\, y, z \tag{5.4}$$

$$\mathrm{Im}\,[\Psi(x, y_v, z)] = 0 \quad \forall\, x, z \,. \tag{5.5}$$

With this method, the quantization of the circulation is ensured in all cases, but the solutions are restricted to the case of straight vortex lines.

We plot in the left panel of Fig. 5.4 the vortex formation energy as a function of the vortex displacement from the center, corresponding to the same condensate as in Fig. 5.3(a) rotating at the critical rotational frequency Ω_c. The distance of the vortex core to the symmetry axis is expressed in units of R_{rms} of the corresponding ground state. The dashed line corresponds to the purely contact interaction BEC (with $a = 5\,a_B$), the dash-dotted line to a condensate with contact plus dipolar interactions, and the solid line corresponds to a purely dipolar BEC ($D = 50$). The three critical barriers have the same qualitative behavior as a function of the dimensionless displacement of the vortex

core $d_v/R_{\rm rms}$. The maximum of the barrier height is located around $d_{v_{\rm max}}/R_{\rm rms} \sim 1.1$ for the contact interaction BEC and around $d_{v_{\rm max}}/R_{\rm rms} \sim 1.2$ for the other cases. As already guessed in Sec. 5.1.2, the nucleation is easier in a condensate with dipolar interactions than with only s-wave interactions, since the repulsion is larger in average. From the figure we can see that the main effect of contact interactions is to decrease the barrier height (compare dipolar and dipolar plus s-wave curves), while the effect of the anisotropic and long-range dipolar interaction is to move the maximum of the barrier towards the surface of the condensate (compare s-wave and dipolar plus s-wave curves).

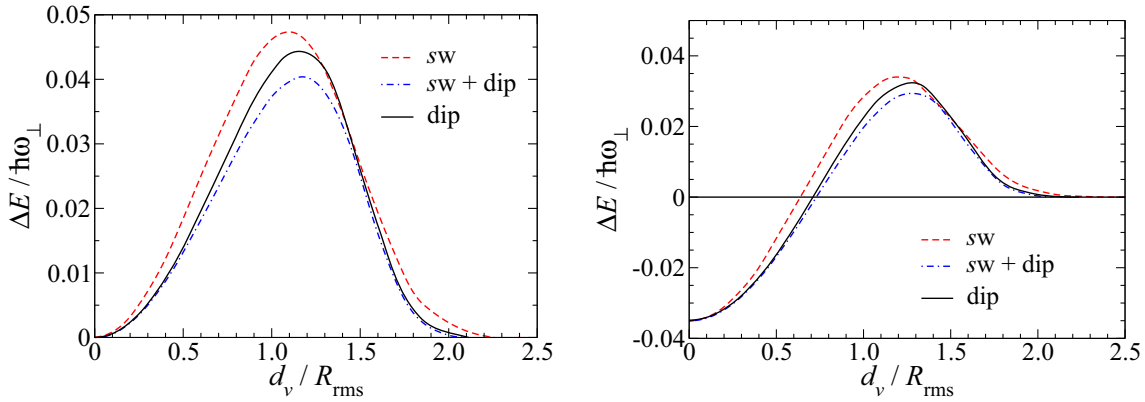

Figure 5.4: Vortex formation energy as a function of the vortex displacement from the center. The dashed line corresponds to the purely contact interaction BEC (sw, with $a = 5\,a_B$), the solid line corresponds to a purely dipolar BEC (dip), and the dash-dotted line to a condensate with contact plus dipolar interactions(sw + dip). Left panel: $\Omega = \Omega_c$; Right panel: $\Omega > \Omega_c$.

We plot in the right panel of Fig. 5.4 the same curves as in the left panel but calculated at larger angular velocities $\Omega > \Omega_c$, namely $\Omega = 0.48\,\omega_\perp$ for the purely contact interaction BEC with $a = 5\,a_B$ (dashed line) and $\Omega = 0.28\,\omega_\perp$ for both the purely dipolar BEC (solid line) and the condensate with the two types of interactions acting simultaneously (dash-dotted line). As expected, for rotational frequencies larger than the corresponding critical one, the state with a centered vortex is preferable. However, the nucleation of the vortex is inhibited by the barrier separating the vortex-free state from the centered vortex state. The effect of the nature of the interactions is the same as in the barriers at Ω_c: contact interactions raise the barrier maximum, while dipolar interactions move it outwards.

Thomas-Fermi models of the energy barrier

In the TF limit it is possible to obtain analytic expressions for the energy barrier for vortex nucleation [Svi00, Kra02, Fet09] (see also [Abad10b] for more details). Although we are dealing with 3D systems, since the trap anisotropy parameter is large, $\lambda = 11$, the 2D limit is worth considering. In these limits the position of the barrier maximum and

its height are given by

$$d_{v_{\max}}^{2D} = R_\perp \sqrt{1 - \frac{\Omega_c^{2D}}{2\Omega}} \tag{5.6}$$

$$\Delta E_{\max}^{2D}(\Omega) \equiv \Delta E^{2D}(d_{v_{\max}}, \Omega) = \frac{(\Omega_c^{2D})^2}{4\Omega} \tag{5.7}$$

for a 2D geometry, and

$$d_{v_{\max}}^{3D} = R_\perp \sqrt{1 - \frac{3}{5}\frac{\Omega_c^{3D}}{\Omega}} \tag{5.8}$$

$$\Delta E_{\max}^{3D}(\Omega) \equiv \Delta E^{3D}(d_{v_{\max}}, \Omega) = \frac{2}{3}\Omega_c^{3D}\left(\frac{3}{5}\frac{\Omega_c^{3D}}{\Omega}\right)^{3/2} \tag{5.9}$$

for a 3D geometry. The radial Thomas-Fermi radius, $R_\perp$, is related to the rms-radius by $R_\perp = \sqrt{3}R_{\rm rms}$ in both cases.

To obtain an order of magnitude for the energy barriers, it is possible to combine the TF results (5.6) and (5.9) with the numerical values of Ω_c and $R_\perp$ (the latter calculated as $\sqrt{3}R_{\rm rms}$) obtained from the simulations. This pseudo-analytical method avoids thus the calculation of the complete energy barrier. Table 5.1 shows the main parameters of the barriers using these approximations at the critical frequency. We see from the table that the 3D approximation is in good agreement with the characteristics of the barriers found in the numerical simulation, whereas the 2D approximation shows some deviation. This means that in spite of the large anisotropy of the trapping potential, the 3D nature of the condensate is important to characterize the vortex energetics. In addition, the energy of the maximum is better reproduced for condensates with dipolar or both interactions. This happens because the corresponding density profiles (see Fig. 5.1) are closer to the TF inverted parabola profile than those of the purely *s*-wave condensate.

Table 5.1: Comparison of the energy barrier maximum and its position obtained in the numerical simulation (GP) and the 2D and 3D pseudo-analytical results.

Case	$\Omega_c/\omega_\perp$	$R_{\rm rms}(\mu{\rm m})$		$\Delta E_{\max}/\hbar\omega_\perp$	$d_{v_{\max}}/R_{\rm rms}$
s-wave	0.45	9.16	GP	0.047	1.09
			2D	0.112	1.22
			3D	0.084	1.09
both	0.25	12.44	GP	0.040	1.17
			2D	0.062	1.22
			3D	0.046	1.09
dipolar	0.25	11.62	GP	0.044	1.16
			2D	0.062	1.22
			3D	0.046	1.09

5.2 Vortex precession

In this section we address the precession dynamics of a slightly off-center vortex in a dipolar condensate. We show that the presence of dipolar interactions reduces the precession frequency of the vortex, as compared to a condensate with only contact interactions. We estimate the precession frequency by applying the results of the Thomas-Fermi approximation for contact interacting condensates, which gives the right order of magnitude.

Figure 5.5 shows the density profiles both for a contact interacting condensate (left panel) and for a dipolar condensate (right panel) of the ground state (solid) and of an off-center vortex at $d_v = 2\,\mu$m (dashed). The two configurations are calculated for the same parameters as in Sec. 5.1 (see also Sec. 4.1): $\omega_\perp = 8.4\times 2\pi\ \mathrm{s}^{-1}$, $\omega_z = 92.5\times 2\pi\ \mathrm{s}^{-1}$, $N = 10^5$, and for $a = 20\,a_B$. At this scattering length, the numerical critical frequency, i.e. obtained from Eq. (3.24), is $\Omega_c = 0.23\,\omega_\perp$ for the dipolar condensate and $\Omega_c = 0.30\,\omega_\perp$ for the s-wave condensate (see Fig. 5.3), and the condensate radii are $R_\perp = 26\,\mu$m and $R_\perp = 23\,\mu$m, respectively for the dipolar and the s-wave condensates. Here $R_\perp$ is estimated as the value of $r_\perp$ at which the densities in Fig. 5.5 would fall to zero if they had parabolic profiles. Numerically, the off-center vortex at $d_v = 2\,\mu$m is generated by imaginary time evolution imposing that the density is zero along a line with coordinates $(d_v, 0, z)$. With this ansatz we do not allow for bending of the core, but it might be a good approximation since we are dealing with large pancakes ($\lambda = 11$) and the vortex core is very close to the trap axis. In contrast to Sec. 5.1.3 we do not need to impose that the wave function vanishes on the nodal planes, since here we are dealing with off-center vortex states that are very close to the trap symmetry axis and the quantization is always preserved.

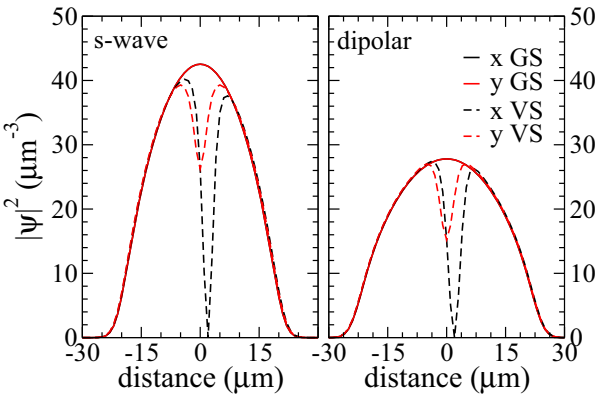

Figure 5.5: Density profiles for a BEC with $a_s = 20\,a_B$ when only contact interactions are taken into account (left panel) or both interactions (right panel).

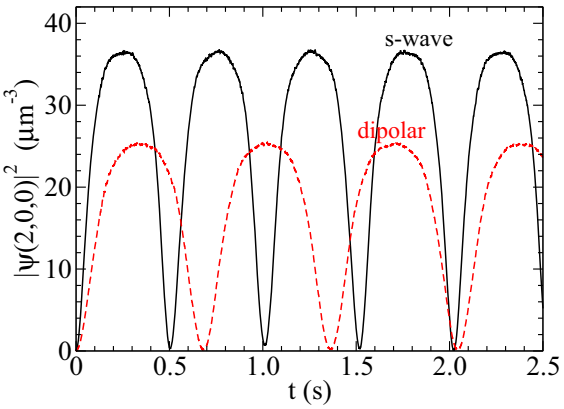

Figure 5.6: Comparison of the precession for a dipolar plus s-wave condensate (dashed) and its purely s-wave counterpart (solid).

To investigate the precession of the vortex, once the imaginary-time simulation is converged, we let the state evolve in real time without pinning the vorticity. We find that the vortex precesses around the symmetry axis in the same sense as its velocity field, that is counterclockwise. In order to measure the period of precession, we have followed the position of the core on the plane $z = 0$ and have measured the time evolution of the local density at the position $\mathbf{r} = (d_v, 0, 0)$, which corresponds to the initial position of the

vortex core at the $z = 0$ plane (Fig. 5.5). The numerical results for $d_v = 2\,\mu$m are shown in Fig. 5.6. We see that the precession periods are $T \sim 0.68\,$s and $T \sim 0.50\,$s, respectively, for dipolar and s-wave condensates.

For a non-rotating disk-shaped condensate in the Thomas-Fermi limit, the precession frequency is related to the metastable frequency Ω_m by [Fet09]

$$\omega_{\rm prec} = \frac{\Omega_m}{1 - d_v^2/R_\perp^2} \ , \tag{5.10}$$

where in this expression $R_\perp$ is the TF radius given by Eq. (2.36). For a vortex near the axis of symmetry, the precession frequency should be Ω_m. Physically, the metastable frequency is the rotation frequency above which a vortex in the center of the trap is no longer sitting in a local energy minimum in the rotating frame (see Sec. 5.1.3). At this particular point, the slope of the energy barrier at the center must be zero (i.e., the derivative of the energy in the rotating frame evaluated at $d_v = 0$ vanishes). For contact interacting condensates, the metastable frequency is given by

$$\Omega_m = \frac{3}{5}\Omega_c = \frac{3}{2}\frac{\hbar}{mR_\perp^2}\ln\frac{0.671R_\perp}{\xi} \ , \tag{5.11}$$

where we have used Eq. (3.25) for the critical frequency.

The factor $1 - d_v^2/R_\perp^2$ appearing in the denominator of Eq. (5.10) comes from the (inverted) parabolic shape of the density profile of a BEC in the Thomas-Fermi limit [Fet09]. Since in the Thomas-Fermi limit the parabolic solution to the density is also exact for a dipolar condensate [Dell04] (see also Ref. [Ebe05]), Eq. (5.10) can still provide an estimate of the precession frequency, provided an appropriate Ω_m is used. A rude approximation to Ω_m would be to calculate it from the numerical critical frequency. With the same spirit as in Ref. [Dell07], where very good agreement was found for Ω_c when Eq. (3.25) was used for dipolar condensates, we calculate the precession frequency using the s-wave Thomas-Fermi approximation applied to dipolar condensates. We will see that this simple calculation gives the correct order of magnitude of the precession frequency.

Table 5.2: Comparison of precession periods calculated using different approaches.

Method	T (s) (s-wave)	T (s) (dipolar)
Pure Thomas-Fermi	0.726	0.726
Mixed Thomas-Fermi	0.661	0.875
Numerical	0.500	0.680

For $d_v = 2\,\mu$m, the period of precession is estimated using Eq. (5.10) and $\Omega_m = 3\Omega_c/5$, giving $T = 0.875$ s for the dipolar condensate and $T = 0.661$ s for the s-wave condensate. In Table 5.2 these periods (named "mixed Thomas-Fermi") are compared to the ones predicted by the "pure Thomas-Fermi" approximation, where $R_\perp$, ξ and n_0 are obtained from Eqs. (2.36), (3.18) and (2.38), respectively, and assume a purely contact interacting condensate. In Table 5.2 there appear also the precession periods found by numerically simulating the precession process, that is by solving the time-dependent Gross-Pitaevskii equation for an off-center vortex (see Fig. 5.6). They give a smaller value value than

Thomas-Fermi approximations. This means that in a real experiment the velocity at which the vortex precesses around the symmetry axis will be higher than the predictions of the TF models.

Chapter 6

Toroidally confined dipolar condensates

The aim of this chapter is to address dipolar Bose-Einstein condensates that have been confined in toroidal traps, emphasizing the role of vortices in such systems. Toroidal confining potentials can be achieved in the laboratory using different methods. In particular, they can be generated by superimposing a blue-detuned Gaussian beam propagating along the z axis to the usual harmonic confinement in the three dimensions [Ram99]. It can be expressed mathematically as

$$V_{\rm ext} = \frac{m}{2}(\omega_\perp^2 r_\perp^2 + \omega_z^2 z^2) + V_0\, e^{-2r_\perp^2/\sigma_0^2} \ , \tag{6.1}$$

where V_0 is proportional to the intensity of the Gaussian beam and σ_0 is the beam waist. When the magnetization axis (y in what follows) is perpendicular to the trap symmetry axis (z), the condensate density becomes inhomogeneous along the torus defined by the confining potential. This angular dependence can be interpreted as a self-induced energy barrier created by the specific atom distribution. In Sec. 6.1 we explore the ground state configuration of such a system, while in Sec. 6.2 vortex states and persistent currents are analyzed. The effective potential landscape of this system can be interpreted as a double-well potential in the azimuthal direction. In Chapter 7 we will show that this self-induced potential constitutes a self-induced bosonic Josephson junction.

The physics addressed in this chapter, as well as in Chapter 7, is scalable in terms of the parameters appearing in the dimensionless GP Eq. (2.29). For the case considered here $\lambda = 11$, $Na/a_\perp = 96.77$ and $D = 24.99$, plus the dimensionless Gaussian parameters $\sigma_0/a_\perp = 2.08$ and $V_0/(\hbar\omega_\perp) = 15$. In the simulations, this is achieved in a ^{52}Cr condensate with $N = 5\times10^4$, $\omega_\perp = 8.4\times2\pi$ s^{-1}, $\omega_z = 92.5\times2\pi$ s^{-1}, $a = 14\,a_B$ and $\sigma_0 = 10\mu$m. Using the dimensionless constants it is easy to export the same physics to another set of parameters experimentally accessible in ^{52}Cr [Gri05, Bea08, Koch08], or even to condensates of alkali gases such as ^{39}K or ^{7}Li, where dipolar effects have been observed in Refs. [Fat08] and [Pol09], respectively, making use of a soft zero crossing of the scattering length near a Feshbach resonance.

Notice that the Gaussian part of the trapping potential scales in a different way as the harmonic part. This means that the virial theorem Eq. (4.8) cannot be used here, but has

to be accordingly modified to

$$2E_{\rm kin} - 2E_{\rm ext} + 2\int {\rm d}\mathbf{r}|\psi|^2 V_0 \left(1 + \frac{2r_\perp^2}{\sigma_0^2}\right) e^{-2r_\perp^2/\sigma_0^2} + 3E_{\rm sw} + 3E_{\rm dip} = 0 \ , \qquad (6.2)$$

where $E_{\rm ext}$ is the energy corresponding to potential Eq. (6.1). We have checked that this virial expression is fulfilled in all cases presented up to 4% of the total energy.

6.1 Ground state in a toroidal trap

The ground state of a dipolar condensate confined in a toroidal trap is found by minimizing the energy functional, Eq. (2.18), via imaginary time evolution (see Appendix A). The Gaussian potential in Eq. (6.1) introduces a repulsive barrier along the z axis. For large scattering lengths this barrier is not enough to burn a hole at the center of the condensate. However, when the scattering length is reduced, the chemical potential of the condensate becomes smaller and eventually equals V_0, under which condition a hole appears at the center. Figure 6.1(a) shows both the chemical potential and the effective height of the Gaussian barrier, ΔV_G, as a function of the scattering length, for a fixed laser intensity $V_0 = 15\hbar\omega_\perp$. This Gaussian barrier arises from the effective potential, $V_{\rm eff}(\mathbf{r}) = V_{\rm ext}(\mathbf{r}) + V_{\rm dip}(\mathbf{r})$, and is defined as the difference between the minimum and central effective potentials along the x axis. Note that the effective Gaussian barrier is not constant with a, even if V_0 is fixed. This comes from the density-dependence of the dipolar potential (that is, the dipolar term in the Gross-Pitaevskii equation). By changing V_0 one can choose the scattering length for the onset of toroidal geometry. In Chapter 7 we will see that the effective potential is responsible for the Josephson junction character of the system. The appearance of $V_{\rm dip}$ in its definition is telling us that in dipolar systems, the mean-field dipolar interaction enters mainly as an anisotropic trapping potential that introduces an extra modulation of the density. This was already guessed in the biconcave density structures of Sec. 4.1.2, but in the toroidal system this fact has dramatic consequences and opens a new physical situation.

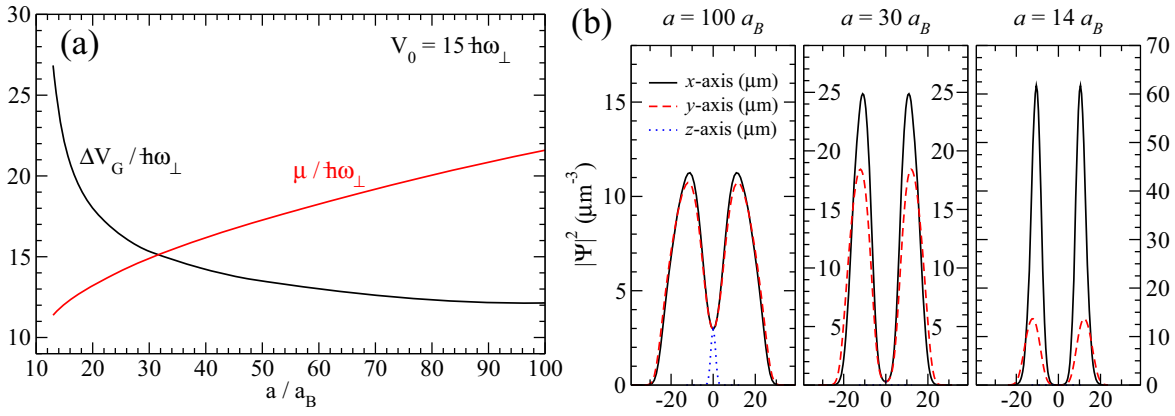

Figure 6.1: (a) Chemical potential and effective Gaussian barrier as a function of the scattering length, for $V_0 = 15\hbar\omega_\perp$. (b) Density profiles of the ground state configuration along x-axis (solid line), y-axis (dashed line) and z-axis (dotted line), for $a = 100,\ 30,\ 14\,a_B$ (from left to right).

The panels of Fig. 6.1(b) show the density profiles for different scattering lengths. As can be seen, they change accordingly to the effective Gaussian potential. When the scattering length is large (case $a = 100\,a_B$), the chemical potential is also large and the main effect of the Gaussian barrier is to decrease the central density of the cloud. In this regime, the dipole-dipole interaction introduces only a slight perturbation of the density, which is almost symmetric in the $z = 0$ plane. As the scattering length is reduced, the toroidal geometry arises when $\mu \sim \Delta V_G$. For $a = 30\,a_B$, the hole is already formed, with a central density reduced one order of magnitude with respect to the density at the maxima[1]. At this scattering length anisotropic dipolar effects start to be noticeable. For lower values of a, the dipolar interaction becomes dominant and the condensate density shows azimuthal dependence. The maximum value of the density lies along the x axis, perpendicularly both to the trap symmetry axis and the magnetization direction. This inhomogeneous density distribution is not particular of condensates, but has also been shown to appear in Fermi gases that interact via dipole-dipole interactions [Dut07, Zol11].

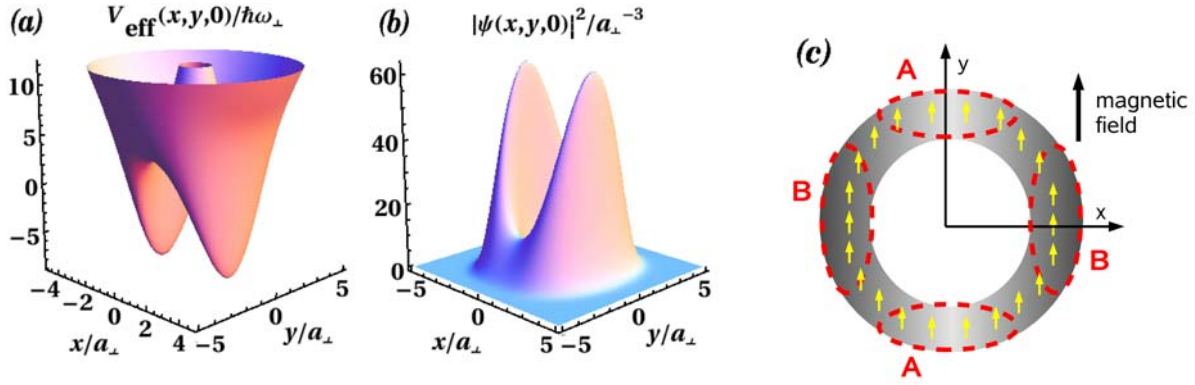

Figure 6.2: (a) Effective potential, $V_{\rm eff}$, as a function of x and y at the $z = 0$ plane for a toroidal condensate with $a = 20\,a_B$ and $V_0 = 15\,\hbar\omega_\perp$. (b) Corresponding condensate density on the plane $z = 0$. (c) Diagram qualitatively showing the effective dipolar interaction in the torus.

To understand the azimuthal density structure, we show Fig. 6.2(a) the effective potential, $V_{\rm eff}$, for a condensate with $a = 20\,a_B$. It presents a maximum at the center due to the Gaussian beam. Far from the center, the potential is dominated basically by the harmonic potential. For intermediate distances, it is the mean-field dipolar interaction, $V_{\rm dip}$, that controls the potential: it is attractive on the x axis, therefore showing two minima, and repulsive on the y axis, where two saddle points are located. These saddle points can be thought of as self-induced potential barriers in the azimuthal direction. The density, Fig. 6.2(b), follows the shape of $V_{\rm eff}(\mathbf{r})$, hence showing a two-peak configuration with two larger maxima on the x axis (at the potential minima) and two saddle points on the y axis (at the potential saddle points). The anisotropic character of the effective potential can be easily understood with the help of the scheme in Fig. 6.2(c). In this figure we have schematically delimited two types of regions A and B with dashed lines. Within region A the dipoles are mainly displayed side-by-side, giving a net repulsive interaction. In region

[1]Note that the density at the center is not exactly zero, as would happen for classical particles, because we are dealing with a quantum gas. The condition $\mu = \Delta V_G$ is in some way equivalent to the classical turning point.

B the atoms are mainly located head-to-tail, which gives an effective attractive interaction. A straightforward effect of the location of regions A and B is that it is energetically favorable for the system to accommodate more dipoles in regions B. Therefore, a dipolar condensate confined in a toroidal trap shows large density maxima in the perpendicular direction to the magnetization axis, and saddle points in the magnetization direction.

To quantitatively analyze the azimuthal density dependence, we show in Fig. 6.3 the evolution of the maximum density values along the x-axis, $n_{\rm gs}(x_m)$, and along the y-axis, $n_{\rm gs}(y_m)$, as a function of the scattering length. A strong deviation of both quantities occurs when the scattering length is reduced below the value in which the condensate geometry becomes multiply connected, $a \sim 30\,a_B$.

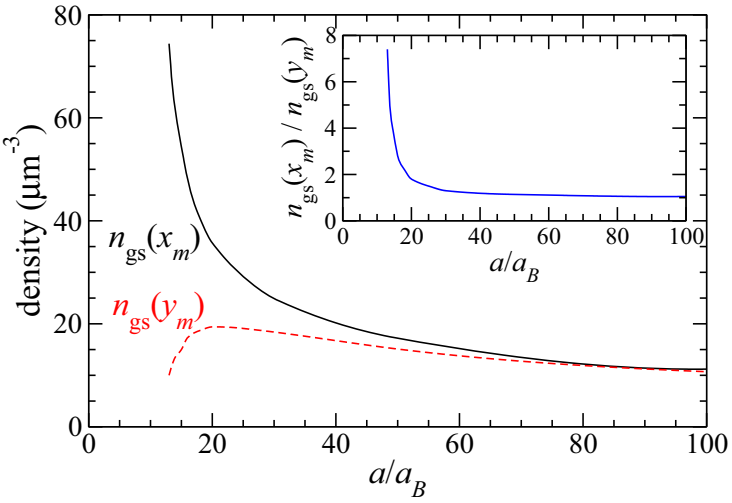

Figure 6.3: Density values at the critical points $(x_m, 0, 0)$ and $(0, y_m, 0)$, which correspond to a maximum (solid line) and a saddle point (dashed line) in the density, respectively. In the inset the quotient of these heights is drawn.

To find the azimuthal density distribution, the smallest scattering length it is possible to achieve with the set of parameters used here is $a = 13\,a_B$. Below this value, a spatial symmetry breaking (SB) occurs. The atoms accumulate around one of the wells of the effective potential and the condensate resembles an origin-displaced cigar-shaped condensate. This can be seen in Fig. 6.4, where we compare the equidensity lines in the $z = 0$ plane of two different configurations with $a = 20\,a_B$ (left) and $a = 12\,a_B$ (right). For $a = 20\,a_B$ the system still presents reflection symmetry but for $a = 12\,a_B$ the symmetry is broken. It is interesting to observe that not only do the atoms accumulate at one side of the ring but also their density distribution appears more resistive to curve. This effect is a consequence of the fact that the dipolar interaction forces the particles to locate themselves head-to-tail. From the mean-field point of view, the phenomenon of symmetry breaking occurs because the attractive part of the dipolar interaction becomes large enough to be energetically favorable for the system to distribute all atoms in only one of the minima of the potential. With the present choice of parameters, a further reduction of the scattering length leads to collapse. Notice that the critical value $a = 12\,a_B$ is the same as in harmonic confinement (see Sec. 4.1). We have checked that the symmetry broken solution is independent of the way the system is initialized, by starting the minimization procedure with different initial wave functions, including a symmetric wave function and a randomly generated one. In all cases we have obtained the same final asymmetric state, which confirms that it is not an artifact of the numerics. The two possible symmetry broken states (with all particles in the left or in the right) are degenerate in energy. The

fact that the numerics converges to one or the other is due to a negligibly small but asymmetric numerical error that favors one state with respect to the other. A change in grid size, for instance, can make the simulation converge to the right state (with all the atoms in the right well) instead of the left state as in Fig. 6.4.

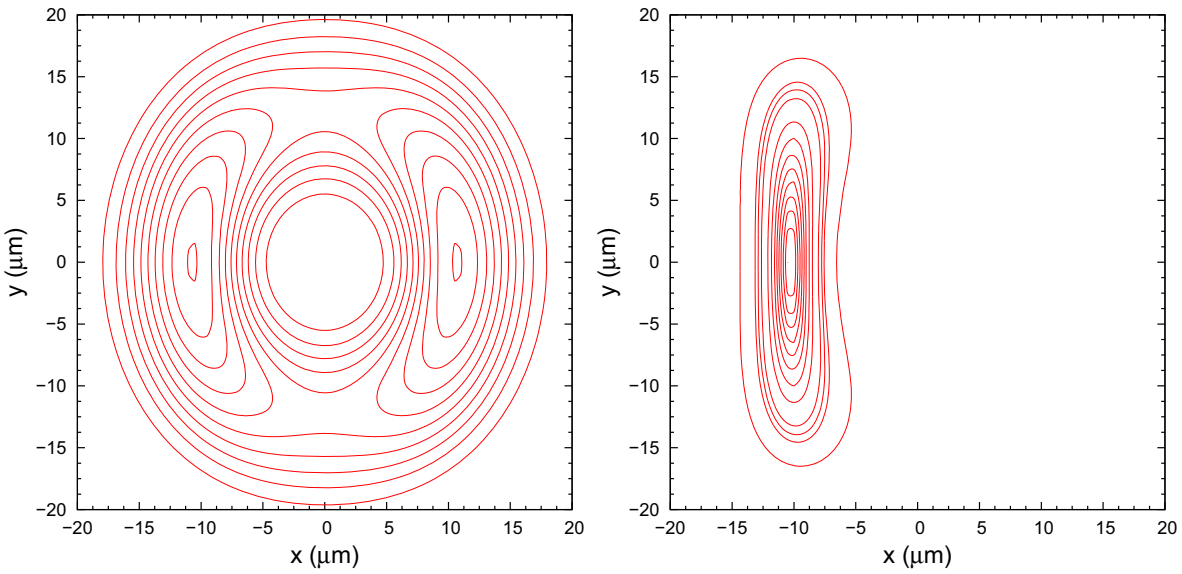

Figure 6.4: Density contours for the ground state configuration in the $z = 0$ plane for a condensate with $a = 20\,a_B$ (left panel) and $a = 12\,a_B$ (right panel).

Symmetry breaking phenomena are a signature of a quantum phase transition and are presently under strong discussion [Cir98, Jul10a]. For purely s-wave condensates, they have been predicted to show mainly in double-well potentials, but also in the vortex nucleation process [Dag09a], in mixtures of Bose gases confined in double-ring traps [Mal10], etc. In dipolar condensates confined in double-well traps, they have been addressed in Refs. [Xio09, Asad09]. In Ref. [Xio09], the magnetization direction was used to induce SB, while in Ref. [Asad09] it was the number of dipoles in the double well that drove it. The mechanism triggering the effect is the presence of a repulsive barrier in systems that are dominated by attractive interactions. The main difference between the present configuration and the ones exposed in Refs. [Xio09, Asad09] is that we deal with a self-induced SB, since it is the dipolar interaction itself and its anisotropic character that brings about the effect. Recently, there has been some effort to relate symmetry breaking phenomena in cold atoms to the existence of a Schrödinger cat state [Dag09a, Jul10a]. For dipolar condensates, such a strongly entangled state has been theoretically proposed in a three-well configuration [Lah10].

6.2 Vortex states in a toroidal trap

Now we turn to the study of vortices in dipolar condensates that are confined in a toroidal trap, with the goal of understanding how the density inhomogeneity introduced by the

dipolar interaction affects the velocity field. Toroidal traps have been experimentally shown to be capable of sustaining persistent flows [Ryu07]. This fact is related to the existence of metastable vortices [Cap09]. The superfluid character of the BEC ensures that the fluid will flow without viscosity, i.e. without dissipation. For instance, the experiment in Ref. [Ryu07] was capable of maintaining the persistent current for up to 10 s (which was the duration of the experiment). This section is devoted to the characterization of the anisotropic velocity flow that a phase-imprinted metastable vortex introduces in the toroidal condensate in presence of dipolar interactions.

To generate a vortex state along the z axis with circulation κ, we first obtain the ground state order parameter $\psi_{\rm gs}$ from Eq. (2.16) and then imprint a velocity field in the form [Jez08b]

$$\psi_{\rm ini}(\mathbf{r}) = \psi_{\rm gs}(\mathbf{r}) \left(\frac{x+iy}{\sqrt{x^2+y^2}} \right)^{\kappa}, \tag{6.3}$$

with κ the quantum number related to the velocity circulation. We use this ansatz as the initial wave function of the imaginary-time evolution of the GP equation (2.16). After convergence, we obtain the κ-vortex state of the system. In the toroidal trap, the core of the vortex is directly the hole created by the laser beam along the z direction. Note that with our choice of magnetization axis (y) the axial symmetry is removed and thus the angular momentum along the z axis is no longer $L_z = \kappa\hbar N$, since the angular momentum operator does not commute with the Hamiltonian anymore.

A signal that the system can sustain metastable vortices (that is, persistent currents in the non-rotating system) is the presence of a valley in the ground state density landscape, which may produce a local vortex energy minimum [Cap09]. In this case, after the minimization process, one can obtain a vortex state captured in the toroidal trap due to a vortex energy barrier produced by the surrounding density maxima. In our system, where the axial symmetry is not achieved, the energy barrier is related to the height of the saddle points of the density landscape which are located along the y-axis (see Fig. 6.2).

In Fig. 6.5 we show the ground and two-vortex state densities for a dipolar condensate with $a = 100\,a_B$. Since the ground state is a simply connected condensate, the density does not vanish at the center, hence we find that multiply quantized vortices are less favored than multiple singly-quantized vortices. Although the initial imprinting method produces a doubly-quantized vortex along the z-axis at $x = 0$ and $y = 0$, during the minimization process the vortex splits into two singly-quantized vortices. Since the density maximum (saddle-point) is smaller along the y direction the final state converges to two vortices placed at the y-axis, as can be seen in the central panel of Fig. 6.5. This stationary configuration is possible because the velocity field due to the other vortex cancels with the contribution to the vortex velocity provided by the density inhomogeneity [Jez08b].

We have found that the initial doubly-quantized vortex always splits in two singly-quantized vortices, even in the case of multiply connected geometry. This happens because for scattering lengths between $a = 25\,a_B$ and $a = 30\,a_B$ the density at the center of the trap is very small, but not exactly zero. This gives rise to two vortex lines instead of one, even if their cores are very close together. Below $a = 25\,a_B$ the system is not capable of sustaining two vortices, since the height at the density saddle-points is not large enough.

To characterize the velocity field in the case of large asymmetric density configurations

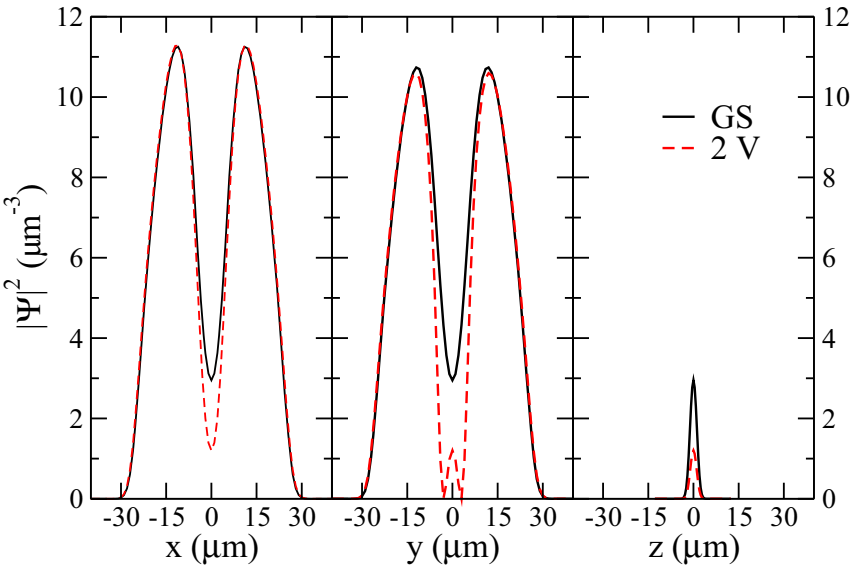

Figure 6.5: Density profiles for the ground state (solid line) and a two vortex state (dashed line) for a condensate with $a = 100\, a_B$.

in the toroidal trap, we have studied singly quantized vortices ($\kappa = 1$). In this case, the vortex is nucleated along the trap symmetry axis. In contrast to the case of a large scattering length, for small scattering lengths the presence of the vortex does not produce a large change in the density distribution compared to the vortex-free configuration, since the vortex core is directly the hole in the toroidal potential.

The initially imprinted velocity field, Eq. (6.3), assumes axial symmetry. Our system is not axially symmetric and thus the modulus of the velocity field, for a given radius, varies around the torus. This is simply understood by reminding that in stationary conditions the current is constant along the torus,

$$I = \int \mathbf{j} \cdot d\boldsymbol{\mathcal{S}} = \int |\psi|^2 \, \mathbf{v}(\mathbf{r}) \cdot d\boldsymbol{\mathcal{S}} \ , \tag{6.4}$$

where $\mathbf{j}$ is the current density given by Eq. (3.2) and $d\boldsymbol{\mathcal{S}}$ is the surface element. The velocity field $\mathbf{v}(\mathbf{r})$ is related to the phase $S(\boldsymbol{r})$ of the wave function through Eq. (3.3). The integral in Eq. (6.4) is calculated in a torus section. Since this quantity has to be constant, it is easy to see from this equation that for the angles where the density is lower (regions A in Fig. 6.2(c)) the velocity is larger, while in the angles where the density shows a maximum (regions B in Fig. 6.2(c)) the velocity is minimum.

In Fig. 6.6(b) we display the x and y components of the velocity field at the positions y_m and x_m of the density maxima, respectively $v_x(y_m)$ and $v_y(x_m)$ (see also Fig. 6.6(a)). For $a = 100\, a_B$, the dipolar effects are small, the densities along each axis are similar and, therefore, the two components of the velocity are equal. When we reduce the value of the scattering length, dipolar effects become sizeable and the density difference increases (see Fig. 6.3), hence increasing the difference in both components of the velocity. This can be used to generate an inhomogeneous local velocity field along the torus, by only tuning the scattering length using a Feshbach resonance.

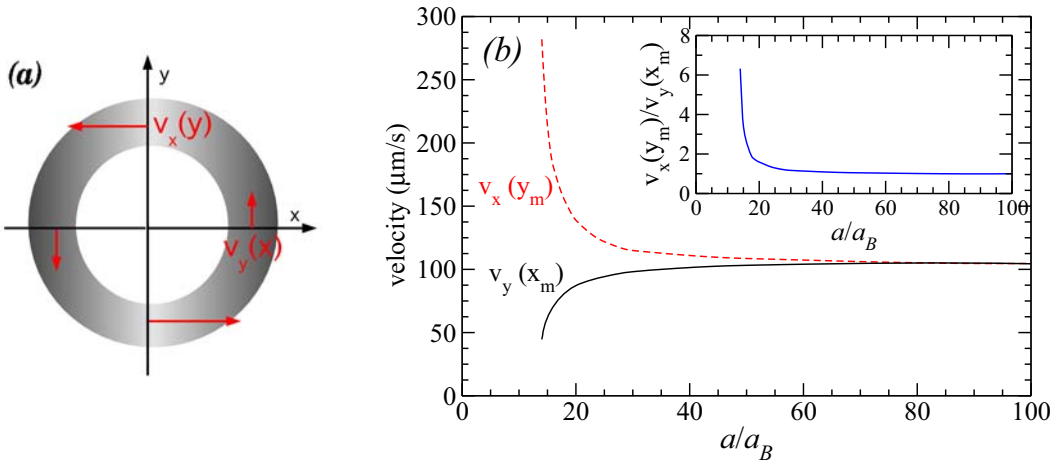

Figure 6.6: (a) Schematic diagram representing the components of the velocity along the ring-shaped dBEC. (b) Velocity field components v_y (solid line) and v_x (dashed line) at the density maxima x_m and y_m, respectively, as a function of the scattering length. In the inset, the ratio between the two is shown.

Although the angular momentum L_z is not conserved, its expectation value $\langle L_z \rangle$ can provide a qualitative estimation of the difference between the velocity field in the different regions of the torus. As expected, for large scattering lengths the angular momentum per particle is almost one, see Fig. 6.7. As a decreases the angular momentum decreases, being the variation much stronger when the condensate exhibits a hole, below $a \sim 30\, a_B$. The reduction in the angular momentum is an evidence of the presence of self-induced energy barriers, which diminish the net particle flow. Since in our case the azimuthal energy barrier is larger when the scattering length is reduced, a measure of the angular momentum in the z direction could provide information of the strength of the dipolar interaction with respect to the contact interaction.

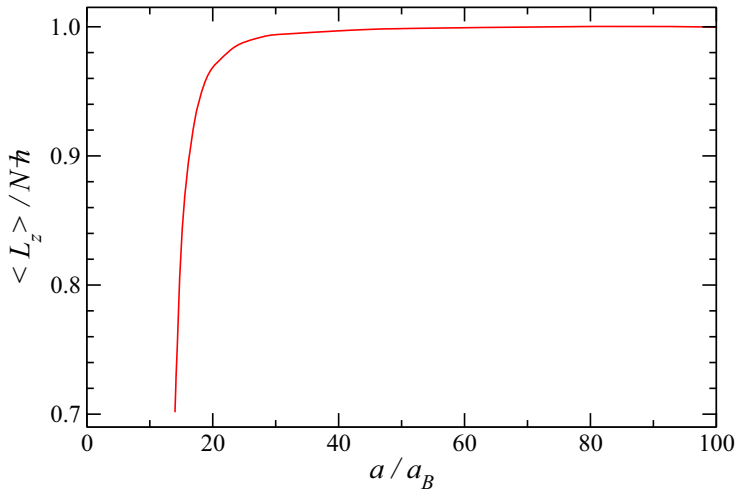

Figure 6.7: Expectation value of the angular momentum as a function of the scattering length.

Chapter 7

The self-induced bosonic Josephson junction

As we have seen in Chapter 6, the combination of the toroidal trapping potential and the anisotropic mean-field dipolar potential gives rise to a self-induced potential that breaks the axial symmetry of the external confinement. This effective potential can be recognized as the effective potential introduced in Sec. 6.1, $V_{\text{eff}}(\mathbf{r}) = V_{\text{ext}}(\mathbf{r}) + V_{\text{dip}}(\mathbf{r})$, and it has the shape of a ring-shaped double well. Figure 7.1(a) shows its projection on the plane $z = 0$ for a dBEC with scattering length $a = 14\,a_B$ and $V_0 = 30\,\hbar\omega_\perp$[1], for the same confining potential as in Chapter 6, Eq. (6.1). The two wells are formed perpendicularly to both the trap symmetry axis (z) and the polarization axis (y). The density adapts to the effective potential, giving rise to an anisotropic distribution along the torus, as can be seen in Fig. 7.1(b). Since the centered Gaussian potential introduces a strong repulsive barrier at $r_\perp = 0$ that prevents the atoms from tunneling through it, the double well structure arises in the azimuthal direction. The top panel of Fig. 7.1(c) shows the minimum effective potential along the azimuthal coordinate, φ, with the two minima at $\varphi = 0$ and $\varphi = \pi$ and the two barriers at $\varphi = \pi/2$ and $\varphi = 3\pi/2$. Note that it is not defined at fixed radius, but $r_\perp$ slightly changes with φ, being however close to $r_\perp \sim 2.5\,a_\perp$. According to this effective ring-shaped double well, the atoms localize mostly in the attractive regions inside the wells, producing the azimuthal density dependence. This is seen in the bottom panel of Fig. 7.1(c), which shows the maximum density along φ on the $z = 0$ plane.

Although the self-induced double-well configuration is highly reminiscent of double-well potentials in one dimension, there are still some differences, namely: i) the potential barriers separating the two wells are self-induced, depending therefore strongly on the condensate density; ii) the two wells are connected via two links instead of one; and iii) the double well appears in the azimuthal coordinate, implying that the whole configuration is clearly far from being one-dimensional. However, under some conditions, the system can behave as a usual bosonic Josephson junction, showing the same kind of physics as in double-well potentials. Note also that this junction really consists of two coupled

[1]Note that we have increased the value of V_0 from $15\,\hbar\omega_\perp$ of Chapter 6 to $30\,\hbar\omega_\perp$. This has been done in order to have a vanishingly small density at the center and thus to prevent atoms from tunneling across the Gaussian barrier. The ratio between central and maximum density is approximately 10^{-4} for $V_0 = 15\,\hbar\omega_\perp$ and 10^{-8} for $V_0 = 30\,\hbar\omega_\perp$, for $a = 14\,a_B$.

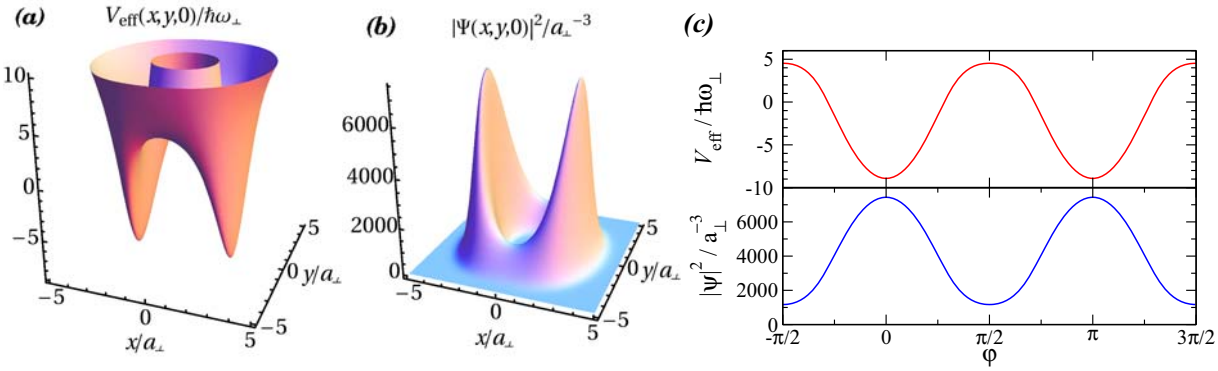

Figure 7.1: Effective potential (a) and corresponding ground state density (b) in the $z = 0$ plane. (c) Minimum effective potential (top) and maximum density (bottom) in the $z = 0$ plane as a function of the azimuthal angle φ.

junctions, which in this scenario behave in phase in much the same way as the array of nano-apertures does in the experiments with helium [Per97, Hos05]. Since it is the mean-field dipolar potential that is responsible for the double-well structure, we call this junction a self-induced Josephson junction (SIJJ).

The aim of this chapter is to study in detail the SIJJ, characterizing its dynamical regimes and exploring its physics by means of numerically simulating the TDGP Eq. (2.12). In Sec. 7.1 the dynamics in the junction is analyzed in terms of two coupled variables, the population imbalance and the phase difference. Both Josephson (Sec. 7.1.1) and self-trapping (Sec. 7.1.2) oscillations are predicted. In Sec. 7.2 we show that they can be qualitatively described by a two-mode model (see also Appendix F for a detailed analysis of this model). The self-trapping regime is analyzed with further detail in Sec. 7.3, where the dynamics is characterized by the phase of the wave function. This allows us to relate self-trapping to a phase-slippage process, which is well known in superfluid helium.

We study the dynamics by evolving the TDGP Eq. (2.12) in real-time (see Appendices B and C). Since there are no external time-dependent potentials both the number of particles and the energy must be conserved. During the simulations, the deviations in the total energy we have found are of 10^{-4} % for the Josephson case and 5×10^{-3} % for the self-trapping case, with respect to the initial total energy. The deviation in the total number of particles is smaller than 10^{-5} % in all cases.

7.1 Characterization of the system as a junction

If the height of the barrier separating the two wells, $\Delta V_{\rm eff}$, is large compared to the chemical potential, μ, the system behaves as two weakly-linked condensates. The weak-link condition can be reached by tuning the s-wave scattering length to small values, which should still be large enough to prevent spatial spontaneous symmetry breaking (see Sec. 6.1). Figure 7.2 shows the height of the potential barrier along the azimuthal direction as a function of the scattering length (solid line), together with the chemical potential of the dBEC (dashed line). The condition $\Delta V_{\rm eff}/\mu = 1$ occurs at $a \simeq 14.5\, a_B$. For smaller scattering lengths we are in a regime of weak coupling between condensates

or high barrier, while for larger scattering lengths the system enters a regime of strong coupling or low barrier.

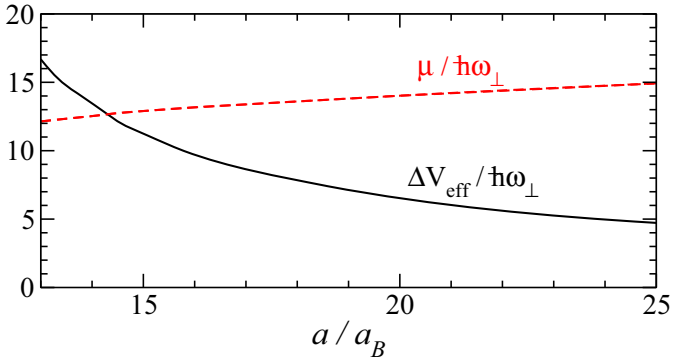

Figure 7.2: Azimuthal barrier height (solid) and chemical potential of the dBEC as a function of the scattering length.

Josephson effects in BECs are characterized by the tunneling dynamics between two potential wells [Sme97, Rag99, Alb05]. The barriers separating the two wells divide the space into left (L) and right (R) sides, respectively defined by $x \leq 0$ and $x \geq 0$. In complete analogy with double-well systems [Sme97], we analyze the tunneling dynamics in terms of the population imbalance (Z) and the phase difference (ϕ) between the left and right wells, given by

$$Z(t) = \frac{N_L(t) - N_R(t)}{N} \tag{7.1}$$

$$\phi(t) = \phi_R(t) - \phi_L(t)\,, \tag{7.2}$$

where $N_{L(R)}(t)$ corresponds to the number of atoms on the left (right) side, and $\phi_{L(R)}(t)$ the phase of the dipolar condensate on the left (right) side. The total number of atoms is $N = N_L(t) + N_R(t)$. These quantities are calculated as a function of time from the condensate wave function $\Psi(\mathbf{r}, t)$, which is obtained by solving the TDGP Eq. (2.12). In the numerical evolution the number of atoms in the left (right) well is found computing the integral: $N_{L(R)}(t) = \int_{L(R)} \mathrm{d}\mathbf{r}|\Psi(\mathbf{r}, t)|^2$. The local phase $\phi(\mathbf{r}, t)$ enters in the wave function as:

$$\Psi(\mathbf{r}, t) = \sqrt{n(\mathbf{r}, t)}\, e^{i\,\phi(\mathbf{r},t)}\,,$$

where the local density is $n(\mathbf{r}, t) = |\Psi(\mathbf{r}, t)|^2$. The phase on the left side is defined as:

$$\phi_L(t) = \frac{1}{N_L} \int_L \mathrm{d}\mathbf{r}\, n(\mathbf{r}, t)\, \phi(\mathbf{r}, t)\,. \tag{7.3}$$

In the numerical implementation, $\phi_L(t)$ has been calculated similarly as in Ref. [Mele11]. We compute the averaged wave function in the left well,

$$\Psi_L = \frac{1}{N_L} \int_L \mathrm{d}\mathbf{r}\, n(\mathbf{r}, t)\, \Psi(\mathbf{r}, t)\,, \tag{7.4}$$

and calculate the corresponding phase by considering the real and imaginary parts of Ψ_L,

$$\phi_L(t) = \arctan \frac{\mathrm{Im}[\Psi_L]}{\mathrm{Re}[\Psi_L]}\,. \tag{7.5}$$

The phase on the right, $\phi_R(t)$, is defined and computed analogously. The dynamic regimes of Josephson junctions depend strongly on the initial conditions, which are defined by the population imbalance and the phase difference at time $t = 0$, respectively $Z(0)$ and $\phi(0)$. Following the method used in experiments in bosonic Josephson junctions [Alb05] we consider the case of initial population imbalance and zero initial phase, that is $Z(0) \neq 0$ and $\phi(0) = 0$. In the experiments the system is firstly prepared in a slightly asymmetric double-well potential, which ensures that there are more atoms in one well than in the other. In the numerics, we mimic this process and obtain the imbalanced wave function using imaginary-time evolution of the GP Eq. (2.16) with a tilting potential $V_{\text{tilt}}(\mathbf{r}) = \tilde{V}_0 x$ that ensures an initial population imbalance between the two wells. At $t = 0$ the asymmetry is removed and the condensate is left to evolve in a symmetric double-well potential with this initial non-zero population imbalance.

7.1.1 Small imbalance regime: Josephson oscillations

The regime of Josephson[2] (or plasma) oscillations consists on the coherent tunneling of atoms through a potential barrier that weakly links two condensates (see Fig. 1.4). These oscillations take place for small values of the initial imbalance. Figure 7.3 shows the dynamic evolution of the population imbalance and the phase difference corresponding to initial conditions $Z(0) = 0.1$ and $\phi(0) = 0$, for three different scattering lengths at both sides of the condition $\Delta V_{\text{eff}}/\mu = 1$. $Z(t)$ and $\phi(t)$ present sinusoidal oscillations shifted by $\pi/2$, and the time average of the population imbalance is zero. In this regime, the atoms tunnel periodically from the left to the right well and back. The wave function of the dBEC at each well remains coherent during this process, that is with a uniform phase. This is translated into a phase difference that oscillates in time at the same frequency as the imbalance.

From Fig. 7.3 it is clear that the SIJJ can sustain Josephson oscillations even though the barriers are self-induced by the interplay between dipolar interaction and the toroidal geometry. Moreover, the ring-shaped double-well structure of the potential is maintained in time even if the two wells and the two barriers present some dynamics (and this indeed happens since we are dealing with a self-induced potential). In other words, we can state that the self-induced barriers are robust because they maintain the sinusoidal shape of the Josephson oscillations. Notice that this is true even for a large density in the barrier position, as is the case of $a = 15.5\, a_B$, for which $\mu > \Delta V_{\text{eff}}$ (see Fig. 7.2). A similar system has been studied in Ref. [Bla11] for a toroidal condensate with one barrier, finding that for large overlaps it is still possible to define a Josephson frequency, but for a certain barrier height another mode appears and the system can no longer be described with just one frequency.

[2]Sometimes the term "Josephson regime" is used to distinguish it from the Fock and the Rabi regimes (as defined in Ref. [Leg01] and references therein). These regimes are classified in terms of the ratio between the coupling energy between the wells (K) and the strength non-linear (on-site) interaction (U): for $K/U \ll N^{-2}$ the system lies in the Rabi regime, for $N^{-2} \ll K/U \ll 1$ the system lies in the Josephson regime, and for $1 \ll K/U$ the system lies in the Fock regime. We keep always within the Josephson regime in this terminology, since the parameter $K/U \sim 0.03$, as can be estimated using the two-mode model discussed below.

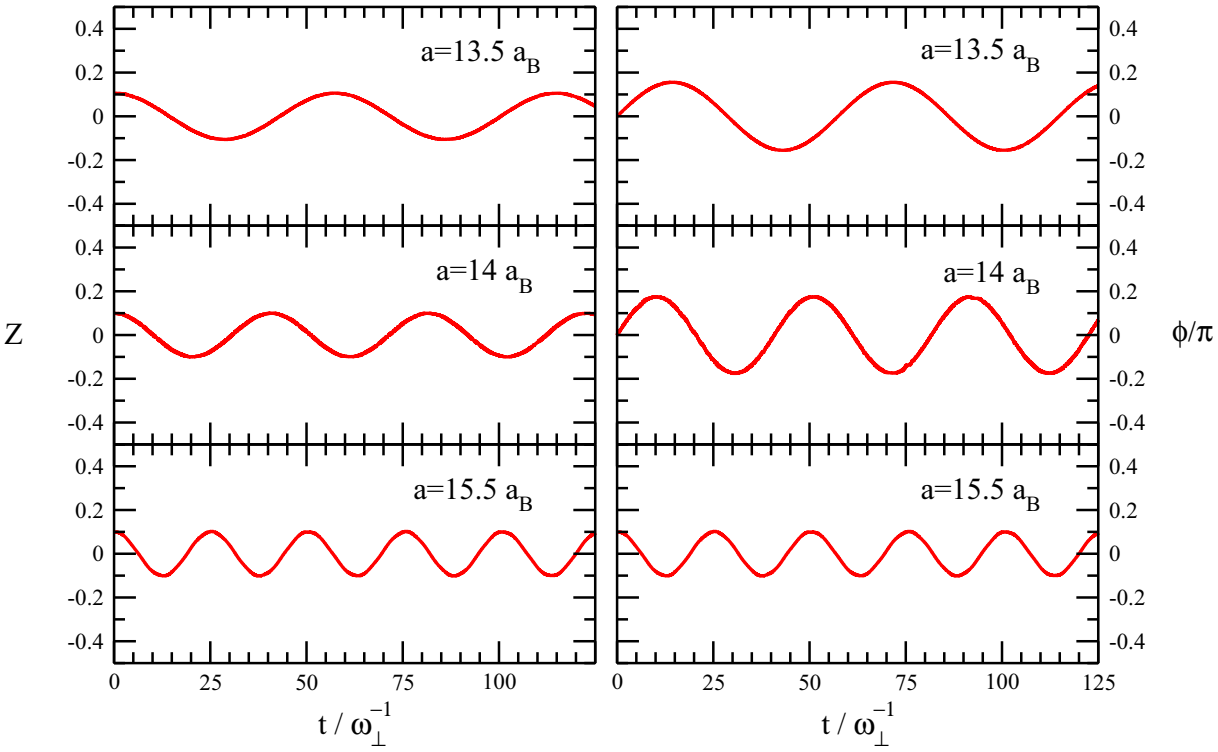

Figure 7.3: Time evolution of the population imbalance (left panels) and phase difference (right panels) with initial conditions $Z(0) = 0.1$ and $\phi(0) = 0$, for scattering lengths $a = 13.5,\ 14,\ 15.5\, a_B$.

7.1.2 Large imbalance regime: macroscopic quantum self-trapping

For a large initial population imbalance, the SIJJ enters the regime of self-trapping oscillations (see Fig. 1.4). This can be clearly seen in Fig. 7.4, where the imbalance and the phase difference are plotted as a function of time for initial conditions $Z(0) = 0.65$ and $\phi(0) = 0$, for $a = 14\, a_B$. In this situation, the time average of the imbalance remains close to 0.5 and the phase difference is unbounded (running phase mode). Although in this regime the atoms remain locked in one of the wells, there is still some tunneling of particles at a frequency higher than in the Josephson regime. From Fig. 7.4 it follows that dipolar condensates in a ring-shaped double-well potential can sustain self-trapping dynamics even though the barriers are self-induced. However, the imbalance oscillations are non-sinusoidal but have a more involved structure, which hints at a rich self-trapping dynamics. In this sense, self-trapping is more sensitive to imperfections of the double-well structure than Josephson oscillations, where the numerical signal was clearly sinusoidal. This situation therefore cannot be described within the framework of two mode models (see Sec. 7.2). To understand better self-trapping dynamics one needs to study the time evolution in a more local way, that is by looking at the information that is hidden in the average quantities Z and ϕ. This will be duly addressed in Sec. 7.3.

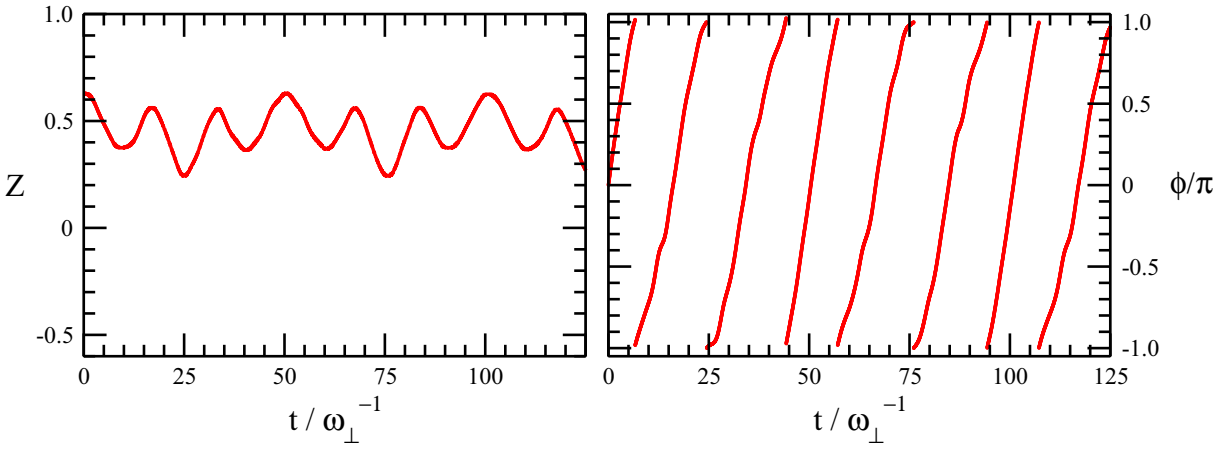

Figure 7.4: Time evolution of the population imbalance (left panel) and phase difference (right panel) for initial conditions $Z(0) = 0.65$ and $\phi(0) = 0$, for a scattering length $a = 14\, a_B$.

7.2 Two-mode models for the SIJJ

To gain insight into the tunneling dynamics obtained by evolving the TDGP equation, we have performed a two-mode analysis of the SIJJ, taking into account both s-wave and dipolar interactions (see Appendix F for a more detailed discussion of the model). The two-mode model (TMM) relies on the assumption that the dynamical behavior of a Josephson junction can be fully captured by analyzing the coherent dynamics between two spatially localized modes: the left and right modes, respectively $\Phi_L(\mathbf{r})$ and $\Phi_R(\mathbf{r})$. In this approximation, the condensate order parameter is written using the ansatz [Sme97, Rag99]

$$\Psi(\mathbf{r}, t) = \psi_L(t)\Phi_L(\mathbf{r}) + \psi_R(t)\Phi_R(\mathbf{r})\,, \tag{7.6}$$

with $\langle \Phi_i | \Phi_j \rangle = \delta_{ij}$, and the coefficients fulfill $\psi_j(t) = \sqrt{N_j(t)} e^{i\phi_j(t)}$, $i, j = L, R$. Note that in this ansatz the time evolution is contained only in the coefficients $\psi_j(t)$.

By substituting ansatz (7.6) into Eq. (2.12) and performing some algebra retaining all the overlapping terms [Gio00, Ana06] (see also Appendix F), one obtains the two-mode equations for a symmetric dipolar SIJJ,

$$\dot{Z} = (-1+\alpha)\sqrt{1-Z^2}\sin\phi + \varepsilon(1-Z^2)\sin 2\phi \tag{7.7}$$

$$\dot{\phi} = \Lambda Z - (-1+\alpha)\frac{Z}{\sqrt{1-Z^2}}\cos\phi - \varepsilon Z\cos 2\phi\,, \tag{7.8}$$

with

$$\Lambda = \frac{U}{2K}N - \frac{B + 2I_1 + D_1}{2K}N \tag{7.9}$$

$$\alpha = \frac{I_2 + D_3}{K}\,N \tag{7.10}$$

$$\varepsilon = \frac{I_1 + D_1}{2K}\,N\,. \tag{7.11}$$

The quantities U, K, B, I_i, D_i are integrals of combinations of the modes Φ_L and Φ_R with the different operators in the GP equation: U contains information of the kinetic

and trapping energies in each of the wells, K is related to the kinetic and trapping energies in the barrier (overlapping region), B is the interaction energy in each well, and I_i and D_i are, respectively, the s-wave and dipolar interactions in the barrier region. Their definitions are given in Appendix F. Also, in this appendix the complete expressions (for non-symmetric configurations) provided by the two-mode model in a SIJJ are given. The only parameters that appear in Eqs. (7.7) and (7.8) are Λ, α and ε, which depend on both dipolar and s-wave interactions. All information regarding the geometry (in particular, the self-induced potential) is self-contained in these parameters. If the system is well in the regime of weak link it is a good approximation to neglect the overlap integrals relating the modes in the two wells. This means $I_i = D_i = 0$. The equations then take a much simpler form while keeping the information about the different dynamical regimes:

$$\dot{Z} = -\sqrt{1 - Z^2}\sin\phi \tag{7.12}$$

$$\dot{\phi} = \Lambda Z + \frac{Z}{\sqrt{1 - Z^2}}\cos\phi \ . \tag{7.13}$$

In the following we will refer to Eqs. (7.12)–(7.13) as *crude* TMM, to distinguish them from the *full* TMM Eqs. (7.7)–(7.8). Note that in the crude TMM the parameter Λ takes a different expression than in the full TMM, but that we keep the same symbol. In Table 7.1 the values of the parameters appearing in the TMM are given for $a = 14\,a_B$. In all these expressions time is expressed in units of the Rabi frequency, $\Omega_R = 2K/\hbar$, which corresponds to the frequency at which the non-interacting system oscillates[3] (Rabi oscillations). However, this regime cannot take place in a SIJJ, since in absence of interactions the two wells do not exist. For $a = 14\,a_B$, the Rabi frequency is $\Omega_R = 0.50 \times 2\pi$ s^{-1}.

Table 7.1: Parameters of the two-mode models for a SIJJ, for $a = 14\,a_B$.

Parameter	crude TMM	full TTM
Λ	18.281	17.836
α	—	0.131
ε	—	0.118

To compute the integrals U, K, B, I_i, D_i (see Appendix F) and therefore to determine the parameters (7.9)–(7.11), we have used the left and right modes defined as [Ana06]: $\Phi_{L(R)}(\mathbf{r}) = (\Phi_{\rm s}(\mathbf{r}) \pm \Phi_{\rm as}(\mathbf{r}))/\sqrt{2}$, where $\Phi_{\rm s}(\mathbf{r})$ and $\Phi_{\rm as}(\mathbf{r})$ are the symmetric (ground state) and antisymmetric (first excited state) wave functions of the double well potential of Fig. 7.1(a). We have numerically generated the wave functions $\Phi_{\rm s}(\mathbf{r})$ and $\Phi_{\rm as}(\mathbf{r})$ by evolving the GP equation in imaginary time. The ground state is obtained without imposing any restriction. To obtain the first excited state, the desired symmetry has to be imposed

[3]Notice that the Rabi frequency is only properly defined for the non-interacting system, where K is calculated using the non-interacting left and right modes (see Appendix F for the definition of K). We use the same term for the interacting system for convenience, but we should keep in mind that now the wave functions are the interacting ones. In other words, the non-interacting system would not oscillate with the Rabi frequency calculated here, since it has been found using the modes obtained for the interacting system.

to the initial wave function, which is forced to be antisymmetric. We use

$$\Phi_{\rm as}^{\rm ini}(\mathbf{r}) = \frac{x}{|x|}\,\Phi_{\rm s}(\mathbf{r}) \tag{7.14}$$

as the initial wave function of the calculation, and let it evolve without any other restriction[4] until it converges to $\Phi_{\rm as}$. The dynamics within the TMM has been obtained by solving Eqs. (7.7)-(7.8) and Eqs. (7.12)-(7.13) using a fourth-order Runge-Kutta method (see Appendix C).

The remaining of this section is organized as follows. Firstly, we calculate the critical condition, Z_c, above which self-trapping occurs for $\phi(0) = 0$. Secondly, we compare the results of the TMM with those given by the TDGP equation.

7.2.1 Critical regime

The critical condition can be obtained using the condition of energy conservation. For this we need to find the Hamiltonian describing the system, which can be obtained from the fact that Z and ϕ are conjugate variables and therefore obey the equations of motion

$$\dot{Z} = -\frac{\partial H}{\partial \phi} \qquad\qquad \dot{\phi} = \frac{\partial H}{\partial Z}\ . \tag{7.15}$$

Solving the system for the TMMs yields

$$H_{\rm crude}(Z,\phi) = \frac{1}{2}\Lambda Z^2 - \sqrt{1-Z^2}\cos\phi \tag{7.16}$$

$$H_{\rm full}(Z,\phi) = \frac{1}{2}\Lambda Z^2 - (1-\alpha)\sqrt{1-Z^2}\cos\phi + \frac{1}{2}\varepsilon(1-Z^2)\cos 2\phi\ . \tag{7.17}$$

To find $Z_{\rm c}$ we need to impose the condition that the energy is conserved throughout the tunneling process, and in particular between the initial configuration and the configuration at a time t when $Z(t) = 0$ for $\phi(t) = \pi$, that is $H(Z_c, 0) = H(0, \pi)$, where we have considered for simplicity that the initial phase difference $\phi(0)$ is zero (see Appendix F for a detailed analysis of the Hamiltonian and its solutions). Note that the condition above arises from the fact that if the imbalance does not reach zero when the phase reaches the value π (moment at which the particle current changes sign), then the imbalance will never be zero and therefore the system will remain in a self-trapped configuration (see for instance Ref. [Rag99]). Proceeding in this way, we find Z_c for the symmetric crude and full TMM, respectively

$$Z_c^{\rm crude} = 2\frac{\sqrt{\Lambda-1}}{\Lambda} \tag{7.18}$$

$$Z_c^{\rm full} = 2\frac{\sqrt{1-\alpha}\sqrt{\Lambda-\varepsilon-1+\alpha}}{\Lambda-\varepsilon}\ . \tag{7.19}$$

[4]Note that, even though the imaginary time method should evolve to the real ground state $\Phi_{\rm s}(\mathbf{r})$ of the Hamiltonian, the symmetry properties imposed in the initial condition (7.14) are hard to break and therefore the calculation converges to a local minimum where the solution is antisymmetric.

In Fig. 7.5 the critical population imbalance above which self-trapping occurs is plotted as a function of the scattering length, both for the crude (dashed) and the full (solid) TMMs. Around $a \approx 14.5\,a_B$ both TMMs predict the same result for the critical imbalance. This happens because the α parameter is very small for $a = 14.5\,a_B$, $\alpha = 0.03$, in comparison with its value at $a = 14\,a_B$, $\alpha = 0.13$. This is an effect of the fact that in dipolar plus s-wave condensates we have two competing interactions. At $a \approx 14.5\,a_B$ they are such that they cancel out in the α parameter, which accounts for the main difference between crude and full TMMs. We have indicated in the figure the time-dependent runs of the Gross-Pitaevskii equation we have carried out. We see that they are consistent with the predictions of TMM, since the TDGP predicts Josephson or self-trapping oscillations in the same regime of parameters as the TMMs do.

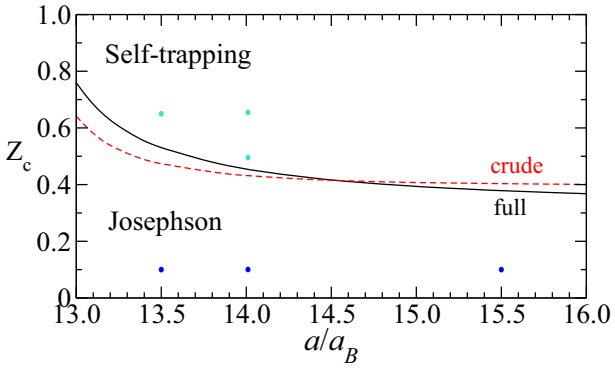

Figure 7.5: Critical initial population imbalance as a function of the scattering length, predicted by the standard and improved two-mode models. The points correspond to the time-dependent simulation: in darker blue for Josephson oscillations and in lighter blue for self-trapping oscillations.

7.2.2 Comparison with the time dependent simulation

In Fig. 7.6 we show the numerical result given by the TDGP and the solutions provided by the TMMs for $a = 14\,a_B$ and initial conditions $Z(0) = 0.1$ and $\phi(0) = 0$. We see from the figure that the TMM is a good qualitative approximation to the full dynamics given by the TDGP Eq. (2.12): the order of magnitude of the frequency and amplitude of the oscillations, as well as the dynamical regime imposed by the initial conditions, are well predicted. As can be expected, though, the full TMM approaches more the TDGP result than its crude counterpart. This tells us that the overlap terms I_i and D_i are important and cannot be neglected. This is consistent with the fact that for $a = 14\,a_B$ the weak-link condition is not fully satisfied, since $\Delta V_{\text{eff}} \simeq 1.1\mu$ (see Fig. 7.2). Table 7.2 provides a comparison of the frequencies obtained in the different methods for different scattering lengths (see also Fig. 7.3). We can conclude that both TMMs predict the order of magnitude of the Josephson oscillations but fail to give a quantitative good approximation.

Table 7.2: Comparison of oscillation frequencies predicted by the different methods.

a/a_B	$\omega_{\text{TDGP}}/\omega_\perp$	$\omega_{\text{full}}/\omega_\perp$	$\omega_{\text{crude}}/\omega_\perp$
13.5	0.11	0.15	0.20
14.0	0.15	0.20	0.26
15.5	0.25	0.33	0.38

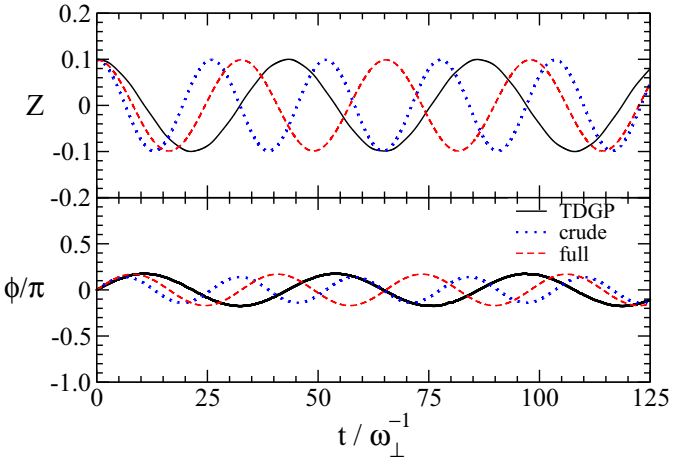

Figure 7.6: Comparison of the Josephson oscillations obtained with the TDGP Eq. (2.12), the crude and the full TMM, for $a = 14\,a_B$.

The discrepancy between the TDGP dynamics and the TMM can be attributed to a combination of different factors. Here we list some of them:

1. As can be seen from Fig. 7.2, with this SIJJ it is not possible to address systems for which $\Delta V_{\text{eff}} \gg \mu$. Therefore the systems analyzed do not lie in a deep weak-link regime. This means that the two-mode ansatz, Eq. (7.6), is not an extremely good approximation. It has been recently shown both experimentally and theoretically that the fact that the system does not lie in the deep weak-link limit gives rise to a frequency in the two-mode approximation larger than the experimental one [Bla11], which is in agreement with our findings (see Fig. 7.6 and Table 7.2). On the other hand, the fact that the junction is not really a weak link causes higher excited states of the double well to contribute to the dynamics [Jul10b].

2. The self-induced nature of the double well means that it depends on time, which is not taken into account in a TMM with time-independent parameters.

3. The SIJJ presented here is clearly two-dimensional, whereas the TMM mimics it as one-dimensional. Dynamics in other directions different than x might affect the behavior of the imbalance and the phase difference [Sme03, Mele11]. The SIJJ is clearly not one-dimensional, and it can be understood that dynamics does not take place in just the azimuthal direction. Since two-mode models treat only the dynamics in only one direction, by assuming a two-mode description we are oblivious of the fact that there can be relevant dynamics occurring in the other directions.

4. Ansatz (7.6) is a good approximation for narrow junctions. For wider junctions, as is the case of the SIJJ, local dynamics within the junction becomes important and leads to a departure of the frequency from the ideal one given by TMMs.

7.3 Vortex-induced phase slippage

In this section the self-trapping regime of a SIJJ is studied in detail and is shown to be very closely related to the process of phase-slippage. This process generally takes place in AC Josephson junctions. In this regime the phase difference increases linearly in time and

proportionally to the external voltage applied or chemical potential difference between two superfluid baths. This linear growth can be interpreted as a periodic change of the phase difference by an amount of 2π, or as the system periodically undergoing a phase-slip. The current understanding is that phase slips are related to the dynamical creation of vortices, which cross the flow path and leave a 2π phase behind [And66].

We consider the case $a = 14\,a_B$, $V = 30\,\hbar\omega_\perp$ and initial population imbalance of $Z(0) = 0.65$ (see Fig. 7.4). The initial density is given in Fig. 7.7(a). The two potential barriers separating the wells are slightly displaced from the y axis. In this section, to perform a more accurate analysis of the self-trapping regime, we have included the displacement of the junctions (of about 15° from the y axis) into the definition of left and right wells, giving rise to a left well slightly larger than the right one. Figure 7.7(b) shows the time evolution of the imbalance and the phase calculated with this definition of left and right sides. There is a slight quantitative improvement in the two signals with respect to Sec. 7.1, since now the zero crossing of the phase corresponds to a maximum of imbalance. The π crossings however are still dephased in relation to the minima of imbalance. Notice that in Fig. 7.7(b) we only show the first three oscillations of the imbalance. As can be seen from Fig. 7.4 this pattern is repeated in time.

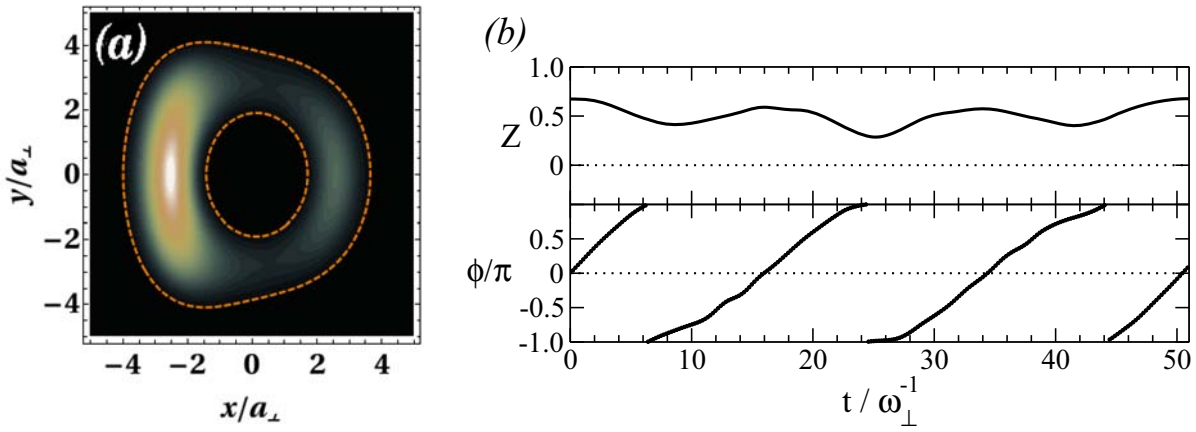

Figure 7.7: (a) Initial density configuration on the plane $z = 0$. As a guide to the eye, the dashed lines mark the points where the density is $n_{\max}/10$. (b) Evolution of the imbalance and the phase with the redefined left and right sides (for comparison, see Fig. 7.4).

The time derivative of the population imbalance is related to the flow of atoms across the junction. At the maxima and minima of the imbalance its slope changes sign, so that the flow of atoms is reversed. In a two mode description, when the imbalance reaches a maximum the phase difference is zero, while in a minimum it reaches π. However, looking more closely to the coupled dynamics given by TDGP, we see that in the minima of imbalance the phase difference does not exactly correspond to $\phi = \pi$. This fact hints at a richer dynamics that is not accounted for in the two macroscopic variables Z and ϕ, but comes from a local behavior. In other words, since the junction is a wide junction, the local currents within it affect the gross dynamics contained in Z and ϕ. To understand better the irregularities of the signal in Fig. 7.7(b), we have to look at the dynamics of the local phase. We find two main results. On the one hand, we see that the flux inversion in the minima of the imbalance is accompanied by the crossing of a vortex through each

junction. These vortices are dynamically created and constitute the phase-slip process that takes place when the phase difference reaches π. On the other hand, the currents generated by the phase gradients within the junction propagate and affect the phase in each one of the wells, giving rise to a slight spatial dependence of the phase and thus to small currents within the wells. This new phase gradients become currents in the wells that are not properly accounted for in Z and ϕ and are mostly the responsible of the dephasing between these two variables. Figure 7.8 shows snapshots of the density distribution (top row) and the phase (bottom row) on the plane $z = 0$ at the minima (odd number panels) and maxima (even number panels) of the imbalance. Note that the final configuration is very close to the initial system, Fig. 7.7(a).

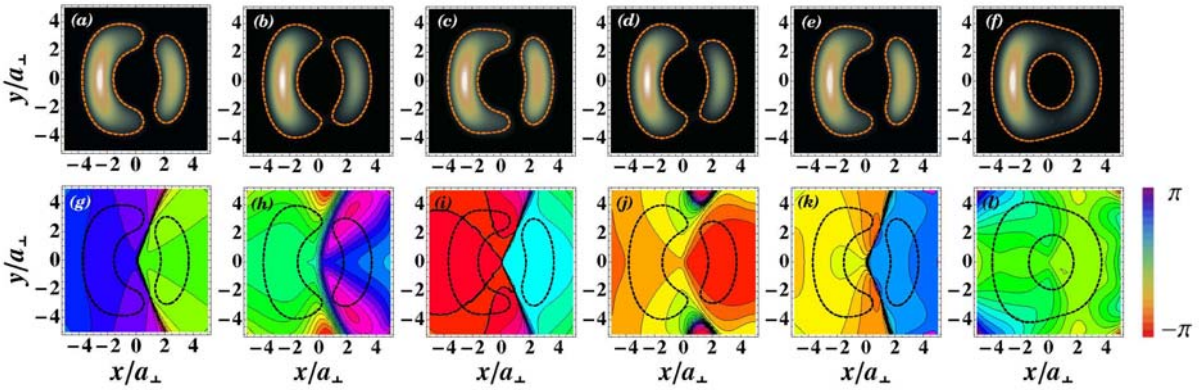

Figure 7.8: Snapshots of the density (top row) and the phase (bottom row) on the plane $z = 0$ at different times: (a) and (g) $t = 8.55\,\omega_\perp^{-1}$, (b) and (h) $t = 17.10\,\omega_\perp^{-1}$, (c) and (i) $t = 25.22\,\omega_\perp^{-1}$, (d) and (j) $t = 33.56\,\omega_\perp^{-1}$, (e) and (k) $t = 41.47\,\omega_\perp^{-1}$, (f) and (l) $t = 50.23\,\omega_\perp^{-1}$. As a guide to the eye, the dashed lines mark the points where the density is $n_{\max}/10$.

Let us examine the dynamical nucleation of vortices in more detail. In the top panels of Fig. 7.9 we schematically describe the vortex-induced phase-slip process that contributes to the flux inversion in the minima of the imbalance. Before reaching the minimum, since the phase difference is very large, there is an accumulation of phase between the two condensates, producing a large phase gradient along the line that connects both junctions. The atoms tunnel from the left to the right well, acquiring a velocity associated to this gradient, as indicated in Fig. 7.9(a). The velocity is larger in the low density regions, namely the central hole giving rise to the toroidal geometry and the external region. When the phase difference is π, the velocity reaches a critical value and two vortices are nucleated, a vortex-antivortex pair to ensure angular momentum conservation, as seen in Fig. 7.9(b). Subsequently both vortices cross simultaneously the section of the torus in opposite directions, each one moving outwards through one link, producing the phase slip in the junction. After the passage of the vortex (antivortex) the sign of the local velocity in the link is changed, leading thus to the inversion of the flux of atoms, as shown schematically in Fig. 7.9(c). The vortex (antivortex) with positive (negative) charge is defined with the phase gradient in the counterclockwise (clockwise) direction.

Panels (d), (e) and (f) of Fig. 7.9 show the phase of the wave function, in the $z = 0$ plane of the upper junction, around the first minimum of $Z(t)$ at the moments schemati-

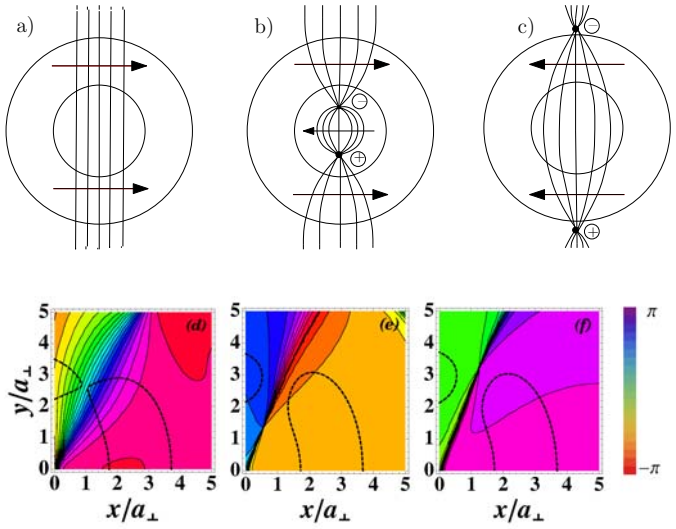

Figure 7.9: Top: scheme of the phase-slippage process in the SIJJ. The solid lines represent constant phase curves and the arrows indicate the phase gradient, and thus the velocity field, along the junctions. We have drawn the following three steps: a) Phase accumulation along the junctions, b) Vortex-antivortex pair separation after the nucleation and c) Inversion of the velocity field after the vortices cross the torus. Bottom: Snapshots of the numerical phase around the upper junction at $z = 0$, as a function of x and y. The times are: (d) $t = 6.41\,\omega_\perp^{-1}$, (e) $t = 8.12\,\omega_\perp^{-1}$, and (f) $t = 8.76\,\omega_\perp^{-1}$.

cally represented in (a), (b) and (c), respectively. A vortex-antivortex pair is nucleated in the center, separates and then the vortex (antivortex) crosses the lower (upper) junction. The same effect is produced if an antivortex and a vortex are nucleated at opposite points of the external surface of the condensate and then cross the torus and annihilate at the center. Analyzing the dynamics we see that both processes take place at different minima. A similar phenomenon has been addressed in Ref. [Pia09], where a single external barrier was raised in a toroidally confined s-wave condensate with a nonzero initial angular momentum. In that work the appearance of vortices from the external or internal surfaces of the torus was controlled by the height of the barrier, while the nonzero angular momentum favored the first process. Here, however, both processes are equivalent. We want to note that all the vortices we predict correspond to quantized vortex lines, with no visible bending along the z direction. The quantization is guaranteed by the fact that the phase changes by 2π around the singularity. The angular momentum remains zero throughout the simulation and there is no net creation of vorticity in the system.

In order to complete the description of the vortex-induced phase slip, we have computed the mean velocity of the atoms across the upper and lower junction as a function of time, see Fig. 7.10. As expected, both junctions behave coherently (in phase) and present the same physics: simultaneously to the nucleation and crossing of the vortices through the junctions, there is a steep drop of the velocity in each junction. In analogy with the experiments carried out in superfluid helium, this drop marks the point at which a phase slip takes place. From the sharp decrease of the mean velocity it is possible to estimate the vortex passage velocity using $v_p = \Delta/\delta t$, where $\Delta \sim 2\,a_\perp$ is the width of the barrier and δt is the time it takes the vortex to cross it as read from Fig. 7.10. For the three minima it gives: $v_p^{(1)} = 2.7\,\omega_\perp a_\perp$, $v_p^{(2)} = 4.2\,\omega_\perp a_\perp$ and $v_p^{(3)} = 8.2\,\omega_\perp a_\perp$.

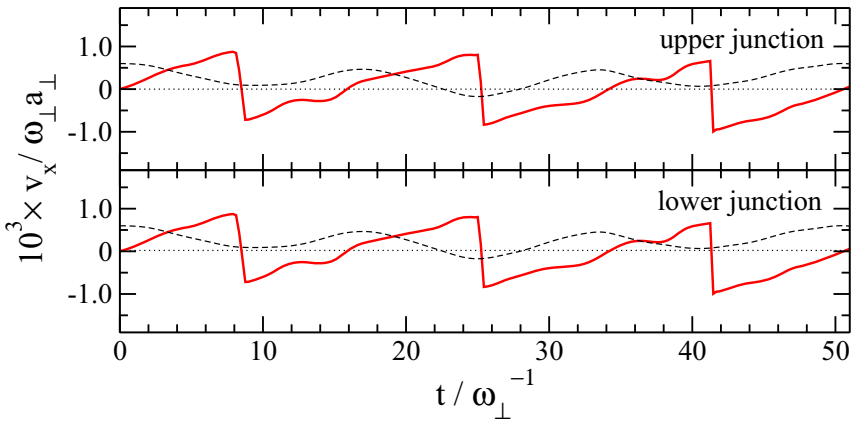

Figure 7.10: Velocity of the atoms at the upper and lower junctions as a function of time. The steep drops correspond to the crossing of a vortex (phase-slip). As a guide to the eye, the imbalance has been plotted in an arbitrary scale as a dashed line.

Chapter 8

Radial quadrupole mode in dipolar Fermi gases

At very low temperature a gas of atoms or molecules is ruled by quantum statistics. Throughout this thesis we have addressed the case of integer spin particles (bosons), which are described by Bose-Einstein statistics and condense below a critical temperature (see for instance [Hua63, Pat88]). In this chapter we address half-integer spin particles (fermions), which are described by Fermi-Dirac statistics. In this case, the Pauli exclusion principle forbids the occupation of the same single-particle state and below a critical temperature the gas becomes degenerate. This degeneration temperature is called Fermi temperature, T_F. Below T_F all single-particle states are occupied up to the Fermi energy, defining thus a filled Fermi sphere or a Fermi surface in momentum space (see for instance [Lip03]). For the ideal uniform gas at $T = 0$ and in 3D, the Fermi energy, ϵ_F, takes the form

$$\epsilon_F = \frac{\hbar^2 k_F^2}{2m} = \frac{\hbar^2}{2m}\left(6\pi^2 n\right)^{2/3} = k_B T_F \ , \tag{8.1}$$

where $k_F = (6\pi^2 n)^{2/3}$ is the Fermi momentum (all states with momentum $k \leq k_F$ are occupied), n is density of the gas and k_B the Boltzmann constant. The Fermi energy of the ideal Fermi gas is its chemical potential at $T = 0$. Notice that expression (8.1) corresponds to a polarized Fermi gas, that is, all particles have the same spin. For the unpolarized case, the expression is the same but has a factor 3 instead of 6 that accounts for the spin degree of freedom. In Appendix E the ideal Fermi gas trapped in a harmonic potential will be analyzed.

The presence of interactions affects this picture, since they lead to a phase transition between the degenerate (normal) state to a superfluid state. The critical temperature is much lower than the degeneration temperature (a typical order of magnitude is $T_c \sim 0.2\, T_F$ for contact interacting Fermi gases[1] [Gio08]). The superfluid state has a different nature depending on the sign of the interactions: attractive interactions give rise to Cooper pairing (Bardeen-Cooper-Schrieffer, or BCS, theory), repulsive interactions give rise to a molecular condensate (BEC), and infinite interactions bring the system into unitarity.

[1] Notice that, due to the Pauli exclusion principle, identical fermions cannot interact via s-wave contact interactions. One then needs a two-species, or unpolarized, Fermi gas.

The crossover between these three manifestations of the superfluid state has received much attention in the literature (see [Gio08] and references therein).

The achievement of a dipolar Bose-Einstein condensate in 2005 [Gri05] has generated a huge interest in dipolar quantum gases. On the fermionic side, there have been important advances in cooling a dipolar Fermi gas to degeneration [Mir11]. Since dipolar interactions are long-range, they are not forbidden for single-species Fermi gases and they can give rise to superfluidity [Bar04]. Also, the transition from normal to superfluid states can be reached by tilting the magnetization axis of the dipoles in a 2D geometry [Bru08]: for a certain angle between the trap axis and the magnetization direction, the attractive part of the dipole-dipole interaction becomes strong enough to allow for Cooper pairing. On the other hand, due to their anisotropic character, dipolar interactions have been shown to deform the Fermi surface through exchange interactions [Miy08, Zha09], which contribute to destabilize the system.

An important subject in quantum gases is the characterization of collective oscillations. Their frequencies can be measured in the experiments, giving information about many properties of the system, such as the equation of state, its collisional regime, the trapping frequencies, or the angular momentum (see for instance [Pet02, Pit03]). For dipolar Fermi gases, collective modes have received some attention in the literature [Gor03, Sogo09, Lima10a, Lima10b]. Among all the different collective modes are of particular interest the surface modes, which are insensitive to the equation of state but depend strongly on the collisional regime of the gas. We distinguish between the collisionless and hydrodynamic regimes. At very low temperatures, interactions are quenched by the Pauli principle and the system is said to be in the collisionless regime, where interactions are so weak and slow than they can be treated as a perturbation and even neglected. At a slightly higher temperature, the system is in the hydrodynamic regime, where interactions are fast enough to obtain local equilibrium in a time scale much smaller than the dynamical process under consideration. In this regime, the equations governing the behavior of the system are hydrodynamic equations. Note that superfluids also obey hydrodynamic equations (see Sec. 3.1.1), but this is due to coherence rather than interactions. When necessary we will distinguish the collisional hydrodynamic regime from the superfluid hydrodynamic regime. An important surface mode is the radial quadrupole mode, since it has been a good tool to experimentally distinguish between hydrodynamic and collisionless regimes in ultracold non-dipolar Fermi gases [Vic99, Alt07].

The aim of this chapter is to study analytically and within mean-field framework the surface quadrupole mode of a quantum gas of dipolar fermions. The dipolar interactions affect the frequency of this mode and shift it to smaller or larger values compared to non-dipolar gases. We show that this mode can be useful experimentally to determine whether the gas is in the hydrodynamic or the collisionless regime, even if the frequencies corresponding to them are shifted with respect to the corresponding s-wave values [Str96, Vic99]. In Sec. 8.1 we describe the ground state of a gas of dipolar fermions within the Thomas-Fermi approximation. In Sec. 8.2 we calculate the frequency of the quadrupole mode both in the collisionless and the hydrodynamic regimes by taking variations of the action (see also Sec. 4.3.2), and show that it can be used as a tool to measure the transition between normal to superfluid states when the trap aspect ratio is brought from very large to smaller values.

8.1 Ground state of dipolar fermions

We consider a quantum gas of identical fermions (atoms or molecules) interacting via dipole-dipole interactions (see Sec. 2.1.2) at $T = 0$, confined in an axially symmetric harmonic trap with $\lambda = \omega_z/\omega_\perp$ (see Eq. (2.28)). If the number of particles is very large, the system can be studied within the local density approximation, also known as Thomas-Fermi regime. In this approximation, the system behaves locally as a uniform gas with a local chemical potential, $\mu(\mathbf{r})$, given by

$$\mu(\mathbf{r}) = \mu_0 - V_{\rm ho}(\mathbf{r}) \ , \tag{8.2}$$

where μ_0 is the chemical potential of the gas, obtained from the normalization of the density, $\int n(\mathbf{r})\mathrm{d}\mathbf{r} = N$. Notice that in the presence of interactions μ_0 can no longer be identified with the Fermi energy, even at $T = 0$. The local chemical potential, μ, depends on $\mathbf{r}$ through the density, that is $\mu[n(\mathbf{r})]$. In the trapped non-interacting gas (see Appendix E), the Thomas-Fermi approximation assumes $\mu(n)$ to locally have the same density dependence as the uniform system. Analogously, we assume that in the interacting case it is given locally by the same density dependence as the chemical potential of the (ideal) uniform gas, Eq. (8.1),

$$\mu(n) = \frac{\hbar^2}{2m}\left(6\pi^2 n\right)^{2/3} \ , \tag{8.3}$$

which gives rise to the density

$$n(\mathbf{r}) = \frac{8}{\pi^2}\frac{N}{R_\perp^2 R_z}\left(1 - \frac{r_\perp^2}{R_\perp^2} - \frac{z^2}{R_z^2}\right)^{3/2} \ , \tag{8.4}$$

where the Thomas-Fermi radii $R_\perp$ and R_z are now variational parameters that contain the corrections due to the dipolar interaction. Let us comment now on the implicit assumption we make in writing Eq. (8.3). This expression is exact when one wants to build the local density approximation for a non-interacting, harmonically trapped Fermi gas (see Appendix E). However, when interactions are taken into account the local chemical potential for the uniform system will not in general go as $\sim n^{2/3}$, but will depend on a different power of n since two-body interactions usually go as $\sim n$. In writing Eq. (8.3), and therefore Eq. (8.4), we are making the further assumption that $\mu \sim n^{2/3}$ even in the presence of dipolar interactions. The effect of this power in what follows only affects the numerical prefactors of the different equations. Notice that in the case of bosons in the Thomas-Fermi regime (see Sec. 2.3) the local chemical potential goes as $\sim n$, and in this case is exact (both for contact and dipolar interactions). The local density approximation is valid for a potential slowly varying in space, whose energy levels form a continuum and do not affect the equation of state of the gas. The condition that the potential is slowly varying in space means that $a_{\rm ho} \gg 1/k_F$, that is the length scale associated to variations in the density of the gas, $1/k_F$, is much smaller than the length scale of variations in the confining potential, $a_{\rm ho}$. It can be easily seen that this condition is equivalent to $\hbar\omega_{\rm ho} \ll \mu_0$, which can be interpreted as a quasi-continuum spectrum of the harmonic oscillator energy states, $\hbar\omega_{\rm ho}$, in comparison to the energy scale provided by the chemical potential.

Within the Thomas-Fermi approximation, the energy functional describing a gas of dipolar fermions is given by

$$E[n] = E_{\rm kin}[n] + E_{\rm ho}[n] + E_{\rm dip}[n] \ , \tag{8.5}$$

where the kinetic, harmonic oscillator and dipolar energies are respectively given by the integrals

$$E_{\rm kin}[n] = \frac{3}{5}\frac{\hbar^2}{2m}(6\pi^2)^{2/3}\int {\rm d}\mathbf{r}\ [n(\mathbf{r})]^{5/3} \tag{8.6}$$

$$E_{\rm ho}[n] = \int {\rm d}\mathbf{r}\, n(\mathbf{r}) V_{\rm ho}(\mathbf{r}) \tag{8.7}$$

$$E_{\rm dip}[n] = \int {\rm d}\mathbf{r_1}\, n(\mathbf{r}_1) \int {\rm d}\mathbf{r}_2 n(\mathbf{r}_2) v_{\rm dip}(\mathbf{r}_1 - \mathbf{r}_2) \ . \tag{8.8}$$

The microscopic dipole-dipole potential, $v_{\rm dip}$, is given by Eq. (2.5), as in the case of bosons. Notice that the exchange term arising from two-body interactions (see for instance [Lip03]) has been neglected. This assumption is supported by the fact that far from instability the exchange energy has a value close zero and is much smaller than the other contributions to the total energy [Sogo09]. The effect of the exchange interaction in dipolar Fermi gases is to deform the Fermi surface and to modify the stability diagram [Miy08, Zha09, Sogo09, Lima10a, Lima10b]. An important effect appears for pancake configurations: when the exchange interaction is neglected, pancake-shaped Fermi gases are always stable above $\lambda \approx 5.3$, while the inclusion of the exchange term leads to instability for all λ values [Miy08]. The results presented in this chapter will be therefore valid away from instability, where corrections due to the Fock exchange term are small.

The ground state properties of the gas are obtained by minimization of the energy functional with the constraint imposed by normalization, $-\mu_0 \int {\rm d}\mathbf{r}\, n(\mathbf{r})$ (see also Appendix D). Taking expression (8.4) for the density, the different ground state energy terms are given by

$$E_{\rm kin} = \frac{3}{8} N \epsilon_F \tag{8.9}$$

$$E_{\rm ho} = \frac{1}{8} N \epsilon_F^0 \left(2\frac{R_\perp^2}{(R_\perp^0)^2} + \lambda^2 \frac{R_z^2}{(R_z^0)^2} \right) \tag{8.10}$$

$$E_{\rm dip} = -\frac{1}{4} N \epsilon_F \varepsilon_{dd} f(\kappa) \ . \tag{8.11}$$

In these expressions $\epsilon_F^0 = (6N)^{1/3}\hbar\omega_{\rm ho}$ is the Fermi energy of the trapped non-interacting gas and $\epsilon_F \equiv \mu_0 = \hbar^2 k_F^2/2m$ is the chemical potential[2], with k_F the Fermi momentum defined from the density through the normalization condition $R_\perp^2 R_z k_F^3 = 48N$. The non-interacting Thomas-Fermi radii are defined through the Fermi energy as $R_i^0 = \sqrt{2\epsilon_F^0/m\omega_i^2}$.

[2]As has been already noted above, the chemical potential coincides with the Thomas-Fermi energy only for the non-interacting gas at $T = 0$. Here we are using the notation ϵ_F instead of μ_0 for convenience, and sometimes we refer to ϵ_F as the Fermi energy of the interacting gas.

The dipolar parameter ε_{dd} is dimensionless and represents the ratio between the dipolar energy and the Fermi energy. It is defined as:

$$\varepsilon_{dd} = \varepsilon^0_{dd}\tilde{k}_F = \frac{2^{11}}{3^4 35\pi^2}\frac{d^2 k_F^3}{\epsilon_F} \ , \tag{8.12}$$

where $\tilde{k}_F = k_F/k_F^0$, with the non-interacting Fermi momentum $k_F^0 = (48N)^{1/6}/a_{\rm ho}$, and d^2 contains information about the dipole moment (see Sec. 2.1.2). The parameter ε^0_{dd}, defined as

$$\varepsilon^0_{dd} = \frac{2^{11}}{3^4 35\pi^2}\frac{d^2 (k_F^0)^3}{\epsilon_F^0} \ , \tag{8.13}$$

is independent of the density and can thus be controlled externally. The non-interacting Fermi energy is related to the non-interacting Fermi momentum through the usual relation $\epsilon_F^0 = \hbar^2(k_F^0)^2/2m$. Figure 8.1 shows the dependence between ε^0_{dd} and ε_{dd} for the ground state of the system. Note that the difference between ε^0_{dd} and ε_{dd} is due to the departure of k_F from the noninteracting value k_F^0, as can be seen from the definition (8.12).

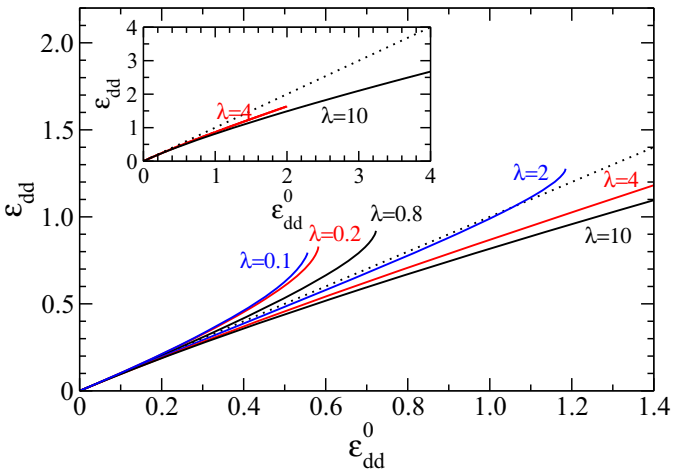

Figure 8.1: Density-dependent dipolar parameter ε_{dd} as a function of the externally controllable dipolar paramenter ε^0_{dd}.

The expression of the dipolar energy, Eq. (8.11), is very similar to the dipolar energy of a condensate in the Thomas-Fermi approximation, Eq. (2.47), once ε_{dd} and k_F are substituted by their definitions. That is, in both cases the dipolar energy has the dependence $E_{\rm dip} \sim f(\kappa)/(R_\perp^2 R_z)$. The function $f(\kappa)$ (with $\kappa = R_\perp/R_z$), which we have already encountered in Sec. 2.3.2 (see Eq. (2.41)), contains all the information about the anisotropy of the interaction. It is shown in Fig. 8.2 (black solid line), together with two of its derivatives that we will meet later. The function $f(\kappa)$ saturates for $\kappa \to 0$ and $\kappa \to \infty$ at the values 1 and -2, respectively. This indicates that for very prolate ($\lambda \ll 1$) or oblate ($\lambda \gg 1$) geometries the dipolar interaction loses its long-range character and effectively acts as a contact interaction. For the spherical gas, $\kappa = 1$, the function $f(\kappa)$ vanishes, which means that the dipolar energy is zero for this configuration. Much information about this function can be found in Refs. [Dell04, Ebe05, Gio06].

Taking the Thomas-Fermi radii as variational parameters, minimization of the energy

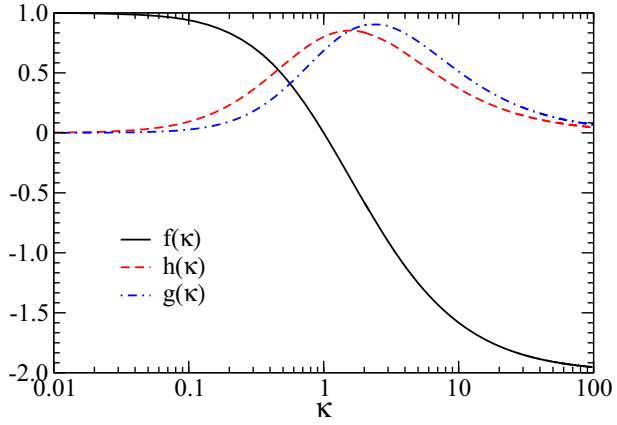

Figure 8.2: Anisotropy function $f(\kappa)$ and its derivatives, $h(\kappa)$ and $g(\kappa)$, that appear in the expressions of the quadrupole frequency, as a function of κ.

functional leads to the equilibrium expressions for the Thomas-Fermi radii [Lima10b]

$$\frac{\widetilde{R}_\perp^2}{\tilde{k}_F^2} = 1 - \varepsilon_{dd}\left[1 - \frac{3}{2}\frac{\kappa^2}{1-\kappa^2} f(\kappa)\right] \tag{8.14}$$

$$\frac{\widetilde{R}_z^2}{\tilde{k}_F^2} = 1 + 2\varepsilon_{dd}\left[1 - \frac{3}{2}\frac{1}{1-\kappa^2} f(\kappa)\right] \ , \tag{8.15}$$

where $\widetilde{R}_i = R_i/R_i^0$. Combining equations (8.14) and (8.15), one can find a transcendental equation for κ as a function of λ and ε_{dd},

$$\frac{\kappa^2}{\lambda^2}\left[3\varepsilon_{dd}\frac{f(\kappa)}{1-\kappa^2}\left(\frac{\lambda}{2}+1\right) - 2\varepsilon_{dd} - 1\right] = \varepsilon_{dd} - 1 \ . \tag{8.16}$$

This expression is the same for bosons and fermions, see Sec. 2.3.2, provided the parameter ε_{dd} is properly defined. With Eq. (8.14) and Eq. (8.16) the ground state of the system is fully determined. The problem contains two independent parameters, ε_{dd} and κ, which depend themselves on the density of the gas via k_F. To make a link with the externally controlled magnitudes, represented by ε_{dd}^0, we need to understand how these two parameters are related, and how they change when the trap aspect ratio λ is changed. Figure 8.3 shows the dependence between κ/λ and ε_{dd} for different values of λ. For zero dipolar interactions we recover the non-interacting limit, for which $\kappa = \lambda$. Note that the magnetostriction (electrostriction) effect (see Sec. 4.1) is larger for $\lambda \sim 1$, while it is much smaller for very small or very large trap aspect ratios. The dashed lines in the figure mark the regions for which the solution including exchange interactions predicts instability [Miy08, Lima10a], while neglecting them gives a stable solution. We will keep this notation in what follows.

8.2 Frequency of the radial quadrupole mode

In the same way as we did for bosons in Sec. 4.3, to find the frequency of the radial quadrupole mode for a quantum gas of fermions, the quantum action,

$$S = \int dt \left\langle \Psi \left| H - i\hbar\frac{\partial}{\partial t} \right| \Psi \right\rangle \ , \tag{8.17}$$

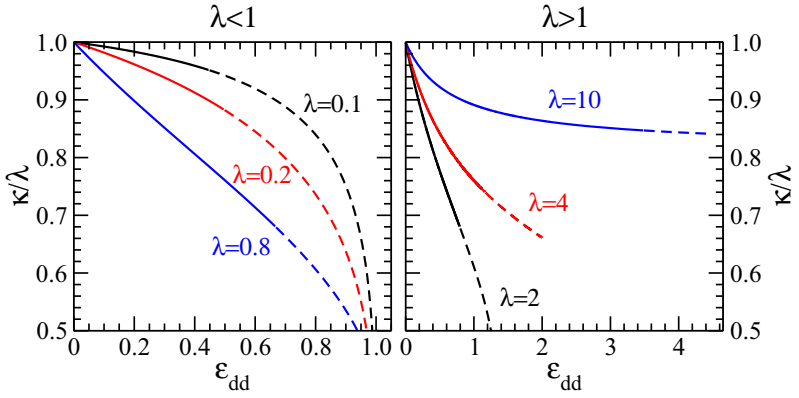

Figure 8.3: Gas aspect ratio normalized by the trap aspect ratio, κ/λ, as a function of ε_{dd}. Left panel: for a cigar-shaped trapping potential; Right panel: for a pancake-shaped trapping potential. Dashed line marks instability as predicted by including exchange interactions (see for instance [Miy08]).

has to be minimized for a state Ψ slightly perturbed from equilibrium. This state is the many-body wave function of the system of N fermions, which is in general a complicated state built as a combination of Slater determinants. In the case of the radial quadrupole excitation, the perturbed wave function is written as a function of two parameters $\alpha(t)$ and $\beta(t)$ (which, respectively, contain the information about the perturbation of the velocity field and the density distribution) as follows:

$$|\Psi\rangle = e^{i\alpha(t)\sum_k (x_k^2 - y_k^2)} e^{i\beta(t)\sum_k ((x_k p_k^x - y_k p_k^y) + h.c.)} |\Psi_0\rangle \ , \tag{8.18}$$

with p_k^i the linear momentum along $i = x, y$ corresponding to particle k and $k = 1, \ldots, N$. For $\alpha = 0$ and $\beta = 0$ we recover the equilibrium wave function Ψ_0 that minimizes the action. The corresponding density is given, as in the case for bosons (Sec. 4.3.2), in terms of $b(t)$, defined as $\beta = e^b - 1$,

$$n(x, y, z) = n_0(e^{-b(t)}x, e^{b(t)}y, z) \ . \tag{8.19}$$

Note that the perturbation (8.18) preserves the norm of the wave function.

The first term in the action integral, Eq. (8.17), is the energy functional of the perturbed state Ψ. At this level, the difference between hydrodynamic (HD) and collisionless (CL) fermions comes from the kinetic energy. In the hydrodynamic regime, fermions are always in local equilibrium due to interactions (in the collisional hydrodynamic regime) or due to coherence (in the superfluid regime). This means that Eq. (8.6) is still valid even when the wave function is perturbed and the kinetic energy becomes

$$E_{\rm kin}^{\rm (HD)}(b) = E_{\rm kin} \, . \tag{8.20}$$

In contrast, collisionless fermions are sensitive to the currents created by the density perturbation and the kinetic energy cannot be reduced to only the energy coming from the Fermi surface (in other words, the currents due to the quantum pressure term $\nabla^2\sqrt{n}$ cannot be neglected). This leads to a kinetic energy

$$E_{\rm kin}^{\rm (CL)}(b) = E_{\rm kin} + 2b^2 E_{\rm kin_\perp} \, , \tag{8.21}$$

where $E_{\mathrm{kin}_\perp}$ is the kinetic energy associated to the radial degree of freedom. In addition, we have the kinetic energy contribution coming from the velocity introduced by the perturbation, $\mathbf{v} \propto \alpha \boldsymbol{\nabla}(x^2 - y^2)$, which gives rise to a term proportional to α^2 (see Sec. 4.3). The action can thus be written as

$$S^{(\mathrm{HD})}(\alpha, b) = S_0 + \int \mathrm{d}t \left[\frac{2\hbar^2}{m} \alpha^2 N \langle r_\perp^2 \rangle + m\omega_\perp^2 b^2 N \langle r_\perp^2 \rangle - \frac{\epsilon_F \varepsilon_{dd}}{8} b^2 N g(\kappa) + 2\hbar \dot{\alpha} b N \langle r_\perp^2 \rangle \right] \tag{8.22}$$

in the hydrodynamic regime, and as

$$\begin{aligned} S^{(\mathrm{CL})}(\alpha, b) =& S_0 + \int \mathrm{d}t \left[\frac{2\hbar^2}{m} \alpha^2 N \langle r_\perp^2 \rangle + 2b^2 E_{\mathrm{kin}_\perp} + m\omega_\perp^2 b^2 N \langle r_\perp^2 \rangle - \frac{\epsilon_F \varepsilon_{dd}}{8} b^2 N g(\kappa) + \right. \\ & \left. + 2\hbar \dot{\alpha} b N \langle r_\perp^2 \rangle \right] \end{aligned} \tag{8.23}$$

in the collisionless regime. In these expressions S_0 is the unperturbed action and the function $g(\kappa)$ is the second derivative of $f(e^b\kappa, e^{-b}\kappa)$ evaluated at $b = 0$,

$$g(\kappa) = \left. \frac{\partial^2 f(e^b\kappa, e^{-b}\kappa)}{\partial b^2} \right|_{b=0} = \frac{3\kappa^2}{2} \frac{\sqrt{1-\kappa^2}(2+13\kappa^2) - \kappa^2(12+3\kappa^2)\tanh^{-1}\sqrt{1-\kappa^2}}{(1-\kappa^2)^{7/2}} \,. \tag{8.24}$$

Notice that we have already found this function in Sec. 4.3.2, when the quadrupole mode in condensates was addressed. It is shown in Fig. 8.2 (blue dash-dotted line).

Minimizing the action with respect to α and b and staying at second order in these parameters[3] we find the frequency of the quadrupole mode. In the hydrodynamic regime it is given by

$$\omega_Q^{(\mathrm{HD})} = \sqrt{2}\omega_\perp \left[1 - \frac{1}{4} \frac{\varepsilon_{dd}}{1 + \varepsilon_{dd}\left(\frac{3}{2}\frac{\kappa^2 f(\kappa)}{1-\kappa^2} - 1 \right)} g(\kappa) \right]^{1/2} , \tag{8.25}$$

where we have used that $\langle r_\perp^2 \rangle = R_\perp^2/4$ for the density (8.4). For zero dipolar interactions the usual hydrodynamic result, $\omega_Q = \sqrt{2}\omega_\perp$, is obtained[4]. In Ref. [Lima10b] this frequency is calculated in the (collisional) hydrodynamic regime taking into account the deformation of the Fermi surface arising from the exchange term. In the collisionless regime the quadrupole frequency is given by

$$\omega_Q^{(\mathrm{CL})} = 2\omega_\perp \left[1 + \frac{1}{2} \frac{\varepsilon_{dd}}{1 + \varepsilon_{dd}\left(\frac{3}{2}\frac{\kappa^2 f(\kappa)}{1-\kappa^2} - 1 \right)} \left(f(\kappa) + \frac{1}{2}h(\kappa) - \frac{1}{4}g(\kappa) \right) \right]^{1/2} , \tag{8.26}$$

[3] The zeroth order is obviously the unperturbed wave function, while the first order must vanish because the action is a minimum (in general, this first order gives rise to the virial theorem associated to the perturbation).

[4] Note that a gas of fermions can never be non-interacting if it is in the HD regime: either it reaches hydrodynamics because of collisions (collisional HD) or because it is superfluid (superfluid HD). In contrast to bosons, superfluidity in fermionic systems can only exist in the presence of interactions.

where $h(\kappa)$ is the first derivative of $f(e^{-b}\kappa)$ evaluated at $b = 0$,

$$h(\kappa) = \left.\frac{\partial f(e^{-b}\kappa)}{\partial b}\right|_{b=0} = \frac{3\kappa^2}{(1-\kappa^2)^{5/2}}\left[-3\sqrt{1-\kappa^2} + (2+\kappa^2)\tanh^{-1}\sqrt{1-\kappa^2}\right] . \quad (8.27)$$

It is shown in Fig. 8.2 (red dashed line). For $\varepsilon_{dd} \to 0$ the non-interacting limit is recovered and the frequency is $2\omega_\perp$.

To write Eq. (8.26) we have used the radial virial theorem for a dipolar Fermi gas:

$$2E_{\mathrm{kin}_\perp} - 2E_{\mathrm{ho}_\perp} + 2E_{\mathrm{dip}} - \frac{1}{4}N\epsilon_F\varepsilon_{dd}h(\kappa) = 0 , \quad (8.28)$$

with $E_{\mathrm{ho}_\perp} = m\omega_\perp^2 N\langle r_\perp^2\rangle/2$ and E_{dip} given by (8.11). The radial virial expression is obtained by considering a scaling transformation of the ground state wave function of the type $\psi(x,y,z) \to \psi_\alpha(e^b x, e^b y, z)$ and imposing that the energy is a minimum. The first order derivative of the scaled energy with respect to b must be zero (equilibrium condition) and this gives rise to the virial relation. Note that this ansatz does not conserve the norm (it is a compressional mode). An alternative method to derive the virial relation based on commutators of the Hamiltonian with the excitation operator will be discussed in Appendix G.

The first thing that can be said about the frequency in the HD regime, Eq. (8.25), is that it is the same functional expression for bosons and for HD fermions (given the proper ε_{dd}), see Eq. (4.22). This is a consequence of the fact that the quadrupole is a surface mode, and it is thus insensitive to the details of the equation of state. In this regime the quadrupole frequency is shifted with respect to the usual $\sqrt{2}\omega_\perp$ result by an amount mainly coming from the anisotropic character of the dipolar interaction. This shift vanishes for $\kappa \to 0$ and $\kappa \to \infty$, since in these two limits the system is so deformed that it is no longer sensitive to the anisotropy of the interaction. This is reflected in the flat behavior of $f(\kappa)$ for very pancake and very cigar-shaped traps, as well as in the fact that $g(\kappa)$ tends to zero in these limits (see Fig. 8.2). The top panels of Fig. 8.4 show the behavior of the quadrupole frequency in the HD regime as a function of the dipolar parameter ε_{dd} for different trap aspect ratios λ (black lines). The dashed lines mark the ε_{dd} values for which the Fermi gas is no longer stable, according to [Sogo09]. We see from the figure that the frequency is always smaller than $\sqrt{2}\omega_\perp$ and that the shift is larger for intermediate trap aspect ratios. The effect of the anisotropic character of the dipolar interaction is to quench even further the value of the quadrupole frequency. However, as discussed in Ref. [Lima10b], the shift is not strongly dependent on the strength of the dipole-dipole interactions.

In the CL regime the situation is much different. In this case the direction of the shift introduced by the dipolar interaction depends strongly on the geometry of the system, as can be seen from the top panels of Fig. 8.4 (red lines). In a general way we can say that for cigar-shaped clouds, the shift is positive and the quadrupole frequency is larger than the non-interacting value ($2\omega_\perp$), while for pancake-shaped clouds the shift is always negative, and therefore the frequency is smaller than its non-interacting value. For $\lambda \sim 2$ we find that the shift is very small for all values of ε_{dd}. Away from this value of λ the shift always increases as the dipolar strength is increased. In contrast to HD regime, the

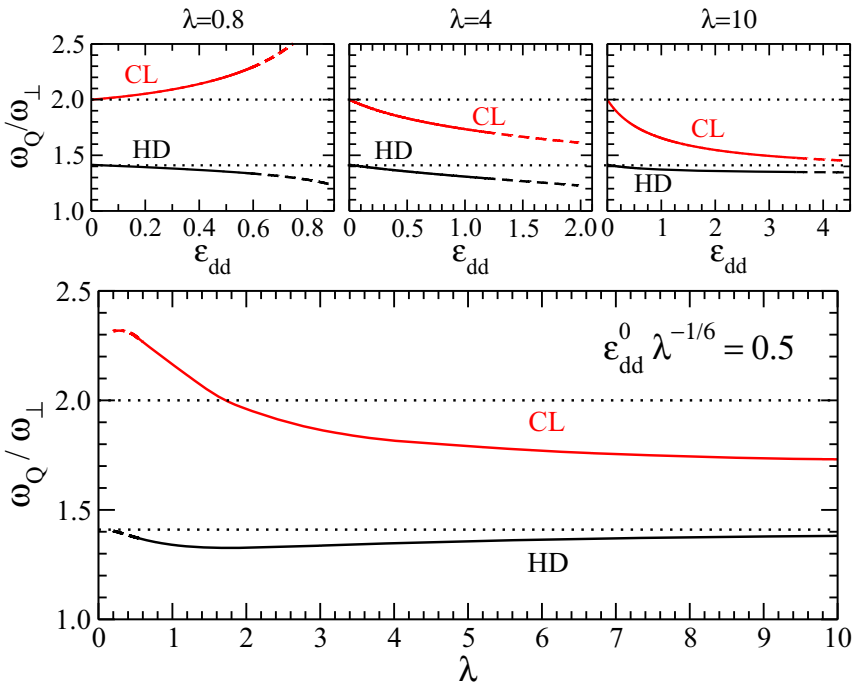

Figure 8.4: Top panels: Quadrupole frequency as a function of the dipolar strength ε_{dd}, both for the CL and the HD regimes and for different trap aspect ratios. Bottom panel: Quadrupole frequency as a function of λ for $\varepsilon^0_{dd}\lambda^{-1/6} = 0.5$.

shift of the quadrupole frequency in the CL regime does not vanish in the limit of large κ, but tends to a value that depends only on ε_{dd},

$$\omega_Q^{\mathrm{CL}}(\kappa \to \infty) = 2\omega_\perp \left(1 - \frac{\varepsilon_{dd}}{1+2\varepsilon_{dd}}\right)^{1/2} . \tag{8.29}$$

For very large ε_{dd} (and in the limit $\kappa \to \infty$) it reaches the HD frequency, $\sqrt{2}\omega_\perp$. We recall at this point that expression (8.29) is only valid far from instability, and that ε_{dd} can not be increased at will. Notice that this situation is very similar to the first and zero sound scenario of Fermi systems: the sound velocity found in the elastic or collisionless regime (zero sound) is larger than the sound velocity that is found in the hydrodynamic regime (first sound). In analogy to what we find for the radial quadrupole mode, the difference between zero and first sound velocities arises due to the restoring force that appears in the collisionless regime, which is in turn brought about by the modification of the Fermi surface due to the perturbation.

For very pancake systems, superfluidity cannot take place because the interactions are mainly repulsive. However, for not so pancake configurations the attractive part of the dipolar interaction can give rise to pairing and superfluidity [Bar04]. The radial quadrupole mode could be a good experimental test of the conditions of this transition. The bottom panel of Fig. 8.4 shows the dependence of the quadrupole frequency on the trap aspect ratio, for a given value of $\varepsilon^0_{dd}\lambda^{-1/6}$. This parameter is independent of the geometry of the gas (λ or κ) or its density, and is fixed by the species considered and the number of particles. For highly pancake traps the frequency should correspond to

the CL prediction, given by the upper (red) line in the figure. As the trap aspect ratio is decreased, at some point the attractive dipolar interactions will cause the gas to go to the superfluid phase, and the quadrupole frequency should drop abruptly to its HD value, given by the lower line (black) in the figure. This jump should be experimentally observable. Following Ref. [Bar04], for a gas containing $N = 10^6$ fermionic particles with $\varepsilon_{dd}^0 = 0.5$, the transition should take place at $\lambda \sim 4$: for larger trap parameters the gas would be collisionless, while for lower aspect ratios it should be superfluid. Notice however that from the point of view of the radial quadrupole mode, there is no way of distinguishing between the superfluid state and a normal gas in the collisional hydrodynamic regime.

Chapter 9

Conclusions and prospects

In this thesis we have studied the effects of the dipole-dipole interaction on the physics of ultracold quantum gases within a mean-field framework. We have focused mainly on dipolar condensates, in particular the effects of the anisotropy of the interaction on the ground state and on quantized vortex states, which are a clear manifestation of the superfluid nature of the quantum gas. In addition, we have found that in a toroidal geometry, for a certain configuration, the system becomes a self-induced Josephson junction when excited properly. We have also addressed ultracold fermionic gases and have analyzed the effect of the dipole-dipole interaction in the frequency of the radial quadrupole mode, both in the hydrodynamic and the collisionless regimes.

Chapter 1 has introduced the physical context in which this thesis is developed, giving the main related results in the literature. Also, an outline has been provided.

Chapters 2 and 3 have been devoted to summarize the theoretical (and briefly, experimental) framework underlying the results exposed in the subsequent chapters. In Chapter 2 we have discussed the mean-field approach to the physics of a Bose-Einstein condensate where the atoms interact both via s-wave contact and dipole-dipole interactions. We have described the interactions present in a dipolar condensate and have sketched the derivation of the Gross-Pitaevskii equation for this system. This equation constitutes the theoretical framework in which the results presented in this thesis (concerning Bose gases) are studied. Also we have given an overview of the Thomas-Fermi approximation both for contact and dipolar condensates.

In Chapter 3 we have reviewed some aspects of the physics of vortices in condensates. We have shown that a vortex in a superfluid presents a quantized velocity field around the axis of rotation. We have calculated the shape of the vortex core in some limiting cases, namely the non-interacting uniform gas, the non-interacting trapped condensate and the Thomas-Fermi regime. We have also discussed the experimental achievements concerning vortices most relevant for this thesis, and have given some hints as how to generate vortices numerically.

Chapter 4 has been devoted to the ground state of dipolar Bose-Einstein condensates confined in harmonic traps. The main results we have obtained are the following:

1. The anisotropy of dipolar interactions modifies the aspect ratio of the condensate compared to an s-wave condensate. In particular, in a pancake-shaped harmonic trap, when the magnetization axis is parallel to the trap symmetry axis, the gas is elongated in both directions of space (parallel and perpendicular to the trap axis), giving the net effect of increasing the condensate aspect ratio. For dipoles aligned perpendicularly to the trap symmetry axis, the anisotropic effects are so strong that can even invert the geometry of the cloud: a dipolar condensate in a pancake trap might become cigar shaped.

2. For certain trap aspect ratios and interaction strengths, biconcave density profiles appear, with the density away from the trap center. We have seen that these structures are a direct consequence of the specific shape of the mean-field dipolar potential, which shows a minimum away from the center.

3. We have derived the virial theorem for a dipolar condensate, by using the fact that the energy must be a minimum irrespective of scaling transformations of the wave function.

4. The dipolar interaction has an effect on the frequency of the collective modes (except for the dipole mode, which due to Kohn's theorem is unaffected by two-body interactions). In particular, the frequency of the radial (or surface) quadrupole mode is shifted to larger values, as predicted by the numerical simulation of the time-dependent Gross-Pitaevskii equation. Within the Thomas-Fermi approximation, however, the shift is always negative, giving rise to a frequency smaller than the hydrodynamic $\sqrt{2}\omega_\perp$ value. The difference between the two results is accounted for by the kinetic energy, which is neglected in Thomas-Fermi approach.

In Chapter 5 we have studied the effects of the dipole-dipole interaction on the properties of quantized vortex states in harmonically confined condensates. The results we have obtained can be summarized in the following list.

1. The anisotropy and long-range character of the dipolar interaction also show up in vortex states, affecting the structure of the vortex core and the critical frequency for vortex nucleation. Also, the nucleation energy barrier is slightly modified by the presence of dipolar interactions. Our results indicate that in rotating systems it is energetically easier to create vorticity in a dipolar condensate than in a condensate without dipolar interactions, for the same strength of the s-wave scattering length.

2. The dipolar interaction slows down the precession of off-centered vortices around the symmetry axis of the trap, compared to vortices in s-wave condensates.

Vortex states in a dipolar condensate are excited states of the system, and therefore are predicted to be less stable than the ground state. This means that the regions in the configuration space where vortices can exist are smaller than those where a stable condensate can form. The main channel of instability appears when the attractive part

of the dipole-dipole interaction for a certain density configuration becomes very strong, resulting in a single high density peak or in several high density peaks (this is sometimes referred to as "pencil-like" instability). For singly quantized vortices, the high density region appears around the vortex core created by the repulsive kinetic energy of the vortex. It might happen that the regions where a single vortex is unstable, a two-vortex state would be stable, since the associated density profile would not reach so high values. Simulations of the Gross-Pitaevskii equation predict this situation to be possible, indicating that the multiple vortex states are energetically stable. However, it remains to be seen if they would also be dynamically stable, and therefore become a possible situation to study in the experiments.

In Chapter 6 we have studied the effects induced by the anisotropic nature of the dipolar interaction in a Bose-Einstein condensate of chromium atoms in the case of a trapping potential with toroidal geometry. We have considered the magnetization axis (y) to be perpendicular to the trap symmetry axis (z) and we have analyzed the system for different scattering lengths. In this configuration, anisotropic effects are enhanced. The main results within this topic are the following.

1. For scattering lengths below the natural one ($a < 100\,a_B$), the density parts from the cylindrical symmetry of contact interactions and becomes inhomogeneously distributed along the toroidal potential, showing density peaks and saddle configurations as the azimuthal angle is varied. The density peaks form on the x-axis, where the net mean-field dipolar interaction is mainly attractive, while the saddle points are located on the y axis, where the interaction is mainly repulsive and the atoms are thus pushed away. The inhomogeneity in the density becomes stronger as the scattering length is reduced, and becomes especially important below $a = 30\,a_B$, which corresponds to the onset of the multiple connected geometry in our configuration.

2. For a low enough value of the scattering length ($a \sim 12\,a_B$) a dipolar-induced symmetry breaking phenomenon occurs: the atoms concentrate in only one of the density peaks, reminding thus of a cigar-shaped condensate parallel to the magnetization direction.

3. Accordingly to the inhomogeneous density structure, vortex velocity fields show a strong azimuthal dependence. Following a given constant radius along the torus, the absolute value of the velocity is smaller (larger) where the density shows a maximum (minimum), in the intersection with the x axis (y axis). Under this situation the expectation value of the z-component of the angular momentum is not quantized, and its reduction with respect to the non-dipolar system is an evidence of the presence of self-induced energy barriers.

Symmetry breakings in mean-field theory are known to be related to the existence of Schrödinger cat states in more quantum approaches (as, for instance, the Bose-Hubbard model). Whether a cat state would be sustained in a self-induced double-well potential is still unknown. On the other hand, the breaking of cylindrical symmetry caused by the dipolar interaction raises the question of how should the system be rotated. In the scheme

presented in this chapter, the system was non-rotating and vortices were obtained through phase imprinting. However, one can think of other interesting schemes. For instance, when the magnetic field is stationary while the trapping potential rotates, or when just the magnetic field is rotated. In the latter case one would expect a different behavior when the magnetic field is rapidly rotating or when it can be treated adiabatically. Notice however that the dynamical evolution would not be energy conserving.

In Chapter 7 we have introduced the concept of a dipolar self-induced bosonic Josephson junction. This junction is created by the anisotropic character of the dipolar interaction modulated by a toroidal trap, which gives rise to a ring-shaped, double-well effective potential. We have learned the following aspects of the physics of such a system.

1. It sustains both Josephson oscillations and a self-trapping regime, depending on the initial population imbalance between the two wells. The Josephson regime is quite robust against a modification of the scattering length, whereas self-trapping oscillations are far from the ideal sinusoidal-like shape and are therefore more sensitive to a change in the parameters.

2. There is qualitative agreement between a two-mode model applied to the junction and the results from the Gross-Pitaevskii equation, especially in the determination of the critical condition that separates Josephson orbits from self-trapped orbits.

3. We have performed a detailed analysis of self-trapping dynamics in the self-induced Josephson junction, especially focusing in the dynamics of the phase. We have seen that the coherent passage of a vortex and an antivortex across the two coupled junctions triggers the inversion of the flux of atoms in the minima of imbalance, where the phase difference reaches π. These results hint at a close relationship between the processes of self-trapping, AC Josephson effect and phase-slippage, and can serve to gain a deeper understanding of non-linear dynamics in bosonic Josephson junctions.

A question that arises in the Josephson junction scheme introduced here is how the system would behave for different couplings between the junctions. In the scheme proposed the two junctions act in phase, which in a more electronic sense means that they are connected in parallel. But they could also behave out of phase (with no need of carrying vorticity). Using an analogy with superconducting Josephson junctions, it might be interesting to see whether quantum coherence is maintained if the two junctions are different, for instance if one is larger than the other. In this case, coherence between vortices might or might not be preserved when the imbalance changes sign during the self-trapping evolution. Still in analogy with superconductors, an inviting question is whether the system formed by the two coupled self-induced Josephson junctions can be understood as the bosonic analog of the superconducting quantum interference device (SQUID). In such a device, the Josephson oscillations would be affected by a small external rotation of the setup (instead of a magnetic field), allowing for a precise determination of the rotation frequency.

In Chapter 8 we have addressed some aspects of the physics of ultracold dipolar Fermi gases. Concretely, the radial (or surface) quadrupole mode has been calculated within

mean-field theory, using a Thomas-Fermi-like density profile. We have considered both the hydrodynamic and collisionless regimes. The first can be reached either because of collisions (when they are so fast that they keep local equilibrium in the time scale provided by the oscillation) or because of coherence (in the superfluid regime). The main results we have found can be summarized in the following points:

1. By minimization of the action with respect to the parameters that characterize the quadrupole excitation, we have found the expressions for the frequency in the hydrodynamic and collisionless regimes. From these equations the frequency can be seen to depend on only two dimensionless parameters, which we call ε_{dd} and κ. The first one contains information about the strength of the dipole-dipole interaction with respect to the Fermi energy, while κ characterizes the deformation of the gas induced by the dipole force. The equation for hydrodynamic fermions has the same formal shape than that for bosons, provided the parameter ε_{dd} is accordingly defined.

2. In the hydrodynamic regime, dipolar interactions introduce a shift in the quadrupole frequency, in contrast to contact interactions. This shift is always negative in this model, giving a frequency smaller than in contact-interacting Fermi gases.

3. In the collisionless regime, dipolar interactions also have an effect on the frequency of the radial quadrupole mode, and introduce a large shift with respect to the non-interacting system. In contrast to the hydrodynamic regime, in the collisionless regime this shift is positive of negative depending on the geometry of the trap.

4. The shift in frequency is larger in the collisionless regime than in the hydrodynamic regime, and could be used experimentally to monitor the transition or the crossover between the two regimes. The phase transition would correspond to the collisionless to superfluid transition, while the crossover would take place between the collisionless and collisional hydrodynamic regimes of a degenerate Fermi gas.

An intriguing question about the physics of dipolar fermions is the dependence of the chemical potential on the density. Provided it is a potential function, $\mu \sim n^{\alpha}$, it remains to be understood what is the right exponent α. In the literature, the value $\alpha = 2/3$ has been widely used, its main motivation being the fact that dipolar interactions are treated as a perturbation to the density of the ideal gas. However, in a situation where the dipole force becomes dominant, this exponent could be different.

Appendix A

Imaginary time step method

The imaginary time step method (ITSM) is a numerical method of the family of relaxation methods used to find the ground state solution of a given Hamiltonian, H. In this appendix we derive the main expressions, and give details of the extra considerations implemented in the programs to make the algorithm more efficient.

Let us call $\{|\psi_n\rangle\}$ a basis set of non-dengenerate eigenfunctions of H. They fulfill the eigenvalue equation

$$H\,|\psi_n\rangle = E_n\,|\psi_n\rangle \ , \tag{A.1}$$

with E_n the energy corresponding the state $|\psi_n\rangle$. We denote the ground state as ψ_0 and the corresponding energy as E_0. E_0 is the smallest of the set of eigenvalues $\{E_n\}$. Given an arbitrary wave function $|\Phi\rangle$, its expansion in terms of the basis of H is given by

$$|\Phi\rangle = \sum_n \langle\psi_n|\Phi\rangle\,|\psi_n\rangle = \sum_n a_n\,|\psi_n\rangle \ . \tag{A.2}$$

The wave function $|\Phi\rangle$ evolves in time according to H. At a time t the time evolution will be given by the evolution operator, $U(t) = e^{-iHt/\hbar}$, as

$$|\Phi(t)\rangle = e^{-iHt/\hbar}\,|\Phi\rangle = e^{-iHt/\hbar}\sum_n a_n\,|\psi\rangle = \sum_n a_n e^{-iE_nt/\hbar}\,|\psi_n\rangle \ . \tag{A.3}$$

We now set the time t to be imaginary (whence the name of imaginary time method). We define a new time $\tau \in \mathbb{R}$ from $t = -i\hbar\tau$ and then we separate the summation over n in Eq. (A.3) into a term containing $n = 0$ and the summation over the rest. Notice that this introduction makes the operator in the exponential become non-unitary, which means that the norm will not in general be preserved. In terms of τ, Eq. (A.3) is rewritten as

$$|\Phi(\tau)\rangle = a_0 e^{-E_0\tau}\,|\psi_0\rangle + \sum_{n\neq 0} a_n e^{-E_n\tau}\,|\psi_n\rangle \ . \tag{A.4}$$

Since the energies (by definition) fulfill $E_0 < E_1 \cdots < E_n < \cdots$, in the limit $\tau \to \infty$ the contribution of the states with $n \neq 0$ will be exponentially killed. The ITSM is based on this fact, which can be stated as

$$\lim_{\tau\to\infty} |\Phi(\tau)\rangle \propto e^{-E_0\tau}\,|\psi_0\rangle \ . \tag{A.5}$$

Therefore, for an infinite time, the wave function converges to the ground state of the system. This is true for whatever initial wave function we are using, provided there is some non-zero component of the ground state, that is provided $a_0 \neq 0$ in Eq. (A.2).

To implement this method numerically, the algorithm is as follows:

(1) Start with an initial normalized guess function, $\phi^{(0)}$.

(2) Propagate it an imaginary time step $\delta\tau$ and build $\phi^{(1)} = e^{-H\delta\tau}\phi^{(0)}$. To first order in $\delta\tau$ we have

$$\phi^{(1)} \simeq \frac{(1 - H\delta\tau)\phi^{(0)}}{1 - E^{(0)}\delta\tau} \ , \tag{A.6}$$

where the denominator accounts for the normalization of $\phi^{(1)}$. We have introduced the energy corresponding to $\phi^{(0)}$,

$$E^{(0)} = \langle\phi^{(0)}|H|\phi^{(0)}\rangle \ . \tag{A.7}$$

(3) Repeat the process n times, with n large enough. At the end, the wave function and the energy will be given, respectively, by:

$$\phi^{(n+1)} = \frac{(1 - H\delta\tau)\phi^{(n)}}{1 - E^{(n)}\delta\tau} \tag{A.8}$$

$$E^{(n)} = \langle\phi^{(n)}|H|\phi^{(n)}\rangle \ . \tag{A.9}$$

For $n \to \infty$, $\phi^{(n)} \to \psi_0$, the ground state wave function. The imaginary time step, $\delta\tau$ has to be small enough to ensure the stability of the algorithm and to let the system evolve smoothly to its ground state, but large enough to make this process efficient. For Schrödinger-like problems, an estimation of the maximum $\delta\tau$ allowed is given by

$$\delta\tau_{\max} \simeq \frac{(\Delta x)^2}{4}\frac{2m}{\hbar^2} \ , \tag{A.10}$$

where Δx is the spacing of the spatial mesh on which the wave function is defined. For a 3D mesh, we can use the minimum grid step size.

In the case of the Gross-Pitaevskii equation, the eigenstate ψ_0 is given by the ground state condensate wave function, $\psi_{\rm gs}$. It is useful to write the eigenvalue equation as $(H - \mu)\Psi = \varepsilon\Psi$, where we have separated out the contribution of the ground state, μ, and where Ψ is still the non-converged wave function. This expression should converge to the state with $\varepsilon = 0$ and $\Psi = \psi_{\rm gs}$. Notice that in the GP Eq. (2.16) the eigenvalues are given by the chemical potential instead of the energy (see Chapter 2). Equation (A.8) is accordingly modified as

$$\Psi(\tau + \delta\tau) = \Psi(\tau) - \delta\tau(H - \mu)\Psi(\tau) \ , \tag{A.11}$$

where we have labeled the step n with the label τ for convenience. Also for convenience in what follows, the wave function at $\tau + \delta\tau$ is not normalized yet. Notice also that now the wave function is a function of four variables, $\Psi = \Psi(x, y, z; \tau)$. The imaginary time

propagation must be carried out for every one of the $n_x \times n_y \times n_z$ points of the spatial grid (with n_i the number of points in direction $i = x, y, z$).

In order to accelerate the convergence process, we have introduced two further features in Eq. (A.11) (see Ref. [Bar03]): a smoothing of the wave function and viscosity terms. The smoothing operation is performed as

$$\overline{\Delta\Psi}(x,y,z;\tau) = \frac{1}{2}\left\{\Delta\Psi(x,y,z) + \frac{1}{6}\left[\Delta\Psi(x-\Delta x,y,z) + \Delta\Psi(x+\Delta x,y,z) + \right.\right.$$
$$\left.\left. + \Delta\Psi(x,y-\Delta y,z) + \Delta\Psi(x,y+\Delta y,z) + \Delta\Psi(x,y,z-\Delta z) + \Delta\Psi(x,y,z+\Delta z)\right]\right\}, \tag{A.12}$$

where $\Delta\Psi(\tau) \equiv \Psi(\tau+\delta\tau) - \Psi(\tau)$. With this operation we can use a slightly higher $\delta\tau$ while keeping the numerical evolution stable. The wave function in the next step is then built as

$$\Psi(\tau+\delta\tau) = \Psi(\tau) + \overline{\Delta\Psi}(\tau) + \alpha_V[\Psi(\tau) - \Psi(\tau-\delta\tau)] \,, \tag{A.13}$$

with $\alpha_V = 0.7$, which characterizes the viscosity term. After this process the wave function has to be normalized.

The convergence of the solution to the ground state of the system is not easily assessed. A possibility is to track the energy change (or the change in chemical potential) between iterations. Since in general this quantity is small between two subsequent iterations, one can track the energy change every, say, 50 iterations and establish a "self-made" convergence criterion. When the energy change is very small (in our simulations, it is typically of the order of $10^{-10}E_{\rm tot}$, with $E_{\rm tot}$ the total energy) we say that the algorithm is converged and that we have found the ground state of H. Sometimes, if the energy of the ground state is very close to the energy of an excited state or the imaginary time step is large or there is some symmetry of the initial wave function that has to be broken, the algorithm can stay in a false minimum for an amount of time, looking as if it was already converged to the ground state (this is sometimes called a metastable solution). There are several possibilities to deal with this situation. One of them is to initialize the ITSM with a different trial function: from random numbers, from a particular shape (for instance, from a Thomas-Fermi profile in the case of BEC problems), etc. Another possibility is to reduce the imaginary time step or the grid spacing when the energy change between two iterations becomes smaller than some quantity. A third possibility is to leave the program running for a very long time. We have applied the first and third methods, which are easier to implement, in several of the calculations presented in the thesis. Sometimes the false minimum solution can be useful, as is the case of a centered vortex in a non-rotating condensate (see Chapter 6) or the asymmetric state of a double well potential (see Chapter 7).

Appendix B

Hamming's method: predictor-corrector-modifier

Hamming's algorithm comes from a family of iterative methods to numerically integrate ordinary differential equations (see, for instance, [Ral60]). They are known as predictor-corrector methods because at each step they make a sensible guess (or prediction) of the solution and correct it using the information contained in the differential equation. This process is repeated several times until a good convergence is found for this step. Some of the methods, such as Hamming's, add an intermediate step where a function, called modifier, is introduced to subtract the error caused by the predictor and the corrector. This allows one to eliminate the iterations, so that the differential equation is solved faster.

Let us assume we want to solve the differential equation

$$\frac{dy}{dx} = f(x, y) \ , \tag{B.1}$$

with the initial conditions given by $y(x_0) = y_0$ and $y'(x_0) = y'_0$. If there are more than one equations, the method works the same but now with y as a vector containing the different functions we want to find. We use the notation $y_n = y(x_n)$, $y'_n = y'(x_n)$ and $h = x_{n+1} - x_n$, where the index n numbers the iteration step. The iterative procedure is based on the general form

$$y_{n+1} = a_0 y_n + a_1 y_{n-1} + \cdots + a_p y_{n-p} + h(b_{-1} y'_{n+1} + b_0 y'_n + \cdots + b_p y'_{n-p}) + E_n \ , \tag{B.2}$$

where E_n is the error associated to step $n+1$. For a given p, the coefficients a_i and b_i are found by expanding each y_i and y'_i in a Taylor series in h around x_i. Equating the coefficients of $1, h, h^2, \ldots$ on both sides of Eq. (B.2) gives the value of a_i and b_i.

In the Hamming's algorithm the p value in Eq. (B.2) is equal to 3, that is the function at a certain iteration step is built from the value of the function and its first derivative in the previous four steps. Numerically, the solution to the differential Eq. (B.1) is found by applying the following four steps recursively:

(1) *Predictor*: give a prediction p_{n+1} of the solution at step $n+1$ using its value at steps n, $n-1$, $n-2$ and $n-3$,

$$p_{n+1} = y_{n-3} + \frac{4h}{3}(2y'_n - y'_{n-1} + 2y'_{n-2}) \ . \tag{B.3}$$

(2) *Modifier*: from the predicted solution p_{n+1} define a modifier function and its derivative as

$$m_{n+1} = p_{n+1} - \frac{112}{121}(p_n - c_n) \tag{B.4}$$

$$m'_{n+1} = f(x_{n+1}, m_{n+1}) \ . \tag{B.5}$$

(3) *Corrector*: use the modifier to define a corrector function

$$c_{n+1} = \frac{1}{8}\left[9y_n - y_{n-2} + 3h(m'_{n+1} + 2y'_n - y'_{n-1})\right] \ . \tag{B.6}$$

(4) *Final Value*: write the function at step $n+1$ as

$$y_{n+1} = c_{n+1} + \frac{9}{121}(p_{n+1} - c_{n+1}) \ . \tag{B.7}$$

Notice that this algorithm requires the knowledge of the functions at steps 0, -1, -2 and -3 to calculate the first iteration, y_1, which means that the Hamming's method is not self-starting. This is usually arranged by using another numerical method, such as the fourth-order Runge-Kutta method (see Appendix C), which is self-starting. Then, the first three time steps are evaluated using the Runge-Kutta method and they are then used in the Hamming's method to evaluate the fourth and subsequent steps. The error associated to Hamming's method is given by the truncation error,

$$E_{n+1} = c_{n+1} - p_{n+1} = \frac{121}{360}h^5 y^{(5)}(\xi) \ , \tag{B.8}$$

where ξ is a value of x in the interval $[x_n, x_{n+1}]$. This error comes from truncating the Taylor series at order h^4, and therefore is of order h^5. If this error grows very much, the numerics becomes unstable and no solution is found. To control E_{n+1}, the step h must be small enough.

Comparing Eq. (B.1) with the TDGP Eq. (2.12) we can identify: $y \to \Psi(\mathbf{r}, t)$, $x \to t$ and

$$f(x, y) \to -\frac{i}{\hbar}\left[-\frac{\hbar^2}{2m}\nabla^2\Psi + V_{\text{ext}}\Psi + g|\Psi|^2\Psi + V_{\text{dip}}\Psi\right] \ . \tag{B.9}$$

The step $h \to \delta t$ is the time step of the numerical simulation. For the simulations carried out in this thesis, the time step of the Hamming's algorithm is typically $\delta t \sim 10^{-6} - 10^{-7}$ s, which gives an error of the order of $E_{n+1} \sim 10^{-12}\,\mu\text{m}^{-3/2}$. On the other hand, since there are no dissipation terms, the energy and the number of particles must be conserved, which gives a measure of the "relative error" associated with the code in a particular implementation. In the calculations presented here, the errors in the energy and the number of particles were less than $5 \times 10^{-3}\,\%$ and $10^{-5}\,\%$ with respect to their initial values. Notice that the time evolution of the wave function requires an extra consideration since Ψ is defined in a three dimensional grid (it is therefore a complex matrix of dimension $n_x \times n_y \times n_z$). The process detailed in (B.3)–(B.7) has to be applied at every point of the grid. This means that p_{n+1}, m_{n+1}, c_{m+1} and their derivatives are themselves matrices of

dimension $n_x \times n_y \times n_z$. The algorithm therefore requires that we keep in memory many big matrices. This makes the simulations very time-consuming, especially if the Fourier transforms associated with the dipolar mean-field potential $V_{\rm dip}$ are computed. To give an example, to calculate the Josephson oscillations in Chapter 7 (Fig. 7.3) the simulation ran for about a week with a Xeon processor, with a spatial grid of $128 \times 128 \times 96$ points.

Appendix C

Fourth-order Runge-Kutta method

Runge-Kutta methods are a family of numerical methods that are used to solve differential equations. They use the function and its first derivatives calculated at a given step to find the solution at the next step. The idea is to solve the set of n differential equations

$$\frac{dy_i}{dx} = y_i'(x) = f_i(y_0(x), y_1(x), \ldots, y_n(x)), \qquad i = 1, \ldots, n \tag{C.1}$$

where for convenience we call $y_0(x) = x$, which gives $y_0'(x) = 1$. The initial conditions are given by the values $y_i(x_0) = y_{i0}$, for $i = 1, \ldots, n$. The idea behind the method is to find the values $y_i(x_0 + h)$, where h is a (small) increment in x. This is done by approximating the functions y_i to their Taylor expansion

$$y_i(x_0 + h) = y_i(x_0) + h y_i'(x_0) + \frac{h^2}{2!} y_i^{(2)}(x_0) + \cdots \ , \tag{C.2}$$

where higher than first-order derivatives are calculated by evaluating several first-order derivatives. In the fourth-order Runge-Kutta method four first-order derivatives are used in the expansion to obtain an agreement of order h^4 with the Taylor series.

The algorithm consists of the following steps (see for instance [Ral60])

(1) Set $j = 1$.

(2) Calculate for $i = 0, 1, \ldots, n$:

$$y_{ij}' = k_{ij} = f_i(y_{0,j-1}, y_{1,j-1}, \ldots, y_{n,j-1}) \ . \tag{C.3}$$

(3) Calculate for $i = 0, 1, \ldots, n$:

$$y_{ij} = y_{i,j-1} + h[a_j(k_{ij} - b_j q_{i,j-1})] \tag{C.4}$$

$$q_{ij} = q_{i,j-1} + 3[a_j(k_{ij} - b_j q_{i,j-1}) - c_j k_{ij}] \ . \tag{C.5}$$

Initially, $q_{i0}(x_0) = 0$ for all i. At the next steps of the solution, $q_{i0}(x + h) = q_{i4}(x)$. The constants a_j, b_j and c_j are

$a_1 = \frac{1}{2}$	$b_1 = 2$	$c_1 = \frac{1}{2}$
$a_2 = 1 - \sqrt{\frac{1}{2}}$	$b_2 = 1$	$c_2 = 1 - \sqrt{\frac{1}{2}}$
$a_3 = 1 + \sqrt{\frac{1}{2}}$	$b_3 = 1$	$c_3 = 1 + \sqrt{\frac{1}{2}}$
$a_4 = \frac{1}{6}$	$b_4 = 2$	$c_4 = \frac{1}{2}$

(4) Repeat steps (2) and (3) for $j = 2, 3, 4$.

At the end of this process the solution is given by $y_i(x+h) = y_{i4}(x)$. This value is used as initial value for the next step, that is $y_{i4}(x) \to y_{i0}(x')$, which after the process (1)–(4) will give the result $y_i(x'+h) = y_{i4}(x')$, where we have introduced the notation $x' = x+h$ for the sake of clarity. This process is repeated until the function $y(x)$ is found in the interesting range of x. In contrast to the Hamming's algorithm (Appendix B), Runge-Kutta methods are self-starting, since only the values at the previous point are needed. However, since it requires the evaluation of the derivatives at each step, it can be time-consuming.

In the results presented, this Runge-Kutta method has been routinely used to initialize the Hamming's algorithm and also to solve the two coupled equations for the two-mode model of a Josephson junction. In the first case, the equation that has to be solved is the TDGP Eq. (2.12). It is only one equation, so $n = 1$ in this case. We can identify the generic variables used above as $x \to t$, $y_1 \to \Psi(\mathbf{r}, t)$ and

$$f_1(y_0, y_1) \to -\frac{i}{\hbar}\left[-\frac{\hbar^2}{2m}\nabla^2\Psi + V_{\text{ext}}\Psi + g|\Psi|^2\Psi + V_{\text{dip}}\Psi\right] , \tag{C.6}$$

with $y_0 = t$. Notice that, as happened in the Hamming's algorithm, the wave function is defined in a three-dimensional mesh of $n_x \times n_y \times n_z$ points, which means that the whole Runge-Kutta process has to be performed in every mesh point.

In the case of the two-mode equations (see Chapter 7), we have two equations so $n = 2$. We can identify $x \to t$, $y_1 \to Z(t)$, $y_2 \to \phi(t)$ and

$$f_1(y_0, y_1, y_2) \to (-1+\alpha)\sqrt{1-Z^2}\sin\phi + \varepsilon(1-Z^2)\sin 2\phi \tag{C.7}$$

$$f_2(y_0, y_1, y_2) \to \Lambda Z - (-1+\alpha)\frac{Z}{\sqrt{1-Z^2}}\cos\phi - \varepsilon Z\cos 2\phi , \tag{C.8}$$

for the full two-mode model and the corresponding expressions (with $\alpha = \varepsilon = 0$) for the crude two-mode model. The initial conditions are given by $y_{1,0} \to Z(0)$ and $y_{2,0} \to \phi(0)$. In this case, we do not need to define any spatial mesh, which makes the algorithm very fast.

Appendix D

GP equations from the quantum action and the energy functional

In Chapter 2 we have derived the Gross-Pitaevskii equation from the many-body Hamiltonian, using the second quantization formalism and performing a mean-field approximation there. The Gross-Pitaevskii equation is therefore semiclassical. In this appendix we discuss an alternative way to arrive at the time-dependent and stationary Gross-Pitaevskii Eqs. (2.12) and (2.16), which is via a variational procedure applied to the action and the energy functional, respectively.

D.1 Quantum action and TDGP equation

To obtain time-dependent properties of a quantum system one considers the quantum action, defined by

$$S = \int dt \left\langle \Phi \left| H - i\hbar \frac{\partial}{\partial t} \right| \Phi \right\rangle \ , \tag{D.1}$$

where H is the many-body Hamiltonian, see Eq. (2.1). Note that there are two terms entering the action. The first of them, $\langle \Phi | H | \Phi \rangle$ is related to the energy of the system at time t. The second term on the right-hand side, $\langle \Phi | - i\hbar \partial_t | \Phi \rangle$, will give us the time dependence of the wave function. In this expression Φ is the many-body wave function of the bosonic system, defined from the single-particle wave functions, φ_0, as

$$\Phi(\mathbf{r}_1, \mathbf{r}_2, \ldots, \mathbf{r}_N, t) = \varphi_0(\mathbf{r}_1, t)\varphi_0(\mathbf{r}_2, t) \cdots \varphi_0(\mathbf{r}_N, t) \ , \tag{D.2}$$

where we assume that all particles occupy the ground state. The bracket in Eq. (D.1) is the Lagrangian density, $\mathcal{L}(t)$, and in terms of single-particle wave functions it reads

$$\begin{aligned} \mathcal{L}(t) = \int \mathrm{d}\mathbf{r_1} \mathrm{d}\mathbf{r_2} \cdots \mathrm{d}\mathbf{r_N} \prod_{k=1}^{N} \varphi_0^*(\mathbf{r}_k, t) \left[\sum_{i=1}^{N} -\frac{\hbar^2}{2m} \nabla_i^2 + \sum_{i=1}^{N} V_{\mathrm{ext},i} + \frac{1}{2} \sum_{i,j=1}^{N} v_{\mathrm{int},ij} \right] \prod_{l=1}^{N} \varphi_0(\mathbf{r}_l, t) - \\ - i\hbar \int \mathrm{d}\mathbf{r_1} \mathrm{d}\mathbf{r_2} \cdots \mathrm{d}\mathbf{r_N} \prod_{k=1}^{N} \varphi_0^*(\mathbf{r}_k, t) \left[\frac{\partial}{\partial t} \prod_{l=1}^{N} \varphi_0(\mathbf{r}_l, t) \right] \ , \end{aligned} \tag{D.3}$$

which can be integrated to give

$$\mathcal{L}(t) = -\frac{\hbar^2 N}{2m}\int \mathrm{d}\mathbf{r}\,\varphi_0^*(\mathbf{r},t)\nabla^2\varphi_0(\mathbf{r},t) + N\int \mathrm{d}\mathbf{r}\,\varphi_0^*(\mathbf{r},t)V_{\mathrm{ext}}(\mathbf{r})\varphi_0(\mathbf{r},t) + \\ + \frac{N(N-1)}{2}\int \mathrm{d}\mathbf{r}\,\mathrm{d}\mathbf{r}'\,\varphi_0^*(\mathbf{r},t)\varphi_0^*(\mathbf{r}',t)v_{\mathrm{int}}(\mathbf{r},\mathbf{r}')\varphi_0(\mathbf{r},t)\varphi_0(\mathbf{r}',t) - \\ - i\hbar N\int \mathrm{d}\mathbf{r}\,\varphi_0^*(\mathbf{r},t)\frac{\partial\varphi_0(\mathbf{r},t)}{\partial t}\ . \tag{D.4}$$

If the number of particles in the condensate is very large, $N(N-1) \simeq N^2$. Let us then write the action in terms of the condensate wave function. This just means changing $\sqrt{N}\varphi_0(\mathbf{r},t)$ by $\Psi(\mathbf{r},t)$, so that the factors N disappear. To obtain the equations of motion we set the variations of the action with respect to Ψ^* or Ψ to zero, that is

$$\frac{\delta S}{\delta\Psi^*} = \frac{\delta}{\delta\Psi^*}\left[\int \mathrm{d}t\,\mathcal{L}(t)\right] = 0\ , \tag{D.5}$$

and analogously for Ψ. Proceeding in this way gives

$$\delta S = \int \mathrm{d}t\int \mathrm{d}\mathbf{r}\left\{-\frac{\hbar^2}{2m}\nabla^2\Psi(\mathbf{r},t) + V_{\mathrm{ext}}(\mathbf{r})\Psi(\mathbf{r},t) + \right. \\ \left. + \left[\int \mathrm{d}\mathbf{r}'\,\Psi^*(\mathbf{r}',t)v_{\mathrm{int}}(\mathbf{r},\mathbf{r}')\Psi(\mathbf{r}',t)\right]\Psi(\mathbf{r},t) - i\hbar\frac{\partial\Psi(\mathbf{r},t)}{\partial t}\right\}\delta\Psi^*(\mathbf{r},t) = 0\ . \tag{D.6}$$

This must be zero irrespective of the shape of $\delta\Psi^*(\mathbf{r},t)$, since the action must always be a minimum. This leads us then to Eq. (2.10),

$$i\hbar\frac{\partial}{\partial t}\Psi(\mathbf{r},t) = \left[-\frac{\hbar^2}{2m}\nabla^2 + V_{\mathrm{ext}}(\mathbf{r}) + \int \mathrm{d}\mathbf{r}'\,\Psi^*(\mathbf{r}',t)v_{\mathrm{int}}(\mathbf{r},\mathbf{r}')\Psi(\mathbf{r}',t)\right]\Psi(\mathbf{r},t)\ . \tag{D.7}$$

Using Eq. (2.11) for v_{int} we find the TDGP Eq. (2.12).

D.2 Energy functional and GP equation

In order to find the stationary GP equation, we need to impose that the energy is a minimum, while conserving the number of particles. This is done by applying the variational procedure

$$\frac{\delta}{\delta\psi^*}\left[E[\psi,\psi^*] - \mu\int \mathrm{d}\mathbf{r}\,\psi^*(\mathbf{r})\psi(\mathbf{r})\right] = 0\ , \tag{D.8}$$

where $E[\psi,\psi^*]$ is the energy functional and μ is the Lagrange multiplier we use to impose the constraint that the number of particles is conserved. The integral is just equal to N for the solutions of the variational equation and μ is the chemical potential. The energy functional is defined as

$$E[\psi,\psi^*] = \langle\Phi\,|\,H\,|\,\Phi\rangle = \int \mathrm{d}\mathbf{r}\left\{-\frac{\hbar^2}{2m}\psi^*(\mathbf{r})\nabla^2\psi(\mathbf{r}) + \psi^*(\mathbf{r})V_{\mathrm{ext}}(\mathbf{r})\psi(\mathbf{r}) + \right. \\ \left. + \frac{1}{2}\psi^*(\mathbf{r})\left[\int \mathrm{d}\mathbf{r}'\,\psi^*(\mathbf{r}')v_{\mathrm{int}}(\mathbf{r},\mathbf{r}')\psi(\mathbf{r}')\right]\psi(\mathbf{r})\right\}\ . \tag{D.9}$$

Taking variations and imposing that the energy must be a minimum irrespective of $\delta\psi^*$, we find

$$-\frac{\hbar^2}{2m}\nabla^2\psi(\mathbf{r})+V_{\rm ext}(\mathbf{r})\psi(\mathbf{r})+\left[\int \mathrm{d}\mathbf{r}'\,\psi^*(\mathbf{r}')v_{\rm int}(\mathbf{r},\mathbf{r}')\psi(\mathbf{r}')\right]\psi(\mathbf{r})=\mu\psi(\mathbf{r})\ . \qquad \text{(D.10)}$$

For the contact plus dipole-dipole interaction potential, Eq. (2.11), we recover the time-independent GP Eq. (2.16). If variations are taken with respect to ψ instead of ψ^*, we find the same equation but for ψ^* instead of ψ.

The energy functional $E[\psi,\psi^*]$ is sometimes treated as a functional of the density, $E[n]$. This is exact for the ground state of the Bose-Einstein condensate, for which ψ is real (except for an arbitrary phase) and $n=\sqrt{\psi}$. In this case the functional (D.9) can be written as

$$E[n]=\int \mathrm{d}\mathbf{r}\left\{\frac{\hbar^2}{2m}\left[\nabla\sqrt{n(\mathbf{r})}\right]^2+V_{\rm ext}(\mathbf{r})n(\mathbf{r})+\frac{1}{2}n(\mathbf{r})\left[\int \mathrm{d}\mathbf{r}'\,v_{\rm int}(\mathbf{r},\mathbf{r}')n(\mathbf{r}')\right]\right\}\ , \qquad \text{(D.11)}$$

and Eq. (2.16) can be found by varying with respect to n.

The energy functional theory is a variational theory, and therefore it provides an upper bound to the real energy (see, for instance, the book by Lipparini, Ref. [Lip03], for a complete discussion of the density functional theory, or DFT). Since the variations are taken with respect to the whole of the wave function, instead of some free parameters, it is sometimes said that it is equivalent to varying with respect to an infinite number of parameters.

Appendix E

Quantum harmonic oscillator

As we have seen during the thesis, the harmonic oscillator confinement is very important, both for Bose and Fermi systems. Non-interacting (ideal) condensates and degenerate Fermi gases are an important limiting case that can be reached experimentally. They constitute the ground state of a many-body quantum harmonic oscillator, which is in itself one of the most important and well-known models of physical systems. For the sake of completeness we devote this Appendix to the quantum harmonic oscillator. We start with the single particle case in 3D and then we build the ground state many-body states, both for bosons (condensate) and for fermions (using the local-density approximation).

E.1 Single-particle harmonic oscillator

The properties of a quantum particle confined in a harmonic trap are given by the harmonic oscillator Hamiltonian

$$\hat{h} = \frac{\hat{\mathbf{p}}^2}{2m} + \frac{1}{2}m(\omega_x^2\hat{x}^2 + \omega_y^2\hat{y}^2 + \omega_z^2\hat{z}^2) \ , \tag{E.1}$$

with m the mass of the particle, ω_k the trapping frequencies along the axes $k = x, y, z$, and $\hat{\mathbf{p}}^2 = \hat{p}_x^2 + \hat{p}_y^2 + \hat{p}_z^2$ the square of the linear momentum operator. Notice the hat symbol in the operators, which we have added to avoid any ambiguity. The momentum operators, $\hat{p}_k = -i\hbar\nabla_k$, do not commute with the position operators, but $[\hat{p}_k, \hat{r}_k] = -i\hbar$. Hamiltonian (E.1) satisfies the eigenvalue equation

$$\hat{h}\,|\varphi_n\rangle = e_n\,|\varphi_n\rangle \ \ , \tag{E.2}$$

where $\{|\varphi_n\rangle\}$ is the set of eigenstates of $\hat{h}$, characterized by the set of quantum numbers n, and e_n is the energy corresponding to state $|\varphi_n\rangle$.

There are several ways of solving the ground state of the quantum harmonic oscillator. A very elegant way is by introducing the creation and annihilation operators[1], as is done

[1]More than *creation* and *annihilation* operators, $\hat{a}^\dagger$ and $\hat{a}$ should be at this stage called *raising* and *lowering* operators, since their effect is to raise a particle to a higher state and to lower it to a lower state, respectively. Here we are dealing with a one-particle "gas". However, when a many-particle gas is considered, for instance in second quantization, these same operators have the meaning of adding or

in Ref. [Coh77]. For every direction r_k (with $r_x = x$, etc.) they are defined through $\hat{r}_k$ and $\hat{p}_k$ as

$$\hat{a}_k^\dagger = \frac{1}{\sqrt{2}} \left[\frac{1}{a_k} \hat{r}_k - i \frac{a_k}{\hbar} \hat{p}_k \right] \tag{E.3}$$

$$\hat{a}_k = \frac{1}{\sqrt{2}} \left[\frac{1}{a_k} \hat{r}_k + i \frac{a_k}{\hbar} \hat{p}_k \right] \ , \tag{E.4}$$

where we have introduced the harmonic oscillator length in each direction, $a_k = \sqrt{\hbar/(m\omega_k)}$. The creation and annihilation operators satisfy the commutation relations $[\hat{a}_k, \hat{a}_{k'}^\dagger] = \delta_{kk'}$ and zero for all the other commutators. In terms of these operators, the Hamiltonian takes the well-known form

$$\hat{h} = \sum_{k=x,y,z} \hbar\omega_k \left(\hat{a}_k^\dagger \hat{a}_k + \frac{1}{2} \right) \ . \tag{E.5}$$

The ground state of this Hamiltonian has energy

$$e_0 = \frac{1}{2} \hbar(\omega_x + \omega_y + \omega_z) \ . \tag{E.6}$$

Since the Hamiltonian can be decomposed in independent terms that depend each on only one variable, $|\varphi_0\rangle$ can be written as $|\varphi_0\rangle \equiv |X\rangle\,|Y\rangle\,|Z\rangle$. An equation for the ground state wave function can be found by multiplying both sides of Eq. (E.4) by $|\varphi_0\rangle$ and recalling that $\hat{a}\,|\varphi_0\rangle = 0$. In coordinate representation, that is multiplying the equation by $\langle \mathbf{r}| \equiv \langle x|\,\langle y|\,\langle z|$, we find

$$\frac{1}{a_k^2} \langle \mathbf{r}|\, \hat{r}_k\, |\varphi_0\rangle + i \frac{1}{\hbar} \langle \mathbf{r}|\, \hat{p}_k\, |\varphi_0\rangle = 0 \ , \tag{E.7}$$

with $k = x, y, z$. This leads to three first-order differential equations. They are identical so we will only solve it for, say, $X(x) \equiv \langle x|X\rangle$:

$$\frac{\mathrm{d}X}{\mathrm{d}x} + \frac{x}{a_x^2} X = 0 \ . \tag{E.8}$$

Now the solution to this is straightforward,

$$\mathrm{d}\ln(X) = -\frac{x}{a_x^2}\,\mathrm{d}x \quad \Rightarrow \quad X(x) = C(y,z) \exp\left[-\frac{x^2}{2a_x^2} \right] \ . \tag{E.9}$$

Taking into account the solution in the other directions we find

$$\varphi_0(\mathbf{r}) = C \exp\left[-\frac{x^2}{2a_x^2} - \frac{y^2}{2a_y^2} - \frac{z^2}{2a_z^2} \right] \ , \tag{E.10}$$

subtracting a particle from a given state. This double interpretation of $\hat{a}^\dagger$ and $\hat{a}$ allows us thus to keep the words *creation* and *annihilation*. Notice also that in the single-particle case $\hat{a}^\dagger$ and $\hat{a}$ obey commutation relations, irrespective of the bosonic or fermionic character of the particle; this will not be the case for the N-particle gas, especially for fermions (see for instance Ref. [Lip03] for more details).

where C is a constant to be determined by normalization. Imposing that the wave function has to be normalized to unity, $\int \mathrm{d}\mathbf{r}|\varphi_0|^2 = 1$, we finally find

$$\varphi_0(\mathbf{r}) = \left(\frac{1}{\pi a_{\mathrm{ho}}^2}\right)^{3/4} \exp\left[-\frac{x^2}{2a_x^2} - \frac{y^2}{2a_y^2} - \frac{z^2}{2a_z^2}\right] , \tag{E.11}$$

where $a_{\mathrm{ho}} = \sqrt{\hbar/(m\omega_{\mathrm{ho}})}$ is the harmonic oscillator length, and $\omega_{\mathrm{ho}} = (\omega_x\omega_y\omega_z)^{1/3}$ is the geometric mean of the frequencies. The ground state wave function of the harmonic oscillator is thus a Gaussian with mean width a_{ho}.

E.2 The ideal quantum gas in a harmonic trap

An ideal gas is one where its components do not interact with each other. The many-body Hamiltonian of an ideal gas confined in a harmonic trap is

$$H = \sum_{i=1}^{N} \frac{\mathbf{p}_i^2}{2m} + \sum_{i=1}^{N} \frac{1}{2}m(\omega_x^2 x_i^2 + \omega_y^2 y_i^2 + \omega_z^2 z_i^2) = \sum_{i=1}^{N} h_i \ , \tag{E.12}$$

where h_i represents the single-particle Hamiltonian acting on particle i. The set of eigenstates of h, $\{|\varphi_k\rangle\}$, defines a basis of the one-body Hilbert space. In this case, the many-body states are defined in a Hilbert space which is the product of one-body Hilbert spaces. The many-body wave functions can therefore be written as linear combinations of products of single-particle wave functions. These products need to have the right symmetry properties: bosons require symmetric many-body wave functions (no sign appears under exchange of two particles) whereas fermions require antisymmetric many-body wave functions (a sign appears under exchange of two particles). Both ideal Bose and Fermi gases are important limiting cases of the real gases that can be achieved experimentally, and also provide a useful limit for theoretical analysis.

E.2.1 Ground state of a harmonically confined ideal Bose gas

For an ideal Bose gas of N particles, the ground state configuration consists on all the particles occupying one (the lowest) single-particle state, $|\varphi_0\rangle$. The many-body state is then defined as a direct product of N single-particle wave functions,

$$|\Phi_0\rangle = |\varphi_0\rangle \otimes |\varphi_0\rangle \otimes \cdots \otimes |\varphi_0\rangle \ . \tag{E.13}$$

The energy corresponding to the many-body state (E.13) is $E_0 = Ne_0$, where e_0 is the energy of the state φ_0. The excited states of the non-interacting Bose system are given by

$$\Psi_B(\mathbf{r}_1, \mathbf{r}_2, \ldots, \mathbf{r}_N) = \sqrt{\frac{n_1!\, n_2! \cdots}{N!}} \sum_P P \prod_{i=1}^{N} \varphi_{k_i}(\mathbf{r}_i) \ , \tag{E.14}$$

where n_k is the occupation number of state k (that is, the number of times the wave function φ_k appears in the product), the operator P indicates permutations of the indices

and k_i represents the quantum number of the state occupied by particle i. The numerical factor in front arises from the indistinguishability of the particles, and the operator P ensures that the wave function is properly symmetrized: the interchange of two particles should leave the many-body wave function unchanged, that is it has to be symmetric.

In coordinate representation the condensate wave function of the non-interacting gas, $\Psi_0(\mathbf{r})$, is given by

$$\Psi_0(\mathbf{r}) = \sqrt{N}\left(\frac{1}{\pi a_{\rm ho}^2}\right)^{3/4} \exp\left[-\frac{x^2}{2a_x^2} - \frac{y^2}{2a_y^2} - \frac{z^2}{2a_z^2}\right] \tag{E.15}$$

and it is normalized to the total number of particles. In the left panel of Fig. E.1 $\Psi_0(\mathbf{r})$ is shown for the isotropic harmonic oscillator (with $N = 10^6$). It corresponds to a Gaussian of width given by $a_{\rm ho}$, which was the solution to the single-particle case, since the many-body wave function is the product of identical single-particle wave functions. This is equivalent to saying that the lowest lying single-particle state is macroscopically occupied, which is the definition of a condensate. This state corresponds to the Bose-Einstein condensate predicted by Bose and Einstein in 1925.

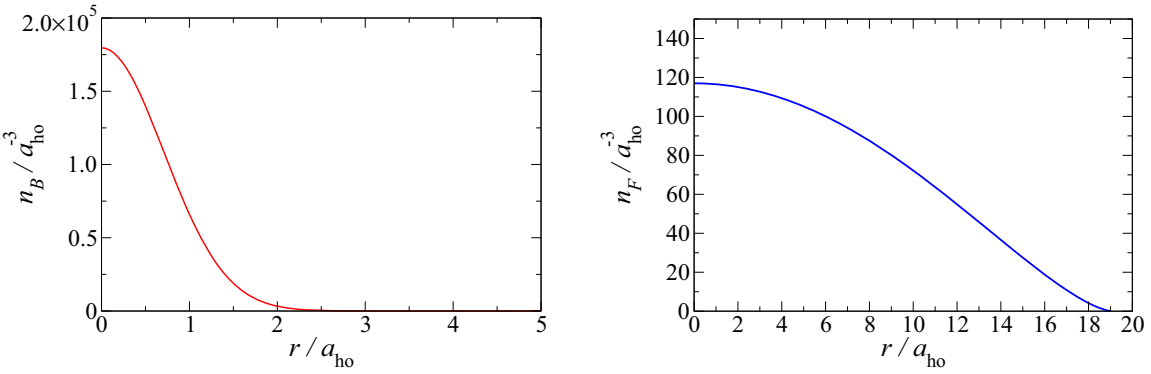

Figure E.1: Density profiles of the ground state of a non-interacting Bose gas (left) and of a non-interacting Fermi gas in the Thomas-Fermi approximation (right) confined in a isotropic harmonic oscillator potential. In both cases $N = 10^6$.

E.2.2 Ground state of a harmonically confined Fermi gas

In the case of non-interacting (or ideal) fermions the Pauli exclusion principle prevents two identical particles to be in the same state, and therefore the ground state consists on a particle occupying each state up to an energy ϵ_F, called the Fermi energy (see Chapter 8). The solution to the non-interacting Fermi gas confined in a harmonic potential, $\Psi_F(\mathbf{r}_1, \mathbf{r}_2, \ldots, \mathbf{r}_N) \equiv \Psi_F$ is in general complicated, since it is given by the Slater determinant

$$\Psi_F = \frac{1}{\sqrt{N!}} \sum_P (-1)^P P \prod_{i=1}^{N} \varphi_{k_i}(\mathbf{r}_i) = \frac{1}{\sqrt{N!}} \begin{vmatrix} \varphi_{k_1}(\mathbf{r}_1) & \varphi_{k_1}(\mathbf{r}_2) & \cdots & \varphi_{k_1}(\mathbf{r}_N) \\ \varphi_{k_2}(\mathbf{r}_1) & \varphi_{k_2}(\mathbf{r}_2) & \cdots & \varphi_{k_2}(\mathbf{r}_N) \\ \vdots & \vdots & \ddots & \vdots \\ \varphi_{k_N}(\mathbf{r}_1) & \varphi_{k_N}(\mathbf{r}_2) & \cdots & \varphi_{k_N}(\mathbf{r}_N) \end{vmatrix},$$

where the permutation operator P ensures the right symmetrization (in this case, the many body wave function must be antisymmetric under the exchange of two fermions). The ground state is obtained by setting the states φ_{k_i} to be the N lowest energy states.

As the number of particles in the gas grows, working in terms of a Slater determinant becomes very hard. If the number of particles is large enough, though, one can use a semiclassical approximation called the *local-density approximation* (see, for instance, Ref. [Gio08]). It relies on the consideration that if the potential is slowly varying in space, the energy levels of the system form a continuum and do not affect the equation of state of the gas. The condition that the potential is slowly varying in space can be stated as $a_{\rm ho} \gg 1/k_F$, that is the length scale associated to variations in the density of the gas, $1/k_F$, is much smaller than the length scale of variations in the confining harmonic potential, $a_{\rm ho}$. It can be easily seen that this condition is equivalent to $\hbar\omega_{\rm ho} \ll \epsilon_F$, which can be interpreted as a quasi-continuum spectrum of the harmonic oscillator energy states, $\hbar\omega_{\rm ho}$, in comparison to the energy scale provided by the Fermi energy. Under these conditions, the kinetic energy density[2] can be taken to be the one of the uniform system (see Chapter 8),

$$\tau(n) = \frac{3}{5}\frac{\hbar^2}{2m}(6\pi^2)^{2/3}n^{2/3} \ . \tag{E.17}$$

With this approximation, the density is given by[3]

$$n(\mathbf{r}) = \frac{1}{6\pi^2}\left(\frac{\mu - V_{\rm ho}(\mathbf{r})}{\hbar^2/2m}\right)^{3/2} = \frac{8}{\pi^2}\frac{N}{R^3}\left(1 - \frac{r^2}{R^2}\right)^{3/2} \ , \tag{E.19}$$

where μ is the chemical potential, which can be seen to be $\mu = (6N)^{1/3}\hbar\omega_{\rm ho}$ from the normalization of the density to N. Since the system is still ideal and we are at $T = 0$, we have $\mu = \epsilon_F$. Notice that we have assumed an isotropic harmonic oscillator of frequency $\omega_{\rm ho}$, which allows us to define the Thomas-Fermi radius, $R = \sqrt{2\mu/(m\omega_{\rm ho}^2)}$. The right panel of Fig. E.1 shows the density distribution of the trapped ideal Fermi gas with $N = 10^6$, which can be compared to that of the equivalent Bose gas (left panel). It can be clearly seen that the Fermi energy behaves as a strong repulsive potential, pushing the atoms away from the center. The extent of the Fermi gas at $T = 0$ is several times larger than the corresponding Bose gas, and the central density is much lower. The quantity

$$\mu(\mathbf{r}) = \mu - V_{\rm ho}(\mathbf{r}) = \frac{\hbar^2}{2m}(6\pi^2)^{2/3}n^{2/3} \tag{E.20}$$

[2]The kinetic energy density, $\tau(n)$, is defined such that its integration in space gives the total energy of an ideal, uniform Fermi gas, that is

$$\frac{E}{N} = \int \tau(n)\, n \, \mathrm{d}\mathbf{r} = \frac{3}{5}\,\epsilon_F \ . \tag{E.16}$$

[3]This can be shown by taking variations of the energy functional with respect to n and setting them to zero,

$$\frac{\delta}{\delta n}\left[\int \tau(n) n \mathrm{d}\mathbf{r} + \int V_{\rm ho}(\mathbf{r}) n \mathrm{d}\mathbf{r} - \mu \int n \mathrm{d}\mathbf{r}\right] = 0 \ , \tag{E.18}$$

where μ is a Lagrange multiplier introduced to keep the number of particles constrained to N.

can be interpreted as a local chemical potential. The local-density approximation, in a way, tells us that the chemical potential of the confined ideal Fermi gas is *locally* the chemical potential of a corresponding uniform system. The local-density approximation is usually referred to as the Thomas-Fermi approximation.

Appendix F

Two-mode equations for a dipolar Josephson junction

Josephson oscillations in a double-well dBEC can be effectively studied by means of a two-mode model (TMM). The basic assumption underlying this method is that the wave function of the condensate $\Psi(\mathbf{r},t)$ can be expressed in terms of the wave functions of the modes localized in the left and right wells, respectively $\Phi_L(\mathbf{r})$ and $\Phi_R(\mathbf{r})$, using ansatz Eq. (7.6),

$$\Psi(\mathbf{r},t) = \psi_L(t)\Phi_L(\mathbf{r}) + \psi_R(t)\Phi_R(\mathbf{r}) \ . \tag{F.1}$$

The dynamical properties are contained in the coefficients $\psi_L(t) = \sqrt{N_L(t)}e^{i\phi_L(t)}$ and $\psi_R(t) = \sqrt{N_R(t)}e^{i\phi_R(t)}$, with N_i and ϕ_i the number of atoms and phase in each of the wells (i.e. $i = L, R$). The two-mode ansatz Eq. (F.1) is an approximation to the solution of the TDGP equation: the TDGP equation is nonlinear, which means that the superposition principle does not hold. However, if the two localized wave functions are well separated and their overlap in the tunneling region is small (condition of weak link), the nonlinear interaction in this region is negligible and the superposition principle is preserved. In the weak link limit, the two mode ansatz Eq. (F.1) is still a good approximation to the real wave function (see, for instance, the discussion in the Appendix A of Ref. [Rag99]).

Substituting Eq. (F.1) into the TDGP Eq. (2.12), multiplying by Φ_L^* (respectively, Φ_R^*), integrating over $\mathrm{d}\mathbf{r}$ and considering $\Phi_i(\mathbf{r})$ real gives:

$$\begin{aligned}
i\hbar\frac{\partial}{\partial t}\psi_L(t) = &\left[\int \mathrm{d}\mathbf{r}\left(-\frac{\hbar^2}{2m}\Phi_L\nabla^2\Phi_L + V_{\mathrm{ext}}\Phi_L^2 + gN_L\Phi_L^4 + 2gN_R\Phi_L^2\Phi_R^2 + g\psi_L\psi_R^\star\Phi_L^3\Phi_R + \right.\right. \\
&\left.\left. + \int \mathrm{d}\mathbf{r}' v_{\mathrm{dip}}\left\{N_L(\Phi'_L)^2\Phi_L^2 + N_R(\Phi'_R)^2\Phi_L^2 + \psi_L\psi_R^\star\Phi'_L\Phi'_R\Phi_L^2 + N_R\Phi'_L\Phi'_R\Phi_L\Phi_R\right\}\right)\right]\psi_L + \\
&+ \left[\int \mathrm{d}\mathbf{r}\left(-\frac{\hbar^2}{2m}\Phi_L\nabla^2\Phi_R + V_{\mathrm{ext}}\Phi_L\Phi_R + gN_R\Phi_L\Phi_R^3 + 2gN_L\Phi_L^3\Phi_R + g\psi_L^\star\psi_R\Phi_L^2\Phi_R^2 + \right.\right. \\
&\left.\left. + \int \mathrm{d}\mathbf{r}' v_{\mathrm{dip}}\left\{N_L\Phi'_L\Phi'_R\Phi_L^2 + N_L(\Phi'_L)^2\Phi_L\Phi_R + \psi_L^\star\psi_R\Phi'_L\Phi'_R\Phi_L\Phi_R + N_R(\Phi'_R)^2\Phi_L\Phi_R\right\}\right)\right]\psi_R
\end{aligned} \tag{F.2}$$

and analogously for $\psi_R(t)$. Notice that we have set by construction $\int \mathrm{d}\mathbf{r}\Phi_R\Phi_L = 0$.

We will discuss first what we call the *crude* two-mode model , in which some overlap integrals are neglected, and then the *full* two-mode model, in which all overlap integrals are taken into account. In the literature these equations have been derived for s-wave condensates [Sme97, Rag99, Ana06] and have been recently applied to purely dipolar condensates [Xio09, Asad09].

F.1 Crude two-mode model for dipolar condensates

If the overlap between the modes in the left and the right is very small, two-body interactions are mainly given by the atoms that are in the same well, not in different wells. This means that the terms with the shape $\int \mathrm{d}\mathbf{r} v_{\mathrm{int}} \Phi_L \Phi_R$, where v_{int} is here a generic two-body potential, can be neglected. Proceeding in such a way gives

$$\begin{aligned} i\hbar\frac{\partial}{\partial t}\psi_L(t) = &\left[\int \mathrm{d}\mathbf{r}\left(-\frac{\hbar^2}{2m}\Phi_L\nabla^2\Phi_L + V_{\mathrm{ext}}\Phi_L^2 + gN_L\Phi_L^4 + \right.\right. \\ &\left.\left. + \int \mathrm{d}\mathbf{r}' v_{\mathrm{dip}}\left\{N_L(\Phi_L')^2 + N_R(\Phi_R')^2\right\}\Phi_L^2\right)\right]\psi_L + \\ &+ \left[\int \mathrm{d}\mathbf{r}\left(-\frac{\hbar^2}{2m}\Phi_L\nabla^2\Phi_R + V_{\mathrm{ext}}\Phi_L\Phi_R\right)\right]\psi_R \qquad \text{(F.3)} \\ i\hbar\frac{\partial}{\partial t}\psi_R(t) = &\left[\int \mathrm{d}\mathbf{r}\left(-\frac{\hbar^2}{2m}\Phi_R\nabla^2\Phi_R + V_{\mathrm{ext}}\Phi_R^2 + gN_R\Phi_R^4 + \right.\right. \\ &\left.\left. + \int \mathrm{d}\mathbf{r}' v_{\mathrm{dip}}\left\{N_R(\Phi_R')^2 + N_L(\Phi_L')^2\right\}\Phi_R^2\right)\right]\psi_R + \\ &+ \left[\int \mathrm{d}\mathbf{r}\left(-\frac{\hbar^2}{2m}\Phi_R\nabla^2\Phi_L + V_{\mathrm{ext}}\Phi_R\Phi_L\right)\right]\psi_L \ . \qquad \text{(F.4)} \end{aligned}$$

Defining the quantities:

$$E_L = \int \mathrm{d}\mathbf{r}\left(\frac{\hbar^2}{2m}|\nabla\Phi_L|^2 + |\Phi_L|^2 V_{\mathrm{ext}}\right) \qquad \text{(F.5)}$$

$$E_R = \int \mathrm{d}\mathbf{r}\left(\frac{\hbar^2}{2m}|\nabla\Phi_R|^2 + |\Phi_R|^2 V_{\mathrm{ext}}\right) \qquad \text{(F.6)}$$

$$K = -\int \mathrm{d}\mathbf{r}\left(-\frac{\hbar^2}{2m}\nabla\Phi_L\nabla\Phi_R + \Phi_L\Phi_R V_{\mathrm{ext}}\right) \qquad \text{(F.7)}$$

$$U_L = \int \mathrm{d}\mathbf{r}\left[g|\Phi_L|^4 + \int \mathrm{d}\mathbf{r}' v_{\mathrm{dip}}|\Phi_L'|^2|\Phi_L|^2\right] \qquad \text{(F.8)}$$

$$U_R = \int \mathrm{d}\mathbf{r}\left[g|\Phi_R|^4 + \int \mathrm{d}\mathbf{r}' v_{\mathrm{dip}}|\Phi_R'|^2|\Phi_R|^2\right] \qquad \text{(F.9)}$$

$$B = \int \mathrm{d}\mathbf{r}|\Phi_L|^2 \int \mathrm{d}\mathbf{r}' v_{\mathrm{dip}}|\Phi_R'|^2 \ , \qquad \text{(F.10)}$$

with $\Phi' \equiv \Phi(\mathbf{r}')$, one can rewrite equations (F.3) and (F.4) as

$$i\hbar\frac{\partial\psi_L}{\partial t} = \Big[\,(E_L + BN) + (U_L - B)\,N_L\Big]\psi_L - K\psi_R \tag{F.11}$$

$$i\hbar\frac{\partial\psi_R}{\partial t} = \Big[\,(E_R + BN) + (U_R - B)\,N_R\Big]\psi_R - K\psi_L\ , \tag{F.12}$$

where the condition $N = N_1 + N_2$ has been used.

We now introduce the population imbalance

$$Z(t) = \frac{N_L(t) - N_R(t)}{N} \tag{F.13}$$

and the phase difference

$$\phi(t) = \phi_R(t) - \phi_L(t)\ . \tag{F.14}$$

It is possible to rewrite equations (F.11) and (F.12) in terms of these conjugate variables, by substituting the expressions for $\psi_L(t)$ and $\psi_R(t)$ in terms of Z and ϕ into Eqs. (F.11) and (F.12), and separating in real and imaginary parts. As a result we find

$$\dot{Z} = -\sqrt{1 - Z^2}\sin\phi \tag{F.15}$$

$$\dot{\phi} = \Delta E + \Lambda Z + \frac{Z}{\sqrt{1 - Z^2}}\cos\phi\ , \tag{F.16}$$

where the dimensionless parameters ΔE and Λ are defined by

$$\Delta E = \frac{E_L - E_R}{2K} + \frac{U_L - U_R}{4K}N \tag{F.17}$$

$$\Lambda = \frac{U_L + U_R - 2B}{4K}N\ . \tag{F.18}$$

In Eqs. (F.15) and (F.16), time has been expressed in units of the Rabi frequency, $\Omega_R = 2K/\hbar$. This is formally the frequency at which the non-interacting system oscillates, which can be seen by setting the interaction integrals (F.8)–(F.10) to zero: in this case $\Lambda = 0$ and Eqs. (F.15) and (F.16) admit harmonic solutions with the frequency given by Ω_R. Notice that the value of Ω_R calculated using the value of K of the interacting case would not be the frequency at which the non-interacting system would oscillate, since to find this latter frequency one should calculate K using the non-interacting left and right modes. The quantity Λ characterizes the departure of the oscillations from the non-interacting case. We can see from its definition that it is determined by the two-body interactions within each well. We will see below that it is this parameter that allows for macroscopic quantum self-trapping, which is not present in superfluid or superconductor Josephson junctions. The parameter ΔE gives the difference in energy between left and right wells. In this thesis we have only considered symmetric double-wells, for which $\Delta E = 0$ and one recovers Eqs. (7.12) and (7.13).

F.2 Full two-mode model for dipolar condensates

If all the terms in Eq. (F.2) (and the corresponding equation for $\psi_R(t)$) are retained, we find

$$i\hbar\frac{\partial\psi_L}{\partial t} = \Big[E_L + U_L N_L + (B + 2I_1 + D_1)N_R + (I_{2L} + D_{2L})\psi_L\psi_R\Big]\psi_L + \\ + \Big[- K + (I_{2L} + D_{2L} + D_{3L})N_L + (I_{2R} + D_{3R})N_R + (I_1 + D_1)\psi_L\psi_R\Big]\psi_R \quad \text{(F.19)}$$

$$i\hbar\frac{\partial\psi_R}{\partial t} = \Big[E_R + U_R N_R + (B + 2I_1 + D_1)N_L + (I_{2R} + D_{2R})\psi_L\psi_R\Big]\psi_R + \\ + \Big[- K + (I_{2R} + D_{2R} + D_{3R})N_R + (I_{2L} + D_{3L})N_L + (I_1 + D_1)\psi_L\psi_R\Big]\psi_L \ , \quad \text{(F.20)}$$

where we have introduced the parameters

$$I_1 = g\int \mathrm{d}\mathbf{r}|\Phi_L|^2|\Phi_R|^2 \quad \text{(F.21)}$$

$$I_{2L} = g\int \mathrm{d}\mathbf{r}|\Phi_L|^2\Phi_L\Phi_R \quad \text{(F.22)}$$

$$I_{2R} = g\int \mathrm{d}\mathbf{r}|\Phi_R|^2\Phi_L\Phi_R \quad \text{(F.23)}$$

$$D_1 = \int \mathrm{d}\mathbf{r}\,\Phi_L\Phi_R\int \mathrm{d}\mathbf{r}' v_{\mathrm{dip}}\Phi'_L\Phi'_R \quad \text{(F.24)}$$

$$D_{2L} = \int \mathrm{d}\mathbf{r}\,|\Phi_L|^2\int \mathrm{d}\mathbf{r}' v_{\mathrm{dip}}\Phi'_L\Phi'_R \quad \text{(F.25)}$$

$$D_{2R} = \int \mathrm{d}\mathbf{r}\,|\Phi_R|^2\int \mathrm{d}\mathbf{r}' v_{\mathrm{dip}}\Phi'_L\Phi'_R \quad \text{(F.26)}$$

$$D_{3L} = \int \mathrm{d}\mathbf{r}\,\Phi_L\Phi_R\int \mathrm{d}\mathbf{r}' v_{\mathrm{dip}}|\Phi'_L|^2 \quad \text{(F.27)}$$

$$D_{3R} = \int \mathrm{d}\mathbf{r}\,\Phi_L\Phi_R\int \mathrm{d}\mathbf{r}' v_{\mathrm{dip}}|\Phi'_R|^2 \quad \text{(F.28)}$$

in addition to those defined in Eqs. (F.5)–(F.10). In these expressions we have used $\Phi' \equiv \Phi(\mathbf{r}')$ to simplify the notation. Note that for a symmetric configuration $I_{2L} = I_{2R} \equiv I_2$, $D_{2L} = D_{2R} \equiv D_2$ and $D_{3L} = D_{3R} \equiv D_3$.

Using the decomposition of ψ_L and ψ_R in terms of N_i and ϕ_i we obtain:

$$i\frac{\hbar}{2N_L}\frac{\partial N_L}{\partial t} - \hbar\frac{\partial\phi_L}{\partial t} = E_L + U_L N_L + (B + 2I_1 + D_1)N_R + (I_{2L} + D_{2L})\sqrt{N_L N_R}e^{i(\phi_L - \phi_R)} + \\ + \Big[- K + (2I_{2L} + D_{2L} + D_{3L})N_L + (I_{2R} + D_{3R})N_R\Big]\sqrt{\frac{N_R}{N_L}}e^{i(\phi_R - \phi_L)} + \\ + (I_1 + D_1)N_R e^{i2(\phi_L - \phi_R)} \ , \quad \text{(F.29)}$$

and equivalently for ψ_R. We separate now these equations in real and imaginary parts,

and recalling the definitions of population imbalance and phase difference, we obtain:

$$\dot{Z} = \frac{2K}{\hbar}\left[-1 + \frac{I_{2L}+I_{2R}+D_{3L}+D_{3R}}{2K}N + Z\frac{I_{2L}-I_{2R}+D_{3L}-D_{3R}}{2K}N\right]\sqrt{1-Z^2}\sin\phi + \frac{I_1+D_1}{\hbar}N(1-Z^2)\sin 2\phi \tag{F.30}$$

$$\begin{aligned}\hbar\dot{\phi} =& E_L - E_R + \frac{U_L-U_R}{2}N + \left(\frac{U_L+U_R}{2} - B - 2I_1 - D_1\right)NZ + \\ &+ \frac{N}{2}\Big[3(I_{2L}-I_{2R}) + 2(D_{2L}-D_{2R}) + D_{3L} - D_{3R}\Big]\sqrt{1-Z^2}\cos\phi + \\ &+ \Big[2K - N(I_{2R}+I_{2L}+D_{3R}+D_{3L})\Big]\frac{Z}{\sqrt{1-Z^2}}\cos\phi + \\ &+ \frac{N}{2}\Big[I_{2R}-I_{2L}+D_{3R}-D_{3L}\Big]\frac{1+Z^2}{\sqrt{1-Z^2}}\cos\phi - (I_1+D_1)NZ\cos 2\phi\ .\end{aligned} \tag{F.31}$$

We define now the following dimensionless parameters:

$$\Delta E = \frac{E_L-E_R}{2K} + \frac{U_L-U_R}{4K}N \tag{F.32}$$

$$\Lambda = \frac{U_L+U_R}{4K}N - \frac{B+2I_1+D_1}{2K}N \tag{F.33}$$

$$\alpha = \frac{I_{2L}+I_{2R}+D_{3L}+D_{3R}}{2K}N \tag{F.34}$$

$$\beta = \frac{I_{2L}-I_{2R}+D_{3L}-D_{3R}}{2K}N \tag{F.35}$$

$$\delta = \frac{3(I_{2L}-I_{2R})+2(D_{2L}-D_{2R})+D_{3L}-D_{3R}}{4K}N \tag{F.36}$$

$$\varepsilon = \frac{I_1+D_1}{2K}N\ . \tag{F.37}$$

Then the full two-mode equations for a dipolar Josephson junction are given by:

$$\dot{Z} = (-1+\alpha+\beta Z)\sqrt{1-Z^2}\sin\phi + \varepsilon(1-Z^2)\sin 2\phi \tag{F.38}$$

$$\dot{\phi} = \Delta E + \Lambda Z + \left[\delta\sqrt{1-Z^2} - (-1+\alpha)\frac{Z}{\sqrt{1-Z^2}} - \frac{1+Z^2}{\sqrt{1-Z^2}}\beta\right]\cos\phi - \varepsilon Z\cos 2\phi\ , \tag{F.39}$$

where the time t in the derivatives has been expressed in units of the Rabi frequency, $\Omega_R = 2K/\hbar$. If the two wells in L and R are symmetric, we have $\Delta E = \beta = \delta = 0$ and we recover Eqs. (7.7) and (7.8).

F.3 Hamiltonian and classification of the orbits

The Hamiltonian of the system described by the two-mode models can be found by integration of Hamilton equations,

$$\dot{Z} = -\frac{\partial H}{\partial\phi} \qquad\qquad \dot{\phi} = \frac{\partial H}{\partial Z}\ . \tag{F.40}$$

Let us consider the crude two-mode model with symmetric double wells, that is $\Delta E = 0$. The discussion that follows can be extended to the full two-mode model and to asymmetric double wells, but the kind of orbits found by taking into account these corrections is qualitatively the same. Using Eqs. (F.15)–(F.16) we find the two-mode Hamiltonian

$$H_{\text{crude}}(Z,\phi) = \frac{1}{2}\Lambda Z^2 - \sqrt{1-Z^2}\cos\phi \ . \tag{F.41}$$

Let us examine the behavior of the Hamiltonian $H_{\text{crude}}(Z,\phi)$. For convenience we restrict to the family of solutions with $\Lambda > 1$, which is the experimentally relevant situation (see, for instance, Refs. [Rag99] and [Mele11] for a detailed discussion for all Λ). The first critical point is $Z = 0, \phi = 0$, where the Hamiltonian is a minimum. The second critical point is $Z = 0, \phi = \pi$, which is a saddle-point. In addition, the Hamiltonian shows a maximum at $Z_{\max} = \sqrt{1-1/\Lambda^2}, \phi = \pi$. Notice that there are equivalent critical points at the negative Z and ϕ regions. They are summarized in Table F.1.

Table F.1: Critical points in the crude two-mode Hamiltonian ($\Lambda > 1$).

Description	Critical point (Z,ϕ)	Value for $\Lambda = 2.5$	Value for $\Lambda = 18$
Minimum	$(0,0)$	$(0,0)$	$(0,0)$
Saddle	$(0,\pm\pi)$	$(0,\pm\pi)$	$(0,\pm\pi)$
Maximum	$(\pm Z_{\max},\pm\pi)$	$(0.916,\pm\pi)$	$(0.998,\pm\pi)$

To analyze the types of orbits predicted by the two-mode Hamiltonian, we look at the curves of constant H in the (Z,ϕ) space. Two examples are shown in Fig. F.1 for $\Lambda = 2.5$ (left panel) and $\Lambda = 18$ (right panel). In these examples, closed orbits exist around the minimum and around the maximum of the Hamiltonian, represented respectively as solid black or solid blue lines. In these orbits both the imbalance and the phase are restricted between two values, either around $(0,0)$, shown as a black point, or around $(\pm Z_{\max},\pm\pi)$, shown as blue points. In the first case they are known as Josephson or plasma oscillations, while in the second case they are referred to as π-modes[1]. In Fig. F.1 π-modes are shown only for small Λ; for large Λ they also exist but the regime of parameters where they can be found becomes vanishingly small as Λ is increased.

The value of the Hamiltonian corresponding to the saddle point $(0,\pi)$, shown as a red point in Fig. F.1, defines the separatrix line, which separates closed from unbound orbits. The separatrix is shown as a red dotted line. In the region of unbound orbits, the value of imbalance oscillates around $Z \neq 0$ (with the time average $\langle Z\rangle \neq 0$) and the phase periodically takes all values in the range $(-\pi,\pi]$, as shown in the dashed lines of Fig. F.1. Setting the initial phase to $\phi(0) = 0$ the separatrix line defines a critical value for the initial imbalance, $Z(0) = Z_c$, given by the condition $H(Z_c,0) = H(0,\pi)$,

$$Z_c = 2\frac{\sqrt{\Lambda-1}}{\Lambda} \ , \tag{F.42}$$

which is valid for $\Lambda > 2$, as will be discussed below. For the examples in Fig. F.1, the critical imbalance takes the value $Z_c = 0.980$ for $\Lambda = 2.5$ and $Z_c = 0.458$ for $\Lambda = 18$.

[1]Notice that these π-modes correspond to self-trapped orbits, since the imbalance is always larger than zero. However, the phase here is bounded too, in contrast to running-phase self-trapped oscillations.

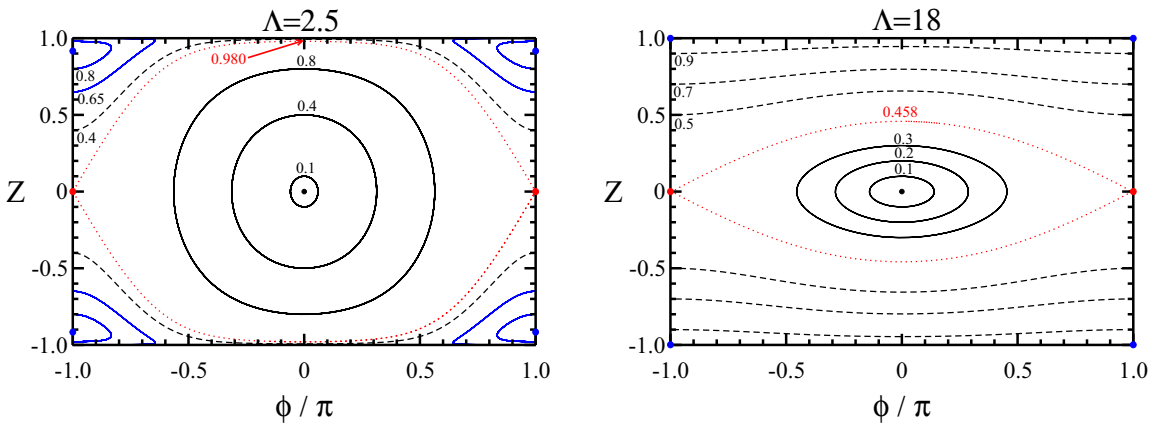

Figure F.1: Orbits predicted by the crude TMM, for $\Lambda = 2.5$ (left panel) and $\Lambda = 18$ (right panel). The small numbers indicate the values of $Z(0)$ for $\phi(0) = 0$ (written along the line $\phi = 0$) and for $\phi(0) = \pi$ (written along the line $\phi = \pi$). The orbits around the minimum (black point) are shown in black, while the orbits around the maximum (blue points) are shown in blue. The running-phase modes are shown as dashed black lines. The separatrix is shown as a red dotted line, and the saddle point is marked in red. The small red numbers indicate the value of Z_c given by Eq. (F.42).

For $Z(0) < Z_c$, the orbits are closed in the space defined by (Z, ϕ), while for $Z > Z_c$ the orbits are unbounded in ϕ and the imbalance never crosses zero. This latter regime is usually known as self-trapping (or running-phase mode), while the former corresponds to Josephson or plasma oscillations.

If instead we set the initial phase to $\phi(0) = \pi$, the condition $H(Z(0), \phi(0)) > H(1, 0)$ defines a second critical initial imbalance,

$$Z_{c2} = \sqrt{1 - \frac{4}{\Lambda^2}}\,, \tag{F.43}$$

which is again valid only for $\Lambda > 2$. For the examples in Fig. F.1, the second critical imbalance takes the value $Z_{c2} = 0.600$ for $\Lambda = 2.5$ and $Z_{c2} = 0.994$ for $\Lambda = 18$. For $Z > Z_{c2}$ the system follows bound orbits around $\phi = \pi$, while for $Z < Z_{c2}$ it evolves according to the running-phase mode. For $\Lambda = 2$, $Z_c = 1$ and $Z_{c2} = 0$, which implies that the only running-phase mode that can exist is the critical orbit (which reaches $Z = 0$ or $\phi = 0$ only in an infinite amount of time). For $\Lambda < 2$ running-phase modes are not possible, but there appears a new orbit (not shown in the figure) where both the imbalance and the phase are bounded (with $\langle Z \rangle = 0$, $\langle \phi \rangle = \pi$).

We have seen that there are four different orbits, which can be classified as zero-phase modes and π-phase modes (or π-modes), according to whether the time average of their phase is zero or π. Table F.2 summarizes the classification of the orbits. There are two zero-phase modes, usually known as Josephson (or plasma) and self-trapping (or running-phase mode). These two modes have been measured experimentally [Alb05] (see also [Cat01, Levy07]) and have been predicted in Chapter 7 of this thesis for a self-induced Josephson junction. Examples of them are given in Fig. F.2, in panels (a) and (b). Correspondingly, the π-modes can also be classified in terms of a self-trapped π-mode (for

which $\langle Z\rangle \neq 0$) and a "plasma" π-mode (for which $\langle Z\rangle = 0$). Notice that both π-phase modes are closed orbits, respectively around the maximum and around the saddle point of H. They are shown in (c) and (d) panels of Fig. F.2. Notice that the phase appears in the figures beyond the range $(-\pi, \pi]$.

Table F.2: Kinds of orbits and their description for $\Lambda > 1$.

Kind of orbit	Description	Regime
Josephson (plasma)	$\langle Z\rangle = 0$, $\langle\phi\rangle = 0$	$Z < Z_c$
Self-trapping (running-phase)	$\langle Z\rangle \neq 0$, $\langle\phi\rangle = 0$	$Z > Z_c$ or $Z < Z_{c2}$, for $\Lambda > 2$
π-mode (self-trapped)	$\langle Z\rangle \neq 0$, $\langle\phi\rangle = \pi$	$Z > Z_{c2}$
π-mode ("plasma")	$\langle Z\rangle = 0$, $\langle\phi\rangle = \pi$	$Z < Z_{c2}$, for $\Lambda < 2$

Finally, the classification of the orbits predicted by TMMs can be carried out by fixing the initial condition $Z(0) = Z_0$ and modifying Λ (see discussions, for instance, in [Rag99, Mele11]). For $\phi(0) = 0$ one can define a critical interaction parameter that takes the value $\Lambda_c = 2(1 - \sqrt{1 - Z_0^2})/Z_0^2$. For $\Lambda < \Lambda_c$ the system will evolve in time according to Josephson oscillations, while for $\Lambda > \Lambda_c$ it will show self-trapping (running-phase mode). For initial condition $\phi(0) = \pi$, and always for $\Lambda > 1$, the system shows self-trapping for $\Lambda < \Lambda_{c2}$ and self-trapped π-modes for $\Lambda > \Lambda_{c2}$. This second critical condition can be found imposing $H(Z_0, \phi_0) = H(1, 0)$ at Λ_{c2}. For the crude TMM it gives $\Lambda_{c2} = 2/\sqrt{1 - Z_0^2}$, where $Z_0 = Z(0)$. Notice again that the running-phase region disappears for $\Lambda_c = \Lambda_{c2} \leq 2$.

F.4 Small-amplitude oscillations

Before concluding this appendix, we will briefly address small-amplitude oscillations, which allow for simple analytical expressions for the frequency of oscillation of the system in the Josephson regime. We take Eqs. (7.12)–(7.13) and Eqs. (7.7)–(7.8), respectively for the crude and the full TMMs, and study the evolution of the imbalance and the phase around an equilibrium position. We write $Z = Z_0 + \delta Z$ and $\phi = \phi_0 + \delta\phi$ and substitute these expressions into the equations. Taking the equilibrium position to be $Z_0 = 0$, $\phi_0 = 0$ and keeping the terms in first order in $\delta\phi$ or δZ gives the linearized equations

$$\dot{Z} = -\delta\phi \tag{F.44}$$

$$\dot{\phi} = \delta Z(\Lambda + 1) \tag{F.45}$$

for the crude TMM, and

$$\dot{Z} = -(1 - \alpha - 2\varepsilon)\delta\phi \tag{F.46}$$

$$\dot{\phi} = (\Lambda + 1 - \alpha - \varepsilon)\delta Z \tag{F.47}$$

for the full TMM. Taking the second derivative and combining the equations, we see that they can be written as $\ddot{Z} + \omega^2 Z = 0$, and analogously for the phase. The frequency ω can

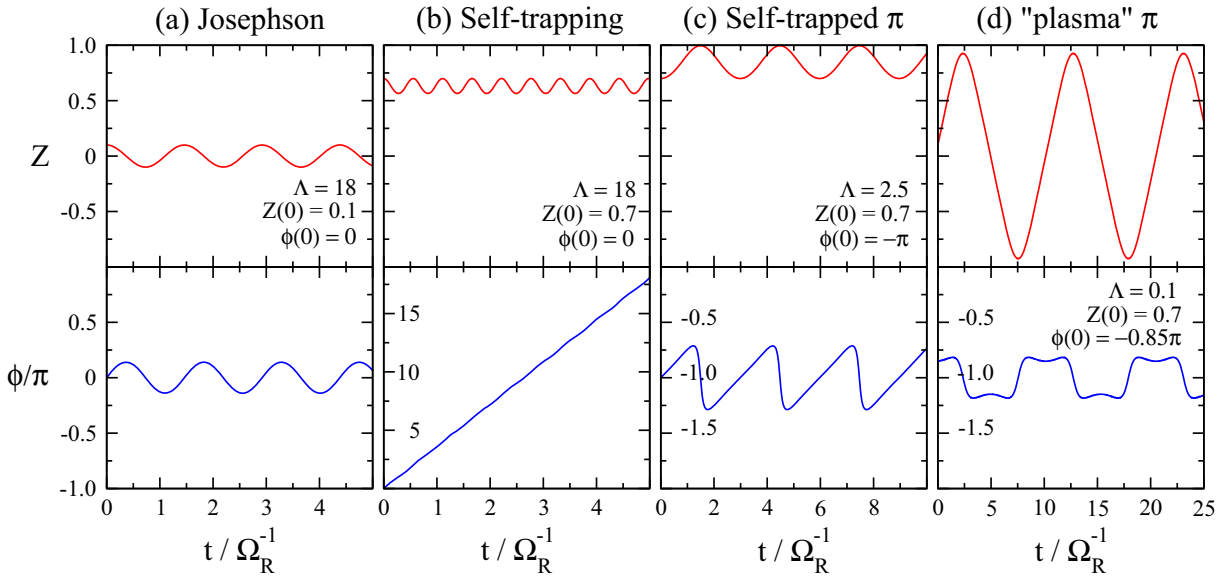

Figure F.2: Examples of the orbits predicted by TMMs: (a) Josephson oscillations, (b) self-trapping (running-phase), (c) self-trapped π-mode, (d) "plasma" π-mode. The initial conditions and the value of Λ are indicated in the labels.

be identified with

$$\omega_{\rm c} = \sqrt{\Lambda + 1} \tag{F.48}$$

$$\omega_{\rm f} = \sqrt{(\Lambda + 1 - \alpha - \varepsilon)(1 - \alpha - 2\varepsilon)} \tag{F.49}$$

for the crude (c) and full (f) TMMs. The solution for $Z(0) = Z_0$ and $\phi(0) = 0$ is given by

$$Z(t) = Z_0 \cos(\omega t) \tag{F.50}$$

$$\phi(t) = \omega Z_0 \sin(\omega t) \ . \tag{F.51}$$

The main result for small amplitude oscillations is that the frequency is independent of the initial conditions, in contrast to large amplitude oscillations.

Appendix G

3D and radial virial relations for ultracold dipolar gases

In Secs. 4.2 and 8.2 we have used the virial theorem (3D and radial, respectively) for a dipolar gas. The procedure to arrive at expressions (4.8) and (8.28) has been by minimization of the energy functional with respect to the parameters characterizing a scaling transformation of the system. There is an equivalent way to derive virial theorems, and is by using commutators. In this appendix we derive the 3D virial theorem and the radial virial theorem for ultracold dipolar gases with the method of commutators. In the case of the radial virial expression, which in the Thomas-Fermi approximation is given by Eq. (8.28), we derive in this appendix a virial relation that is general for any ground state of the system. This derivation is constructive in the sense that it allows us to understand better the dipole-dipole potential, since it requires that the dipolar potential, in analogy to the Coulomb potential, is treated as a distribution, properly taking care of the divergence at $\mathbf{r} \to 0$.

To derive the virial expressions, the many-body Hamiltonian is needed. For a system of quantum particles interacting both via s-wave contact and dipolar interactions it is given by

$$H = H_{\rm kin} + H_{\rm ho} + H_{\rm sw} + H_{\rm dip} \tag{G.1}$$

$$H_{\rm kin} = \sum_i \frac{p_i^2}{2m} \tag{G.2}$$

$$H_{\rm ho} = \sum_i \frac{m}{2}(\omega_x^2 x_i^2 + \omega_y^2 y_i^2 + \omega_z^2 z_i^2) \tag{G.3}$$

$$H_{\rm sw} = \frac{1}{2}\sum_{i\neq j} g\,\delta(\mathbf{r}_i - \mathbf{r}_j) \tag{G.4}$$

$$H_{\rm dip} = \frac{1}{2}\sum_{i\neq j} \frac{d^2}{|\mathbf{r}_i - \mathbf{r}_j|^3}\left(1 - 3\frac{(z_i - z_j)^2}{|\mathbf{r}_i - \mathbf{r}_j|^2}\right), \tag{G.5}$$

where $i = 1, \ldots, N$ and $j = 1, \ldots, N$, with N the total number of particles. Notice that we consider both s-wave interactions and dipolar interactions, so that the results are easily restricted to the case of identical bosons (for which $g \neq 0$ in general) or identical fermions

(for which $g = 0$). The definition of the coupling constants g and d^2 is given in Sec. 2.1. To simplify the notation, we use $|\mathbf{r}_i - \mathbf{r}_j| \equiv r_{ij}$ and analogously for each coordinate.

Given a perturbation operator A and a strength of the perturbation λ, the energy of the system is given by

$$\begin{aligned} E(\lambda) &= \langle 0| e^{-i\lambda A} H e^{i\lambda A} |0\rangle = \\ &= \langle 0| (1 - i\lambda A - \frac{1}{2}\lambda^2 A^2 + O(\lambda^3)) H (1 + i\lambda A - \frac{1}{2}\lambda^2 A^2 + O(\lambda^3)) |0\rangle = \\ &= \langle 0| H |0\rangle + i\lambda \langle 0| [H, A] |0\rangle + \frac{1}{2}\lambda^2 \langle 0| [A, [H, A]] |0\rangle + O(\lambda^3) \ , \end{aligned} \tag{G.6}$$

where $|0\rangle$ refers to the ground state wave function. By expanding the energy around the equilibrium configuration, $\lambda = 0$, we find

$$E(\lambda) = E_0 + \lambda \frac{\partial E}{\partial \lambda}\bigg|_{\lambda=0} + \frac{\lambda^2}{2} \frac{\partial^2 E}{\partial \lambda^2}\bigg|_{\lambda=0} + O(\lambda^3) \ . \tag{G.7}$$

Recalling that the energy is a minimum and therefore the first derivative must vanish, and comparing expressions (G.6) and (G.7) we find the following identity,

$$\langle 0| [H, A] |0\rangle = 0 \ , \tag{G.8}$$

which leads to the virial relation. We see that setting to zero the expectation value of the commutator $[H, A]$ is equivalent to setting to zero the first order derivative of the energy functional with respect to the scaling parameter. The two methods are equivalent, but sometimes one of them turns out to be more complicated than the other. Notice that Eq. (G.8) can be also obtained form the Ehrenfest theorem of quantum mechanics,

$$\frac{d}{dt}\langle A \rangle = \frac{1}{i\hbar}\langle [A, H] \rangle + \left\langle \frac{\partial A}{\partial t} \right\rangle \ , \tag{G.9}$$

which in Heisenberg picture can be obtained just by taking the expectation value of the Heisenberg equation. For an operator A that does not explicitly depend on time (and this is the case, since we will only address operators of the type $A \sim \mathbf{r} \cdot \mathbf{p}$), the second term on the right-hand side is zero. At equilibrium, for the ground state wave function, the time derivative of $\langle A \rangle$ will also be zero. This lead us thus to the relation Eq. (G.8).

G.1 3D virial theorem

The 3D virial theorem can be found from a scaling transformation of the density (see Sec. 4.2), which can be related to the excitation of the breathing mode. The operator associated to this excitation is $A = \sum_k (\mathbf{r}_k \cdot \mathbf{p}_k + \mathbf{p}_k \cdot \mathbf{r}_k)/2$, with $k = 1, \ldots, N$. Notice that the operator A has to be hermitian, whence the introduction of the factor $1/2$ and the scalar product $\mathbf{p} \cdot \mathbf{r}$. Introducing this operator in Eq. (G.8) we find

$$2E_{\rm kin} - 2E_{\rm ho} + 3E_{\rm sw} + 3E_{\rm dip} = 0 \ , \tag{G.10}$$

where the different terms of the Hamiltonian, Eqs. (G.2)–(G.5), give the following contributions

$$\langle 0|\,[A, H_{\rm kin}]\,|0\rangle = 2i\hbar E_{\rm kin} \tag{G.11}$$
$$\langle 0|\,[A, H_{\rm ho}]\,|0\rangle = -2i\hbar E_{\rm ho} \tag{G.12}$$
$$\langle 0|\,[A, H_{\rm sw}]\,|0\rangle = 3i\hbar E_{\rm sw} \tag{G.13}$$
$$\langle 0|\,[A, H_{\rm dip}]\,|0\rangle = 3i\hbar E_{\rm dip} \tag{G.14}$$

and where the different energy contributions are given by

$$E_{\rm kin} = \left\langle 0 \left| \sum_i \frac{p_{x_i}^2 + p_{y_i}^2 + p_{z_i}^2}{2m} \right| 0 \right\rangle \tag{G.15}$$
$$E_{\rm ho} = \left\langle 0 \left| \sum_i \frac{m}{2}(\omega_x^2 x_i^2 + \omega_y^2 y_i^2 + \omega_z^2 z_i^2) \right| 0 \right\rangle \tag{G.16}$$
$$E_{\rm sw} = \left\langle 0 \left| \frac{1}{2}\sum_{i\neq j} g\delta(\mathbf{r}_i - \mathbf{r}_j) \right| 0 \right\rangle \tag{G.17}$$
$$E_{\rm dip} = \left\langle 0 \left| \frac{1}{2}\sum_{i\neq j} \frac{d^2}{r_{ij}^3}\left(1 - 3\frac{z_{ij}^2}{r_{ij}^2}\right) \right| 0 \right\rangle \ . \tag{G.18}$$

G.1.1 Derivation of the 3D virial theorem

The Hamiltonian is given by Eqs. (G.1)-(G.5). To get the virial theorem for a dipolar gas in 3D, Eq. (G.10), we have to calculate the commutator

$$\begin{aligned}[A, H] = &\left[\sum_k \frac{1}{2}(\mathbf{r}_k\cdot\mathbf{p}_k + \mathbf{p}_k\cdot\mathbf{r}_k), \sum_i \frac{p_i^2}{2m} + \sum_i \frac{m}{2}(\omega_x^2 x_i^2 + \omega_y^2 y_i^2 + \omega_z^2 z_i^2)\right] + \\ &+ \left[\sum_k \frac{1}{2}(\mathbf{r}_k\cdot\mathbf{p}_k + \mathbf{p}_k\cdot\mathbf{r}_k), \frac{1}{2}\sum_{i\neq j}\delta(\mathbf{r}_i - \mathbf{r}_j) + \frac{1}{2}\sum_{i\neq j}\frac{d^2}{r_{ij}^3}\left(1 - 3\frac{z_{ij}^2}{r_{ij}^2}\right)\right] \ . \end{aligned} \tag{G.19}$$

The only commutators that will survive in the summations are those that involve variables with the same indices. Then

$$\begin{aligned}[A, H] = &\frac{1}{2}\sum_i \left[\mathbf{r}_i\cdot\mathbf{p}_i + \mathbf{p}_i\cdot\mathbf{r}_i, \frac{p_i^2}{2m} + \frac{m}{2}(\omega_x^2 x_i^2 + \omega_y^2 y_i^2 + \omega_z^2 z_i^2)\right] + \\ &+ \sum_{i\neq j}\frac{1}{2}\left[\mathbf{r}_i\cdot\mathbf{p}_i + \mathbf{p}_i\cdot\mathbf{r}_i + \mathbf{r}_j\cdot\mathbf{p}_j + \mathbf{p}_j\cdot\mathbf{r}_j, \frac{1}{2}\delta(\mathbf{r}_i - \mathbf{r}_j) + \frac{d^2}{2}\frac{1}{r_{ij}^3}\left(1 - 3\frac{z_{ij}^2}{r_{ij}^2}\right)\right] \ . \end{aligned} \tag{G.20}$$

Now using $\mathbf{r}_i \cdot \mathbf{p}_i = -i\hbar(x_i\partial_{x_i} + y_i\partial_{y_i} + z_i\partial_{z_i})$ we can write

$$\begin{aligned}
&\mathbf{r}_i \cdot \mathbf{p}_i + \mathbf{r}_j \cdot \mathbf{p}_j = -i\hbar(x_i\partial_{x_i} + y_i\partial_{y_i} + z_i\partial_{z_i}) - i\hbar(x_j\partial_{x_j} + y_j\partial_{y_j} + z_j\partial_{z_j}) = \\
&= -i\hbar\left(x_i\frac{\partial x_{ij}}{\partial x_i}\partial_{x_{ij}} + x_j\frac{\partial x_{ij}}{\partial x_j}\partial_{x_{ij}} + y_i\frac{\partial y_{ij}}{\partial y_i}\partial_{y_{ij}} + y_j\frac{\partial y_{ij}}{\partial y_j}\partial_{y_{ij}} + z_i\frac{\partial z_{ij}}{\partial z_i}\partial_{z_{ij}} + z_j\frac{\partial z_{ij}}{\partial zji}\partial_{z_{ij}}\right) = \\
&= -i\hbar\left(x_i\partial_{x_{ij}} - x_j\partial_{x_{ij}} + y_i\partial_{y_{ij}} - y_j\partial_{y_{ij}} + z_i\partial_{z_{ij}} - z_j\partial_{z_{ij}}\right) = \\
&= -i\hbar(x_{ij}\partial_{x_{ij}} + y_{ij}\partial_{y_{ij}} + z_{ij}\partial_{z_{ij}}) \ . \qquad \text{(G.21)}
\end{aligned}$$

And the expression for the commutator becomes

$$\begin{aligned}
[A,H] = &\frac{1}{2}\sum_i\left[(\mathbf{r}_i\cdot\mathbf{p}_i + \mathbf{p}_i\cdot\mathbf{r}_i), \frac{p_i^2}{2m} + \frac{m}{2}(\omega_x^2x_i^2 + \omega_y^2y_i^2 + \omega_z^2z_i^2)\right] + \\
&+ \sum_{i\neq j}\frac{1}{2}\left[\mathbf{r}_{ij}\cdot\mathbf{p}_{ij} + \mathbf{p}_{ij}\cdot\mathbf{r}_{ij}, \frac{1}{2}\delta(\mathbf{r}_i - \mathbf{r}_j) + \frac{d^2}{2}\frac{1}{r_{ij}^3}\left(1 - 3\frac{z_{ij}^2}{r_{ij}^2}\right)\right] = \\
= &\frac{1}{2}\frac{1}{2m}\sum_i\left[\mathbf{r}_i\cdot\mathbf{p}_i + \mathbf{p}_i\cdot\mathbf{r}_i, p_i^2\right] - i\hbar\frac{m}{2}\sum_i\mathbf{r}_i\cdot\nabla_i(\omega_x^2x_i^2 + \omega_y^2y_i^2 + \omega_z^2z_i^2) - \\
&- i\hbar\frac{1}{2}\sum_{i\neq j}\mathbf{r}_{ij}\cdot\nabla_{ij}\delta(\mathbf{r}_i - \mathbf{r}_j) - i\hbar\frac{d^2}{2}\sum_{i\neq j}\mathbf{r}_{ij}\cdot\nabla_{ij}\left[\frac{1}{r_{ij}^3}\left(1 - 3\frac{z_{ij}^2}{r_{ij}^2}\right)\right] \ , \qquad \text{(G.22)}
\end{aligned}$$

where we have used the property

$$[A, H(\mathbf{r})] = \frac{1}{2}[\mathbf{r}\cdot\mathbf{p} + \mathbf{p}\cdot\mathbf{r}, H(\mathbf{r})] = -i\hbar\,\mathbf{r}\cdot(\nabla H(\mathbf{r})) \ . \qquad \text{(G.23)}$$

The commutator corresponding to the kinetic energy has three contributions, corresponding to the components x, y and z. Dropping the indices i for simplicity we find

$$\begin{aligned}
[xp_x + p_xx, p_x^2] &= [xp_x, p_x^2] + [p_xx, p_x^2] = [x, p_x^2]p_x + [x, p_x^2]p_x = \\
&= 2[x, p_x]p_x^2 + 2[x, p_x]p_x^2 = 4i\hbar p_x^2 \ . \qquad \text{(G.24)}
\end{aligned}$$

Note that p_x is an operator so it should be extracted from the commutator accordingly, but since the commutator is a scalar (identity operator) it commutes with p_x. Summing for x, y and z we have

$$[\mathbf{r}\cdot\mathbf{p} + \mathbf{p}\cdot\mathbf{r}, p^2] = 4i\hbar p^2 \ . \qquad \text{(G.25)}$$

The whole commutator will be

$$\begin{aligned}
[A,H] = &2i\hbar\frac{1}{2m}\sum_i p_i^2 - 2i\hbar\frac{m}{2}\sum_i(\omega_x^2x_i^2 + \omega_y^2y_i^2 + \omega_z^2z_i^2) + 3i\hbar\frac{1}{2}\sum_{i\neq j}\delta(\mathbf{r}_i - \mathbf{r}_j) + \\
&+ 3i\hbar\frac{d^2}{2}\sum_{i\neq j}\frac{1}{r_{ij}^3}\left(1 - 3\frac{z_{ij}^2}{r_{ij}^2}\right), \qquad \text{(G.26)}
\end{aligned}$$

where we have used the properties of the Delta function[1] and that the derivative of the dipole-dipole interaction is

$$\mathbf{r}\cdot\nabla\left[\frac{d^2}{r^3}\left(1-3\frac{z^2}{r^2}\right)\right]=-3\frac{d^2}{r^3}\left[1-3\frac{z^2}{r^2}\right]\ . \tag{G.27}$$

Notice that this result can be obtained taking the derivative naively, without taking care of the divergence of the dipole-dipole interaction for $\mathbf{r}\to 0$. This happens because some of the terms associated to the derivative in the three directions cancel out exactly. This is better understood in $\mathbf{k}$-space, where the Fourier transform of the dipole-dipole interaction does not present any problem. Fourier transforming the last equation we find[2]

$$\begin{aligned}\mathcal{F}\left[\mathbf{r}\cdot\nabla\left[\frac{d^2}{r^3}\left(1-\frac{3z^2}{r^2}\right)\right]\right]&=d^2\frac{4\pi}{3}\nabla_{\mathbf{k}}\cdot\mathbf{k}\left(1-3\frac{k_z^2}{k^2}\right)=\\&=d^2\frac{4\pi}{3}\left[3\left(1-3\frac{k_z^2}{k^2}\right)+6\frac{k_x^2k_z^2}{k^4}+6\frac{k_y^2k_z^2}{k^4}+6\frac{k_z^4}{k^4}-6\frac{k_z^2}{k^2}\right]=3d^2\frac{4\pi}{3}\left(1-3\frac{k_z^2}{k^2}\right)\ .\end{aligned} \tag{G.28}$$

We can recognize the right-hand side as -3 times the Fourier transform of the dipole-dipole interaction, Eq. (2.27).

The expectation value of the commutator evaluated in the ground state gives

$$\langle 0|\,[A,H]\,|0\rangle=2i\hbar E_{\rm kin}-2i\hbar E_{\rm ho}+3i\hbar E_{\rm sw}+3i\hbar E_{\rm dip}\ . \tag{G.29}$$

Equating this quantity to zero gives the 3D virial relation

$$2E_{\rm kin}-2E_{\rm ho}+3E_{\rm sw}+3E_{\rm dip}=0\ , \tag{G.30}$$

which is Eq. (G.10).

G.2 Radial virial theorem

When the perturbation operator is $A=\sum_k(\mathbf{r}_{\perp_k}\cdot\mathbf{p}_{\perp_k}+\mathbf{p}_{\perp_k}\cdot\mathbf{r}_{\perp_k})/2$, corresponding to a breathing excitation on the plane xy, then the virial reads

$$2E_{\rm kin}^{\perp}-2E_{\rm ho}^{\perp}+2E_{\rm sw}+\mathcal{E}_{\rm dip}=0\ , \tag{G.31}$$

[1] We use the property

$$x\frac{\partial\delta(\mathbf{r})}{\partial x}=-\delta(\mathbf{r})$$

of the distribution $\delta(\mathbf{r})$, which is valid under the integration sign introduced by the expectation value in Eq. (G.8).

[2] Notice that we use the following properties of the Fourier transform

$$\begin{aligned}&\mathcal{F}[\partial_x f(x)]=2\pi ik\mathcal{F}[f(x)]=2\pi ik\tilde{f}(k)\\&\partial_k\tilde{f}(k)=\partial_k\mathcal{F}[f(x)]=-2\pi i\mathcal{F}[xf(x)]\ .\end{aligned}$$

with the different terms defined as

$$E_{\rm kin}^{\perp} = \left\langle 0 \left| \sum_i \frac{p_{x_i}^2 + p_{y_i}^2}{2m} \right| 0 \right\rangle \tag{G.32}$$

$$E_{\rm ho}^{\perp} = \left\langle 0 \left| \sum_i \frac{m}{2}(\omega_x^2 x_i^2 + \omega_y^2 y_i^2) \right| 0 \right\rangle \tag{G.33}$$

$$E_{\rm sw}^{\perp} = \left\langle 0 \left| \frac{1}{2}\sum_{i\neq j} g\delta(\mathbf{r}_i - \mathbf{r}_j) \right| 0 \right\rangle \tag{G.34}$$

$$\mathcal{E}_{\rm dip} = \left\langle 0 \left| \frac{1}{2}\sum_{i\neq j} \left[3\frac{d^2}{r_{ij}^3}\frac{r_{\perp_{ij}}^2}{r_{ij}^2}\left(1 - 5\frac{z_{ij}^2}{r_{ij}^2}\right) - d^2\frac{16\pi}{15}\delta(\mathbf{r}_{ij}) \right] \right| 0 \right\rangle \ . \tag{G.35}$$

Note that $\mathcal{E}_{\rm dip}$ is not the dipolar energy, but rather the quantity that comes from the derivative of the dipolar potential as a distribution. We have checked that the virial theorem Eq. (G.31) is fulfilled by the ground state of a dipolar condensate in different harmonic trapping potentials, obtained from the numerical solution of the Gross-Pitaevskii equation Eq. (2.16).

G.2.1 Derivation of the radial virial theorem

Let us calculate the different contributions to the radial virial, Eq. (G.31), separately. We will use the results given in Sec. G.1.1 whenever possible, adapting them to the 2D geometry. Also, to simplify the notation, the summation symbols and the subscripts will be dropped, as well as the hermitian form of the operator A, since it gives exactly twice the value of the non-hermitian form, which cancels with the 1/2 in front.

For the kinetic energy term we have

$$\begin{aligned}[A, H_{\rm kin}] &= \left[\mathbf{r}_\perp \cdot \mathbf{p}_\perp, \frac{p^2}{2m}\right] = \frac{1}{2m}[xp_x + yp_y, p_x^2 + p_y^2] = \frac{1}{2m}[xp_x, p_x^2] + [yp_y, p_y^2] = \\ &= \frac{2}{2m}[x, p_x]p_x^2 + \frac{2}{2m}[y, p_y]p_y^2 = 2i\hbar\frac{p_\perp^2}{2m} \ .\end{aligned} \tag{G.36}$$

For the (harmonic) trapping potential we have

$$\begin{aligned}[A, H_{\rm ho}] &= \left[\mathbf{r}_\perp \cdot \mathbf{p}_\perp, \frac{m}{2}(\omega_x^2 x^2 + \omega_y^2 y^2 + \omega_z^2 z^2)\right] = \frac{m}{2}[xp_x + yp_y, \omega_x^2 x^2 + \omega_y^2 y^2] = \\ &= 2\frac{m\omega_x^2}{2}x^2[p_x, x] + 2\frac{m\omega_y^2}{2}y^2[p_y, y] = -2i\hbar\frac{m}{2}(\omega_x^2 x^2 + \omega_y^2 y^2) \ .\end{aligned} \tag{G.37}$$

For the contact interaction term we have (see footnote 1)

$$[A, H_{\rm g}] = [\mathbf{r}_\perp \cdot \mathbf{p}_\perp, g\delta(\mathbf{r})] = -i\hbar g\mathbf{r}_\perp \cdot \nabla_\perp \delta(\mathbf{r}) = -2i\hbar\delta(\mathbf{r}) \ . \tag{G.38}$$

For the dipolar interaction term, the situation is slightly more complicated, since the dipolar potential can not be treated as a normal function, but has to be treated as a distribution, less well known than $\delta(\mathbf{r})$. The reason for this is that (even though it is

integrable) the dipole potential Eq. (G.5) is not well defined at $r = 0$. It is a similar situation to what happens with the Coulomb potential $1/r$. One possible way to circumvent this situation is to work in Fourier space, since the Fourier transform of $v_{\rm dip}(\mathbf{r})$, given by Eq. (2.27), is well defined in all the domain. The contribution of the dipolar interaction to the commutator will be

$$[A, H_{\rm dip}] = -i\hbar \mathbf{r}_\perp \cdot \nabla_\perp v_{\rm dip}(\mathbf{r}) = -i\hbar x \partial_x v_{\rm dip}(\mathbf{r}) - i\hbar y \partial_y v_{\rm dip}(\mathbf{r}) \ . \tag{G.39}$$

Fourier transforming the commutator gives

$$\begin{aligned}
\mathcal{F}\left[A, H_{\rm dip}\right] &= +i\hbar \partial_{k_x} k_x \tilde{v}_{\rm dip}(\mathbf{k}) + i\hbar \partial_{k_y} k_y \tilde{v}_{\rm dip}(\mathbf{k}) = \\
&= -i\hbar \frac{4\pi d^2}{3} \left\{ \frac{\partial}{\partial_{k_x}} \left[k_x \left(1 - 3\frac{k_z^2}{k^2} \right) \right] + \frac{\partial}{\partial_{k_y}} \left[k_y \left(1 - 3\frac{k_z^2}{k^2} \right) \right] \right\} = \\
&= -i\hbar \frac{4\pi d^2}{3} \left\{ 1 - 3\frac{k_z^2}{k^2} + 6\frac{k_z^2 k_x^2}{k^4} + 1 - 3\frac{k_z^2}{k^2} + 6\frac{k_z^2 k_y^2}{k^4} \right\} = \\
&= 6i\hbar \frac{4\pi d^2}{3} \frac{k_z^2}{k^2} \left(1 - \frac{k_x^2 + k_y^2}{k^2} \right) - i\hbar \frac{8\pi d^2}{3} = i\hbar 8\pi d^2 \frac{k_z^4}{k^4} - i\hbar \frac{8\pi d^2}{3} = \\
&= -i\hbar 8\pi d^2 \left(\frac{1}{3} - \cos^4 \theta_p \right) \ ,
\end{aligned} \tag{G.40}$$

where we have used the expressions in footnote 2. To calculate the commutator in real space we can use expression (see Sec. G.2.2)

$$\mathcal{F}[v_\perp] = \mathcal{F}\left[\frac{1}{r^3} \frac{r_\perp^2}{r^2} \left(1 - 5\frac{z^2}{r^2} \right) \right] = -\frac{8\pi}{3} \left(\frac{1}{5} - \cos^4 \theta_p \right) \ , \tag{G.41}$$

from where we find the relation

$$\mathcal{F}\left[A, H_{\rm dip}\right] = 3i\hbar d^2 \mathcal{F}\left[\frac{1}{r^3} \frac{r_\perp^2}{r^2} \left(1 - 5\frac{z^2}{r^2} \right) \right] - i\hbar d^2 \frac{16\pi}{15} \ . \tag{G.42}$$

Transforming back to real space we find

$$[A, H_{\rm dip}] = 3i\hbar d^2 \frac{1}{r^3} \frac{r_\perp^2}{r^2} \left(1 - 5\frac{z^2}{r^2} \right) - i\hbar d^2 \frac{16\pi}{15} \delta(\mathbf{r}) \ . \tag{G.43}$$

Note that the first term on the right-hand-side is the same term that we would have obtained if we had taken the *naive* derivative (i.e. as a function instead of a distribution) of the dipolar interaction, Eq. (G.5). The second term regularizes thus the divergence of $(x\partial_x + y\partial_y)v_{\rm dip}$ at $r = 0$.

Adding all the contributions we finally find the 2D virial theorem for a dipolar condensate, as expressed in Eqs. (G.31)–(G.35).

G.2.2 Fourier transform of $v_\perp$

In this section we derive the Fourier transform of the quantity, $v_\perp$, defined as

$$\begin{aligned} v_\perp &= \frac{1}{r^3}\frac{x^2+y^2}{r^2}\left(1-5\frac{z^2}{r^2}\right) = \frac{1}{r^3}\sin^2\theta(1-5\cos^2\theta) = \\ &= -\frac{1}{r^3}\frac{1}{9}\left(2-\sqrt{\frac{16\pi}{5}}Y_{20}\right)\left(2+5\sqrt{\frac{16\pi}{5}}Y_{20}\right) = -\frac{1}{r^3}\frac{4}{9}\left(1+2\sqrt{\frac{16\pi}{5}}Y_{20}-4\pi Y_{20}^2\right) = \\ &= -\frac{1}{r^3}\frac{4}{9}\left(\sqrt{4\pi}Y_{00}+2\sqrt{\frac{16\pi}{5}}Y_{20}-4\pi Y_{20}^2\right)\ , \end{aligned} \tag{G.44}$$

where we have used the spherical harmonics

$$Y_{00} = \sqrt{\frac{1}{4\pi}} \tag{G.45}$$

$$Y_{20} = \sqrt{\frac{5}{16\pi}}(3\cos^2\theta-1) \quad \Rightarrow \quad \cos^2\theta = \frac{1}{3}\left(\sqrt{\frac{16\pi}{5}}Y_{20}+1\right) \tag{G.46}$$

$$\Rightarrow \quad \sin^2\theta = \frac{1}{3}\left(2-\sqrt{\frac{16\pi}{5}}Y_{20}\right) \tag{G.47}$$

The Fourier transform will then be

$$\begin{aligned} \mathcal{F}[v_\perp] &= \int \mathrm{d}\mathbf{r} r e^{-2\pi i\mathbf{p}\cdot\mathbf{r}} v_\perp = \int r^2 \mathrm{d}r\mathrm{d}\Omega 4\pi \sum_{\ell=0}^{\infty} i^\ell j_\ell(2\pi pr) \sum_{m=-\ell}^{m=\ell} Y_{\ell m}^*(\hat{p}) Y_{\ell m}(\hat{r}) v_\perp = \\ &= -\frac{16\pi}{9}\sum_{\ell=0}^{\infty} i^\ell \int \mathrm{d}r \frac{1}{r} j_\ell(2\pi pr) \sum_{m=-\ell}^{m=\ell} Y_{\ell m}^*(\hat{p}) \times \\ &\quad \times \int \mathrm{d}\Omega Y_{\ell m}(\hat{r}) \left(\sqrt{4\pi}Y_{00}+2\sqrt{\frac{16\pi}{5}}Y_{20}-4\pi Y_{20}^2\right) = \\ &= -\frac{16\pi}{9}\sum_{\ell=0}^{\infty} i^\ell \int \mathrm{d}r \frac{1}{r} j_\ell(2\pi pr) \sum_{m=-\ell}^{m=\ell} Y_{\ell m}^*(\hat{p}) I\ , \end{aligned} \tag{G.48}$$

where we have used the expansion of the exponential in terms of the spherical Bessel function, j_ℓ, and spherical harmonics,

$$e^{-2\pi i\mathbf{p}\cdot\mathbf{r}} = 4\pi \sum_{\ell=0}^{\infty} i^\ell j_\ell(2\pi pr) \sum_{m=-\ell}^{m=\ell} Y_{\ell m}^*(\hat{p}) Y_{\ell m}(\hat{r})\ , \tag{G.49}$$

and where we have defined the integral I as

$$\begin{aligned} I &= \int \mathrm{d}\Omega Y_{\ell m}(\hat{r}) \left(\sqrt{4\pi}Y_{00}+2\sqrt{\frac{16\pi}{5}}Y_{20}-4\pi Y_{20}^2\right) = \\ &= \sqrt{4\pi}\delta_{\ell 0}\delta_{m0} + 2\sqrt{\frac{16\pi}{5}}\delta_{\ell 2}\delta_{m0} - 4\pi \int \mathrm{d}\Omega\, Y_{20} Y_{\ell m} Y_{20}^*\ . \end{aligned} \tag{G.50}$$

The last integral can be evaluated making use of the Clebsch-Gordan coefficients

$$\int \mathrm{d}\Omega\, Y_{\ell_1 m_2} Y_{\ell_2 m_2} Y^*_{\ell_3 m_3} = \sqrt{\frac{(2\ell_1+1)(2\ell_2+1)}{4\pi(2\ell_3+1)}}\, \langle \ell_1\ell_2 00|\ell_1\ell_2\ell_3 0\rangle\, \langle \ell_1\ell_2 m_1 m_2|\ell_1\ell_2\ell_3 m_3\rangle \ . \tag{G.51}$$

We get

$$\begin{aligned}\int \mathrm{d}\Omega\, Y_{20} Y_{\ell m} Y^*_{20} &= \sqrt{\frac{5(2\ell+1)}{4\pi\cdot 5}}\, \langle 2\ell 00|2\ell 20\rangle\, \langle 2\ell 0 m|2\ell 20\rangle = \\ &= \sqrt{\frac{2\ell+1}{4\pi}}\, |\langle 2\ell 00|2\ell 20\rangle|^2\, \delta_{m0} = \left(\sqrt{\frac{1}{4\pi}}\delta_{\ell 0} + \frac{2}{7}\sqrt{\frac{5}{4\pi}}\delta_{\ell 2} + \frac{2}{7}\sqrt{\frac{9}{4\pi}}\delta_{\ell 4}\right)\delta_{m0} \ , \end{aligned} \tag{G.52}$$

since the coefficients $\langle 2000|2020\rangle = 1$, $\langle 2200|2220\rangle = -\sqrt{2/7}$ and $\langle 2400|2420\rangle = \sqrt{2/7}$ are the only ones that survive once the sum over ℓ is taken. The integral I is then

$$\begin{aligned} I &= \sqrt{4\pi}\delta_{\ell 0}\delta_{m0} + 2\sqrt{\frac{16\pi}{5}}\delta_{\ell 2}\delta_{m0} - 4\pi\left(\sqrt{\frac{1}{4\pi}}\delta_{\ell 0} + \frac{2}{7}\sqrt{\frac{5}{4\pi}}\delta_{\ell 2} + \frac{2}{7}\sqrt{\frac{9}{4\pi}}\delta_{\ell 4}\right)\delta_{m0} = \\ &= \sqrt{\frac{4\pi}{5}}\left(4 - \frac{10}{7}\right)\delta_{\ell 2}\delta_{m0} - \frac{6}{7}\sqrt{4\pi}\delta_{\ell 4}\delta_{m0} = \frac{18}{7}\sqrt{\frac{4\pi}{5}}\delta_{\ell 2}\delta_{m0} - \frac{6}{7}\sqrt{4\pi}\delta_{\ell 4}\delta_{m0} \ . \end{aligned} \tag{G.53}$$

Substituting into the expression of the Fourier transform Eq. (G.48), we find

$$\begin{aligned}\mathcal{F}[v_\perp] &= -\frac{16\pi}{9}\sum_{\ell=0}^{\infty} i^\ell \int \mathrm{d}r \frac{1}{r} j_\ell(2\pi p r) Y^*_{\ell 0}(\hat{p}) \left[\frac{18}{7}\sqrt{\frac{4\pi}{5}}\delta_{\ell 2} - \frac{6}{7}\sqrt{4\pi}\delta_{\ell 4}\right] = \\ &= \frac{32\pi}{7}\sqrt{\frac{4\pi}{5}} Y^*_{20}(\hat{p}) \int \mathrm{d}r \frac{1}{r} j_2(2\pi p r) + \frac{32\pi}{21}\sqrt{4\pi} Y^*_{40}(\hat{p}) \int \mathrm{d}r \frac{1}{r} j_4(2\pi p r) = \\ &= \frac{4}{7} 4\pi \sqrt{\frac{16\pi}{5}} Y^*_{20}(\hat{p}) \int \mathrm{d}r \frac{1}{r} j_2(2\pi p r) + \frac{32\pi}{21}\sqrt{4\pi} Y^*_{40}(\hat{p}) \int \mathrm{d}r \frac{1}{r} j_4(2\pi p r) \ . \end{aligned} \tag{G.54}$$

The integrals of the spherical Bessel functions can be calculated as follows. For the sake of clarity in the expressions we use the variable $z \equiv 2\pi p r$. The integral containing j_2 gives[3]

$$\int \mathrm{d}z \frac{1}{z} j_2(z) = \int \mathrm{d}z \frac{1}{z}\left[\left(\frac{3}{z^3} - \frac{1}{z}\right)\sin z - \frac{3}{z^2}\cos z\right] = \cdots = -\frac{\sin z}{z^3} + \frac{\cos z}{z^2} \ . \tag{G.55}$$

[3]We have used the following results for the $\sin z$ and $\cos z$ integrals,

$$\begin{aligned} \int \mathrm{d}z \frac{1}{z^n}\sin z &= -\frac{\sin z}{(n-1)z^{n-1}} + \frac{1}{n-1}\int \mathrm{d}z \frac{\cos z}{z^{n-1}} \\ \int \mathrm{d}z \frac{1}{z^n}\cos z &= -\frac{\cos z}{(n-1)z^{n-1}} - \frac{1}{n-1}\int \mathrm{d}z \frac{\sin z}{z^{n-1}} \\ \int \mathrm{d}z \frac{1}{z}\cos z &= \ln|z| + \sum_{k=1}^{\infty}(-1)^k \frac{z^{2k}}{2k\cdot(2k)!} + C \equiv I_{\cos} \ . \end{aligned}$$

This integral has to be evaluated between 0 and ∞. The second limit gives directly 0 and the first limit gives indetermination. We have to study the limit of the expression for $z \to 0$,

$$\int_0^\infty \mathrm{d}z \frac{1}{z} j_2(z) = -\lim_{z\to 0}\left[-\frac{\sin z}{z^3}+\frac{\cos z}{z^2}\right] = -\lim_{z\to 0}\left[-\frac{1}{z^2}+\frac{1}{6}+\frac{1}{z^2}-\frac{1}{2}\right] = \frac{1}{3}\,. \tag{G.56}$$

Analogously, the integral containing j_4 can be calculated as (see footnote 3)

$$\begin{aligned}\int \mathrm{d}z \frac{1}{z} j_4(z) &= \int \mathrm{d}z \frac{1}{z}\left[\left(-\frac{105}{z^4}+\frac{10}{z^2}\right)\cos z + \left(\frac{105}{z^5}-\frac{45}{z^3}+\frac{1}{z}\right)\sin z\right] = \cdots = \\ &= -21\frac{\sin z}{z^5}+21\frac{\cos z}{z^4}+8\frac{\sin z}{z^3}-\frac{\cos z}{z^2}\,.\end{aligned} \tag{G.57}$$

Again this integral has to be evaluated between 0 and ∞. The second limit gives directly 0 and the first limit gives indetermination. We have to study the limit of the expression for $z \to 0$,

$$\begin{aligned}\int_0^\infty \mathrm{d}z \frac{1}{z} j_4(z) &= -\lim_{z\to 0}\left[-21\frac{\sin z}{z^5}+21\frac{\cos z}{z^4}+8\frac{\sin z}{z^3}-\frac{\cos z}{z^2}\right] = \\ &= -\lim_{z\to 0}\left[-21\left(\frac{1}{z^4}-\frac{1}{6}\frac{1}{z^2}+\frac{1}{120}\right)+21\left(\frac{1}{z^4}-\frac{1}{2}\frac{1}{z^2}+\frac{1}{24}\right)+\right. \\ &\quad \left.+8\left(\frac{1}{z^2}-\frac{1}{6}\right)-\left(\frac{1}{z^2}-\frac{1}{2}\right)\right] = \frac{2}{15}\,.\end{aligned} \tag{G.58}$$

Substituting these two results into Eq. (G.54) gives

$$\begin{aligned}\mathcal{F}[v_\perp] &= \frac{4}{7}4\pi\sqrt{\frac{16\pi}{5}}Y_{20}^*(\hat{p})\frac{1}{3}+\frac{32\pi}{21}\sqrt{4\pi}Y_{40}^*(\hat{p})\frac{2}{15} = \\ &= \frac{16\pi}{21}(3\cos^2\theta_p-1)+\frac{4\pi}{7}\left(35\cos^4\theta_p-30\cos^2\theta_p+3\right)\frac{2}{15} = \\ &= \frac{8\pi}{3}\cos^4\theta_p+\left(\frac{16\pi}{7}-\frac{16\pi}{7}\right)\cos^2\theta_p-\frac{16\pi}{21}+\frac{8\pi}{35} = \frac{8\pi}{3}\cos^4\theta_p-\frac{8\pi}{15}\,,\end{aligned} \tag{G.59}$$

where we have used

$$Y_{40} = \frac{3}{8\sqrt{4\pi}}\left(35\cos^4\theta_p-30\cos^2\theta_p+3\right)\,. \tag{G.60}$$

Rewriting,

$$\mathcal{F}[v_\perp] = \frac{8\pi}{3}\left(\cos^4\theta_p-\frac{1}{5}\right)\,. \tag{G.61}$$

List of publications

Vortices in Bose-Einstein condensates with dominant dipolar interactions,
M. Abad, M. Guilleumas, R. Mayol, M. Pi, and D. M. Jezek, Phys. Rev. A **79**, 063622 (2009).

Dipolar condensates confined in a toroidal trap: Ground state and vortices,
M. Abad, M. Guilleumas, R. Mayol, M. Pi, and D. M. Jezek, Phys. Rev. A **81**, 043619 (2010).

Energy barriers for vortex nucleation in dipolar condensates,
M. Abad, M. Guilleumas, R. Mayol, M. Pi, and D. M. Jezek, Laser Physics **20**, 1190 (2010).

A dipolar self-induced bosonic Josephson junction,
M. Abad, M. Guilleumas, R. Mayol, M. Pi, and D. M. Jezek, EPL **94**, 10004 (2011).

Phase slippage and self-trapping in a self-induced bosonic Josephson junction,
M. Abad, M. Guilleumas, R. Mayol, M. Pi, and D. M. Jezek, Phys. Rev. A **84**, 035601 (2011).

Quadrupole oscillation in a trapped dipolar Fermi gas: hydrodynamic vs collisionless regime,
M. Abad, A. Recati, and S. Stringari, arXiv:1110.3670 (2011). Submitted to Physical Review A.

Bibliography

[Abad09] M. Abad, M. Guilleumas, R. Mayol, M. Pi, and D. M. Jezek, Phys. Rev. A **79**, 063622 (2009).

[Abad10a] M. Abad, M. Guilleumas, R. Mayol, M. Pi, and D. M. Jezek, Phys. Rev. A **81**, 043619 (2010).

[Abad10b] M. Abad, M. Guilleumas, R. Mayol, M. Pi, and D. M. Jezek, Laser Physics **20**, 1190 (2010).

[Abad11a] M. Abad, M. Guilleumas, R. Mayol, M. Pi, and D. M. Jezek, EPL **94**, 10004 (2011).

[Abad11b] M. Abad, M. Guilleumas, R. Mayol, M. Pi, and D. M. Jezek, Phys. Rev. A **84**, 035601 (2011).

[Abad11c] M. Abad, A. Recati, and S. Stringari, arXiv:1110.3670 (2011).

[Abo01] J. R. Abo-Shaeer, C. Raman, J. M. Vogels, and W. Ketterle, Science **292**, 476 (2001).

[Abr72] *Handbook of mathematical functions*, M. Abramowitz and I. A. Stegun (Dover Publications, 1972).

[Alb05] M. Albiez, R. Gati, J. Fölling, S. Hunsmann. M. Cristiani, and M. K. Oberthaler, Phys. Rev. Lett. **95**, 010402 (2005).

[Alt07] A. Altmeyer, S. Riedl, M. J. Wright, C. Kohstall, J. Hecker Denschlag, and R. Grimm, Phys. Rev. A **76**, 033610 (2007).

[Ana06] D. Ananikian and T. Bergeman, Phys. Rev. A **73**, 013604 (2006).

[And06] M. F. Andersen, C. Ryu, P. Cladé, V. Natarajan, A. Vaziri, K. Helmerson, and W. D. Phillips, Phys. Rev. Lett. **97**, 170406 (2006).

[And66] P. W. Anderson, Rev. Mod. Phys. **38**, 298 (1966).

[And95] M. H. Anderson, J. R. Ensher, M. R. Matthews, C. E. Wieman, and E. A. Cornell, Science **269**, 198 (1995).

[And00] B. P. Anderson, P. C. Haljan, C. E. Wieman, and E. A. Cornell, Phys. Rev. Lett. **85**, 2857 (2000).

[And01] B. P. Anderson, P. C. Haljan, C. A. Regal, D. L. Feder, L. A. Collins, C. W. Clark, and E. A. Cornell, Phys. Rev. Lett. **86**, 2926 (2001).

[Asad09] M. Asad-uz-Zaman and D. Blume, Phys. Rev. A **80**, 053622 (2009).

[Ave95] O. Avenel and E. Varoquaux, Phys. Rev. Lett. **55** 2704 (1985).

[Bar04] M. A. Baranov, Ł. Dobrek, and M. Lewenstein, Phys. Rev. Lett. **92**, 250403 (2004).

[Bar03] M. Barranco, M. Guilleumas, E. S. Hernández, R. Mayol, M. Pi, and L. Szybisz, Phys. Rev. B **68**, 024515 (2003).

[Bea08] Q. Beaufils, R. Chicireanu, T. Zanon, B. Laburthe-Tolra, E. Maréchal, L. Vernac, J.-C. Keller, and O. Gorceix, Phys. Rev. A **77**, 061601(R) (2008).

[Bij07] R. M. W. van Bijnen, D. H. J. O'Dell, N. G. Parker, and A. M. Martin, Phys. Rev. Lett. **98**, 150401 (2007).

[Bij09] R. M. W. van Bijnen, A. J. Dow, D. H. J. O'Dell, N. G. Parker, and A. M. Martin, Phys. Rev. A **80**, 033617 (2009).

[Bij10] R. M. W. van Bijnen, N. G. Parker, S. J. J. M. F. Kokkelmans, A. M. Martin, and D. H. J. O'Dell, Phys. Rev. A **82**, 033612 (2010).

[Bis10] G. Bismut, B. Pasquiou, E. Maréchal, P. Pedri, L. Vernac, O. Gorceix, and B. Laburthe-Tolra, Phys. Rev. Lett. **105**, 040404 (2010).

[Bla11] L. J. LeBlanc, A. B. Bardon, J. McKeever, M. H. T. Extavour, D. Jervis, J. H. Thywissen, F. Piazza, and A. Smerzi, Phys. Rev. Lett. **106**, 025302 (2011).

[Blo08] I. Bloch, J. Dalibard, and W. Zwerger, Rev. Mod. Phys. **80**, 885 (2008).

[Bose24] S. N. Bose, Z. Phys. **26**, 178 (1924).

[Bra95] C. C. Bradley, C. A. Sackett, J. J. Tollett, and R. G. Hulet, Phys. Rev. Lett. **75**, 1687 (1995).

[Bre03] V. Bretin, P. Rosenbusch, F. Chevy, G. V. Shlyapnikov, and J. Dalibard, Phys. Rev. Lett. **90**, 100403 (2003).

[Bru08] G. M. Bruun and E. Taylor, Phys. Rev. Lett. **101**, 245301 (2008).

[Cap09] P. Capuzzi and D. M. Jezek, J. Phys. B **42**, 145301 (2009).

[Cat09] H. M. Cataldo and D. M. Jezek, Eur. Phys. J. D **54**, 585 (2009).

[Cat01] F. S. Cataliotti, S. Burger, C. Fort, P. Maddaloni, F. Minardi, A. Trombettoni, A. Smerzi, and M. Inguscio, Science **293**, 843 (2001).

[Che00] F. Chevy, K. W. Madison, and J. Dalibard, Phys. Rev. Lett. **85**, 2223 (2000).

[Che01] F. Chevy, K. W. Madison, V. Bretin, and J. Dalibard, Phys. Rev. A **64**, 031601 (2001).

[Chin10] C. Chin, R. Grimm, P. Julienne, and E. Tiesinga, Rev. Mod. Phys. **82**, 1225 (2010).

[Cir98] J. I. Cirac, M. Lewenstein, M. Mølmer, and P. Zoller, Phys. Rev. A **57**, 1208 (1998).

[Coh77] *Quantum Mechanics*, C. CohenTannoudji, B. Diu and F. Laloë (Wiley-VHC, 1977).

[Coo05] N. R. Cooper, E. H. Rezayi, and S. H. Simon, Phys. Rev. Lett. **95**, 200402 (2005).

[Cor96] E. Cornell, J. Res. Natl. Inst. Stand. Technol. **101**, 419 (1996).

[Dag09a] D. Dagnino, N. Barberán, and M. Lewenstein, Phys. Rev. A **80**, 053611 (2009).

[Dag09b] D. Dagnino, N. Barberán, M. Lewenstein, and J. Dalibard, Nature Physics **5**, 431 (2009).

[Dal00] F. Dalfovo and S. Stringari, Phys. Rev. A **63**, 011601(R) (2000).

[Dal99] F. Dalfovo, S. Giorgini, L. Pitaevskii, and S. Stringari, Rev. Mod. Phys. **71**, 463 (1999).

[Dav95] K. B Davis, M.-O. Mewes, M. R. Andrews, N. J. van Druten, D. S. Durfee, D. M. Kurn, and W. Ketterle, Phys. Rev. Lett. **75**, 3969 (1995).

[Dell04] D. H. J. O'Dell, S. Giovanazzi and C. Eberlein, Phys. Rev. Lett. **92**, 250401 (2004).

[Dell07] D. H. J. O'Dell and C. Eberlein, Phys. Rev. A **75**, 013604 (2007).

[Don91] *Quantized Vortices in Helium II*, R. J. Donnelly (Cambridge University Press, Cambridge, 1991).

[Dut06] O. Dutta, M. Jääskeläinen, and P. Meystre, Phys. Rev. A **73**, 043610 (2006).

[Dut07] O. Dutta and P. Meystre, Phys. Rev. A **75**, 053604 (2007).

[Dut01] Z. Dutton, M. Budde, C. Slowe, and L. V. Hau, Science **293**, 663 (2001).

[Ebe05] C. Eberlein, S. Giovanazzi, and D. H. J. O'Dell, Phys. Rev. A **71**, 033618 (2005).

[Ein24] A. Einstein, Sitzber. Kgl. Preuss. Akad. Wiss. 261 (1924).

[Ein25] A. Einstein, Sitzber. Kgl. Preuss. Akad. Wiss. 3 (1925).

[Eng03] P. Engels, I. Coddington, P. C. Haljan, V. Schweikhard, and E. A. Cornell, Phys. Rev. Lett. **90**, 170405 (2003).

[Fat08] M. Fattori, G. Roati, B. Deissler, C. D'Errico, M. Zaccanti, M. Jona-Lasinio, L. Santos, M. Inguscio, and G. Modugno, Phys. Rev. Lett. **101**, 190405 (2008).

[Fet09] A. L. Fetter, Rev. Mod. Phys. **81**, 647 (2009).

[Fri98] D. G. Fried, T. C. Killian, L. Willmann, D. Landhuis, S. C. Moss, D. Kleppner, and T. J. Greytak, Phys. Rev. Lett. **81**, 3811 (1998).

[Fri05] M. Frigo and S. G. Johnson, Proc. IEEE **93**, 216 (2005).

[Gio08] S. Giorgini, L. P. Pitaevskii, and S. Stringari, Rev. Mod. Phys. **80**, 1215 (2008).

[Gio00] S. Giovanazzi, A. Smerzi, and S. Fantoni, Phys. Rev. Lett. **84**, 4521 (2000).

[Gio02] S. Giovanazzi, A. Görlitz, and T. Pfau, Phys. Rev. Lett. **89**, 130401 (2002).

[Gio06] S. Giovanazzi, P. Pedri, L. Santos, A. Griesmaier, M. Fattori, T. Koch, J. Stuhler, and T. Pfau, Phys. Rev. A **74**, 013621 (2006).

[Gor00] K. Góral, K. Rzążewski and T. Pfau, Phys. Rev. A **61**, 051601(R) (2000); see also [Mar01a].

[Gor02] K. Góral and L. Santos, Phys. Rev. A **66**, 023613 (2002).

[Gor03] K. Góral, M. Brewczyk, and K. Rzążewski, Phys. Rev. A **67**, 025601 (2003).

[Gri05] A. Griesmaier, J. Werner, S. Hensler, J. Stuhler, and T. Pfau, Phys. Rev. Lett. **94**, 160401 (2005).

[Gro61] E. P. Gross, Nuovo Cimiento **20**, 454 (1961).

[Gui01] M. Guilleumas and R. Graham, Phys. Rev. A **64**, 033607 (2001).

[Hal01] P. C. Haljan, I. Coddington, P. Engels, and E. A. Cornell, Phys. Rev. Lett. **87**, 210403 (2001).

[Henn09a] E. A. L. Henn, J. A. Seman, E. R. F. Ramos, M. Caracanhas, P. Castilho, E. P. Olimpio, G. Roati, D. V. Magalhes, K. M. F. Magalhes, and V. S. Bagnato, Phys. Rev. A **79**, 043618 (2009).

[Henn09b] E. A. L. Henn, J. A. Seman, G. Roati, K. M. F. Magalhaes, and V. S. Bagnato, Phys. Rev. Lett. **103**, 045301 (2009).

[Hod02] E. Hodby, G. Hechenblaikner, S. A. Hopkins, O. M. Maragò, and C. J. Foot, Phys. Rev. Lett. **88**, 010405 (2002).

[Hos05] E. Hoskinson, R. E. Packard, and T. M. Haard, Nature **433**, 376 (2005); see also E. Hoskinson, Y. Sato, I. Hahn, and R. E. Packard, Nature Physics **2**, 23 (2006).

[Hua63] *Statistical Mechanics*, K. Huang (John Wiley & Sons, 1963).

[Hua10] C.-C. Huang and W.-C. Wu, Phys. Rev. A **82**, 053612 (2010).

[Jac99] *Classical Electrodynamics*, J. D. Jackson (3rd edition, John Wiley & Sons, 1999).

[Jez08a] D. M. Jezek, P. Capuzzi, and H. M. Cataldo, J. Phys. B: At. Mol. Opt. Phys. **41**, 045304 (2008).

[Jez08b] D. M. Jezek, P. Capuzzi, M. Guilleumas, and R. Mayol, Phys. Rev. A **78**, 053616 (2008).

[Joc03] S. Jochim, M. Bartestein, A. Altmayer, G. Hendl, S. Riedl, C. Chin, J. Hecker Denschlag, and R. Grimm, Science **302**, 2101 (2003).

[Jul10a] B. Juliá-Díaz, D. Dagnino, M. Lewenstein, J. Martorell, and A. Polls, Phys. Rev. A **81**, 023615 (2010).

[Jul10b] B. Juliá-Díaz, J. Martorell, M. Melé-Messeguer, and A. Polls, Phys. Rev. A **82**, 063626 (2010).

[Kas03] K. Kasamatsu, M. Tsubota and M. Ueda, Phys. Rev. A **67**, 033610 (2003).

[Kla08] M. Klawunn, R. Nath, P. Pedri, and L. Santos, Phys. Rev. Lett. **100**, 240403 (2008).

[Kla09] M. Klawunn and L. Santos, New J. Phys. **11** (5), 055012 (2009).

[Koch08] T. Koch, T. Lahaye, J. Metz, B. Fröhlich, A. Griesmaier, and T. Pfau, Nature Physics **4**, 220 (2008).

[Koh06] T. Köhler, K. Góral, and P. S. Julienne, Rev. Mod. Phys. **78**, 1311 (2006).

[Kom07] S. Komineas and N. R. Cooper, Phys. Rev. A **75**, 023623 (2007).

[Kra02] M. Krämer, L. P. Pitaevskii, S. Stringari, and F. Zambelli, Laser Physics **12**, 113 (2002).

[Kra09] S. Kraft, F. Vogt, O. Appel, F. Riehle, and U. Sterr, Phys. Rev. Lett. **103**, 130401 (2009).

[Lag10] L. G. Lagoudakis, B. Pietka, M. Wouters, R. André, and B. Deveaud-Plédran, Phys. Rev. Lett. **105**, 120403 (2010).

[Lah07] T. Lahaye, T. Koch, B. Fröhlich, M. Fattori, J. Metz, A. Griesmaier, S. Giovanazzi, and T. Pfau, Nature **448**, 672 (2007).

[Lah08] T. Lahaye, J. Metz, B. Fröhlich, T. Koch, M. Meister, A. Griesmaier, T. Pfau, H. Saito, Y. Kawaguchi, and M. Ueda, Phys. Rev. Lett. **101**, 080401 (2008).

[Lah09] T. Lahaye, C. Menotti, L. Santos, M. Lewenstein, and T. Pfau, Rep. Prog. Phys. **72**, 126401 (2009).

[Lah10] T. Lahaye, T. Pfau, and L. Santos, Phys. Rev. Lett. **104**, 170404 (2010); see also *ibid.* **105**, 239904 (2010).

[Leg01] A. J. Leggett, Rev. Mod. Phys. **73**, 307 (2001).

[Levy07] S. Levy, E. Lahoud, I. Shomroni, and J. Steinhauer, Nature **449**, 579 (2007).

[Lima10a] A. R. P. Lima and A. Pelster, Phys. Rev. A **81**, 021606(R) (2010).

[Lima10b] A. R. P. Lima and A. Pelster, Phys. Rev. A **81**, 063629 (2010).

[Lima11] A. R. P. Lima and A. Pelster, arXiv:1111.0900 (2011).

[Lip03] *Modern Many-Particle Physics. Atomic Gases, Quantum Dots and Quantum Fluids*, E. Lipparini (World Scientific, 2003).

[Lobo04] C. Lobo, A. Sinatra and Y. Castin, Phys. Rev. Lett. **92**, 020403 (2004).

[Lon38] F. London, Nature (London) **141**, 643 (1938).

[Lu10] H.-Y. Lu, H. Lu, J.-N. Zhang, R.-Z. Qiu, H. Pu, and S. Yi, Phys. Rev. A **82**, 023622 (2010).

[Lu11] M. Lu, N. Q. Burdick, S. H. Youn, and B. L. Lev, Phys. Rev. Lett. **107**, 190401 (2011).

[Lun97] E. Lundh, C. J. Pehtick, and H. Smith, Phys. Rev. A **55**, 2126 (1997).

[Mad00] K. W. Madison, F. Chevy, W. Wohlleben, and J. Dalibard, Phys. Rev. Lett. **84**, 806 (2000).

[Mad01] K. W. Madison, F. Chevy, V. Bretin, and J. Dalibard, Phys. Rev. Lett. **86**, 4443 (2001).

[Maik11] M. Maik, P. Buonsante, A. Vezzani, and J. Zakrzewski, arXiv:1107.1103v2 (2011).

[Mal10] F. Malet, G. M. Kavoulakis, and S. M. Reimann, Phys. Rev. A **81**, 013630 (2010).

[Mal11a] F. Malet, T. Kristensen, S. M. Reimann, G. M. Kavoulakis, Phys. Rev. A **83**, 033628 (2011).

[Mal11b] F. Malet, G. M. Kavoulakis, and S. M. Reimann, Phys. Rev. A **84**, 043626 (2011).

[Mar01a] J.-P. Martikainen, M. Mackie, and K.-A. Suominen, Phys. Rev. A **64**, 037601 (2001).

[Mar01b] J.-P. Martikainen, K.-A. Suominen, L. Santos, T. Schulte, and A. Sanpera, Phys. Rev. A **64**, 063602 (2001).

[Mar09] Y. N. Martinez de Escobar, P. G. Mickelson, M. Yan, B. J. DeSalvo, S. B. Nagel, and T. C. Killian, Rhys. Rev. Lett. **103**, 200402 (2009).

[Mas09] P. Mason and N. G. Berloff, Phys. Rev. A **79**, 043620 (2009).

[Mat99] M. R. Matthews, B. P. Anderson, P. C. Haljan, D. S. Hall, C. E. Wieman, and E. A. Cornell, Phys. Rev. Lett. **83**, 2498 (1999).

[Mat11] N. Matveeva, A. Recati, and S. Stringari, Eur. Phys. J. D **65**, 219 (2011).

[Maz09] F. Mazzanti, R. E. Zillich, G. E. Astrakharchik, and J. Boronat, Phys. Rev. Lett. **102**, 110405 (2009).

[Mele11] M. Melé-Messeguer, B. Juliá-Díaz, M. Guilleumas, A. Polls, and A. Sanpera, New J. Phys. **13**, 033012 (2011).

[Metz09] J. Metz, T. Lahaye, B. Fröhlich, A. Griesmaier, T. Pfau, H. Saito, Y. Kawaguchi, and M. Ueda, New J. Phys. **11**, 055032 (2009).

[Mir11] M. H. G de Miranda, A. Chotia, B. Neyenhuis, D. Wang, G. Quéméner, S. Ospelkaus, J. L. Bohn, J. Ye and D. S. Jin, Nat. Phys. **7**, 502 (2011).

[Miy08] T. Miyakawa, T. Sogo and H. Pu, Phys. Rev. A **77**, 061603(R) (2008).

[Mod01] G. Modugno, G. Ferrari, G. Roati, R. J. Brecha, A. Simone, and M. Ignuscio, Science **294**, 1320 (2001).

[Nee10] T.W. Neely, E. C. Samson, A. S. Bradley, M. J. Davis, and B. P. Anderson, Phys. Rev. Lett. **104**, 160401 (2010).

[Ni08] K.-K. Ni, S. Ospelkaus, M. G. H. de Miranda, A. Pe'er, B. Neyenhuis, J. J. Zirbel, S. Kotochigova, P. S. Julienne, D. S. Jin, and J. Ye, Science **322**, 231 (2008).

[Par09] N. G. Parker, C. Ticknor, A. M. Martin, and D. H. J. O'Dell, Phys. Rev. A **79**, 013617 (2009).

[Pat88] *Statistical Mechanics*, R. K. Pathria (Pergamon Press, 1988).

[Per97] S. V. Pereverzev, A. Loshak, S. Backhaus, J. C. Davis, and R. E. Packard, Nature **388**, 449 (1997).

[Pet02] *Bose-Einstein condensation in dilute gases*, C. J. Pethick and H. Smith (Cambridge University Press, 2002).

[Pia09] F. Piazza, L. A. Collins, and A. Smerzi, Phys. Rev. A **80**, 021601 (2009).

[Pia11] F. Piazza, L. A. Collins, and A. Smerzi, arXiv: 1011.5041v2 (2011).

[Pit61] L. P. Pitaevskii, Zh. Eksp. Teor. Fiz. **40**, 646 (1961); Sov. Phys. JETP **13**, 451 (1961).

[Pit03] *Bose-Einstein Condensation*, L. Pitaevskii and S. Stringari (Clarendon Press, Oxford, 2003).

[Pol09] S. E. Pollack, D. Dries, M. Junker, Y. P. Chen, T. A. Corcovilos, and R. G. Hulet, Phys. Rev. Lett. **102**, 090402 (2009).

[Rag99] S. Raghavan, A. Smerzi, S. Fantoni, and S. R. Shenoy, Phys. Rev. A **59**, 620 (1999).

[Ral60] *Mathematical methods for digital computers* (Vol. I), A. Ralston and H. S. Wilf (John Wiley & Sons, 1960).

[Ram99] C. Raman, M. Khl, R. Onofrio, D. S. Durfee, C. E. Kuklewicz, Z. Hadzibabic, and W. Ketterle, Phys. Rev. Lett. **83**, 2502 (1999).

[Ram11] A. Ramanathan, K. C. Wright, S. R. Muniz, M. Zelan, W. T. Hill, III, C. J. Lobb, K. Helmerson, W. D. Phillips, and G. K. Campbell, Phys. Rev. Lett. **106**, 130401 (2011).

[Reg04] C. A. Regal, M. Greiner and D. S. Jin, Phys. Rev. Lett. **92**, 040403 (2004).

[Rob01] A. Robert, O. Sirjean, A. Browaeys, J. Poupard, S. Nowak, D. Boiron, C. I. Westbrook, and A. Aspect, Science **292**, 461 (2001).

[Ron06a] S. Ronen, D. C. E. Bortolotti and J. L. Bohn, Phys. Rev. A **74**, 013623 (2006).

[Ron06b] S. Ronen, D. C. E. Bortolotti, D. Blume, and J. L. Bohn, Phys. Rev. A **74**, 033611 (2006).

[Ron07] S. Ronen, D. C. E. Bortolotti and J. L. Bohn, Phys. Rev. Lett. **98**, 030406 (2007);

[Ryu07] C. Ryu, M. F. Andersen, P. Cladé, Vasant Natarajan, K. Helmerson, and W. D. Phillips, Phys. Rev. Lett. **99**, 260401 (2007).

[San00] L. Santos, G. V. Shlyapnikov, P. Zoller, and M. Lewenstein, Phys. Rev. Lett. **85**, 1791 (2000).

[San03] L. Santos, G. Shlyapnikov, and M. Lewenstein, Phys. Rev. Lett. **90**, 250403 (2003).

[Sch07] D. R. Scherer, C. N. Weiler, T. N. Neely, and B. P. Anderson, Phys. Rev. Lett. **98**, 110402 (2007).

[Sho09] I. Shomroni, E. Lahoud, S. Levy and J. Steinhauer, Nat. Phys. **5**, 193 (2009).

[Sme97] A. Smerzi, S. Fantoni, S. Giovanazzi, and S. R. Shenoy, Phys. Rev. Lett. **79**, 4950 (1997).

[Sme03] A. Smerzi and A. Trombettoni, Phys. Rev. A **68**, 023613 (2003).

[Sogo09] T. Sogo, L. He, T. Miyakawa, S. Yi, H. Lu and H. Pu, New J. Phys. **11**, 055017 (2009).

[Ste09] S. Stellmer, M. K. Tey, B. Huang, R. Grimm, and F. Schreck, Phys. Rev. Lett. **103**, 200401 (2009).

[Str96] S. Stringari, Phys. Rev. Lett. **77**, 2360 (1996).

[Stu05] J. Stuhler, A. Griesmaier, T. Koch, M. Fattori, T. Pfau, S. Giovanazzi, P. Pedri, and L. Santos, Phys. Rev. Lett. **95**, 150406 (2005).

[Sun10] K. Sun, C. Wu, and S. Das Sarma, Phys. Rev. B **82**, 075105 (2010).

[Svi00] A. A. Svidzinsky and A. L. Fetter, Phys. Rev. A **62**, 063617 (2000).

[Tak03] Y. Takasu, K. Maki, K. Komori, T. Takano, K. Honda, M. Kumadura, T. Yabuzaki, and Y. Takahashi, Phys. Rev. Lett. **91**, 040404 (2003).

[Tic08] C. Ticknor, N. G. Parker, A. Melatos, S. L. Cornish, D. H. J. O'Dell, and A. M. Martin, Phys. Rev. A **78**, 061607(R) (2008).

[Tic10] C. Ticknor, R. M. Wilson, and J. L. Bohn, Phys. Rev. Lett. **106**, 065301 (2011).

[Tin96] *Introduction to Superconductivity*, M. Tinkham (McGraw-Hill, New York, 1996).

[Tre11] C. Trefzger, C. Menotti, B. Capogrosso-Sansone, and M. Lewenstein, J. Phys. B: At. Mol. Opt. Phys. **44**, 193001 (2011).

[Tsu02] M. Tsubota, K. Kasamatsu, and M. Ueda, Phys. Rev. A **65**, 023603 (2002).

[Vic99] L. Vichi and S. Stringari, Phys. Rev. A **60**, 4734 (1999).

[Web03] T. Weber, J. Herbig, M. Mark, H.-C. Nägerl, and R. Grimm, Science **299**, 232 (2003).

[Wei08] C. N. Weiler, T. W. Neely, D. R. Scherer, A. S. Bradley, M. J. Davis, and B. P. Anderson, Nature **455**, 948 (2008).

[Wer05] J. Werner, A. Griesmaier, S. Hensler, J. Stuhler, and T. Pfau, Phys. Rev. Lett. **94**, 183201 (2005).

[Wil08] R. W. Wilson, S. Ronen, and J. L. Bohn, Phys. Rev. Lett. **100**, 245302 (2008).

[Wil09a] R. M. Wilson, S. Ronen, and J. L. Bohn, Phys. Rev. A **79**, 013621 (2009).

[Wil09b] R. M. Wilson, S. Ronen, and J. L. Bohn, Phys. Rev. A **80**, 023614 (2009).

[Xio09] B. Xiong, J. Gong. H. Pu, W. Bao, and B. Li, Phys. Rev. A **79**, 013626 (2009).

[Yas10] M. Yasunaga and M. Tsubota, Phys. Rev. A **81**, 023624 (2010).

[Yi02] S. Yi and L. You, Phys. Rev. A **66**, 013607 (2002).

[Yi06] S. Yi and H. Pu, Phys. Rev. A **73**, 061602(R) (2006).

[Yuce10] C. Yuce and Z. Oztas, J. Phys. B: At. Mol. Opt. Phys. **43**, 135301 (2010).

[Zam98] F. Zambelli and S. Stringari, Phys. Rev. Lett. **81**, 1754 (1998).

[Zar09] *Bose-condensed Gases at Finite Temperatures*, E. Zaremba, A. Griffin, and T. Nikuni (Cambridge University Press, 2009).

[Zib10] T. Zibold, E. Nicklas, C. Gross, and M. Oberthaler, Phys. Rev. Lett. **105**, 204101 (2010).

[Zol11] S. Zöllner, G. M. Bruun, C. J. Pethick, and S. M. Reimann, Phys. Rev. Lett. **107**, 035301 (2011).

[Zha05] J. Zhang and H. Zhai, Phys. Rev. Lett. **95**, 200403 (2005).

[Zha09] J.-N. Zhang and S. Yi, Phys. Rev. A **80**, 053614 (2009).

[Zwi03] M. W. Zwierlein, C. A. Stan, C. H. Schunck, S. M. F. Raupach, S. Gupta, Z. Hadzibabic, and W. Ketterle, Phys. Rev. Lett. **91**, 250401 (2003).